# Aircraft Wake Vortex Evolution and Prediction

Das Verhalten von Flugzeug-Wirbelschleppen und ihre Vorhersage

presented to the

Faculty of Mechanical Engineering of the Technical University Munich

in order to obtain the postdoctoral lecture qualification in Fluid Mechanics

der Fakultät für Maschinenwesen der Technischen Universität München zur

Habilitation im Fachgebiet der Strömungsmechanik

vorgelegte wissenschaftliche Arbeit

Dr.-Ing. Frank Holzäpfel

| | |
|---|---|
| Day of Colloquium / Tag des Kolloquiums: | 12 October 2005 / 12. Oktober 2005 |
| Chairman / Vorsitzender: | Prof. Dr.-Ing. habil. Rudolf Schilling |
| 1. Referee / 1. Berichterstatter: | Prof. Dr.-Ing. habil. Ulrich Schumann |
| 2. Referee / 2. Berichterstatter: | Prof. Dr.-Ing. habil. Rainer Friedrich |

*to Marcela*

## Abstract

Aircraft trailing vortices constitute both a kaleidoscope of instructive fluid dynamics phenomena and a challenge for the sustained development of safety and capacity of the air-transportation industry. The current manuscript gives an overview on the wake vortex issue which commences at its historical roots and concludes with the current status of knowledge regarding the nature and characteristics, and the modeling of aircraft wakes. The incentive of today's wake vortex research still rests on the empirically motivated separation standards between consecutive aircraft introduced in the 1970s. These aircraft separations fix the capacity of congested airports in a rapidly growing aeronautical environment. Advanced solutions for dynamically adjusted weather-dependent aircraft separations hold significant economizations without compromising safety. Appropriate separation distances are also crucial for the success of the twin-deck A380 airliner which will enter service in 2006. On the search for technical answers, applied wake vortex research must always consider its complex operational, political, and business environment and it must be aware of its serious responsability for passenger safety. The extensive introductory survey concludes with a delineation of scientific windows on wake vortex physics, connected chances and limitations, and a list of controversial issues that motivate the author's contributions to the field. The second part of the manuscript guides through these contributions which are detailed in eight integrated journal publications. Four of these papers treat the analysis of wake vortex evolution and decay in the stably stratified, sheared, turbulent, and convective atmospheric boundary layer and lead to a theoretical foundation for the physics of vortex decay. A subgrid-scale closure modification for large eddy simulation with strong streamline curvature is suggested and the accuracy of lidar measurements of wake vortices is assessed. Finally, the devised parametric real-time wake vortex prediction model is introduced. Validations against observation data from five different field deployments indicate that the probabilistic model has reached a high degree of maturity which suggests that the model may enter operational use in the near future.

## Zusammenfassung

Die zahlreichen Facetten des Themas Wirbelschleppe enstehen aus dem Spannungsfeld einer beeinduckenden Vielfalt instruktiver und nur zum Teil verstandener fluiddynamischer Phänomene und der grundlegenden Herausforderung, die Wirbelschleppen für die nachhaltige Entwicklung der zivilen Luftfahrt darstellen. Das vorliegende Manuskript gibt eine Übersicht über verschiedene Aspekte des Themas, die bei den historischen Wurzeln der Erforschung der Wirbelschleppe beginnt und mit dem aktuellen Wissensstand bezüglich ihrer Eigenschaften und Modellierung schließt. Nach wie vor leitet sich die Motivation aktueller Wirbelschleppenforschung von der Einführung empirischer Sicherheitsabstände zwischen aufeinanderfolgenden Flugzeugen in den siebziger Jahren ab. Diese Mindestabstände fixieren die Kapazität verkehrsreicher Flughäfen in einem schnell wachsenden wirtschaftlichen Umfeld. Ein beträchtliches Potenzial zur Erhöhung der Kapazität großer Flughäfen, bei mindestens gleichbleibender Sicherheit, liegt in der Entwicklung von Systemen für dynamische wetterabhängige Flugzeugstaffelungen. Auch für den Markterfolg des doppelstöckigen Großraumflugzeugs A380, das im Jahr 2006 den kommerziellen Betrieb aufnehmen wird, sind angemessene Sicherheitsabstände von maßgeblich Bedeutung. Jegliche Systeme zur Erhöhung der Flughafenkapazität müssen stets das vielschichtige operationelle, wirtschaftliche und politische Umfeld der Wirbelschleppenproblematik berücksichtigen; insbesonders aber muss die angewandte Wirbelschleppenforschung ihrer großen Verantwortung für die Sicherheit der Passagiere gerecht werden. Eine Liste kontroverser Fragestellungen, die die Beiträge des Autors zum Thema motivieren, leitet in den zweiten Teil des Manuskripts über. Dieser führt durch acht ausgewählte und in das Manuskript eingebundene Zeitschriftenveröffentlichungen. Vier dieser Veröffentlichungen behandeln das Verhalten der Wirbelschleppe und ihres Zerfalls in der stabil geschichteten, gescherten, turbulenten und konvektiven atmosphärischen Grenzschicht. Wesentliche Mechanismen der Wirbelschleppenentwicklung werden herausgearbeitet und in verallgemeinerter Form dargestellt. Eine Korrektur für Schließungsansätze der Grobstruktursimulation mit starker Stromlinienkrümmung wird entwickelt und Strategien zur Messung der Wirbelschleppe mittels Lidar Techniken werden vorgestellt und bewertet. Abschließend wird ein parametrisches Modell zur Echtzeitvorhersage von Wirbelschleppen präsentiert. Die Validierung mittels Daten aus fünf Feldmesskampagnen verdeutlicht, dass das probabilistische Modell einen hohen Reifegrad erreicht hat, der es ermöglicht, das Modell bereits in naher Zukunft zur Optimierung von Flugzeugstaffelungen einzusetzen.

# Contents

# 1 Introduction

As an unavoidable consequence of lift, aircraft generate a pair of counter-rotating vortices, the so-called wing-tip vortices, aircraft trailing vortices, or aircraft wake vortices. Already one century ago, the significance of these vortices was recognized by Lanchester (1907) and Prandtl (1918, 1919) during their pioneering search for a theory of human flight. The conceived Lifting-Line Theory recognizes that the strength of the bound vortex*, expressed as its circulation $\Gamma$, decreases from the wing's root towards its tips (see Figure 1). As a consequence, vorticity detaches from the wing continuously and forms a trailing vortex sheet. This vortex sheet rolls up at its ends driven by self-induction and generates the trailing vortices (see Figure 2). The theory further elucidates the generation of induced drag which is zero for an airfoil of infinite span. For wings of finite span, the induced drag arises from an effective reduction of the wing's attitude which is caused by the downwash induced ahead of the wing by the trailing vortices. The induced drag roughly equals the kinetic energy of the wake vortices and can be understood in analogy to the wave drag experienced by a ship.

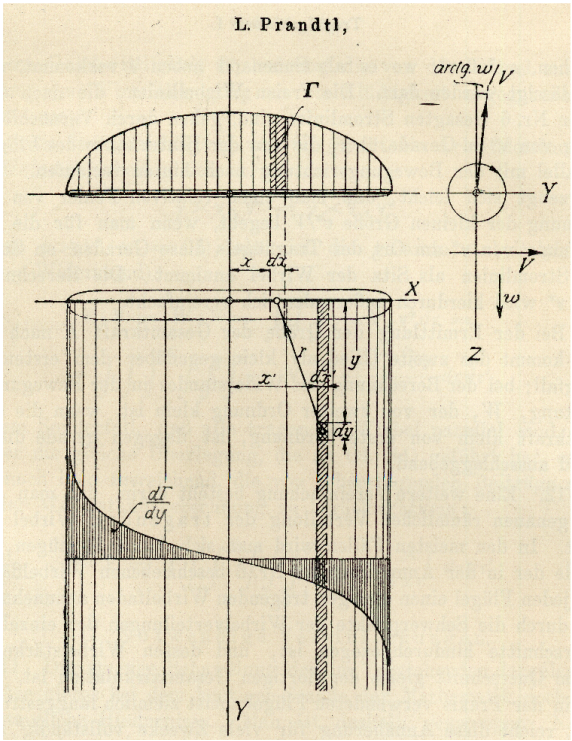


Figure 1: Prandtl's sketch illustrating the elliptical circulation distribution along the lifting line (above) and the detachment of differential vortex filaments (below).

Further descriptive explanations for wake vortex formation are: (i) The pressure difference between suction side and pressure side of the wing accelerates fluid around the wing tips and thus initiates a pair of counter-rotating vortices trailing behind. Another demonstrative approach (ii) uses the notion that the fluid exerts an upward lift force on the wing, and, therefore, the aircraft wings deflect freestream flow downwards imparting a downwards directed momentum onto the fluid. At the edges of the generated uniform downwash, a shear layer develops which rolls up to the wake vortex pair. (iii) Finally, the first Helmholtz vortex theorem states that a vortex tube cannot end within the fluid. It must either end at a solid boundary or form a closed loop. For trailing vortices, the closed loop consists of the bound vortex

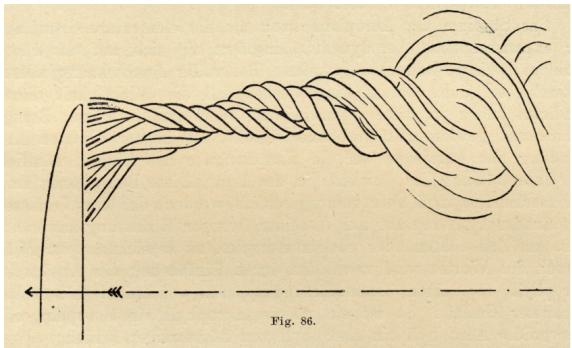


Figure 2: Lanchester's perception of vortex roll-up and decay about one century ago.

*The bound vortex is a hypothetical vortex filament located on a lifting line which represents a straight wing. In a uniform flow perpendicular to its axis, the bound vortex experiences a lift force according to the Kutta-Zhukhovski lift theorem.

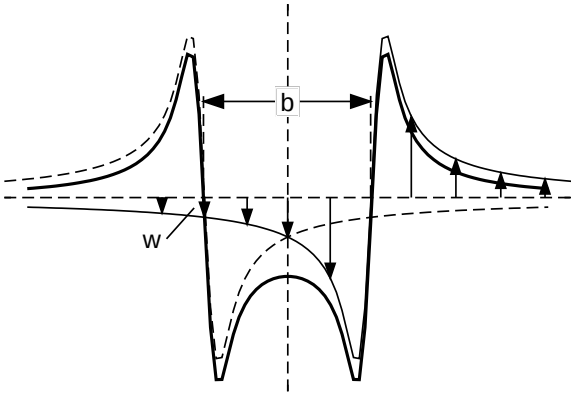


Figure 3: Schematic of vertical velocity profiles of two counter-rotating vortices (fine lines) separated by $b$ and corresponding vertical velocity envelope (bold line).

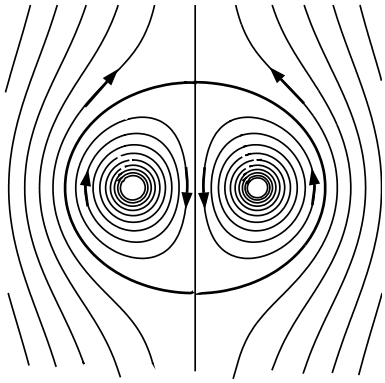

Figure 4: Streamlines of the vortex pair in a coordinate system descending with the vortices.

along the wings, it is continued by the trailing vortices and completed by the starting vortex.

The strength of wake vortices is usually expressed by their circulation, $\Gamma$. When the forces which act on the aircraft are in balance, the initial circulation corresponds approximately to

$$\Gamma_0 = \frac{Mg}{\pi/4\ \rho B V} \quad . \tag{1}$$

Thus, the strength of the vortices is proportional to the weight of the aircraft, $Mg$, and inversely proportional to the air density, $\rho$, the wing span, $B$, and the flight velocity, $V$. Interestingly, the circulation achieves similar magnitudes for both a cruising aircraft at high altitude and an aircraft during approach to an airport at low altitude because the inverse variation of flight velocity and air density roughly compensate each other, respectively.

Due to the major difficulties connected with measurements in the vicinity of high-Reynolds-number wake vortex cores, there is no common agreement on the actually prevailing tangential velocity profiles in wake vortices. Several vortex models are available (Gerz et al. 2002) which are at least consistent with respect to their limits: They approach a forced vortex in the vortex center and a potential vortex on large radii. Notable extremal values have been measured in the transition zone between these regimes. Maximum peak tangential velocities of 99 m/s have been determined for a B757 vortex on a 200-foot tower equipped with hot-film anemometers (Garodz and Clawson 1993). The corresponding minimum wake vortex core radii may be less than 1% of the wingspans of aircraft with retracted flaps (Delisi et al. 2003).

As depicted in Figure 3, the vortices mutually induce a descent speed which amounts to

$$w = \frac{\Gamma}{2\pi b} \quad , \tag{2}$$

where $b$ denotes the vortex separation. Initial descent speeds of trailing vortices of commercial aircraft range from 1 to 2 m/s and maximum descent distances may reach out more than 300 m. During the descent the vortex pair transports fluid within an oval-shaped streamline (see Fig. 4, Lamb 1879) which connects two stagnation points above and below the vortices, respectively. The motion at external points corresponds to the inviscid flow around an equally-shaped rigid body. This quasi inviscid flow topology explains the low drag of the descending oval and the sizeable descent distances travelled by wake vortices.

The impulse or momentum of the oval per unit length

$$I = \rho b \Gamma \tag{3}$$

consists of contributions from translational momentum of the descending oval and from angular momentum of the rotating vortices (Holzäpfel and Gerz 1999).

Characteristic scales used for normalization of wake vortex parameters consist of the initial vortex separation, $b_0$, and the time $t_0 = b_0/w_0$ that the vortex pair initially takes to descend one vortex spacing.

Depending on meteorological conditions, wake vortices may persist for several minutes and, therefore, may pose a potential risk to aircraft following behind. Serious problems with wake vortices were first recognized back in the 1970s when the Boeing 747 came into service. To avoid wake-vortex encounters, the Federal Aviation Administration (FAA) and the International Civil Aviation Organization (ICAO) established separation standards between consecutive aircraft. These separation distances vary between 3 and 6 nautical miles for different combinations of a $3 \times 3$ weight class matrix for preceding and follower aircraft on approach.

No accident under adherence to separation standards is reported to date, indicating that the currently effective separation standards, which are largely empirical and lack full rationale, are sufficient. On the other hand, flying through wake vortices turned out to be almost daily practise. Flight data recorder analyses performed within the European project S-Wake indicate more than one wake vortex encounter every 200 approaches to London-Heathrow Airport (de Bruin 2003), yet without serious consequences. An explanation is that aircraft reactions to wake vortex encounters make it extremly unlikely to hit the hazardous vortex core region. Therefore, pilots often do not even attribute the encountered turbulence to wake vortices.

If, however, separation standards are not obeyed, which is common practice under Visual Flight Rule (VFR) conditions, severe encounters may occur. Statistics state (Aviation Week 2002) that aircraft wake turbulence constituted the most frequent reason for loss of control (almost 100 incidents) of multiengine turbojet within a time period from 1987 to 1995.

Unfortunately, the currently effective separation standards may heavily degrade aviation efficiency when traffic congestion limits airport capacity during landing and take-off. A system that would allow to relax current aircraft separations under favorable weather conditions, whilst keeping safety at least at the same level, could provide significant economizations. Hemm et al. (1999) estimate annual savings of $15 million per year and airport as an average over 10 international US airports. This estimation accounts only for cost avoidance based on reductions in arrival delays. Savings due to reduced departure delays, value of passenger time, additional airline revenue, avoidance of runway or airport construction and airline relocation are not considered.

With the Airbus A380 an aircraft with larger span and larger weight as the currently operating transport aircraft will enter airline service in 2006. The twin-deck, four-aisle airliner will be less attractive if its advantage in terms of arriving seats per hour will be diminished by increased separations. In order to verify whether current operational standards are still adequate for the A380, existing knowledge and tools have to be utilized for the assessment of potential risks exerted by A380 wake vortices on following aircraft (Holzäpfel et al. 2004).

The development of a sustainable system that aims to re-stagger aircraft separations necessitates an interdisciplinary effort where disciplines like fluid dynamics, flight dynamics, and flight guidance must cooperate tightly. The final acceptance of such a system though, requires early cooperation between a much larger community of interest groups. Research groups must cultivate the discourse with aircraft manufacturers, air traffic control, and airport service providers, aviation authorities, airlines, and pilots. But already

simply the fluid dynamics part comprises a kaleidoscope of instructive and only partly understood phenomena. For example, the impact of rotation on turbulence, which may give rise to strong anisotropy and may impede dissipation, represents a fundamental research topic that is not likely to be solved in near future.

A principal objective of wake vortex research is first to understand and then predict, or even accelerate vortex decay.[†] However, the longevity of wake vortices inhibits investigations of vortex decay in wind tunnels and complicates them in unusual facilities like catapults and large towing tanks. The only and indispensable access to real wake vortex behavior is provided by lidar measurement techniques[‡] that trace full-scale wake vortices in the free atmosphere. Here, environmental conditions that can neither be controlled nor reproduced have a strong impact on vortex evolution. Furthermore, advection of the vortices beyond the observation domain and intrinsic difficulties connected with the interpretation of the complex velocity fields of eroded wake vortices impede detailed insights into vortex decay mechanisms.

As a consequence, high-resolution numerical simulation constitutes an essential resource in order to elaborate comprehensive understanding of vortex decay characteristics. The great advantage is that all desired quantities are readily available for analysis. Unfortunately, numerical simulations of wake vortices in the atmosphere unavoidably suffer from limited resolution, in particular, in the vortex core region. Whereas direct numerical simulation (DNS) only reaches small Reynolds numbers, it is the type of subgrid-scale closure that controls vortex core evolution in large eddy simulation (LES). Both approaches do not meet the complex interaction of turbulence and rotation at high Reynolds-number flows together with the peculiarities of specific aircraft configurations and environmental conditions. Such limitations will persist despite the enormous increase of computational power and the development of smart numerical methods. Full-scale experiments remain both challenging and mandatory to ensure the validity of the conclusions drawn from numerical simulations.

A number of surveys and reviews on wake vortex research have been published over the years. In 1975 the Annual Review by Widnall and the extensive monograph of Donaldson and Bilanin appeared, the latter still being a repository for analytical wake vortex methods. Twenty-three years later, Hallock et al. provided a retrospection on mainly the US wake vortex activities and Spalart presented his discerning and sobering review on the understanding of wake vortex physics as relevant to safety and productivity of aviation. One year later in 1999, Rossow gave a historical review with a focus on wake structure and alleviation. In the year 2002, Gerz et al. presented a consolidated European view on the status of knowledge on aircraft wake characteristics, technical and operational procedures of minimizing and predicting vortex strength, and avoiding wake encounters. Throughout these years, James Hallock maintained an extensive and probably almost complete on-line wake vortex bibiliography with abstracts (http://www.volpe.dot.gov/wv/).

More than 30 years of wake vortex research were characterized by a number of pressing questions and fundamental controversies (Spalart 1998). Below the subset of issues is listed that is adressed by the author. References that are integrated into the current manuscript are flagged by numbers in brackets.

(i) Is the age of wake vortices better described by the distance to the generating aircraft, $x$, or by a non-dimensional time, $t^* = t/t_0$, where the reference time, $t_0 = 2\pi b_0^2/\Gamma_0$, consists of trailing vortex parameters? This issue is discussed in Gerz et al. (2002).

(ii) Which method is best suited to uniquely derive circulation from both measurement and simulation data and, at the same time, to meet operational

[†]The latter issue, which is not addressed in this manuscript, is mainly pursued via constructive measures at the wings.

[‡]LIght Detection And Ranging – Remote sensing technique to determine the line-of-sight velocity component by measuring the Doppler shift of a laser beam.

requirements, as e.g. the correlation with effects of potential wake encounters? [5]

(iii) The behavior of wake vortices in a stably stratified atmosphere has been discussed controversially for a long time. Is the descent decelerated or accelerated, a sequence of both or even an oscillation? Does stable temperature stratification prolongate or shorten vortex lifetimes? [1, 3]

(iv) Can environmental conditions prevent wake vortices from descending or even cause a potentially hazardous rebound to flight level? Candidate meteorological conditions comprise wind shear, stable temperature stratification, and the convective boundary layer. [1, 2, 3], Meleshko et al. (2001), Frech and Holzäpfel (2002), Holzäpfel et al. (2002), Hofbauer and Holzäpfel (2003)

(v) Which are the relevant decay mechanisms? Do vortices decay from inside like a laminar vortex[§] or are they eroded from outside? [2, 6]

(vi) How does vortex decay proceed in time? Fundamentally different concepts were debated, namely the concept of gradual and predictable decay, the concept of stochastic collapse, and the concept of a two-phase decay. [2, 6], Gerz et al. (2002)

(vii) How to design a reliable parametric real-time wake vortex prediction model? Should it be based on impulse balances, employ discrete vortex methods, or are there superior alternatives? [4, 8]

(viii) Are deterministic wake vortex predictions feasible or do appropriate approaches have to be probabilistic? [4, 8]

(ix) How to model poorly resolved vortex cores in a numerical simulation? Does an insufficient resolution adulterate the results? [7]

Only the synopsis of simulation, measurement, and theory allows to answer these questions and to elaborate the sustainable groundwork of comprehensive knowledge of wake vortex behavior which is necessary for the design of a reliable wake vortex warning and prediction system.

In the following sections, eight peer reviewed publications are described which provide contributions to all of the named elements – simulation, measurement, and theory. The key method applied in all the investigations, though, is the large eddy simulation. The descriptions rather focus on the logic and structure of the complete work than to provide a summary of all individual findings which are described in the respective publications.

Section 2 deals with the analysis of wake vortex evolution and decay in the stably stratified, sheared, and turbulent atmospheric boundary layer which is detailed in papers [1-3, 6]. It starts with the more simple and clear two-dimensional simulations and analyses. These findings are generalized to three-dimensional, turbulent flows which are mainly studied by LES. The investigations finally lead to a number of postulates that provide a theoretical foundation for the physics of vortex decay.

Section 3 introduces the intrinsic problem of insufficient resolution of all relevant length scales in LES of wake vortex evolution in the atmospheric boundary layer [7]. A subgrid-scale modification is suggested that allows for a more physical representation of poorly resolved vortex cores. It is shown that even inadequately resolved vortex cores do not disqualify the simulations because well-resolved secondary vorticity structures control vortex decay.

Section 4 investigates the accuracy of lidar measurements of wake vortices [5]. Knowledge on lidar data characteristics is pre-requisite for the validation of numerical predictions. Systematic deviations from nominal circulation and the scatter of circulation data caused by the genuine variability of wake vortices in the atmospheric boundary layer are assessed.

Section 5 describes the parametric real-time wake vortex prediction model P2P [4] which was devised

[§] Note that the half-life period of the radii-averaged circulation $\Gamma_{5-15}$ (see [5]) of a laminarly decaying trailing vortex would theoretically amount to 26.6 days.

based on the results of the previous sections. The primary objective of such a model is to reliably predict vortex positions and strengths in real-time in order to re-adjust aircraft separations dynamically. Input data for P2P prognoses are aircraft parameters and measured or forecasted environmental parameters along the glide path. P2P predictions are compared to observation data from five different field deployments. The predictive skills of the model as well as the aircraft spacing reduction potential are quantitatively assessed [8]. Finally, recent enhancements of the P2P model are presented.

# 2 Wake Vortex Evolution in the Atmospheric Boundary Layer

This section deals with the transport and decay of wake vortices within the three generic categories of atmospheric environments: the stably stratified and the neutral environment, and the convective boundary layer. The mechanisms that control vortex descent and decay are analysed first by means of two-dimensional simulations, potential flow theory, and integral descriptions in terms of impulse. Then, three-dimensional and fully turbulent simulations reveal that two-dimensional effects are damped by turbulence and that, in general, turbulent decay prevents wake vortices from a hazardous rebound to the flight level. Finally, turbulent decay mechanisms are analysed in detail, generalized for any sources of disturbances, and pinpointed in eleven postulates.

## 2.1 Stably Stratified Atmosphere

### 2.1.1 Two-Dimensional Investigations [1]

The first publication [1] within the presented series already demonstrates that wake vortex physics is preferentially analysed by consideration of vorticity distributions and their effects on their surroundings in terms of induced velocities. Primary vorticity, which

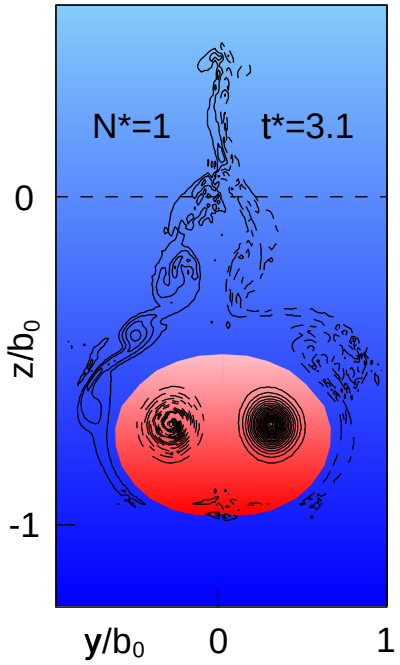


Figure 5: Axial vorticity distribution of trailing vortices in strongly stably stratified environment. Red oval denotes adiabatically warmed fluid descending with the vortices; dashed lines mark negative vorticity.

is associated with the wake vortex pair, interacts with secondary vorticity, which may stem from turbulence, wind shear, or is produced by baroclinity. Both types of vorticity are rearranged by tilting, intensified by stretching, attenuated by squeezing, and annihilated by mutual compensation of vorticity of opposite signs.

In the stably stratified environment, the oval around the vortex pair descends and warms adiabatically. The evolving bouyancy force does not simply decelerate the sinking motion of the oval but it creates counter-rotating secondary vorticity along the oval-shaped interface between warmed internal flow and colder ambient flow (see Figure 5). The generated baroclinic vorticity is left behind the oval and constitutes a secondary wake. Within the oval the secondary vorticity induces an upwards directed flow which re-

duces the descent speed in consistence with the effect of the bouyancy force. But it also induces the mutual approach of the vortex pair leading to counterintuitive effects: Approaching vortices with constant circulation and, nevertheless, decreasing descent speed are in contradiction to equation (2). Dimensional analysis and potential flow methods, which excellently reproduce the flow topology found with the high-resolution simulations, elucidate the functioning of the competing effects of induced acceleration and deceleration and herewith resolve the apparent contradiction.

Dimensional analysis further allows to derive a local shear-number, *Sh*, which takes into account the interaction of primary and secondary vorticity and describes the instantaneous tendency of wake vortices to accelerate for $Sh < 1$ or to decelerate for $Sh > 1$. Furthermore, it is shown that a normalized Brunt-Väisälä frequency of $N^* = 1$ (for definition of $N^*$ see equations (2), (3) in Ref. [1]) constitutes the threshold for the degree of temperature stratification which separates steadily descending from rebounding wake vortices. For $N^* = 1.4$ the trailing vortices only descend about one vortex spacing and subsequently rebound to flight level.

The potential flow method is extended to the analysis of buoyancy oscillations which develop from any mass of buoyant fluid released in its environment. Various examples for such oscillations may be found in geophysical flows such as overshooting thunderstorms or cloud turrets. By deviding the oscillation into quarter periods, four different regimes can be identified, where the vortex pair either accelerates or decelerates and entrains or detrains ambient flow, respectively.

Evaluations of the impulse of the wake oval itself and the total wake, including primary and secondary produced vorticity, demonstrate that the Brunt-Väisälä oscillation assumed in theory is executed by the *whole* system and not by the oval alone. The vortex oval performs complex displacement patterns which, at a first glance, seem to contradict the laws of conservation.

### 2.1.2 Turbulent Investigations [3]

For the three-dimensional investigations of trailing vortex evolution in stably stratified environments, two different approaches concerning the initialized turbulence were pursued. As a baseline case, the wake vortices develop in quiescent atmosphere; turbulence then only stems from the turbulent aircraft boundary layer, the mixing of the separated flows at the trailing edges, and the turbulent exhaust jets. This case is a conservative approach which explores maximum life spans. The respective turbulence initialisation is derived from in-situ five-hole-probe velocity measurements performed with the DLR research aircraft FALCON chasing B737, A340, A310, B727, and VFW614 aircraft in small distances up to 40 m. In a second case, in addition to the aircraft-boundary layer turbulence, weak to moderate, anisotropic, and decaying atmospheric turbulence is superimposed on the whole velocity field. This flow scenario represents the typical atmospheric state at aircraft cruising altitudes.

The simulations show that initially neither stratification nor turbulence alter the behavior of the vortex pair. Later on, the level of stratification controls vortex separation and descent; the introduction of turbulence and changes of the type of turbulence modify this behavior only marginally. The late acceleration of descent, which is seen for moderate to strong stratification in 2D, is impeded by turbulent decay. The authors conclude that the agreement between turbulent and laminar cases regarding vortex descent and spacing clearly indicates that the underlying physics of the early development is intrinsically two-dimensional.

Further, the simulations indicate that circulation decay progresses in two phases (cf. figure 11). The initial decay, which is due to internal diffusion and stretching of secondary vorticity (see section 2.3), is similar for all cases. Then, a phase of rapid circulation decay is initiated at times depending on environmental conditions. The higher the turbulence and the stronger the stratification, the earlier starts the final

decay of circulation. In the neutral and quiescent atmosphere, the vortices may last beyond times of 6 minutes and descend to altitudes below 470 m for an A340. Either weak stratification or weak atmospheric turbulence is sufficient to approximately halve the lifetime to 3 minutes.

It is noteworthy that at the time when the vortices have rebounded to 10 m below the glide path in the very stably stratified ($N^* = 1.4$) and quiescent atmosphere, the circulation has reduced already to 5% of its initial value. Hence, the vortex rebound expected at strong inversion layers, which is suspected to be very hazardous from an operational point of view, appears harmless because of advanced erosion of vortex coherence and strength.

The structural development of the vortices is governed by the interaction of short-wave and long-wave disturbances and baroclinic vorticity depending on the type of initialized turbulence and the degree of stratification. For the initiation of rapid vortex decay a sequence of events is identified. Here it is exemplified for vortex evolution in the quiescent stably stratified environment (see Figure 6). For different environmental conditions the sequence is modified but can be explained by similar reasoning. First, the baroclinic torque perturbed by aircraft-induced small-scale turbulence produces rip-like structures of baroclinical vorticity (cyan, blue). Second, the rip-like structures above the vortex pair induce below a wavy velocity field (colored iso-lines). Third, the vorticity of the wavy velocity field is strongly stretched by the accelerating downward motion midway between the main vortices, yielding intense vorticity-streaks (orange, magenta). Fourth, the central vertical streaks, which act like counter-rotating rolls, exchange fluid between the two vortices outmost effectively. The coherent lateral exchange of fluid across the vortex pair centerplane is prerequisite for the rapid turbulent decay of vortex pairs because only this particular process enables the mutual annihilation of the wake vortices' opposite-signed vorticity.

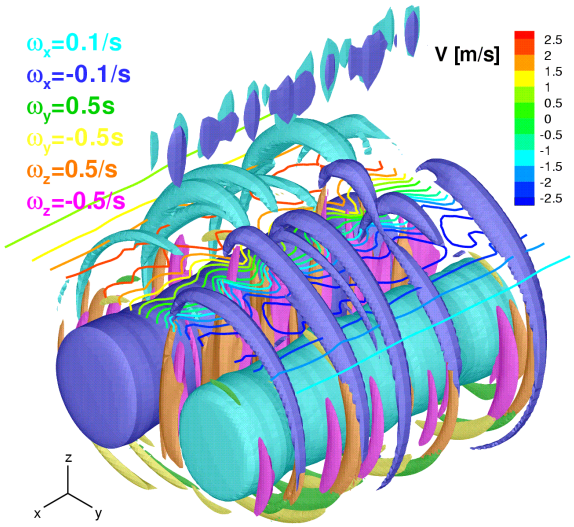


Figure 6: Turbulent wake vortices in a weakly stably stratified and quiescent atmosphere at $t^* = 2.8$. Isosurfaces of all three vorticity components in a perspective view and iso-lines for lateral velocity, $v$, in a horizontal plane above the vortices.

## 2.2 Convective Boundary Layer [2]

Wake vortex evolution in the convectively driven atmospheric boundary layer (CBL) was controversially disputed in the context of the further development of the wake vortex warning system (WVWS) of Frankfurt airport (Frech et al. 2002). The WVWS is supposed to predict statistically the propagation and lifespan of wake vortices in a safety box of 80 m height above ground. Pilot associations argued that above that safety box, the updrafts in a CBL may cause wake vortices to stall or even to rise up to the glide slope. In the CBL, buoyancy driven thermals form highly energetic updrafts due to the radiative heating of the ground, where the updrafts are surrounded by less turbulent downdraft regions.

The simulation of wake vortex evolution within a CBL poses demanding requirements on numerical resolution. Ideally, the resolved length scales should span a range from the order of approximately 0.1 m

in the vortex cores to the order of 1000 m in the atmosphere, where the latter length scale roughly corresponds to the inversion height of a CBL. An appropriate equidistant numerical mesh would need $O(10^{12})$ mesh points, which is far beyond current computational capabilities. The devised compromise was to simulate wake vortices with relatively large vortex cores in an *evolving* CBL with an inversion height of 512 m. The CBL simulation was driven by a constant vertical heat flux at the lower surface and three wake vortex pairs were superimposed on the turbulent flowfield after the evolving CBL was well established (see figure 7).

The comparison of velocity and temperature fluctuation patterns and spectra of the turbulent kinetic energy obtained along instrumented aircraft flight path segments with respective simulation data indicates that typical features of a CBL are well met by the simulation. In particular, the LES comprises quite well the energy levels of real atmospheric CBLs in the wavelength range that is relevant for wake vortex decay.

The LES results illustrate that the primary rectilinear vortices are rapidly deformed on the scale of the alternating updraft and downdraft regions which reduces the impact time of forces and moments exerted onto encountering aircraft. Actually, vortex segments remain on or even rise up to 20 m above the flight level as argued by pilot associations but are, fortunately, quickly eroded by the enhanced turbulence of an updraft. The longest living sections of the vortices are found in regions of relatively calm downdraft flow which augments their descent.

The described investigation treats exactly the situation where the strength of the updrafts just compensates the self-induced descent speed of the wake vortices. This allows to extend the conclusions to CBL cases with stronger and weaker thermals: In the weaker CBL case, the common situation prevails where wake vortices descend below the glide path. In a stronger CBL, pieces of the wake may even rise considerably above flight level but the turbulence

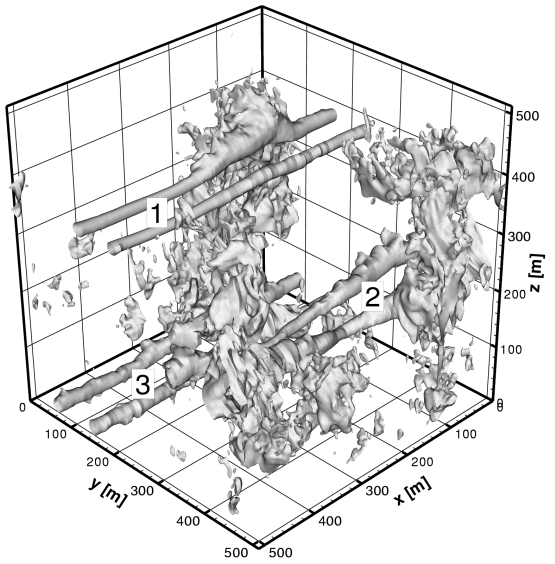


Figure 7: Iso-surfaces of the positive vertical velocity value, $w = 2$ m/s, of the evolving CBL with three pairs of 10 seconds old wake vortices.

level is also increased in the updrafts which further augments the decay rate of those vortex segments.

The simulated flowfield was employed to estimate the encounter probability and severity for a B737 aircraft following a B747 by means of strip theory. It is found that the deformation and decay of the vortex pairs counteract and dominate the potentially hazardous effects of rising wake vortices. At a vortex age of 60 seconds, which corresponds roughly to minimum radar separation of 2.5 nautical miles, the probability to encounter a potentially hazardous rolling moment has decreased to 0.009%. At this time, the wake induced rolling moments have almost decayed to the background level of atmospheric turbulence.

## 2.3 Generalization of Decay Mechanisms [6]

To provide outmost universal understanding of wake vortex decay mechanisms, four different cases, simulated with different numerical codes by different groups, were analysed in manuscript [6]. The cases comprise (i) the near-field interaction of a trailing vortex with an exhaust jet, (ii) the evolution of single vortices and counter-rotating vortex pairs in homogeneous isotropic turbulence, (iii) the decay of wake vortices in a turbulent stably stratified atmosphere, and (iv) wake vortex evolution in a weakly turbulent sheared environment. The dissimilar approaches and specifics of the described cases on one hand, and the, nonetheless, similar topologies of the resulting vortex evolutions on the other hand, indicate the independency of results from particular scenarios and methodological aspects. This observation encourages the authors to consider the extracted aspects of wake vortex decay as generic and universally valid.

Case (i) demonstrates that disintegrated and incoherent exhaust jet vorticity regains coherence by tilting and stretching which is exerted by the potential vortex flow of the primary vortex. In general, this means that the primary vortex may aligne (tilting) and reinforce (stretching) any proximate random vorticity such that spiral-shaped secondary vorticity structures (SVS) are produced. The tilt-rates and stretch-rates found in the direct numerical simulation can be reproduced analytically.

Case (ii) addresses the similarities and differences between decay mechanisms of single vortices and counter-rotating vortex pairs. In both cases, single vortices and vortex pairs, SVS are created by tilting and stretching mechanisms. A primary vortex that stretches SVS performes work on the SVS. Simple model assumptions indicate that a doubling of length of a SVS corresponds directly to a doubling of rotational energy of the flow in the vortex core of the SVS. Hence, during the stretching process the SVS gain rotational energy, whereas the primary vortex, in turn, loses rotational energy. It is shown that this transfer of rotational energy together with diffusion processes leads to an initial gradual circulation decay.

However, the generation of vertical vorticity streaks midway between the vortex pair and the consequential mutual exchange of primary vorticity between counter-rotating vortex pairs (as described in section 2.1.2) does not apply for single vortices. Therefore, rapid circulation decay is only observed for counter-rotating vortex pairs, whereas the decay of single vortices is strongly reduced when the energy transfer from primary to secondary vortices ceases because the secondary vortices are no longer stretched substantially when they tend to be aligned azimuthally.

In highly turbulent environments, the primary vortices are too weak and the time scales of vortex decay are too short to essentially stretch atmospheric eddies. As a consequence, the single vortices and wake vortices both are rapidly disrupted directly by ambient turbulence.

Case (iii) follows up decay mechanisms described in [3] and demonstrates that stable temperature stratification amplifies effects of turbulence by an intensification of disturbances induced above the vortex pair. As a consequence, the resulting vertical vorticity streaks, which initiate rapid vortex decay, are produced earlier and become stronger.

Case (iv) deals with effects of wind shear on trailing vortex evolution. Shear flows exhibit vigorous and variform influences on wake vortex transport and decay. Wake vortices that interact with a shear layer may experience vortex tilting, separation and subsequent rebound, whereupon the vortex with opposite-signed vorticity compared to the vorticity of the shear layer shows the stronger tendency to rebound (Hofbauer and Holzäpfel 2003). It is again the vortex with opposite-signed vorticity that decays distinctly faster when the vortex pair immerges into a turbulent shear-layer. Also the spectacular rebound observed at London-Heathrow Airport can be at least in part attributed to shear-layer effects (Holzäpfel et al. 2002).

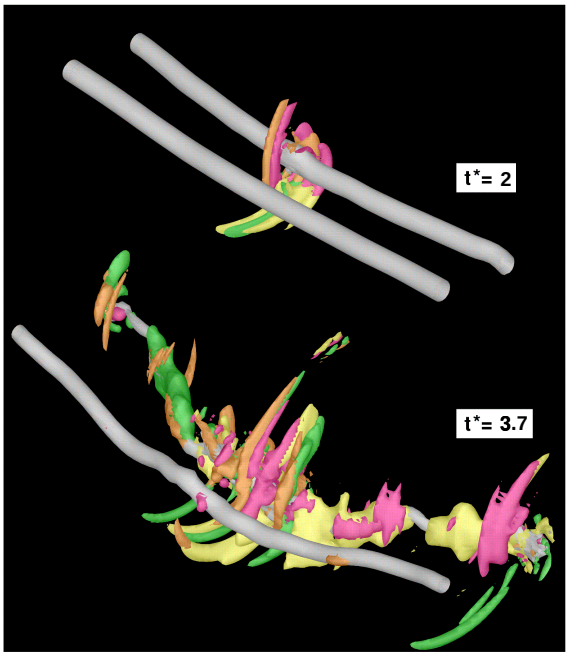


Figure 8: Perspective view of wake vortices in turbulent sheared environment at two instants of time. Iso-surfaces of lateral and vertical vorticity components plotted in colors; wake vortices represented by grey tubular contours.

Figure 8 demonstrates that the constant background shear imposed in case (iv) breaks the symmetry of vortex evolution. For the vortex with opposite-signed vorticity (right vortex in figure 8), the SVS structures cover a distinctly smaller distance to completely encompass the vortex and, consequently, the SVS experience much stronger acceleration and, hence, much stronger stretching in the vicinity of that vortex. This leads to unbalanced decay rates and prolongated lifetimes of one of the vortices in the sheared environment.

The investigated cases suggest a ranking of the efficiency of the different environmental parameters regarding vortex decay rates. Basically, the life span of the vortices is correlated to the intensity of ambient turbulence. Imposing additionally a stable temperature stratification with $N^* = 1$ may reduce wake vortex lifetime by roughly two time units ($t_0 \approx 15 - 30\,\mathrm{s}$) whereas an increase of ambient turbulence fluctuation velocities by a factor of four may shorten wake vortex life by four time units. In contrast, it is found, in agreement with dimensional analysis, that the life span of wake vortices in a given environment may be halved by a reduction of vortex spacing by a factor of $\sqrt{2}$.

# 3 Adjustment of Subgrid-Scale Parametrization [7]

Large eddy simulation (LES) explicitly simulates the Navier-Stokes equations and, thus, fully considers the effects of curvature and rotation in the resolved scales. Smaller scale fluctuations are smoothed and modeled by subgrid-scale (SGS) closures. If the scales of eddies that dominate turbulent transport are resolved, the subgrid model primarily has to provide an appropriate energy sink that prevents a tailback of small scale energy. If, however, the larger-scale turbulence is suppressed by stabilizing body forces – as the buoyancy force in a stably stratified environment or centrifugal forces in a rotating flow – or is damped in the vicinity of a wall, the SGS model may locally control turbulent transport. As a consequence, the flow regions that are strongly affected by body forces may rather represent a solution of the SGS model than of the Navier-Stokes equations. An example where an appropriate resolution of all relevant length scales is not feasible and, therefore, the solution is locally controlled by the SGS model is given in section 2.2 by the LES of wake vortex evolution in the convective atmospheric boundary layer.

To come up against these dissatisfiable resolution requirements, an adjustment of subgrid-scale parametrizations to strong streamline curvature effects is proposed. The devised correction termed NaCoo identifies the local degree of centrifugal stability via a rotational Richardson number which is determined from local streamline curvature at every grid point. The Richardson number, in turn, is used

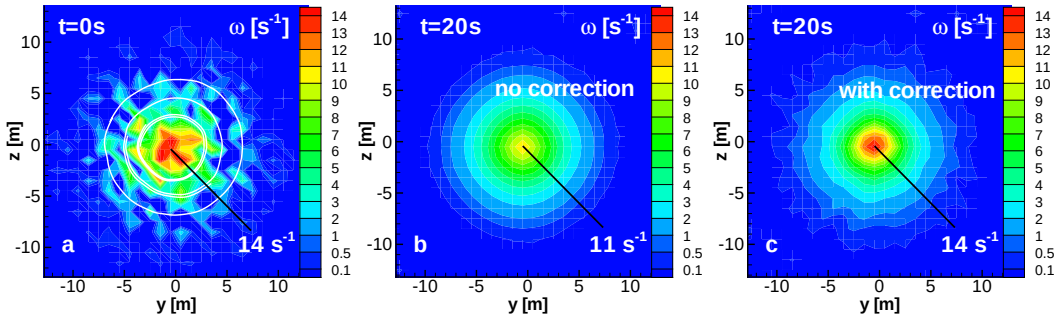


Figure 9: Vorticity distribution of a single vortex with initially superimposed random perturbations at (a) $t = 0\,\mathrm{s}$ with white streamlines and at $t = 20\,\mathrm{s}$ applying (b) the standard Smagorinsky closure and (c) NaCoo.

to modify the SGS viscosity such that SGS momentum transport is increased in instable and decreased in stable situations.

Figure 9 demonstrates main benefits of NaCoo: (i) conservation of peak vorticity in the vortex cores and (ii) allowance for appropriate turbulence levels in the vicinity of the vortices. Further benefits are (iii) reduction of vortex core radius growth rates, (vi) an approach to properties of tangential velocity profiles found in experiments, and (v) non suppression of vortex core meandering. These features, which are in line with experimental studies of turbulent vortices, denote a significant step towards a more physical modeling of inadequately resolved vortices by LES.

Applications of NaCoo to single vortices and to aircraft wake vortices in a quiescent and turbulent environment illustrate the performance of the streamline curvature correction. In particular, it is shown that streamline curvature constitutes a robust criterion for coherent rotation even in fully turbulent and apparently incoherent flow topologies (cf. figure 9a). A relation is derived that allows the selective adjustment of vortex growth rates caused by SGS viscosity depending on the numerical resolution of the vortex and its circulation. The relation, which indicates that vortex cores grow according to $t^{1/4}$ after a transient constancy, is corroborated by different applications.

For wake vortices, the turbulence structure within the vortices becomes more realistic and resembles flow topologies found in high-Reynolds number laboratory experiments. Vortex core growth rates can be substantially reduced to growth rates found in vortex cores of aircraft with retracted flaps. Nevertheless, global parameters like wake vortex transport and decay are little affected by the correction because the well-resolved secondary vorticity structures discussed in section 2.3 dominantly control vortex evolution.

# 4 Lidar Circulation Evaluation Capabilities [5]

Both the complexity of wake vortex physics and the limited experimental access impede comprehensive analyses of wake vortex physics. In particular, in laboratory experiments the far-field evolution of wake vortices is not accessible and in both laboratory experiments and numerical simulations the achievable Reynolds numbers are far from reality. The only and indispensable access to real wake vortex behavior is provided by lidar measurement techniques that trace full-scale wake vortices in the free atmosphere. Lidar (LIght Detection And Ranging) operates by transmitting a laser beam and coherently detecting the radia-

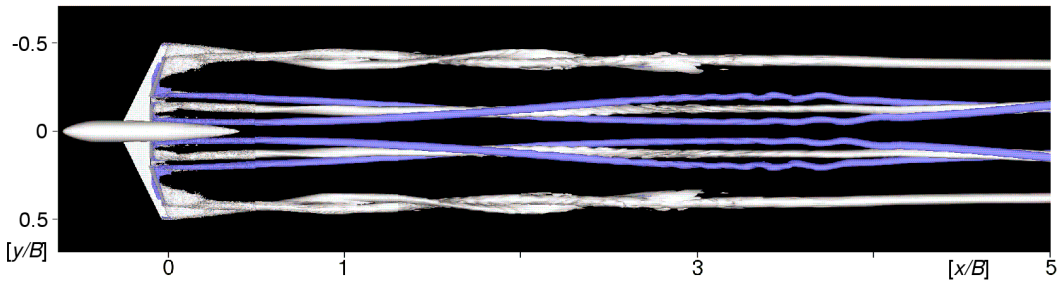


Figure 10: View from below on simulated near-field wake evolution up to 5 spans behind wing tips of an aircraft in high-lift configuration. Vortex topology illustrated by iso-surfaces of vorticity (blue iso-surfaces indicate counter-rotating vorticity).

tion back-scattered by aerosols. The spectrum of Doppler shifts in the frequency of the back-scattered radiation is analysed to give the line-of sight (LOS) velocity component of the aerosols, and hence the air motion, along the beam.

From the LOS velocities vortex position and circulation can be deduced. Circulation constitutes the most important parameter for wake vortex characterization since it describes vortex strength in a form that is correlated with effects of potential wake encounters.

Unlike in the case for single vortices, where the circulation converges to a definite value at large radii, the proximity of a neighboring vortex affects circulation values wherefore the circulation of vortex pairs strongly depends on the method of its evaluation. Three different methods for circulation evaluation are investigated in manuscript [5]. The surface integral of vorticity serves as baseline case that is compared to a method that evaluates the lidar line-of-sight velocity midway between the vortices and to another method that calculates radii-averages of circulations derived from tangential velocities. It is shown that for an ideal vortex pair the systematic deviation of the circulation is a function of vortex spacing, vortex core radius, vortex tilt angle, and lidar viewing angle. For reasonable parameter settings the systematic deviations are below some 10%.

Nevertheless, initial circulation overestimations of typically $30-70\,\%$ are frequently observed by lidar. That overestimation is associated with an ostensible strong initial "decay" such that at a vortex age of roughly one time scale normalized circulation attains a value of one. For the development of parametric wake vortex models the real circulation evolution is crucial. To resolve the reason for the overestimations, virtual lidar measurements are performed based on high-resolution numerical simulation data that cover the generation and merger of multiple vortex pairs behind an aircraft model in high-lift landing configuration (see figure 10). The observed multiple vortex topology clearly illustrates that the assumption that the sensed maximum line-of-sight velocities can be attributed to the tangential velocities of a pair of axisymmetric vortices is heavily violated as long as the roll-up process to a single vortex pair is not completed. More precisely, the LOS velocities stemming from the secondary vortices, which detach from the edges of the flaps, are interpreted as high tangential velocities on large radii appendant to the primary vortex, hence, high circulation. The virtual lidar measurements reproduce exactly the range of initial circulation overestimations known from measurements. The analysis of the phenomenon suggests that initial circulation overestimations should be simply disregarded for the interpretation of trailing vortex evolution and, in particular, the development of wake vor-

tex models and systems.

The simulation data of vortex evolution in the convective boundary layer (see section 2.2) are applied to assess the effects of a realistic inhomogeneous turbulent environment on lidar measurements. The virtual lidar measurements are compared to data of three 10 $\mu$m continuous-wave lidars that were operated to trace the wake vortices generated by DLR's VFW 614 aircraft ATTAS during the wake vortex forecasting and measurement campaign WakeOP. WakeOP has been accomplished at the airfield of Fairchild–Dornier in Oberpfaffenhofen, Germany, from 29 March to 4 May 2001.

In both simulation and experiment, the different circulation evaluation methods applied to the same vortex pairs yield deviations of almost $\pm 20\%$ and the standard deviations of a series of measurements are of the order of 10 to 20%. These results indicate that the degree of scatter of circulation data, observed after the completion of roll-up, appears to be mostly due to the variability caused by the complex response of wake vortices to turbulent environments. We conclude that errors originating from lidar measurement accuracy appear to be negligible compared to the genuine circulation scatter. For the late vortex evolution findings are different. The LES data indicate that considerably eroded vortices which already have lost the classical signature and, therefore, can scarcely be identified as wake vortices, nevertheless, may still possess more than 50% of their initial circulation. This result emphasizes the difficulties associated with the investigation of final vortex decay.

In summary, the radii-averaging circulation evaluation method appears most appropriate for wake vortex characterization. For medium size and heavy aircraft an averaging interval of 5 m to 15 m is recommended. $\Gamma_{5-15}$ restricts evaluations to the sub-range of wake vortex induced velocities that can be reliably sensed by lidar and that would also be experienced by an encountering aircraft. Further advantages are low sensitivity to observation angles, smoothing of scatter by averaging over several radii, and automatic compensation of ambient wind and vortex motion.

# 5 Real-Time Wake Vortex Prediction

The primary objective of a parametric wake vortex model is to reliably predict vortex positions and strengths in real-time in order to re-adjust aircraft separations dynamically. Other applications of approximate wake vortex models include encounter investigations within flight simulators, safety analyses that estimate the hazard probability of new aircraft or of new approach and landing procedures, studies that simulate various aspects of reduced spacing systems as, for example, the predictability of wake vortex evolution based on virtual environmental measurement data, and, finally, cost-benefit analyses.

## 5.1 Probabilistic Two-Phase Wake Vortex Decay and Transport Model [4]

Despite the significant number of available wake vortex models (listed in [4]) none of these models considers all effects of the first order impact parameters that are aircraft configuration, wind, turbulence, stable stratification, wind shear, and proximity of the ground. In particular, they are all deterministic. Not specified are deviations from predicted values that are inherently caused by the complex response of vortex behavior on turbulence[¶].

The current version of the Probabilistic Two-Phase wake vortex decay and transport model termed P2P considers all of the above listed parameters (for windshear and axial-wind effects see section 5.3). P2P is designed to include as much knowledge as possible gained from both experimental and numerical wake

[¶]Recently, the VFS (Ref. 13 in [4]) has adapted parameterizations for stratification and probabilistic behavior and herewith completely considers all mentioned effects. Not yet published.

vortex research with a focus on operational needs[‖]. For this purpose the model concept comprises the following elements.

First, in contrast to most other models, P2P employs a well-defined and experimentally accessible definition for vortex strength. Benefits of the employed radii-averaged circulation $\Gamma_{5-15}$ are discussed in section 4.

Second, the complex wake vortex behavior found in LES (see section 2) indicates that the development of a thorough real-time model based on an LES-independent approach is hardly feasible. Therefore, the basic concept for model development was the conferment of the detailed and complex wake vortex behavior found in LES upon a simple but well-founded equation for vortex evolution. Since there is no rigorous solution for the evolution of turbulent vortex pairs, the hydrodynamical basis of P2P relies on the equation that describes the spatio-temporal circulation evolution of the decaying potential vortex. In P2P this relation, which constitutes an analytical solution of the Navier-Stokes equations for a non-stationary, plane, rotating flow, is extended and adapted to LES results of different groups to describe vortex decay and descent.

For the prediction of vortex strength, the concept of two-phase circulation decay (see figure 11 and sections 2.1.2 and 2.3) is pursued. Decay parameters are determined as functions of turbulence and temperature stratification. An analysis of 525 wake vortex measurements of the Memphis database indicates normalized eddy dissipation rate, $\varepsilon^*$, as most suitable parameter for the characterization of turbulence effects. This result reflects that the length scale range of wake vortices, which is most susceptible to ambient disturbances, usually resides in the turbulent inertial subrange of the atmospheric boundary layer[**]. In contrast, turbulent kinetic energy is sensitive to the choice of the averaging time frame; that is the longer the averaging interval the more energy is contributed from larger scales that are irrelevant for vortex decay.

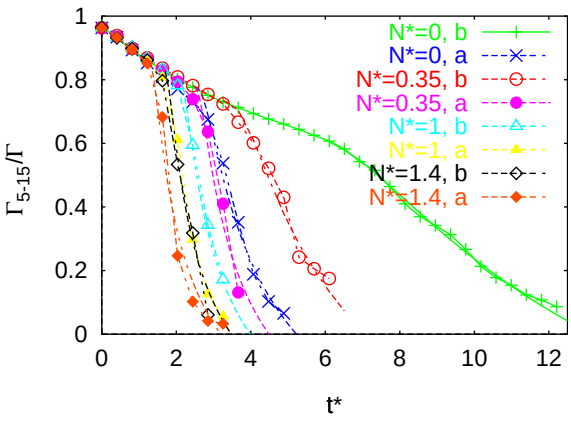


Figure 11: Temporal evolution of normalized circulation from LES [3] (symbols) and respective fits of P2P for different turbulence scenarios and different degrees of stratification.

Linear relations between descent speed and circulation hold only if the circulation value attributed to the wake vortices likewise represents the velocity induced at the neighbouring vortex. For radii-averaged circulations as $\Gamma_{5-15}$ this is not valid. Therefore, the parameterized descent rate obeys a non-linear dependence on circulation which confers P2P the following capabilities. It allows for (i) a reduction of circulation without the reduction of the descent rate during the early vortex evolution, and for (ii) stagnating vortices with non-zero circulation in strongly stably stratified environments. In other models circulation and descent are coupled directly such that both quantities become zero at identical times. (iii) It enables rebounding vortices in very strongly stratified environments which is of high relevance for the safety of following aircraft. All these features are in accordance with LES and observation data.

Third, P2P predicts probabilistic wake vortex behavior. Precise deterministic wake vortex predictions are not feasible operationally due to several reasons.

[‖] A substantial part of the basis for model development is described in the preceding sections.

[**] The spectral distribution of kinetic energy in the inertial subrange is characterized by the single parameter $\varepsilon$.

Primarily, it is the nature of turbulence that deforms and transports the vortices in a stochastic way and leads to considerable spatio-temporal variations of vortex position and strength. Moreover, aircraft parameters and especially the state of the atmospheric boundary layer with its intrinsic variability can only be measured or predicted with limited accuracy. The scatter resulting from all these factors only allows to predict wake vortex behavior within uncertainty bounds and a respective probability. For this purpose, P2P varies decay parameters in subsequent model runs and it adds various static and dynamic uncertainty allowances (cf. figures 13, 14) that consider the increased scatter of vortices in turbulent and sheared environments.

## 5.2 Application and Assessment [8]

P2P is supposed to conservatively predict wake vortex evolution in order to eventually guide the readjustment of aircraft separations under favorable weather conditions. To guarantee the high degree of reliability, which is indispensable for the operation of safety-relevant aviation systems, the model must be validated for all weather conditions over which it must finally operate. To date, P2P has been applied to data accomplished at five different field measurement campaigns. These comprise the two US-campaigns performed at International Airports Memphis, TN (December 1994, August 1995) and Dallas Fort Worth, TX (September/October 1997), the WakeOP campaign at the special airfield in Oberpfaffenhofen, Germany (April/May 2001), and the WakeTOUL (May/June 2002) and AWIATOR (August 2003) campaigns both at Tarbes Airport, France[††]. A severe complication, however, arises from the fact that the quality of measurements used for assessment strongly affects the performance of the model. For validation of the model itself, dedicated high-quality measurements are necessary. For the operational realization of a complete wake vortex prediction system, the accuracy and the spatial and temporal resolution of measured and/or predicted environmental parameters along the glide slope determine the capacity gain.

For validation purposes either individual cases are analysed in detail or statistics are derived from a larger data set. To evaluate the basic performance of a model, deterministic predictions can be averaged to analyse the mean behavior of the vortices [4] or the deviations of measurement and prediction are estimated within a scoring procedure [8]. Probabilistic model performance, on the other hand, cannot be evaluated based on scoring approaches because increased uncertainty allowances would always improve ratings. Therefore, the probability that the vortices actually evolve within predicted confidence intervals is discussed with regard to potential runway capacity gains [8]. Alternatively, the actual probability density distributions of wake vortex measurements within the upper and lower bounds of the predicted uncertainty allowances, are best suited to estimate wake prediction skills comprehensively (see section 5.3). Only the latter approach allows to adjust the probabilistic model to confidence levels prescribed by generally accepted risk metrics for operational use. Results of all of the above listed approaches are described in the current and the next section.

Data from the Memphis campaign were extensively used for the first assessments of P2P described in Refs. [4] and [8]. Deterministic predictions of 144 cases of vortex evolution in the stably stratified atmosphere and 138 cases in a turbulent atmosphere are averaged and compared to measurements, respectively. Neglecting the initial circulation overestimation by the lidar data (cf. section 4), predicted and measured vortex decay agree saliently well. In contrast, the first approximate vortex model devised by Greene in 1986 (Ref. 9 in [4]) underestimates consistently and non-conservatively the circulation measurements. Notably, the two-phase decay of P2P is

[††]WakeOP and WakeTOUL campaigns were part of DLR's "Projekt Wirbelschleppe" and were co-funded by the EC project C-Wake. AWIATOR is a multilateral technology platform funded by the European Commission.

masked completely in the mean evolution, just as it is hidden in the scatter of the Memphis lidar data.

Further, 211 Memphis cases are used in a scoring procedure to compare the predictive capabilities of the deterministic version of P2P (termed D2P) and Sarpkaya's model (Ref. 9 in [8]). Sarpkaya's model, which is part of the current NASA Aircraft Vortex Spacing System, AVOSS, was best rated in a previous comparison with two further models. Although, D2P was not designed to predict deterministic vortex behavior, the comparison is quite good. However, the calculated rms deviations of all the investigated models differ only slightly. This indicates that major contributions to the rms deviations are caused by inconsistencies of the data basis and by inherent deviations of wake evolution from deterministic model predictions.

The 211 Memphis cases indicate that the probabilistic predictions of P2P are conservative. Only flawed crosswind information or pronounced wind shear may cause deficient predictions. Detailed investigations of individual cases from several campaigns reveal, in agreement with results of numerical simulations described in section 2.3, that constant wind shear may prolong vortex lifetime whereas shear layers may modify vertical and lateral transport.

Based on the finding that in the majority of cases P2P is capable of predicting upper bounds for circulation, the respective aircraft spacing reduction potential is assessed using over four-hundred cases from Memphis and Dallas Fort Worth deployments. The resulting comparison of the predicted aircraft separations to the currently effective ICAO separations is depicted in figure 12. It clearly indicates that, at least for the two considered data sets, conservative decay predictions do not allow for noticeable reduced spacings. In the majority of the cases, durations predicted by P2P exceed ICAO standards significantly. These findings clearly indicate that it is mainly the descent and/or advection by crosswind that transports the vortices away from the glide path which is responsible for the high level of safety provided by the currently

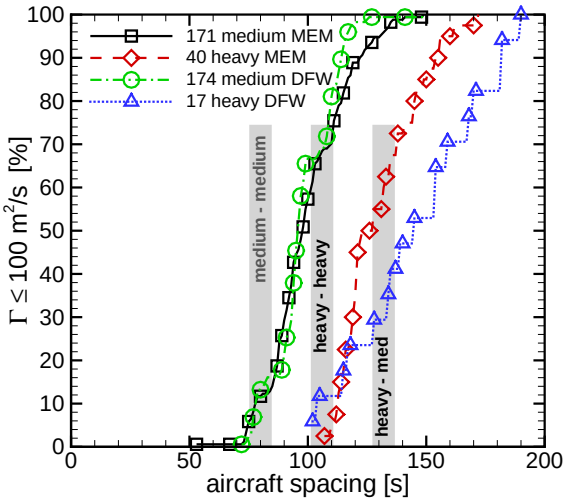


Figure 12: Cumulative distributions of aircraft separations based on conservative decay predictions of P2P assuming a threshold of $\Gamma = 100$ m$^2$/s for acceptable vortex strengths.

effective aircraft separation standards. Consequently, in many cases only wake vortex transport bears the potential to allow for reduced spacing operations with appreciable capacity benefits.

However, predictions of vortex transport are hampered by the substantial spatiotemporal variability of environmental conditions. During the WakeOP campaign, crosswind jumps of almost 5 m/s along less than 200 m length of flight track were observed which point up the importance of probabilistic predictions. Clearly, vortex prediction quality depends on available crosswind data sources. Predictions based on Lidar crosswind measurements yield the least dispersed results. Possibly, the averaging time of 80 s is most appropriate because it corresponds roughly to the life span of the vortices. Larger deviations reflect the suboptimal averaging times of 10 min and 10 s employed by Sodar and aircraft crosswind data, respectively.

Forty-one cases of the WakeOP campaign are used to evaluate the potential of P2P to predict the time when the vortices have left a safety corridor around the flight track. Depending on crosswind data sources

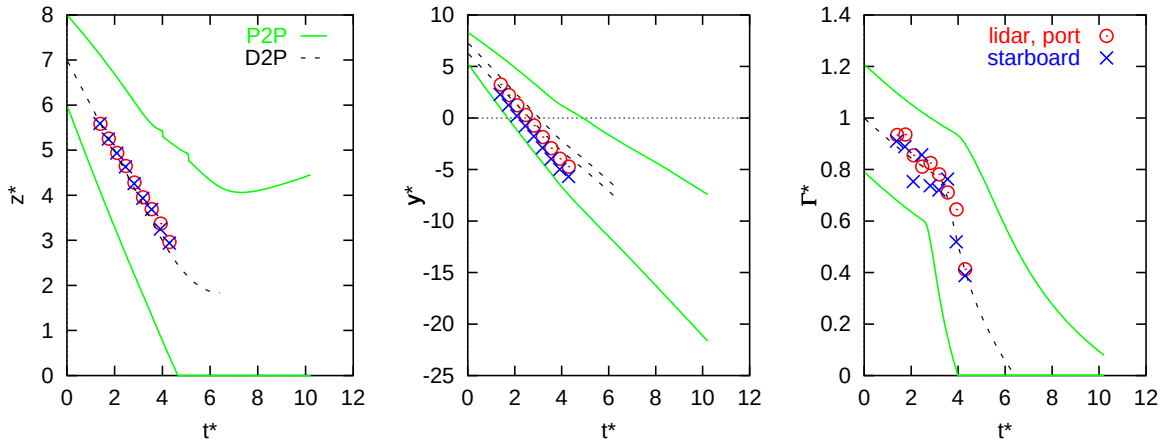


Figure 13: Measured (symbols) and predicted (lines) evolution of normalized vertical and lateral positions and circulation of trailing vortices from WakeTOUL flight 4-17. Black dashed lines denote deterministic behavior, green solid lines the respective probabilistic envelope.

aircraft separations could have been safely reduced in 46% - 66% of the overflights. Almost surprisingly, also crosswind provided by dedicated short-term weather forecasts would have allowed the safe reduction of separations to below 50 s in 39% of the cases.

## 5.3 Further Development

With the field experiments WakeTOUL and AWIATOR at Tarbes airfield the superior suitability of the $2-\mu$m pulsed Doppler lidar for wake vortex characterization has been demonstrated (Köpp et al. 2004). Two decisive factors, the long-range capability of more than 1 km and a four-stage data processing, enable observations over periods from vortex generation to a progressed state of vortex decay. Figure 13 demonstrates that the two-phase decay anticipated by simulations and theory (sections 2.1.2 and 2.3) now for the first time could be unambiguously corroborated by measurements. More than 40 overflights clearly supply evidence of the previously controversly discussed two-phase vortex evolution (Spalart 1998, Gerz et al. 2002) predicted by P2P.

In the following, the further developments of P2P regarding circulation decay, effects of axial wind and glide slope angle, axial- and crosswind shear, and model validation are briefly introduced.

The long observation times achieved during WakeTOUL and AWIATOR campaigns suggest to increase the onset time of rapid decay, $T_2^*$, by a factor of 1.2. This delayed decay approximately also covers prolongated lifetimes caused by constant background shear described in sections 2.3 and 5.2.

Compared to a calm situation, headwind (tailwind) advects younger (older) vortex segments into the fixed lidar observation plane which is usually spanned perpendicular to the flight direction and in which P2P predicts vortex evolution. The resulting difference in age, $\Delta t$, depends on axial wind velocity, $u$, and aircraft ground velocity, $V$, according to

$$\Delta t = \frac{u/V}{1-u/V}\, t \quad . \tag{4}$$

Equation (4) implies that the younger (older) vortex has covered a smaller (larger) transport distance at a given observation time.

Another effect arises from axial wind for descending and climbing aircraft. For instance, for descend-

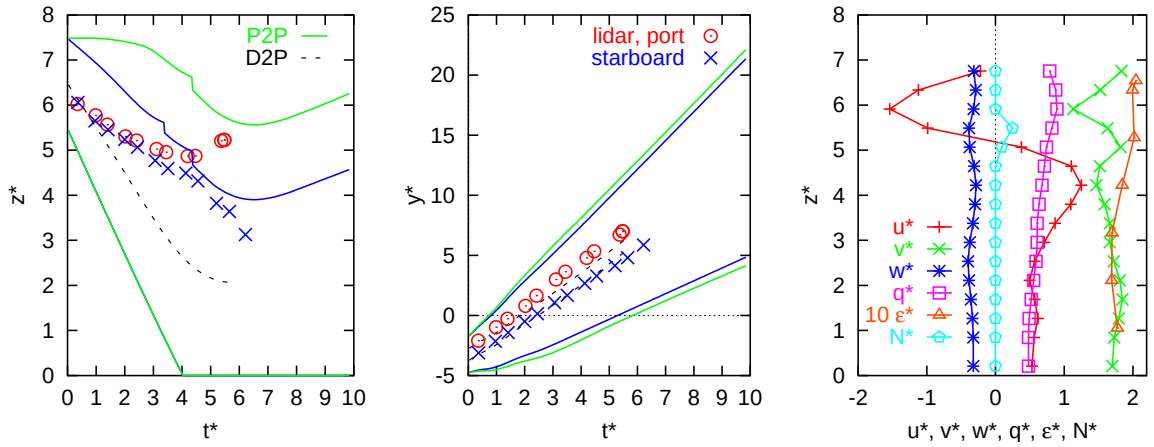


Figure 14: Measured (symbols) and predicted (lines) evolution of normalized vertical and lateral positions of trailing vortices penetrating a pronounced shear layer (AWIATOR flight 1-04). Black dashed lines denote deterministic behavior, green (blue) solid lines the probabilistic envelope with (without) the shear-layer model. Right, vertical profiles of normalized environmental data which serve as input for P2P.

ing aircraft the vortex advected by headwind (tailwind) is generated at lower (higher) altitude compared to the generation height within the control plane. The respective height difference, $\Delta z$, depends on age difference, flight speed, and glide slope angle, $\varepsilon$, according to

$$\Delta z \;=\; \Delta t \; V \; \tan\varepsilon \quad . \tag{5}$$

For example, for an aircraft facing a headwind of $-7$ m/s at an approach speed of $V = 70\,\mathrm{m/s}$ on a glide slope of 3 deg, the age difference amounts to more than -9% with a corresponding altitude offset of -33 m at a nominal vortex age of 100 s.

Simulation and experiment both indicate vigorous influences of wind shear on wake vortex fate. Unfortunately, wake-vortex/shear-layer interaction is extremly sensitive to a number of shear layer parameters (Hofbauer and Holzäpfel 2003). Correspondingly, Ref. [8] illustrates that sufficiently precise observations and, in particular, predictions of shear-layer characteristics are hardly feasible. Even with the dedicated wind measurement devices applied in [8] it was not always possible to measure shear layers with sufficient accuracy to fully explain the observed vortex behavior. Therefore, deterministic predictions that aim to directly emulate the interaction of wake vortices and the vorticity in the shear layer do not seem to have potential for operational applications. At most, probabilistic approaches may cover shear-layer effects.

A series of measurements from the WakeToul and AWIATOR campaigns suggest that the interaction of wake vortices with shear layers can be categorized by a normalized shear rate according to

$$sh^* \;=\; \frac{\partial v}{\partial z}\,\frac{b_0}{w_0} \quad . \tag{6}$$

Tilting and stalling or even rebounding vortices (see figure 14) are only observed when wake vortices penetrate shear layers with $|sh^*| > 1$.

For the parameterization within P2P, the wind velocity difference across a one vortex spacing height difference, $\Delta v = \partial v/\partial z \cdot b_0$, normalized by the vortex descent speed, $w_0$, can be used as a superimposed shear-induced propagation velocity, $v^*_{sh}$. If wake vortices encounter a shear layer with $|sh^*| > 1$, the normalized shear velocity widens the envelopes for vortex transport (see figure 14) in analogy to the appro-

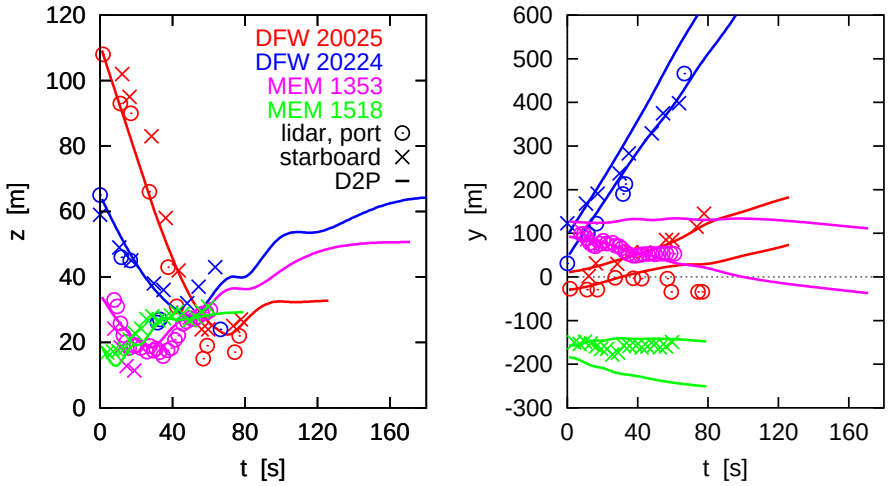


Figure 15: Measurements (symbols) and deterministic predictions (lines) of wake vortex trajectories of four overflights at different altitudes close to the ground.

ach proposed for turbulent spreading in [4]. Turbulence velocity, $q^*$, and shear velocity, $v^*_{sh}$, are superimposed quadratically to consider the connatural effects of shear and turbulence. An example of this applied to the upper bound of lateral position is

$$y^*_u = y^* + \int \sqrt{q^{*2} + (C v^*_{sh})^2}\, dt^* \quad , \qquad (7)$$

where $C$ is a constant. Shear layer uncertainty allowances are applied to both lateral bounds and the upper vertical bound. Increased shear-layer-induced descent speeds are covered by unmodified uncertainty allowances.

Some AWIATOR cases provide evidence that also axial wind shear, $\partial u/\partial z$, may cause similar effects as pure crosswind shear. This may be explained by the fact that wake vortices in the atmospheric boundary layer usually are deformed immediately, whereby the vortices become susceptible to both components of vertical shear. As consequence, $v^*_{sh}$ employs the magnitude of both vertical wind shear components. Further, it is assumed that shear-induced propagation velocities may at maximum achieve the magnitude of the current vortex descent speed, and a temporal relaxation of $v^*_{sh}$ is adopted which considers that shear-layer effects persist beyond the passage of the shear layer.

When trailing vortices approach the ground, a viscous response is provoked in the near-surface flow. The vorticity created along the ground first causes the wake vortices to diverge much like a pair of image vortices would have been introduced below the surface. Later, the surface vorticity may erupt abruptly leading to the formation of secondary vortex structures that provoke a lurching rebound of the newly created vortex pairs. In P2P this sequence is modeled by the subsequent introduction of image vortices, a first set, and a second set of secondary vortices with images following the approach of Robins et al. (Ref. 29 in [4]). Although effects of the ground are yet neither assessed nor optimized, the performance of the two-phase model appears excellent (see Figure 15) based on a few Memphis and Dallas Fort Worth cases selected for a benchmark comparison of wake vortex models[‡‡].

Comprehensive evaluation of wake prediction

[‡‡]The benchmark exercise was performed on the occasion of the NASA Workshop on The Prediction of Wake Vortices In-Ground Effect in an Operational Context, New Orleans, LA, April 27 - 29, 2004.

skills is achieved by the compilation of probability density distributions (PDD) which set wake vortex measurements into relation to the upper and lower bounds of the predicted uncertainty allowances (see figure 16). For this purpose, the value of every single vortex measurement (exemplarily shown for lateral position) is normalized according to

$$\hat{y} = (y_{meas} - y_l)/(y_u - y_l) \quad . \tag{8}$$

Equation (8) assigns a value of one to a vortex measurement situated on the predicted upper bound (index $u$) and the value zero to measurements on the lower bound (index $l$).

Measurements of the whole vortex evolution - from generation to decay - are included in the statistics. The shown PDD employs data of 49 overflights out of 2 campaigns, 6 days, and 872 vortex observations, respectively. Only overflights are used where vortex and meteorological data were measured completely and with high quality. Therefore, the PDDs should mainly represent the intrinsic variability of vortex evolution and to a lesser extent the uncertainties of the input parameters of P2P.

The data sample includes many long-lived and complex cases with e.g. pronounced shear effects. Note that the PDD for vortex descent is skewed due to a few cases with retarded descent caused by shear layers. Also the PDD for circulation is not centered around $\hat{\Gamma} = 0.5$ because it is only optimized regarding the relevant upper boundary $\hat{\Gamma} = 1$. The lower bound for circulation is irrelevant. All other flanks of the PDDs decline steeply when approaching the probabilistic bounds 0 and 1 which indicates that the applied uncertainty allowances are close to an optimum. The probabilistic 2P model could predict wake vortex behavior conservatively in 99.7%, 99.7%, and 97.9% of the observations for lateral position, vertical position, and circulation, respectively.

Figure 16 indicates further that normal distributions (dotted lines) fit reasonably well to the PDDs. The normal distributions are useful for prediction of stochastic deviations from deterministic vortex behavior in a Monte-Carlo-simulation approach as it is employed in the WakeScene Package (Holzäpfel et al. 2004).

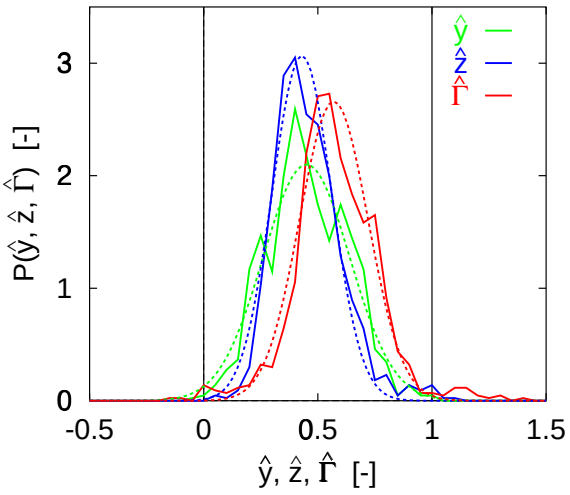


Figure 16: Probability density distributions of measured lateral position, vertical position, and circulation of wake vortices normalized with respect to the uncertainty bounds predicted by P2P. Values of zero and one denote lower and upper bounds, respectively. Fits of normal distributions denoted by dotted lines.

Although the underlying data sample is not very large it, nonetheless, comprises a variety of complex wake vortex cases. Presumably, the shape of the distributions will not be basically modified by an enlarged data sample. It is evident that already now the performance of P2P documents a high level of skill and the uncertainty allowances appear appropriate. Nevertheless, future high-quality measurement data are needed to augment the validity of this assessment.

# 6 Outlook

To date, the predictive skills of the P2P model have been successfully assessed for operations out of ground effect based on data of five different measurement campaigns. Though a few selected bench-

mark cases indicate excellent performance also close to the ground, the model has neither been explicitly optimized nor validated yet for vortex prediction in ground proximity. Given the manifold of wake vortex behavior and the high safety requirements regarding intended operational wake vortex prediction systems, further comprehensive analyses based on high-quality measurements remain mandatory. Future measurement campaigns are expected to contribute qualified data.

In case that the model performance in ground proximity will turn out not to be reliably enough, LES may help to provide further insights in the governing physical mechanisms. High-resolution grids and appropriate subgrid-scale modeling of the boundary layer flows, which are characterized by complex pressure fields and abrupt eruptions of surface fluid, will be indispensable to yield credible results. Competing effects of atmospheric turbulence, wind shear, and ground-induced secondary vortices on wake vortex decay must be evaluated and parameterized for real-time wake vortex prediction.

The integration of the P2P model into the Wake Vortex Prediction and Monitoring System (WVPMS), which is developed within the DLR project Wirbelschleppe, must be advanced. Direct interfaces pertain to quality controlled meteorological measurement data which are merged from various sensors and to numerical short-term weather forcast data provided by the model system NOWVIV (Nowcasting Wake-Vortex Impact Variables, see [8]). Moreover, the combination with the SHAPe model (Simplified Hazard Area Prediction, [8]), which predicts the dimensions of potentially hazardous areas around wake vortex cores for a given following aircraft, must be refined. The resulting model chain for the prediction of environmental conditions, vortex behavior, and respective hazard areas must be combined with lidar observation systems that monitor smooth operations. The challenge will be to map the temporal and spatial resolution, availability, and accuracy of environmental and aircraft data on the uncertainty allowances pertaining to probabilistic predictions of minimum separations such that the requirements on capacity and safety gains envisaged by the WVPMS are met. Finally, the WVPMS must be integrated into existing ATC environments taking into account appropriate time horizons for planning, adequate human-machine interfaces, and acceptable controler work load. During three-month trial operations, planned for spring 2006 at Frankfurt airport, the WVPMS will have to demonstrate its qualification to safely reduce aircraft separations.

Further activities will be devoted to enhancements of the WakeScene Package which is supposed to assess the probability to encounter A380 wake vortices in different air traffic scenarios and the respective encounter severity. The package components, which model air traffic mix, aircraft trajectories, meteorological conditions, wake vortex evolution, and potential hazard area, must be brought to an adequate and consistent degree of realism. For wake vortex prediction, sub-models for vortex core growth, as well as for the orientation and deformation of vortex axes have to be developed to enable detailed encounter investigations.

Another future application will be wake vortex prediction in cruise. With regard to the step by step world-wide accomplished Reduced Vertical Separation Minima (RVSM), which reduce vertical separations between aircraft from 2000 ft to 1000 ft above flight level 290, the risk to encounter wake vortices in cruise increases. New data link technologies like ADS-B (Automatic Dependent Surveillance-Broadcast) supply information on nearby aircraft and environmental conditions. This data can be utilized to avoid wake vortex incidents by providing the pilot with information regarding an impending potential wake vortex encounter. For airborne wake vortex warning systems the limited availability and accuracy of environmental data will require the determination of new and relatively large uncertainty allowances.

# 7 Acknowledgments

Sincere thanks are addressed to Prof. Dr.-Ing. Rudolf Schilling for his kind and spontaneous acceptance to take the chair of the council of referees and to Prof. Dr.-Ing. Rainer Friedrich for his encouragement and continuous interest in my research. I am indepted to Prof. Dr.-Ing. Ulrich Schumann for his cordial support of my work, stimulating challenges in numerous discussions, and his reliance that prepared the freedom for creative research throughout many years. Dr. Thomas Gerz, who introduced me to the secrets of his LESTUF code, always contributed in his friendly and reliable manner precise and enriching comments and support to any issue. Dr. Michael Frech, who candidly shared his meteorological background with me, was always patiently prepared for any discussion. I am grateful for the essential contributions of numerous DLR colleagues, from whom only a few representatives as Robert Baumann, Dr.-Ing. Klaus-Uwe Hahn, Friedrich Köpp, Dr. Igor Smalikho, and Dr. Arnold Tafferner are named here. Many thanks are expressed for all the constructive cooperations with colleagues from Airbus, CERFACS, DFS, NASA, NLR, NWRA, ONERA, and QinetiQ. Wake vortex research was also the occasion to make friends far abroad with colleagues like Dr. Donald P. Delisi and Robert E. Robins. Last not least, I want to thank my familiy for encouraging me to compile this manuscript. The financial support within the DLR Projekt Wirbelschleppe and by the European projects ATC-Wake, AWIATOR, C-WAKE, S-WAKE, WakeNet, and WAVENC is gratefully acknowledged.

# 8 Integrated Journal Publications

[1]

## Two-Dimensional Wake Vortex Physics in the Stably Stratified Atmosphere

F. Holzäpfel, T. Gerz

Aerospace Science and Technology, 1999

Volume 3, Number 5, Pages 261–270

*Aerospace Science and Technology*, 1999, no. 5, 261–270

# Two-dimensional wake vortex physics in the stably stratified atmosphere

F. Holzäpfel *, T. Gerz

Institut für Physik der Atmosphäre, DLR Oberpfaffenhofen, 82234 Weßling, Germany

(Received 15 February1999, revised and accepted 12 May 1999)

Holzäpfel F., Gerz T., *Aerospace Science and Technology*, 1999, no. 5, 261–270

**Abstract**

The effects of stable stratification on aircraft wake vortices are investigated by means of high-resolution two-dimensional simulations. The simulations elucidate that the vortices first decelerate and then accelerate their descent, where they largely conserve their circulation. However, for very stable stratification the tip vortices may rise again to the flight path. The underlying physical mechanisms are revealed by means of a point vortex method and are examined complementarily by balancing the impulse of the wake vortices. It is shown that the prominant effects, deceleration, detrainment and acceleration, are caused by the kinematic interaction of the vorticity generated by baroclinity and the primary vorticity. Furthermore, it is found that the impulse of the 'whole' system, including the detrained secondary vorticity, is oscillating with the Brunt-Väisälä frequency which implies that the wingtip vortices themselves do not. Finally, a local shear-number is proposed which takes into account the interaction of primary and secondary vorticity and can describe the instantaneous tendency of wake vortices to accelerate or to decelerate. © Elsevier, Paris

**wake vortex / stable stratification / numerical simulation**

**Zusammenfassung**

**Zur Physik der Wirbelschleppe in der stabil geschichteten Atmosphäre.** Der Einfluß stabil geschichteter Atmosphäre auf die Entwicklung von Flugzeug-Wirbelschleppen wird mittels hochauflösender, zweidimensionaler Simulationen untersucht. Zunächst sinken die Wirbel verzögert und in einer späteren Phase beschleunigt ab. Dabei wird die Zirkulation der Wirbel weitgehend erhalten. Jedoch steigen die Wirbel in einer sehr stabil geschichteten Umgebung wieder bis auf Flugniveau auf. Die zugrundeliegende Physik der beobachteten Effekte wird mit Hilfe einer Punktwirbelmethode und anhand von Impulsbilanzen untersucht. Es wird gezeigt, daß die wichtigsten Phänomene, die Verzögerung, das Detrainment und die Beschleunigung der Wirbel, durch die kinematische Wechselwirkung primärer und baroklin erzeugter Vorticity verursacht werden. Weiterhin wird gezeigt, daß der Impuls des gesamten Wirbelsystems, einschließlich der detrainten Vorticity, mit der Brunt-Väisälä Frequenz oszilliert, während die eigentliche Wirbelschleppe dies nicht tut. Schließlich wird eine lokale Scherzahl abgeleitet, die die momentane Neigung der Wirbelschleppe verzögert oder beschleunigt abzusinken beschreibt. © Elsevier, Paris

**Wirbelschleppe / stabile Schichtung / numerische Simulation**

* Correspondence and reprints.

## 1. Introduction

Aircraft wake vortices may exert a serious danger on following aircraft if the separation between leading and following aircraft is not sufficient. In view of the expected growth of air traffic [29], increasing demands on the capacity and safety of international airports have to be faced. In order to increase airport capacities whilst at least maintaining safety levels, the knowledge of wake vortex behavior under varying meteorological conditions merits considerable significance. In principle, wake vortices descend below the glide path caused by mutual velocity induction. But under certain meteorological conditions, wake vortices may stall or rise again into the glide path corridor [8, 16, 30]. We show that, at least in the limits of 2D investigations, this hazardous situation actually may occur in strongly stratified atmospheres. Also, in the quite often prevailing moderately stratified environments, wake vortex behavior is considerably modified.

The climatology, based on nine years worth of data from nine different aerological stations in Germany [9], reports nocturnal inversions with potential temperature gradients of more than 1 °C/100 m in the lower troposphere in 59 % of all cases. In Munich 70 % inversions were found at midnight and at 9:00 LST 12 % were still persisting.

The impact of stable stratification on wake vortices has been a controversial discussion for years. Whereas some studies indicate that the vortices decelerate and stop their descent roughly after 1/4 of the oscillation period [7, 10, 11, 18, 21] or may even oscillate in a similar way as a displaced buoyant parcel of fluid [20], other analyses show that wake vortices may accelerate their descent due to baroclinic effects [2, 26]. Some works [4, 15, 22, 27] demonstrate that both events may occur in sequence. Consensus seems to emerge from recent 3D simulations [19, 24]. These corroborate our recent 3D simulation results which are part of ongoing work and will be published later: All 3D simulations show that during the early descent the wake vortices simultaneously decelerate and approach each other. This behavior is almost identically observed in 2D investigations and, furthermore, is also confirmed by experiments (see *figure 1*). The subsequent acceleration seen in 2D is widely damped in 3D by different instability mechanisms, whereas the type of instability depends on the state of turbulence in and around the vortex pairs.

The current work, although limited to two dimensions, is to deepen and to reach a consensus on the basic understanding of wake vortices in a stably stratified atmosphere. Among others, the physics of basic effects such as the deceleration and detrainment phenomena is investigated in detail. Please note, that the authors assume these early effects to be intrinsically two–dimensional. On the other hand, 3D studies are clearly needed to understand the subsequent trailing vortex decay.

## 2. Numerical model, initial conditions and normalized variables

The 2D code is based on a Boussinesq large-eddy simulation code which uses the classical Smagorinsky closure and was originally developed to simulate turbulence, i.e. fluctuations of velocity and temperature, under the influence of constant background shear and stratification [12]. The LES code was then tuned to model the dynamics of aircraft wakes and the associated exhaust distribution under cruising conditions [5]. In this context it proved its reliability, for it reproduced the typical wake structure and quantitative exhaust properties as observed in measurement campaigns [6].

For our purposes here, we chose a domain size of $L_x \times L_y \times L_z = 6 \times 384 \times 600\ \mathrm{m}^3$ with a uniform grid volume of $\Delta x \times \Delta y \times \Delta z = 1 \times 1 \times 1\ \mathrm{m}^3$. The flight direction is denoted by $-x$, the span by $y$ and the height by $z$. Periodic boundary conditions are employed in all three directions. The influence of neighbouring wakes on the descent velocity, $w$, due to the boundary conditions, was reduced by choosing appropriate distances between the vortices and the domain boundaries and is proven to be less then 2.3 % for neutral stratification (see *figure 2*).

The wake vortices were initialized as superposition of two Lamb-Oseen vortices where the tangential velocity profile of one vortex is given by

$$v_t(r) = \frac{\Gamma_0}{2\pi r}\left(1 - \exp\frac{-r^2}{r_0^2}\right) \quad , \quad r_0 = \frac{r_c}{1.121} \quad , \quad (1)$$

with a core radius of $r_c = 4$ m. A root-circulation of $\Gamma_0 = 565\ \mathrm{m}^2/\mathrm{s}$ and a vortex spacing of $b_0 = 47$ m were employed to represent the B-747 aircraft with an elliptical wing loading. The mean temperature gradient of the atmosphere, $d\Theta/dz$, was constant in each calculation and the corresponding Brunt-Väisälä frequencies

$$N = \left(\frac{g}{\Theta_0}\frac{d\Theta}{dz}\right)^{1/2} \quad (2)$$

varied between 0 and 0.056/s ($0 \le d\Theta/dz \le 10$ K/100 m), i.e. between neutral and very stable stratification.

All results are presented in non-dimensionalized form. The characteristic scales are based on the initial vortex separation, $b_0$, and circulation, $\Gamma_0$, leading to the time scale

$$t' = \frac{2\pi {b_0}^2}{\Gamma_0} = \frac{b_0}{w_0} \, . \quad (3)$$

For the normalized time and Brunt-Väisälä frequency it follows $t^* = t/t'$ and $N^* = Nt'$, respectively. $1/N^*$ corresponds to the vortex Froude number.

## 3. General characteristics and phenomena

*Figure 1* depicts the temporal development of the normalized descent height $z/b_0$, which was determined by searching the local pressure minima. For reference the linear descent for neutral stratification is included. In the most stable case, $N^* = 1.4$, the vortex behavior differs considerable from the other cases and, therefore, is discussed later in this section and partially omitted in the following sections. In the stable cases with $N^* \leq 1.0$ the descent is first decelerated and then progresses with an acceleration. The vortices reach their minimum descent velocity roughly at $t^* = 3$ (see *figure 2*) and, for $N^* = 1$, stall and even rise again a few meters to a height of approximately one initial vortex separation below flight level. Then they continue to descend and accelerate up to three times their initial speed.

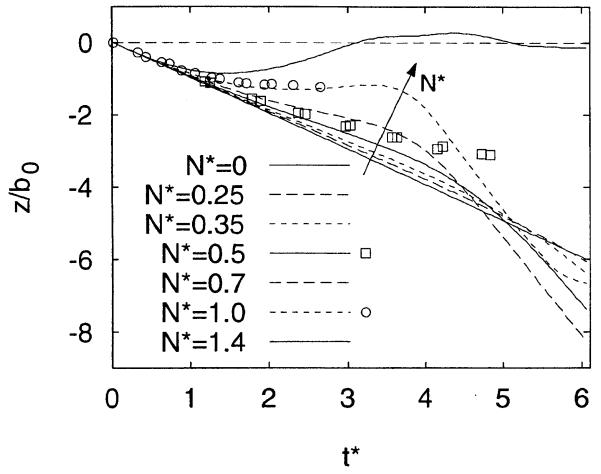


**Figure 1.** Normalized descent distance versus time for different stratifications. 2D-simulations (lines) and Sarpkaya's experimental data [21] (symbols).

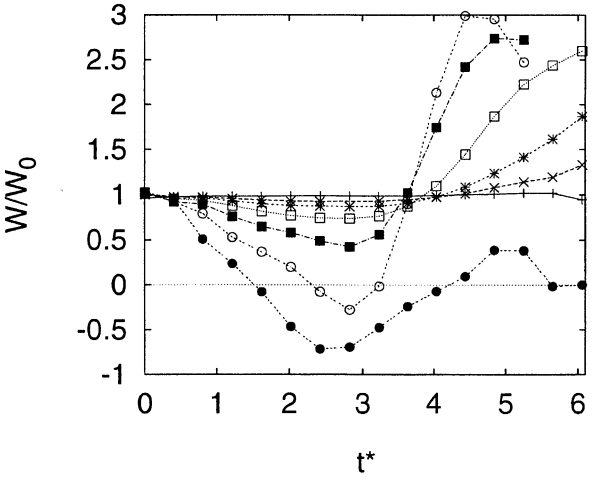


**Figure 2.** Simulated wake descent speed normalized by initial speed; legend see *figure 4*.

Please note that during the deceleration period the 2D results agree well with Sarpkaya's towing tank experiments [21] which are delineated with symbols in *figure 1*. The agreement clearly indicates that the physics of the early deceleration is intrinsically 2D. For the further evolution of the trailing vortices Sarpkaya states that the vortices were primarily destroyed by different 3D instability mechanisms which are, of course, excluded in the 2D simulations.

*Figures 3* and *4* indicate that the vortex separation $b/b_0$ decreases drastically when $t^* > 2$ whereas the circulation $\Gamma$ is largely conserved. (Note that $\Gamma$ was integrated along the oval-like streamline which separates the fluid belonging to the wingtip vortices and the surrounding fluid. The lower values of $\Gamma$ observed between $0.5 \leq t^* \leq 3.5$ result from the fact that at that time the oval encloses also counter-rotating vorticity, see below.) Our findings of a circulation remaining constant over a

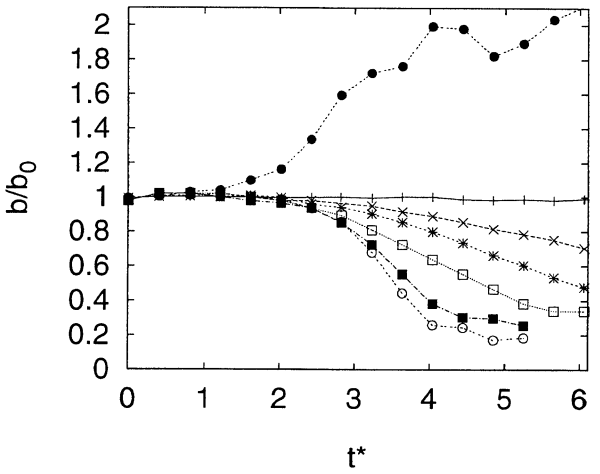


**Figure 3.** Simulated vortex spacing normalized by initial spacing; legend see *figure 4*.

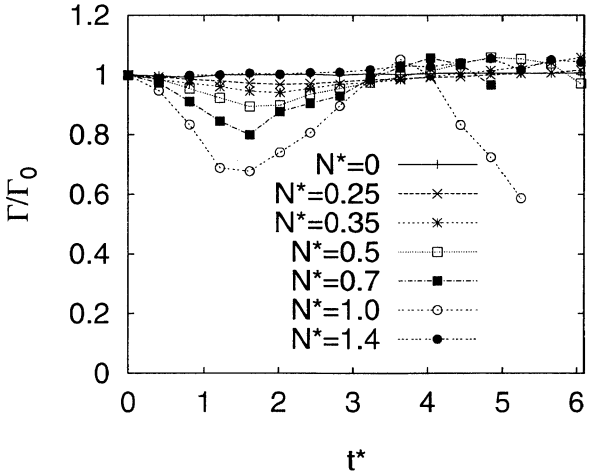


**Figure 4.** Simulated circulation normalized by initial circulation.

long period and dropping suddenly afterwards are in good agreement with measurements [8] but are in contrast to other work [7] which assumes a monotonous decrease of $\Gamma$. We notify that the approach of the vortices which de facto keep their initial circulation may explain the late acceleration of the vortex pair by the increased mutual velocity induction. It, however, leaves the early deceleration unexplained which may have led to some controversy in earlier works.

For $N^* = 1.4$ the vortices descend only about one vortex spacing, then rise again to remain, finally, on the flight level with unaltered circulation. The increasing vortex spacing, which reaches two times the initial spacing at $t^* = 6$, presumably, will impede rapid mutual destruction mechanisms such as the Crow instability. Here, the hazardous situation of two almost solitary and, thus, persistent vortices in the flight path may occur. 3D simulations will be needed to show whether this is likely to happen in reality. Since $N^* = 1$ constitutes the weakest stratification bearing slightly rising vortices it may be considered as a conservative threshold for this hazardous scenario.

## 4. Detailed analysis of phenomena

Basically, the oval around the vortex pair, which contains the primary vorticity and is termed the primary wake, descends and warms adiabatically in a stably stratified environment owing to compression. The evolving force does not simply decelerate the sinking motion of the oval as is often assumed when considering the oval as an ideal particle. But it creates secondary vorticity which has the opposite sign to the primary vorticity [26] in terms of the baroclinic torque according to

$$\frac{D\omega}{Dt} \sim \frac{1}{\rho^2} \nabla\rho \times \nabla p \,. \qquad (4)$$

This torque is effective when the gradients of density, $\rho$, and pressure, $p$, have perpendicular components as it is displayed schematically in a plot of isolines of the integrated streamfunction in *figure 5*.

The temperature contour plots in *figure 6* elucidate that the largest horizontal density gradients are not always found directly at the separating streamline as anticipated in previous work [11, 26]. In early stages ($t^* = 0.7$) when stratification effects still play a minor role, the vertical displacement of individual fluid particles is dominated by vortical advection resulting in the largest horizontal density gradients and, thus, in strongest baroclinical vorticity (BV) production 'inside' the oval. (This explains the transient decay of $\Gamma$ as discussed above, see *figure 4*). Later ($t^* = 3.1$), the mean descent altitude causes the dominant density deviation from the ambient air.

*Figure 7* displays contours of axial vorticity, $\omega_x$, for $N^* = 1$. At $t^* = 3.1$ the vorticity of the primary vor-

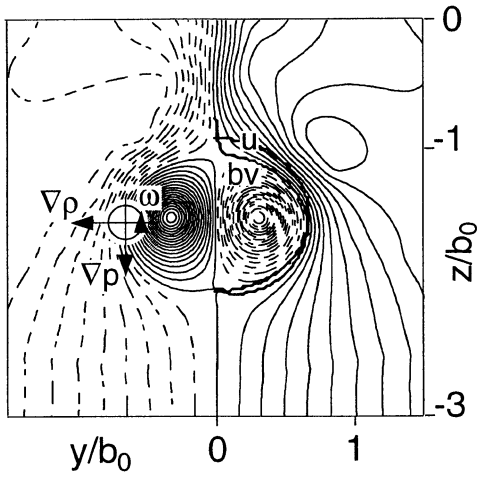


**Figure 5.** Sketch of vorticity production by the baroclinic torque. Integrated streamfunction contours are shown for $N^* = 1$ and $t^* = 3.1$. bv marks the actual and u the analytically achieved separating streamline.

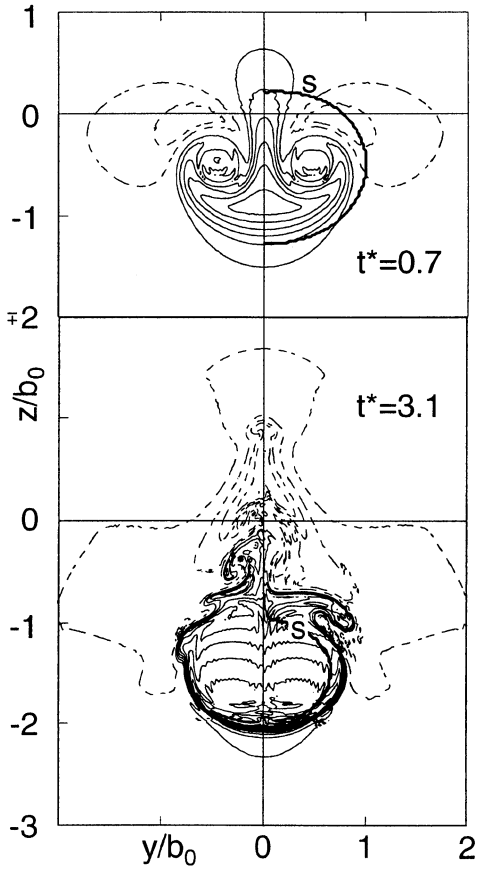


**Figure 6.** Temperature deviation for $N^* = 1$. Contour increments: 0.5 K, dashed lines mark negative values. Separating streamline is marked with $s$.

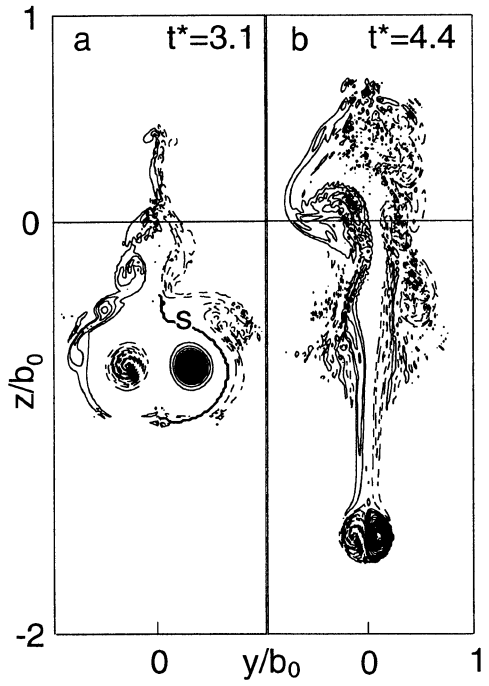


**Figure 7.** Axial vorticity $\omega_x$ at different times; $N^* = 1$. Contour increments: 0.25/s, dashed lines mark negative values. Separating streamline is marked with s.

tices still is isolated in the cores but almost entirely surrounded by BV. At the upper stagnation point the BV is completely left behind the oval and constitutes the secondary wake which extends from the primary wake to a height above the flight level. The temperature plot at $t^* = 3.1$ (*figure 6*) shows that the moving oval 'pushes' (below the lower stagnation point) and 'pulls' (above the upper stagnation point) ambient air downwards. Therefore, the steepest temperature gradients and, consequently, the maximum vorticity production occur just outside the separating streamline. This implies that the opposite vorticity is advected around the oval and is completely left behind the wake vortices. Hence, at this stage ($t^* = 3.1$) the question whether opposite vorticity can also be entrained into the oval is denied which is of great interest for the formation of instabilities and the decay of the vortices [26, 27].

The half rings of secondary vorticity surrounding the primary wake lead to a disturbance of the velocity field. *Figure 8* shows swirl velocity distributions $v_\theta(r)$ at three different times (these were derived by transforming the respective velocity fields into the tangential components of two axisymmetric vortices). The vortex at $t^* = 0.7$ is only little influenced by stratification which results in an induced descent velocity close to one at $r = b_{0.7}$. At $t^* = 2.3$, the swirl velocity decreases steeply in the vicinity of the separating streamline and $v_\theta(b_{2.3})$ almost vanishes. Hence, the primary wake stalls because the BV induces an upward motion inside the oval which compensates the downward motion of the primary vortex pair. However, such swirl velocity profiles are highly unstable according to the stability criterion defined by Rayleigh [17]. As a consequence, Taylor-Görtler instabilities evolve which can clearly be observed in the vorticity distribution displayed in *figure 7a*. Presumably, in the unstable region tiny roundoff errors in the initialization and discretization method are sufficient to raise the asymmetries observed in *figures 6* and *7*. But they do not generate a non-zero axial velocity component. At this stage, the secondary vorticity, which is still produced by the baroclinity, moves slowly upwards along the separating streamline. As we explain in the following section, the oval begins to lose mass (detrainment) in the vicinity of the upper stagnation point. To fulfil mass conservation constraints, the two main vortices have to strongly approach each other which, in turn, increases the induced descent speed (see *figures 2* and *3*) such that the vortices can eventually escape from their 'buoyancy trap' by quick downward motion (*figure 7b*). Note that the typical vortex profiles are established again during the fast descent (*figure 8*, $t^* = 4.4$). Hence, the main vortices have recovered from the 'buoyancy disease' but only to approach each other more and more which finally leads to their destruction by direct interaction as indicated by the sudden loss of their – so far conserved – circulation (*figure 4*). We remark here that the late stages are of academic interest because in 3D instability mechanisms would suppress the final acceleration.

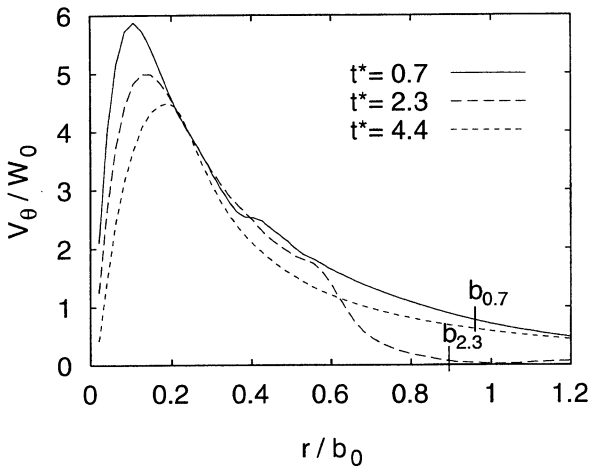


**Figure 8.** Swirl velocity profiles, $v_\theta(r)$, and respective vortex spacings at three different times; $N^* = 1$.

## 5. Kinematic description – deceleration and detrainment

One simple and evident explanation for the deceleration of the vortex pair is given by buoyancy. However, the inconsistence of the approaching vortices with

constant circulation and, nevertheless, decreasing descent speed remains unresolved. A more comprehensive view which also explains the detrainment phenomenon is achieved by considering the mutual velocity induction of primary and BV. Please note that this purely kinematic arguments provide a full reasoning of all effects since in the vorticity equations the influence of bouyancy exclusively is expressed by the baroclinic term.

Assuming the density discontinuity along the separating streamline, the BV production can readily be calculated according to equation (4) [26]. In (4) only the contributions of pressure gradients caused by the hydrostatic balance ($\partial p/\partial z = -\rho g$) have to be considered. Contributions from centrifugal forces vanish, since centrifugal pressure gradients and density gradients always are perpendicular to streamlines and, thus, parallel. For the axial vorticity component we obtain

$$\frac{D\omega_x}{Dt} = -\frac{g}{\rho}\frac{\partial \rho}{\partial y}. \tag{5}$$

The lateral density gradient over a layer of thickness $\delta$ can be expressed in terms of the Brunt-Väisälä frequency

$$\frac{\partial \rho}{\partial y} = \frac{\partial \rho}{\partial n}\sin\psi \equiv \frac{\Delta\rho}{\delta}\sin\psi = -\rho\frac{N^2 z}{g\,\delta}\sin\psi \tag{6}$$

where $\psi$ is the angle made by gravity and the normal $n$ to the separating streamline. The equation resulting from equations (5) and (6) can be non-dimensionalized using the time scale (3) and

$$\omega' = N^2\, t'\,\frac{z}{\delta} \tag{7}$$

which yields

$$\frac{D\omega_x^*}{Dt^*} = \sin\psi\,. \tag{8}$$

Note that equation (8) gives the BV production independent from the individual parameters. The produced BV accumulates during the advection of fluid particles along the separating streamline being weighted with the respective residence times. Hence, the strength of the vortex sheet increases from zero at the lower stagnation point to a maximum at the upper stagnation point, whereas the production rate is maximum at the height of the vortex cores and zero at the stagnation points.

*Figure 9a* depicts the velocity field which is induced by 164 point vortices situated along the separating streamline. The point vortices represent the BV for $N^* = 1.0$ during the stall in a descent height of $z/b_0 = -1.4$. Different descent heights and stratifications do not change the shape but only modify the magnitudes of the self–similar velocity field.

The upwards directed flowfield inside the oval together with the downwards velocities around the oval induce a reduction of the descent speed. The topology of the flowfield inside the oval is illustrated in a simple sketch (*figure 10*). Horizontally opposite point vortices 1, 2 induce vertical velocities which increase from below to above (see stronger vortices 3, 4). Vertically separated vortices 2, 3 induce upwards directed velocities with an additional horizontal component which manifests the approach of the vortex pair.

The superposition of the primary and the BV induced velocity fields is shown in *figure 9b*. Now, the calculation of the separating streamfunction *bv* leads to a basically modified shape: A part of the surrounding fluid is entrained below whereas a bigger part which used to belong to the oval is detrained above. The net fluxes reflect the detrainment mechanism. See also the shapes of the separating streamfunctions in the simulations (*figure 5*) which agree saliently well with the kinematic

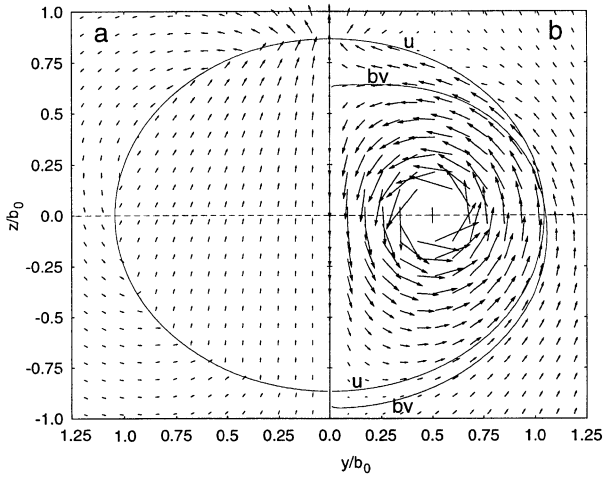


**Figure 9.** Velocity vectors from point vortex model. **a**) explicitly BV induced, **b**) superposition of BV induced and primary velocity field. *u* undisturbed and *bv* modified separating streamfunctions.

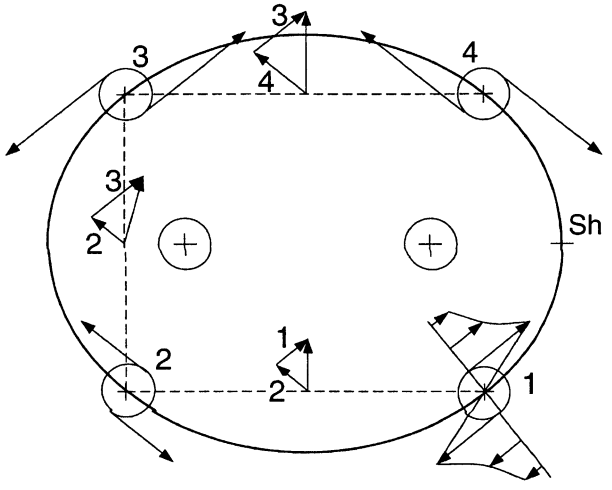


**Figure 10.** Sketch to illustrate the velocity field induced by BV. *Sh* denotes the position where the local shear–number is derived.

model, and, thus, 'prove' that the major effects are well demonstrated by the model.

The accelerated descent after $t^* = 3$ is also included in the kinematic approximation. For acceleration the vortex cores have to approach each other close enough to dominate the BV induced velocities.

Furthermore, the point vortex model may also be used to analyse buoyancy oscillations of spherical vortices which develop from any mass of buoyant fluid released in its environment [25, 28]. Various examples may be found in geophysical flows such as overshooting thunderstorms [23] or cloud turrets [3]. By dividing the oscillation into quarter periods, four different regimes can be identified which are delineated in *table I*. The sign of the temperature difference across the separating streamline determines the sign of the BV and, thus, together with the sign of the primary vorticity which changes during the transition from ascent to descent and vice versa, the ratio of the primary and BV. This leads, in turn, to entrainment of mass for positive vorticity ratios and to detrainment for negative vorticity ratios according to the above presented mechanisms. During one oscillation the regimes alternate such that after one oscillation the vortex ring has recovered to its initial mass.

**Table I.** Classification of the de- and entrainment behavior of an oscillating spherical vortex as function of the temperature of the vortex, $T_{vor}$, its environment, $T_{amb}$, and the signs of the primary, $\omega_{vor}$, and baroclinic vorticity, $\omega_{bv}$.

| Descent | Ascent |
|---|---|
| $T_{vor} < T_{amb}$<br>$\omega_{vor}/\omega_{bv} > 0$<br>entrainment | $T_{vor} < T_{amb}$<br>$\omega_{vor}/\omega_{bv} < 0$<br>detrainment |
| $T_{vor} > T_{amb}$<br>$\omega_{vor}/\omega_{bv} < 0$<br>detrainment | $T_{vor} > T_{amb}$<br>$\omega_{vor}/\omega_{bv} > 0$<br>entrainment |

## 6. Deceleration or acceleration – the local shearnumber

By relating the BV produced shear $S_B$ to the shear of one primary vortex $S_V$ a local shear–number $Sh = S_B/S_V$ can be deduced which describes the instantaneous tendency of wake vortices to accelerate or to decelerate. The local shear–number is derived at the vertical flanks of the oval (see $Sh$ in *figure 10*). This position is considered to be representative for the whole oval, because here the accumulated BV amounts to 50 % of its maximum value.

The BV produced at the flanks in a layer of thickness $\delta$ can be calculated numerically from equation (8) and amounts to $\omega_x^* = 0.6775$. Using (7) and (3) we obtain

$$\omega_x = 0.6775\, N^2 \frac{2\pi b^2}{\Gamma} \frac{z}{\delta}. \qquad (9)$$

$\omega_x = \dfrac{\partial w}{\partial y} - \dfrac{\partial v}{\partial z}$ corresponds directly to $S_B = \partial w/\partial y$ at the vertical flanks, because $\partial v/\partial z = 0$ for symmetry reasons. For the primary vorticity the shear of a Rankine vortex, at a radius corresponding to the distance of the vortex core to the vertical flank of $0.545\,b$, is used, which amounts to $S_V = 3.37\Gamma/(\pi b^2)$. This leads to the local shear number

$$Sh = \frac{S_B}{S_V} = 3.97\, z\, N^2 b^4/(\Gamma^2 \delta). \qquad (10)$$

Assuming one unit thickness for $\delta$, *figure 11* characterizes well the regimes of deceleration for $Sh > 1$ (BV dominates) and acceleration for $Sh < 1$ (primary induced velocities dominate).

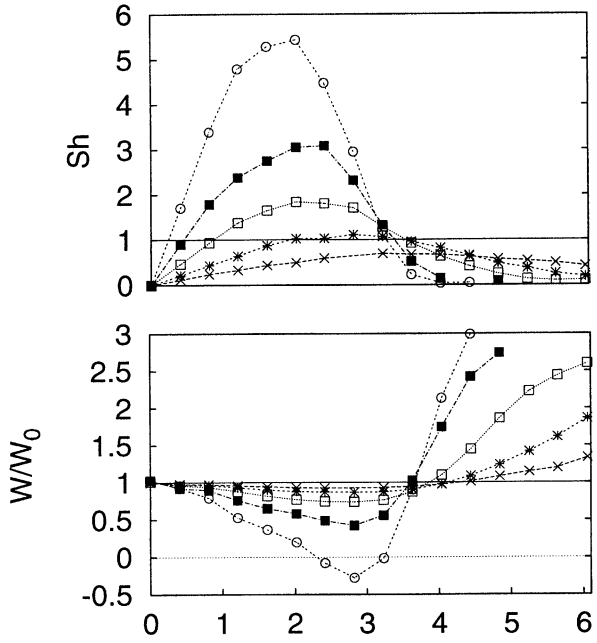


**Figure 11.** Local shear number, above, describing the state of acceleration or deceleration, below. Legend see *figure 4*.

## 7. Integral description - the impulse

After the analysis of the impact of local effects upon the wake flow behavior, this section deals with an integral description of the generic phenomena in terms of impulse. Such approaches are needed as part of wake vortex prediction algorithms [1, 7, 13, 26, 27] which are designed to predict the lifespan of particular wake vortices as a function of aircraft parameters and meteorological conditions. Approaches based on impulse are

thought to be more general because they do not rely on assumptions of specific tangential velocity profiles, as do approaches based on the kinetic energy. Nevertheless, the contribution of the rotational motion to the development of the impulse is not clear and will, therefore, be addressed in this section.

*Figure 12* displays various formulations of the impulse per unit length normalized by its initial value, $I_0 = \rho b_0 \Gamma_0$, as function of the oscillation period. Three different approaches, according to equations (11), (14), and (15) are employed, where the curves with symbols denote evaluations of our simulations following equations (11) and (15). Please note that in spite of the differing characteristics at varying stratification levels (see *figures 1* to *3*), the respective graphs clearly coincide with both methods.

Full symbols represent the impulse determined for the oval. It is calculated using

$$I_{\text{oval}} = \rho A w + 0.55\, \rho b \Gamma . \tag{11}$$

Here, $A$ denotes the area of the oval; the vertical coordinate $z$ and hence $I$ are defined positive downwards for convenience in this subsection. The first term represents the translational momentum of the descending oval and the second term the contribution of the rotation to the oval's impulse (in a manner similar to the concepts of the reduced mass of a rolling wheel, which is used to calculate its resistance to acceleration). The factor 0.55 may be derived as follows: By considering the differential equation for the undamped oscillation of a vortex pair confined in an oval with the area $A$ [7]

$$\frac{d^2 z}{dt^2} + \underbrace{\frac{\rho A}{2\pi \rho b^2}}_{0.45} N^2 z = 0 \tag{12}$$

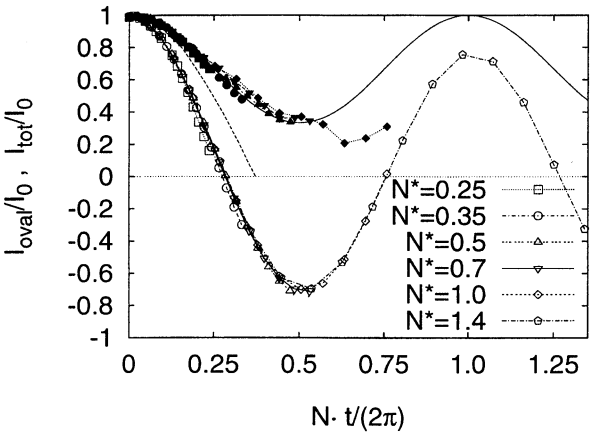


**Figure 12.** Normalized impulses versus the oscillation period. Impulses integrated over the oval of the primary wake ($I_{\text{oval}}/I_0$, full symbols; fit according to equation (13), solid line), over the area of the total wake ($I_{\text{tot}}/I_0$, open symbols), and according to equation (14) (dashed line).

a factor 0.45 arises in the linear term compared to the equivalent term in the equations for a non-rotating equal-area fluid particle. 1/0.45 represents the ratio of the reduced mass to the oval's mass. Hence, the contribution of the rotational motion is determined as $1 - 0.45 = 0.55$.

*Figure 12* shows further that the impulse of the oval may be fitted (solid line) by

$$\frac{I_{\text{oval}}}{I_0} = \frac{1}{3} \cos Nt + \frac{2}{3} . \tag{13}$$

Please note the independence of $N$. Even the change of sign of the descent speed and, thus, the translational momentum for $N^* = 1$ in the interval $0.38 \leq Nt/(2\pi) \leq 0.51$ does not cause deviations. Obviously, the impulse is *stored* in the rotational motion. Likewise, the subsequent acceleration does not result in an increase of $I_{\text{oval}}$ because it is compensated by the decrease of $A$.

In Greene's well-known wake vortex prediction approach [7], the influence of stable stratification is modeled in terms of impulse per unit length which is reduced by the buoyancy force

$$\frac{dI}{dt} = F_b = -\rho A N^2 z . \tag{14}$$

The wake is assumed to decay within a quarter of the oscillation period when the impulse of the oval reaches zero (see *figure 12*, dashed line). The oscillation period, however, is augmented for a factor of $1/\sqrt{0.45} \approx 1.5$ by taking into account the contribution of the rotation to the impulse in terms of reduced mass (see above). Nevertheless, our calculations show that $I_{\text{oval}}$ has merely reduced to $0.44\, I_0$ at one quarter of the modified oscillation period. We argue that the assumption of a constant vortex spacing is responsable for the deviation.

In contrast to that, the development of the impulse for the whole system, $I_{\text{tot}}$, including both primary and secondary wake, excellently confirms the Brunt-Väisälä theory, see open symbols in *figure 12*. This impulse is integrated according to [14]

$$I_{\text{tot}} = -\iint \rho\, \omega_x\, y\, dy\, dz . \tag{15}$$

To achieve this result the secondary wake must be considered, i.e. the boundaries for integration must be well defined.

A more refined interpretation of the underlying mechanisms can be given by considering the bouyancy force, $F_b$ (equation 14), which acts on the oval. *Figure 13* depicts the temporal evolution of the integrated $F_b$ (open symbols) and the corresponding development of the idealized buoyant particle (solid line). The interesting fact that both coincide at least 0.25 periods means that the product of the decreasing size of the oval, $A$, and the increasing vertical displacement, $z$, of the primary wake equals the corresponding product for a constant $A$ and the sinusoidal oscillation of $z$ of an idea-

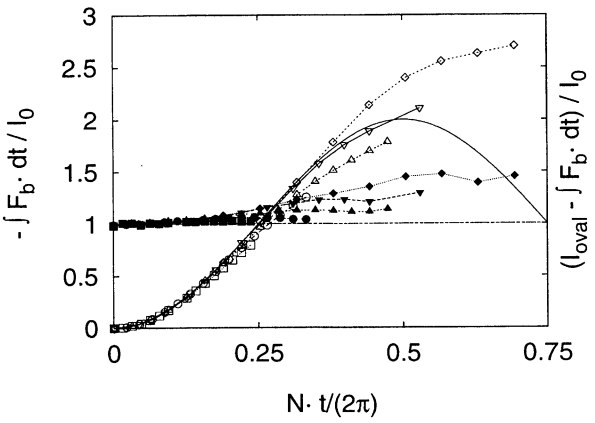


**Figure 13.** Integrated normalized bouyancy force of the oval (open symbols) and an idealized particle (solid line), left ordinate. Normalized difference between impulse and integrated bouyancy force (full symbols), right ordinate.

lized particle. Therefore, a relation between the descent height and the size of the oval - and, thus, implicitly of the vortex spacing - can be deduced from

$$z(t)A(t) = \frac{A_0 w_0}{N} \sin Nt \,. \qquad (16)$$

According to equation (14), the difference between the impulse and the time integral of $F_b$ must be $I_0$. The graphs (full symbols) in *figure 13* show a growing contribution to the impulse of the oval. This increase again is caused by the neglect of the secondary wake. *Figure 5* elucidates that during the stagnation of the oval the surrounding fluid is *blown* upwards. Hence, the primary and secondary vortices may be considered as a two-mass system in which the primary wake balances its impulse by accelerating the secondary wake upwards.

## 8. Conclusions

We have performed 2D simulations of wake vortices in stable stratification evaluating the temporal development of characteristic quantities such as descent height and speed, vortex spacing and circulation. Together with instantaneous flow pictures in terms of streamlines, temperature and vorticity fields, these data give a survey and detailed insight in 2D wake vortex physics. Considering additionally the kinematic model presented and the derived local shear–number the results clearly suggest that the sequential deceleration and acceleration as well as the detrainment phenomenon are dominantly caused by mutual velocity induction of the primary vorticity caused by the aircraft and the secondary vorticity produced by baroclinity.

The evaluations of the impulse of the wake oval itself and the total wake, including primary and secondary produced vorticity, demonstrate that the oscillation assumed in theory is executed by the whole system and not by the oval alone. The vortex oval performs complex displacement patterns which, at a first glance, seem to contradict the laws of conservation.

The similarity of the phenomena reported here (with a constant temperature gradient in the entire domain) and by Pavlenko [15] suggest that the interpretations also can hold for the immersion of wake vortices into stable layers. We argue that a gradually increasing temperature difference (as here) or a sudden jump in the temperature difference (as observed during the penetration of the vortices into an inversion layer) only result in second-order differences but will lead to the same fate in principal for an aircraft wake.

Our findings complement recent findings of the 3D trailing vortex behavior in stable stratification by elucidating intrinsically 2D elements of the complex wake vortex physics. Thus, they may help to bring together contrary results and assumptions in the analysis and modeling of vortices in stably stratified environments.

## Acknowledgements

This work was supported by the European Commission in the frame of the Brite/EuRam project WAVENC (No. BE97-4112).

## References

[1] Corjon A., Poinsot T., Vortex Model to Define Safe Aircraft Separation Distances, J. Aircraft 33 (1996) 547–553.

[2] Crow S.C., Motion of a vortex pair in a stably stratified fluid, Poseidon Research Rep. 1, Santa Monica, CA, (1974).

[3] Fujita T.T., Overshooting Tops observed from ATS and Learjet, SMRP Research Paper 117, University of Chicago.

[4] Garten J.F., Arendt S., Fritts D.C., Werne J., Dynamics of counter-rotating vortex pairs in stratified and sheared environments, J. Fluid Mech. 361 (1998) 189–236.

[5] Gerz T., Ehret T., Wingtip vortices and exhaust jets during the jet regime of aircraft wakes, Aerospace Sci. Techn. 1 (1997) 463–474.

[6] Gerz T., Holzäpfel F., Wingtip Vortices, Turbulence and the Distribution of Emissions, AIAA J., in press.

[7] Greene G.C., An Approximate Model of Vortex Decay in the Atmosphere, J. Aircraft 23 (1986) 566–573.

[8] Greenwood J.S., Vaughan J.M., Measurements of Aircraft Wake Vortices at Heathrow by Laser Doppler Velocimetry, Air Traffic Control Quarterly 6 (1998) 179–203.

[9] Gutsche A., Inversionen in der unteren Troposphäre nach Radiosondenaufstiegen in der Bundesrepublik Deutschland, Deutscher Wetterdienst, Zentralamt Abteilung Klimatologie, (1978).

[10] Hecht A.M., Bilanin A.J., Hirsh J.E., Turbulent Trailing Vortices in Stratified Fluids, AIAA J. 19 (1981) 691–698.

[11] Hill F.M., A numerical study of the descent of a vortex pair in a stably stratified atmosphere, J. Fluid Mech. 71 (1975) 1–13.

[12] Kaltenbach H.-J., Gerz T., Schumann U., Large-eddy simulation of homogeneous turbulence and diffusion in stably stratified shear flow, J. Fluid Mech. 280 (1994) 1–40.

[13] Kantha L.H., Empirical Model of Transport and Decay of Aircraft Wake Vortices, J. Aircraft 35 (1998) 649–653.

[14] Lamb Sir H., in: Hydrodynamics, Dover publ., 1945, 214–216.

[15] Pavlenko A.A., Influence of the Calm Atmosphere Stratification on the Evolution of the Vortex Behind an Aircraft, ISTC Moscow, Annual Report, Project No. 201–95 (1996) 33–40.

[16] Proctor F.H., Hinton D.A., Han J., Schowalter D.G., Lin Y.-L., Two Dimensional Wake Vortex Simulations in the Atmosphere: Preliminary Sensitivity Studies, 35th Aerospace Sciences Meeting & Exhibit, Reno, NV, AIAA 97-0056 (1997).

[17] Rayleigh Lord O.M., On the Dynamics of Revolving Fluids, P. Roy. Soc. Lond. A Mat. 93 (1917) 148–154.

[18] Robins R.E., Delisi D.P., Numerical Study of Vertical Shear and Stratification Effects on the Evolution of a Vortex Pair, AIAA J. 28 (1990) 661–669.

[19] Robins R.E., Delisi D.P., Numerical Simulation of Three-Dimensional Trailing Vortex Evolution in Stratified Fluid, AIAA J. 3 (1998) 981–985.

[20] Saffman P.G., The Motion of a Vortex Pair in a Stratified Atmosphere, SIAM LI (1972) 107–119.

[21] Sarpkaya T., Trailing vortices in homogeneous and density-stratified media, J. Fluid Mech. 136 (1983) 85–109.

[22] Schilling V., Siano S., Etling D., Dispersion of aircraft emissions due to wake vortices in stratified shear flows: A two-dimensional numerical study, J. Geophys. Res. 101 (1996) 20965–20974.

[23] Schlesinger R.E., Overshooting Thunderstorm Cloud Top Dynamics as Approximated by a Linear Lagrangian Parcel Model with Exact Solutions, J. Atmos. Sci. 47 (1990) 988–998.

[24] Schowalter D.G., DeCroix D.S., Switzer G.F., Lin Y.–L., Arya S.P., Toward Three-Dimensional Modeling of a Wake Vortex Pair in the Turbulent Planetary Boundary Layer, 35th Aerospace Sciences Meeting & Exhibit, Reno, NV, AIAA 97-0058 (1997).

[25] Scorer R.S., Experiments on convection of isolated masses of buoyant fluid, J. Fluid Mech. 2 (1957) 583–594.

[26] Scorer R.S., Davenport L.J., Contrails and aircraft downwash, J. Fluid Mech. 43 (1970) 451–464.

[27] Spalart P.R., On the motion of laminar wing wakes in a stratified fluid, J. Fluid Mech. 327 (1996) 139–160.

[28] Turner J.S., Buoyant vortex rings, P. Roy. Soc. Lond. A Mat. 239 (1917) 61.

[29] Urbatzka E., Wilken D., Estimating Runway Capacities of German Airports, Transportation Planning and Technology 20 (1997) 103–129.

[30] Zak J.A., Rodgers Jr. W.G., Documentation of Atmospheric Conditions During Observed Rising Aircraft Wakes, NASA Contractor Rep. 4767 (1997).

[2]

# Wake Vortices in Convective Boundary Layer and Their Influence on Following Aircraft

F. Holzäpfel, T. Gerz, M. Frech, A. Dörnbrack

Journal of Aircraft, 2000

Volume 37, Number 6, Pages 1001–1007

JOURNAL OF AIRCRAFT
Vol. 37, No. 6, November–December 2000

# Wake Vortices in Convective Boundary Layer and Their Influence on Following Aircraft

Frank Holzäpfel,* Thomas Gerz,* Michael Frech,† and Andreas Dörnbrack†
*DLR, German Aerospace Research Center, D-82234 Weßling, Germany*

**The decay of three wake vortex pairs of a B-747 aircraft in an evolving and convectively driven atmospheric boundary layer is investigated by means of large-eddy simulations (LES). Convective boundary layers are considered hazardous because the updraft velocities of a thermal may compensate the induced descent speed of the vortex pair such that the vortices stall in the flight path. The LES results illustrate that 1) the primary rectilinear vortices are rapidly deformed on the scale of alternating updraft and downdraft regions; 2) parts of the vortices stay on flight level but are quickly eroded by the turbulence of the updraft; 3) the longest living sections of the vortices are found in regions of relatively calm downward flow, which augments their descent. Strip theory calculations are used to illustrate the temporal and spatial development of lift and rolling moments experienced by a following medium weight class B-737 aircraft. Characteristics of the respective distributions are analyzed. Initially, the maximum rolling moments slightly exceed the available roll control of the B-737. After 60 s the probability of rolling moments exceeding 50% of the roll control has decreased to 0.009% in a safety corridor around the glide path.**

## Nomenclature

| | |
|---|---|
| $b$ | = aircraft span |
| $b_0$ | = initial vortex spacing |
| $c$ | = section chord |
| $c_l$ | = section lift coefficient |
| $\mathrm{d}P$ | = probability difference |
| $g$ | = gravitational acceleration |
| $k$ | = wave number |
| $L$ | = lift |
| $L_x$, $L_y$, $L_z$ | = domain size in different directions |
| $L_0$ | = neutral lift |
| $M$ | = rolling moment |
| $M_c$ | = available roll control |
| $m$ | = aircraft mass |
| $P$ | = probability |
| $r$ | = radial coordinate |
| $r_c$ | = initial core radius |
| $S$ | = one-dimensional power density spectrum |
| $T_*$ | = free convection temperature scale |
| $t$ | = time |
| $u$ | = axial velocity |
| $u_\infty$ | = flight speed |
| $v$ | = lateral velocity |
| $v_t$ | = tangential velocity |
| $w$ | = vertical velocity |
| $w_0$ | = initial vortex descent speed |
| $w_*$ | = free convection velocity scale |
| $x$ | = axial coordinate in flight direction |
| $y$ | = spanwise coordinate |
| $z$ | = vertical coordinate |
| $z_i$ | = inversion height |
| $\alpha$ | = angle of attack |
| $\alpha_0$ | = mean angle of attack |
| $\Gamma_0$ | = root circulation |
| $\lambda$ | = wavelength |
| $\lambda_2$ | = measure for coherent vorticity |
| $\rho$ | = density |
| $'$ | = fluctuating quantity |

Received 29 December 1998; presented as Paper 99-0984 at the AIAA 37th Aerospace Sciences Meeting, Reno, NV, 11–14 January 1999; revision received 6 July 2000; accepted for publication 20 July 2000. 

*Research Scientist, Institut für Physik der Atmosphäre, Oberpfaffenhofen. Member AIAA.

†Research Scientist, Institut für Physik der Atmosphäre, Oberpfaffenhofen.

## Introduction

AS a response to lift, aircraft create counter-rotating vortices at the wing tips and at the edges of the flaps, the so-called wake vortices. The wake vortices may exert a serious danger on following aircraft. Therefore, separation standards were established that already limit the capacity of many airports.

Naturally, wake vortices descend below the glide path by mutual induction. However, measurements[1,2] and simulations[3,4] indicate that under certain atmospheric conditions wake vortices stop their descent or even rise again. This hazardous situation is of great concern for reduced spacing operations. As a result, the probability of encountering stalled vortices during approach increases considerably. Therefore, the question of vortex aging achieves primary significance.

The question of what type of meteorological phenomena are candidates to cause this hazardous situation was also raised in the context of the further development of the wake vortex warning system of the Frankfurt airport.[5] The system was established to run the closely spaced parallel runways separately at appropriate meteorological conditions. It predicts the propagation and lifespan of wake vortices in a safety box of 80 m height above ground, based on statistical analyses. This particular height of 80 m was chosen because measurements at Frankfurt airport showed that wake vortices in ground effect do not rebound to this level. Pilot associations recently argued that above the safety box the updrafts in a convectively driven atmospheric boundary layer (CBL) may cause wake vortices to stall or even to rise up to the glide slope. In a CBL, the buoyancy-driven thermals form highly energetic updrafts due to the radiative heating of the ground. The updrafts are surrounded by less turbulent downdraft regions.

In this study, large-eddy simulations (LES) of the evolving CBL have been performed that indicate that wake vortices actually may rise in the CBL when the velocity of the updraft exceeds the induced descent speed of the wake vortices. However, at the same time they are strongly deformed by the large-scale velocity field of the CBL and decay quickly due to the large turbulence intensity prevailing in the updrafts of the CBL.‡

To quantify these qualitative results, lift and rolling moments are assessed by means of strip theory. It is assumed that a B-737

‡The animated simulation can be found at http://www.pa.op.dlr.de/wirbelschleppe/conv.html [cited 10 October 2000].

aircraft crosses the CBL along various paths and thereby encounters the wake of B-747 aircraft. Lift and rolling moment distributions are first analyzed as averages along the flight path. Averaging takes into account that the large-scale deformation of the wake vortices reduces the impact time of the encountering aircraft. Then, probabilities of local rolling moments are evaluated in terms of probability density distributions and time series of rolling moments based on various selected threshold levels.

To the authors' knowledge, only one previous example of a numerical simulation of wake vortices in a CBL-similar environment exists.[6] There, the prime interest was to study the effect of atmospheric turbulence on vortex decay. Here, an attempt is made to understand how the peculiarities of the CBL structure (alternating thermals and downdrafts) alter the wake-vortex behavior. Furthermore, the resulting complex flowfield data are used for encounter assessments. Rossow and Tinling[7] give a still up-to-date survey of techniques to compute forces and moments exerted by wake vortices on encountering aircrafts. A more recent overview on numerical and experimental research to characterize wake vortex encounters is given in Ref. 8.

## Methods

### LES Code and Its Initialization

LES is used to simulate the CBL and the evolution of three superimposed vortex pairs. The numerical method is described in detail by Schmidt and Schumann.[9] The numerical scheme integrates the full primitive equations of motion in their nonhydrostatic form, together with the thermodynamic equation, in three dimensions and as a function of time.[9,10] The subgrid-scale fluxes are determined by means of a first-order closure as described by Dörnbrack.[11]

To achieve an appropriate resolution of both the characteristic scales of the CBL and the wake vortices, a domain size of $L_x = L_y = L_z = 512$ m with a grid volume of $\Delta x \times \Delta y \times \Delta z = 8 \times 2 \times 2$ m$^3$ is chosen. Periodic boundary conditions are employed in the horizontal directions. At the top and bottom of the domain, free-slip and no-slip conditions are prescribed, respectively.

The dry and quiescent atmospheric boundary layer is intitialized with a uniform temperature and superimposed random perturbations. The CBL is driven by a constant vertical heat flux at the lower surface until the growing thermals reach the top of the domain. Although the convective cells are still growing at this stage, the turbulent variances agree well with empirical scaling relations of the stationary CBL.[12] The ongoing evolution of the CBL is neglectable because the convective timescale is about six times larger than the lifespan of the wake vortices. The mean value of the turbulent kinetic energy (TKE) amounts to 0.9 m$^2$/s$^2$.

After three convective timescales, three wake vortex pairs are superimposed on the turbulent flowfield at three selected locations of the domain (Fig. 1). The right part of vortex pair 1 is placed on the shoulder of an updraft ($y = 199$ m and $z = 404$ m) to study the effect of lateral gradients of the vertical wind. The left part is situated in a quite homogeneous low-turbulence downdraft area to investigate maximum lifespans. The second vortex pair is superimposed on a region that covers a strong updraft, a moderate downdraft, and a rather calm area ($y = 386$ m and $z = 222$ m) to examine the effects of axially varying conditions. The third vortex pair, placed on a low altitude ($y = 132$ m and $z = 64$ m) allows investigation of ground effects. The three vortex pairs are sufficiently separated from each other such that mutual influences can be neglected.

The wake vortices are initialized as the superposition of two Lamb–Oseen vortices

$$v_t(r) = \frac{\Gamma_0}{2\pi r}\left(1 - \exp\frac{-1.26\,r^2}{r_c^2}\right) \qquad (1)$$

representing a B-747 aircraft with a root circulation of $\Gamma_0 = 565$ m$^2$/s and a vortex spacing of $b_0 = 47$ m. An unrealistically large vortex core radius of $r_c = 8$ m has to be chosen to resolve the forced vortex region with four grid points. It is known that the wavelength and growth rates of wave instabilities are a function of $r_c/b_0$ (Refs. 13 and 14) and that the decay rate of wake vortices with larger core radii may be increased.[15] Therefore, another CBL run was performed

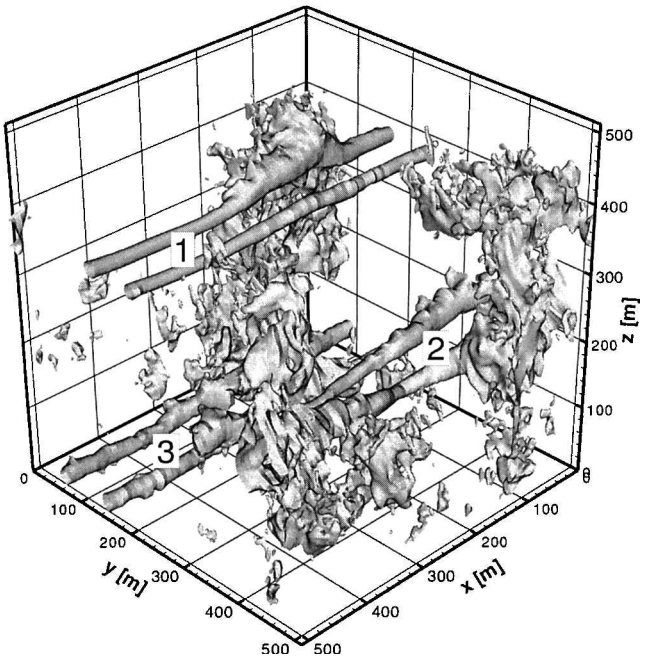


**Fig. 1 Isosurfaces of the positive vertical velocity value, $w = 2$ m/s, of the evolving CBL with 10-s-old wake vortices; numbers denote the vortex pairs.**

with vortex pair 2, which had an initial core radius of 4 m, resolved by two gridpoints. That run yielded almost identical decay rates compared to the case with $r_c = 8$ m. Another simulation of wake vortices in the CBL with relatively tight vortex cores ($r_c/b_0 = 0.125$) was published[16] that corroborates our current results. Vortex core radii also influence the results of encounter analyses for span ratios of follower to generator $b_f/b_g < 0.5$ (see Ref. 7). Reducing the core radius in our study to $r_c = 4$ m would increase the initial rolling moment experienced by the following B-737 by a factor of 1.4. In piloted simulator investigations[17] of wake vortex encounters, it was found that core radius effects are negligible.

### Encounter Analysis

The hazard reduction for aircraft that encounter the deformed and decaying vortex pairs is assessed by strip theory. In strip theory, the load on each wing section is calculated from the local section angle of attack and integrated to estimate the forces and moments exerted on an aircraft for a given velocity field.[18] This straightforward method is chosen because it provides an economic approach to perform the calculations at every one of the more than $4 \times 10^6$ grid points. A recent comparison of various simple wake vortex interaction models elucidates the good predictive capabilities of strip theory.[19] A well-known limitation of strip theory is an unreliable load distribution in the vicinity of the vortex cores.[18] For our purpose, the accuracy of strip theory achieved for the overall loading is sufficient to give an insight into the prominent phenomena and to give a realistic estimation of the time span in which the wake vortices alleviate to harmless strengths. Sufficient accuracy is particularly expected for the most interesting final decay of the vortices because then no more intact vortex core structures are observed.[20]

The rolling moment constitutes the most hazardous effect on aircraft that encounter wake vortices coaxially or at small angles.[7] Therefore, this study focuses on the evaluation of rolling moments $M$, which are normalized by 50% of the available roll control, $M_c = 2.8 \times 10^6$ Nm. The threshold $|M/0.5M_c| = 1$ represents an acceptable value for wake vortex encounters[7] although piloted studies state that the maximum bank angle provides the most appropriate measure for a wake vortex hazard.[17] However, evaluations of the bank angle would have to include aircraft as well as pilot reactions, which is beyond the scope of this study. The current approach resembles, rather, the common arrangement used to study encounter effects in wind-tunnel experiments. There, the following aircraft is mounted fixedly on a traversing mechanism and is equipped with

a force balance or pressure taps on the wings to evaluate loads. To give a more comprehensive view of the forces experienced by the aircraft, the effects of down- and upwashes are also presented in terms of loss and gain of lift $(L - L_0)/L_0$ normalized by neutral lift (weight), $L_0 = m \cdot g$.

As encountering aircraft, the common medium-weight-class B-737 aircraft is chosen; this enables comparisons with flight-test experiments of the NASA Langley Research Center B-737 (Ref. 8). Typical flight conditions prevailing during the early approach are prescribed for the whole domain: The B-737 with a span of $b = 28.4$ m and a weight of 450,000 N flies in clean configuration at a speed of $u_\infty = 150$ m/s in an atmosphere with density $\rho = 1$ kg/m$^3$.

In the evaluation, the B-737 penetrates the domain in $x$ direction at every $(y, z)$ grid point. Lift $L$ and rolling moment $M$ are integrated according to

$$L = \frac{\rho}{2} u_\infty^2 \int_{-b/2}^{b/2} c(y) c_l[y, \alpha(y)]\, \mathrm{d}y \tag{2}$$

$$M = \frac{\rho}{2} u_\infty^2 \int_{-b/2}^{b/2} c(y) c_l[y, \alpha(y)]\, y\, \mathrm{d}y \tag{3}$$

The section lift coefficients $c_l$ are taken from pressure tapping measurements of the DLR-F6 wing–body–engine configuration, which were carried out in the S2MA wind tunnel of ONERA.[21] Eight spanwise $c_l[\alpha(y)]$ sections are interpolated to the 2-m-spaced grid points. The local spanwise section angle of attack is

$$\alpha(y) = w(y)/u_\infty + \alpha_0 \tag{4}$$

where $\alpha_0 = 0.2$ deg.

## Discussion of Results

### Convective Boundary Layer

For the purpose of this study, which is to describe the main features of the interaction of the CBL with aircraft wake vortices, the flowfield of the simulated CBL should be as realistic and representative as possible. Therefore, our simulated CBL is compared with data obtained in field and laboratory experiments as well as from other LES.

Figure 1 depicts an isosurface of the positive vertical velocity, $w = 2$ m/s, of the evolving CBL and the three 10-s-old wake vortex pairs in a perspective view. Three convective cells or updraft regions can be identified that are partially merged with the tubular isosurfaces of the upwashes of the trailing vortices. In between the updrafts, a moderate downward flow prevails.

Figure 2 shows normalized velocity and temperature fluctuation patterns along an instrumented aircraft flight path segment and respective simulation data. The data have been collected in evolving CBLs during the European Field Experiment in a Desertification-Threatened Area (EFEDA)[22] at a height of about 50% of the inversion height $z_i$. The scaling parameters $w_*$ and $T_*$ are taken from free convection scaling.[12] Another data segment would obviously show different curves. Nevertheless, some typical features of a CBL can be well illustrated with this juxtaposition: The updraft velocities exceed the downdraft velocities and distinct small-scale fluctuations are superimposed to the up- and downdraft regions. In the up- and downdraft segments, $w'$ and $T'$ are correlated such that the heat flux $w'T' > 0$. Because of the turbulence, smaller-scale segments exist where $w'$ and $T'$ are anticorrelated ($w'T' < 0$). The area fraction with a positive heat flux is larger than that of negative heat fluxes.[12]

For the interaction of the CBL and the wake vortices, the TKE of the CBL and its spectral distribution is of particular importance. Figure 3 depicts a one-dimensional TKE spectrum from the LES at $z_i/2$ after three convective timescales and before the wake vortices have been inserted. The range covered by TKE spectra from field measurements is included with crosshatches[12,23]; the spectrum range found in wind tunnel, water tank, and other LES studies[24] is denoted with dots. [The TKE spectra from the literature are calculated according to $k \cdot S_{\mathrm{TKE}}(k)/w_*^2 = 0.5(k \cdot S_{uu}(k)/w_*^2 + k \cdot S_{vv}(k)/w_*^2 + k \cdot S_{ww}(k)/w_*^2$. Values for the normalized dissipation rate that are needed to transfer the spectra of field measurements[23] into the current form are taken from Ref. 12, page 164.]

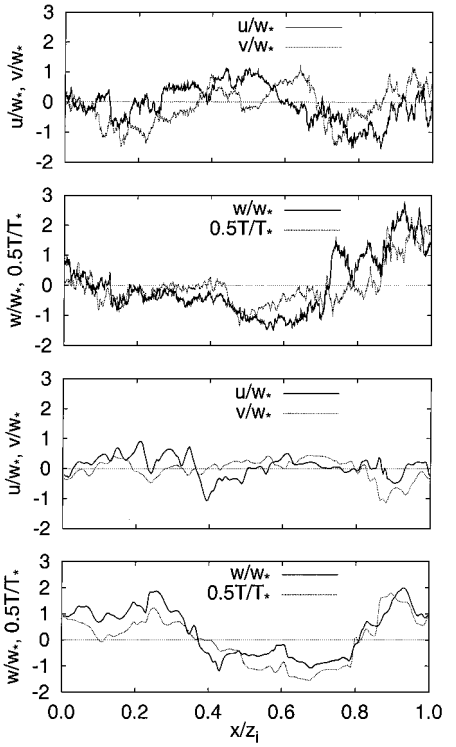


**Fig. 2 Normalized velocity and temperature fluctuation patterns along an arbitrary flight path at $z_i/2$; measurement (top) and LES (bottom).**

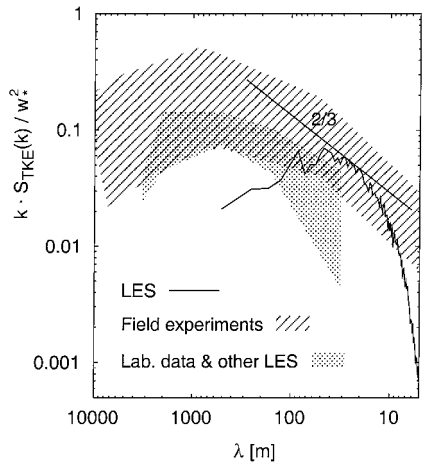


**Fig. 3 One-dimensional TKE spectra from the LES at $z_i/2$; range covered by spectra found in field experiments[12,23] indicated with cross hatches; spectra from wind tunnel, water tank, and other LES studies[24] denoted by dots.**

Current computer capabilities do not allow us to simulate sufficiently high effective Reynolds numbers to achieve the wide spectra as observed in field measurements. However, at its most energetic part, the simulated spectrum lies in the range of the field-measured data. Only the largest and smallest scales carry less energy than observed. This reflects that the current CBL is still evolving (energy maximum at smaller scales) and that the LES suffers from too strong effective (turbulent) viscosity at the smallest scales. However, in the wavelength range of 10–100 m of the CBL, which is certainly most sensitive for the interaction with the wake vortices and their turbulent decay,[20] the LES comprises quite well the energy levels of real atmospheric CBLs. The underestimation of energy at smallest scales (below 10 m) extenuates the direct impact of CBL turbulence on the vortex cores; the underestimation of energy at

the scales above 100 m reduces the excitation of Crow-unstable modes.[13] Hence, both effects provide conservative bounds for all results discussed thereafter.

### Wake Vortex Behavior

To illustrate the wake vortices graphically, the second eigenvalue $\lambda_2$ of the symmetric tensor $S^2 + \Omega^2$ is calculated, which is a measure of the coherent vortex structures.[25] $S$ and $\Omega$ are the symmetric and antisymmetric components of the velocity gradient tensor $\nabla \boldsymbol{u}$. Figure 4 shows surfaces of $\lambda_2 = -0.5/\mathrm{s}^2$ at $t = 10$ and 40 s. The (arbitrary) temperature isosurface elucidates the fine-scale structure of the surface plumes. Already, at the early stage of $t = 10$ s, the wake vortices are deformed according to their position relative to the up- and downdrafts. At 40 s, the vortices are partially destroyed due to turbulent erosion, especially in the updraft regions. Noticable height differences can be observed for the vortices of pair 1, which was placed on the shoulder of the thermals. The resulting situation of almost solitary vortices may be more dangerous because a solitary vortex decays relative slowly[26] because the mutually induced destruction mechanisms (shortwave and longwave instability, stretching of external turbulent eddies) are less effective.[4,15] The vortex pair in ground effect is moving laterally (compare Fig. 5) and thereby displaces the small-scale surface layer plumes. At $t =$ 70 s, all coherent vortices are essentially destroyed.[§]

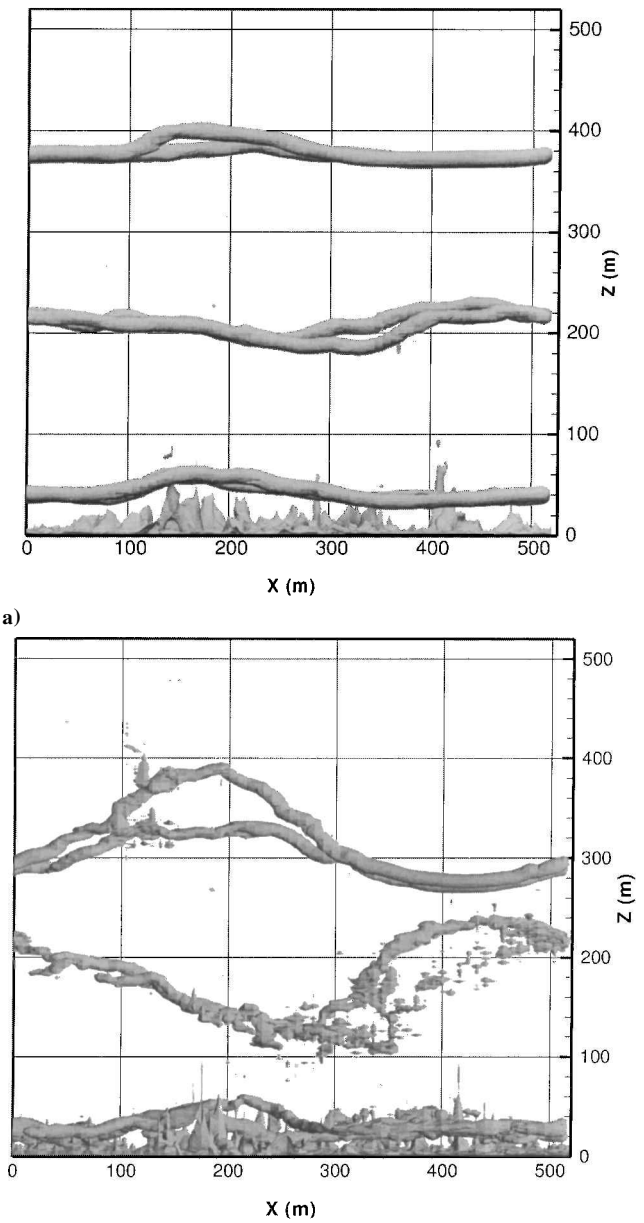


**Fig. 4 Side view of $\lambda_2 = -0.5/\mathrm{s}^2$ (for definition see text) of the three vortex pairs and an arbitrary temperature isosurface at a) $t = 10$ s and b) $t = 40$ s.**

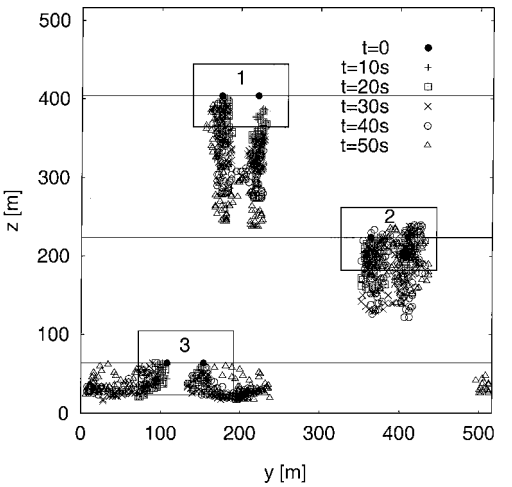


**Fig. 5 Evolution of vortex positions seen in flight direction; rectangles surrounding the initial height of vortex pairs denote safety corridors.**

Figure 5 depicts the evolution of the vortex positions as seen in flight direction for the time span in which they can be uniquely determined by searching local $\lambda_2$ minima. The initial vortex heights are denoted by horizontal lines. Because of the different vertical velocities in updrafts and downdrafts, the vortices out of ground effect are mainly stretched in the vertical direction. Maximum height differences of 150 m are estimated. The descent speed varies between $-0.4$ and 1.8 times the initial descent speed $w_0 = -1.9$ m/s. Some vortex segments of the pairs 1 and 2 actually remain on or even rise up to 20 m above the flight level. In regions with moderate spanwise gradients of $w$, vortex tilting leads to an increased lateral scatter of vortex positions (pair 2). The vortex pair 3 in ground effect is considerably stretched along typical trajectories of separation and rebound. Some parts even return to their initial position after 50 s.

### Encounter Analysis

In this section, lift deviations and rolling moments that are exerted by the vortices and the CBL on a B-737 aircraft are discussed. These are averaged along each flight path to condense the three-dimensional data to two-dimensional plots. The averaging is performed primarily because it takes into account that the large-scale deformation of the vortices reduces the impact time of forces and moments. On the other hand, averaging includes the drawback that contributions of opposite sign may compensate for each other, which will result in an underestimation of the disturbances. Therefore, probabilities of local rolling moments will also be analyzed subsequently.

Figures 6a and 6b display the averaged and normalized lift deviations $(L - L_0)/L_0$ at $t = 0$ and 40 s, respectively. These lift deviations can be interpreted as vertical accelerations of the following B-737 aircraft normalized by the gravitational acceleration. At $t = 0$, the concentric areas with negative accelerations are significantly larger and of about twice the intensity (almost $-1\ g$) of the adjacent areas with positive accelerations. Later, at $t = 40$ s, the areas with lift deviations out of ground effect are mainly stretched in the vertical direction in a similar way to the vortex positions (see Fig. 5). The maximum negative acceleration at $t = 40$ s of $L/L_0 - 1 = -0.52$ is caused by the vortex pair 1 close to $z = 300$ m. This is due to several effects: A large part of these vortices is situated in a homogeneous downdraft of the CBL, where lower turbulence intensities leave the

[§]A comprehensive view on the wake evolution can be gained from the animated simulation results, which may be found at http://www.pa.op.dlr.de/wirbelschleppe/conv.html [cited 20 October 2000].

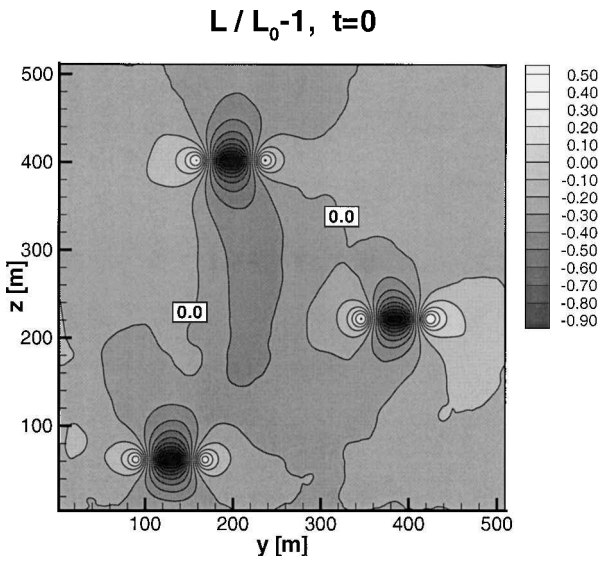


a)

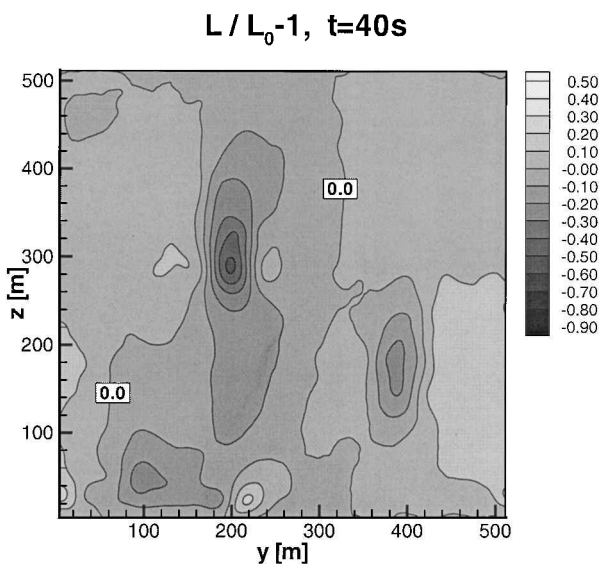


b)

**Fig. 6 Mean lift deviations, $L - L_0$, normalized by neutral lift, $L_0 = m \cdot g$, experienced by B-737 aircraft crossing the domain in $x$ direction at every $(y, z)$ position at a) $t = 0$ s and b) $t = 40$ s.**

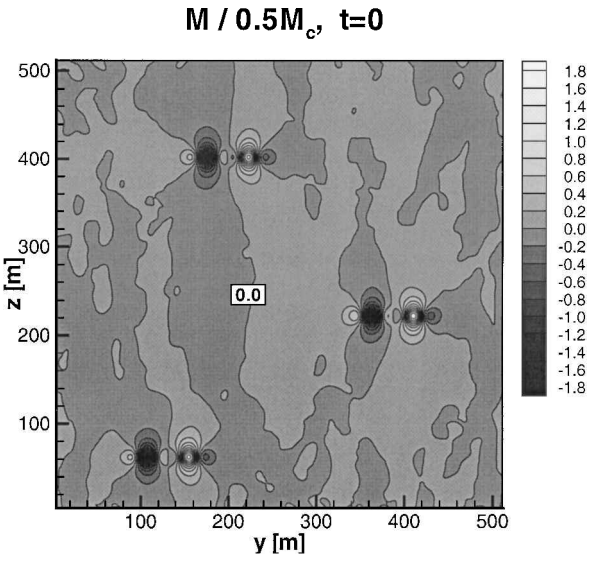


a)

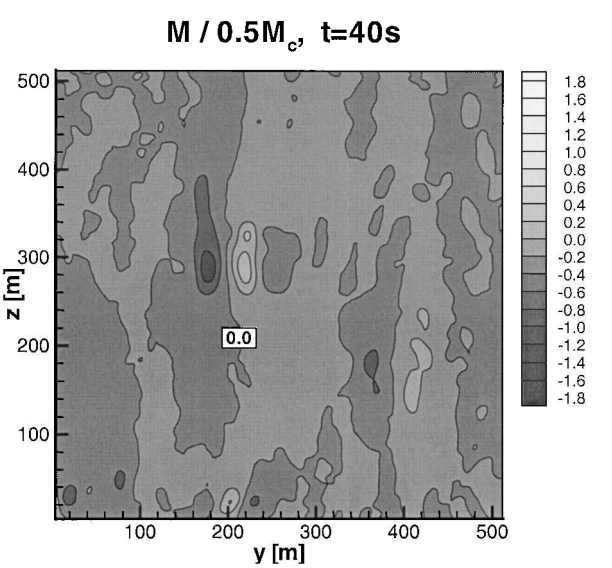


b)

**Fig. 7 Mean rolling moment distribution normalized by 50% of available roll control $M_c$ at a) $t = 0$ s and b) $t = 40$ s; $|M \lhd 0.5M_c| = 1$ is used as a threshold level for acceptable encounters.**

vortices quite intact. Furthermore, the descent speed in this area of the CBL augments the downwash experienced by the B-737. Finally, the vortices have approached each other, which also intensifies the downwash. At $t = 60$ s only vortex pair 1 still causes accelerations of up to $-0.36$, and at $t = 80$ s, a maximum value of $-0.26$ is found. However, these accelerations occur at vertical positions of 180 and 250 m below the glide path, respectively.

The rolling moments at $t = 0$ (Fig. 7a) reach almost the full roll control capability of the B-737, that is, $|M/0.5M_c| = 2$, in the vortex centers. The rolling moment signature of one vortex pair consists of two strong primary and four relatively weak counter-rotating secondary areas. Along a horizontal line through the vortex centers, the rolling moments change their sign five times. These multiple sign changes are also found in wind-tunnel experiments.[27] The magnitude and sign of the resulting rolling moment that acts on the encountering aircraft depend on its wing span and its position relative to the vortex pair: The outer secondary areas emerge when only one wing is placed into the updraft of a vortex. The central alternating moments act on the wings when the aircraft has a span smaller than the vortex spacing and is flying in line with the preceding aircraft. It is then solely exposed to the downwash region of the predecessor's wake.

Because of the large-scale deformation of the vortices, the secondary maxima of the moments have already disappeared at $t = 20$ s. As for the lift distribution, the areas of increased rolling moments are stretched vertically, and the lower part of pair 1 maintains the highest moments, which are reduced to a maximum of 0.53 at $t = 40$ s (Fig. 7b). At $t = 60$ s, only the part of pair 1 that is situated in the downdraft area of the CBL can still be identified in a small zone with $|M/0.5M_c| < 0.34$. This elucidates that wake vortices in the rather calm downdraft areas are intact for longer time spans. However, far below the glide path, they are a little hazardous.

The probability density distributions (PDD) of nonaveraged rolling moments $(M/0.5M_c)$ are delineated in Fig. 8a for the CBL with and without wake vortices. In this presentation, the shapes of the PDDs are almost identical. The narrow-banded curves suggest two interpretations: First, the probability of experiencing high rolling moments is small because of the small volumes occupied by wake vortices. Second, the thermals in the CBL itself exert enhanced rolling moments. We found local maxima of about $M = \pm 0.3M_c$ in our simulation, that define the background level to which the wake-induced rolling moments will decay asymptotically. Indeed, the forces and moments exerted by individual thermals can be enormous. For example, vertical gust velocities of up to 11.4 m/s

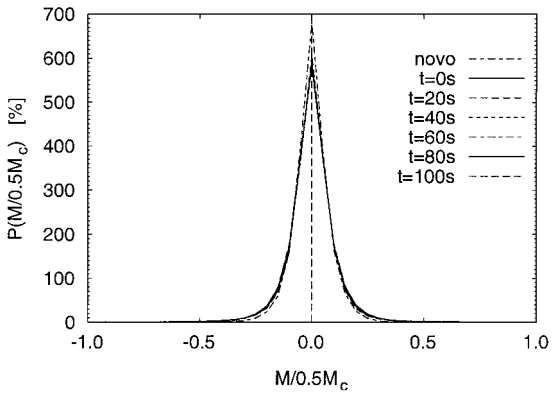


**Fig. 8a Probability density distributions of normalized rolling moments without (labeled as novo) and with wake vortices.**

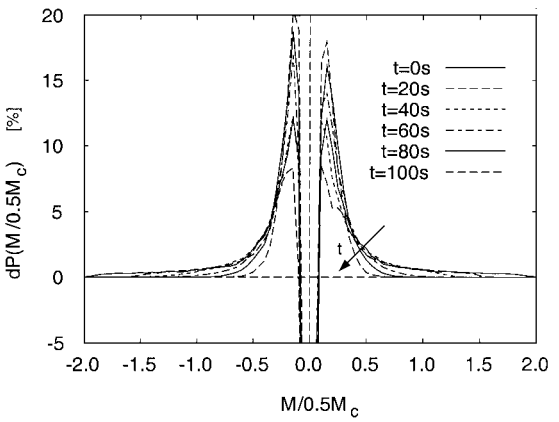


**Fig. 8b Difference of the probability density distributions of normalized rolling moments with and without wake vortices; arrow indicates the temporal sequence of the curves.**

associated with a vertical acceleration of 1.42 $g$ were reported by a research aircraft flying at low altitudes over the boreal forest.[28]

To elaborate the rolling moment effects of the wake vortices compared to the CBL, the differences of the respective PDDs are shown in Fig. 8b. The central negative probability differences with values of from −104 to −74% (not shown in Fig. 8b) indicate that the superposition of wake vortices reduces the probability of very small rolling moments. The most probable moments caused by the wake vortices in the simulated CBL amount to $0.15M_c/2$. Maximum values of $|M/0.5M_c|$ with probabilities of the order of $10^{-5}$% decrease from 2.25 at $t = 0$ s to 0.8 at $t = 100$ s. In the further simulation, with core radii of 4 m instead of 8 m, $|M/0.5M_c| \leq 2.97$ and 0.98 at the respective times are obtained.

Figure 9a depicts the probability of finding rolling moments exceeding threshold levels of $|M/0.5M_c| = 1$ and 0.5 in the entire computational domain for initial wake-vortex radii of 8 and 4 m. The threshold level of 0.5 is appropriate to separate wake-vortex induced and CBL induced rolling moments. $P(|M/0.5M_c|) > 0.5$ decreases slightly until $t = 40$ s from 1.6 to 1.2% (as long as the vortex structures are intact) and reaches the probability of 0.06% at $t = 100$ s. Hazardous normalized rolling moments above one are likely to occur with an initial probability of 0.6%. Then the probabilities decrease almost linearly for about 30 s. After 60 s, the probability of hazardous rolling moments has decreased to almost 1% of the initial probability. Note that the probabilities decrease more than two orders of magnitude from 40 to 70 s. This implies that the treatment of encounter by more sophisticated methods is expected to give minor differences in results compared to the simple strip theory. Moreover, even different choices of acceptable threshold levels or encounter probabilities lead to minor time shifts only. Figure 9a further elucidates that the simulation of vortex pair 2 with an initial core radius of 4 m yields almost identical results. (To enable the comparison of simulations with one and three vortex pairs

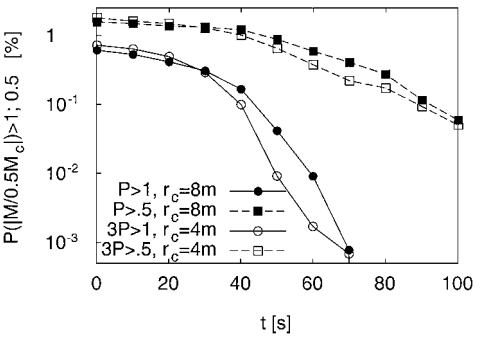


**Fig. 9a Frequency of occurrence of normalized rolling moments greater than 1, respectively, 0.5; results of simulations with initial core radii of $r_c$ = 8 and 4 m.**

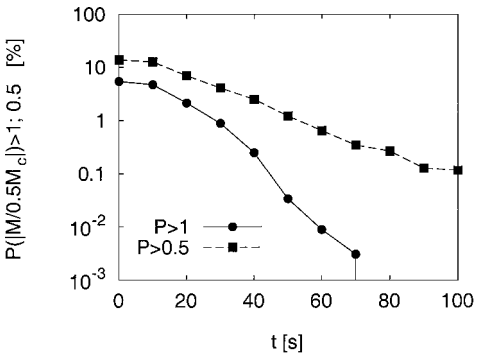


**Fig. 9b Frequency of occurrence of normalized rolling moments greater than 1, respectively, 0.5 in the three saftey corridors, $r_c$ = 8 m.**

the probability of rolling moments in the single vortex-pair data had to be multiplied by three.)

Flight-corridor specific probabilities of critical encounters are achieved by evaluating the flight track of the follower aircraft in a safety window around the glide path. The size of the window is determined by the accuracy with which aircraft can follow the nominal glide path of the instrument landing system (ILS). At Frankfurt airport a study yielded approximate lateral and vertical standard deviations of 30 and 20 m, respectively, at a distance of 10 mile from the threshold for over 36,000 aircraft approaches, (private communication with M. Maiss, DFS Deutsche Flugsicherung, Offenbach, Germany, May 2000). The accuracy increases with decreasing distance to the runway. Given a safety corridor that extends over two standard deviations in all four directions from the nominal glide path (a window width of $120 \times 80$ m$^2$, see Fig. 5), Fig. 9b shows that the initial probability of encountering a critical rolling moment ($|M/0.5M_c| = 1$) amounts to 5.4%. At $t = 60$ s, which corresponds to minimum radar separation of 2.5 n mile when assuming a flight velocity of 75 m/s, the probability has decreased to 0.009%.

At $t = 60$ s probabilities of rolling moments almost coincide in the safety corridor and in the whole simulation domain. This reveals and confirms our earlier finding that at about 1 min after the virtual passage of the wake-vortex producing B-747, the simulated rolling moments experienced by the wake encountering B-737 are mainly due to the natural turbulence of the CBL to which the wake-induced rolling moments have decayed in the meantime.

## Conclusions

The accelerated decay of aircraft wake vortices in a convectively driven and evolving atmospheric boundary layer was investigated by means of LES. The main challenge was the appropriate representation of the CBL on one side and the wake vortices on the other because the respective characteristic length scales differ by a factor of about 1000. A compromise between the two scale regimes was found by choosing a relatively small domain size that allowed us to study an evolving CBL where typical turbulence and velocity distributions prevail at inversion heights below 500 m. On the other

hand, the wake vortices were modeled with relatively large initial core radii to account for their proper resolution. With an additional simulation it could be shown that vortex cores with 50% smaller radii do not change the rolling moments of an encountering aircraft and the respective probabilities significantly.

The LES elucidate that the wake vortices are rapidly deformed at scales of the alternating updraft and downdraft regions. It is shown that segments of the wake vortices can stall at flight level but that they are quickly eroded by the turbulent updrafts at the same time. The longest living sections of the vortices are found in regions of relatively calm downdraft flow that augments their descent.

The current investigation treats exactly the situation where the strength of the updrafts just compensates the self-induced descent speed of the wake vortices. This allows extension of the conclusions to CBL cases with stronger and weaker thermals: In the weaker CBL case, the common situation prevails where wake vortices descend below the glide path. In a stronger CBL, pieces of the wake may even rise considerably above flight level, but the turbulence level is also increased in the updrafts, which further augments the decay rate of those vortex pieces.

Encounter analyses by means of strip theory elucidate that the deformation and decay of the vortex pairs counteract and dominate the potentially hazardous effects of rising wake vortices. In the LES results, the probability of encountering a potentially hazardous rolling moment ($|M/0.5M_c| = 1$) in a saftey corridor has decreased to 0.9% at $t = 30$ s and is reduced to 0.009% after 60 s. At this time, the wake-induced rolling moments have almost decayed to the background level that originates from turbulence in the CBL.

Main differences from the presented results are expected when a following aircraft flies in high-lift configuration at half the speed used in the current study. This would probably double the normalized rolling moments. Furthermore, the large core radii imply an underestimation of the rolling moments by a factor of 1.4 initially. Although both effects are strong in early times after fly-by, they, nevertheless, will modify the potentially hazardous timespan behind the B-747 wake-generator aircraft only slightly because the vortex decay is so rapid in a CBL.

## Acknowledgments

This work was supported by the European Commission in the frame of the Brite/EuRam project Wake Vortex Evolution and Wake Vortex Encounter (WAVENC) (BE97-4112). The processing of the EFEDA data by R. Baumann are gratefully acknowledged.

## References

[1]Zak, J. A., and Rodgers, W. G., Jr., "Documentation of Atmospheric Conditions During Observed Rising Aircraft Wakes," NASA CR-4767, 1997.

[2]Greenwood, J. S., and Vaughan, J. M., "Measurements of Aircraft Wake Vortices at Heathrow by Laser Doppler Velocimetry," *Air Traffic Control Quarterly*, Vol. 6, No. 3, 1998, pp. 179–203.

[3]Proctor, F. H., Hinton, D. A., Han, J., Schowalter, D. G., and Lin, Y.-L., "Two Dimensional Wake Vortex Simulations in the Atmosphere: Preliminary Sensitivity Studies," AIAA Paper 97-0056, 1997.

[4]Holzäpfel, F., Gerz, T., and Baumann, R., "The Turbulent Decay of Trailing Vortex Pairs in Stably Stratified Environments," *Aerospace Science and Technology* (to be published); also AIAA Paper 2000-0754, 2000.

[5]Gurke, T., and Lafferton, H., "The Development of the Wake Vortices Warning System for Frankfurt Airport: Theory and Implementation," *Air Traffic Control Quarterly*, Vol. 5, No. 1, 1997, pp. 3–29.

[6]Corjon, A., Darracq, D., Venzac, P., and Bougeault, P., "Three-Dimensional Large Eddy Simulation of Wake Vortices. Comparison with Field Measurements," AIAA Paper 97-2309, 1997.

[7]Rossow, V., and Tinling, B., "Research on Aircraft/Vortex–Wake Interactions to Determine Acceptable Level of Wake Intensity," *Journal of Aircraft*, Vol. 25, No. 6, 1988, pp. 481–492.

[8]Vicroy, D., Brandon, J., Greene, G., Rivers, R., Shah, G., Stewart, E., and Stuever, R., "Characterizing the Hazard of a Wake Vortex Encounter," AIAA Paper 97-0055, 1997.

[9]Schmidt, H., and Schumann, U., "Coherent Structure of the Convective Boundary Layer Derived from Large-Eddy Simulations," *Journal of Fluid Mechanics*, Vol. 200, 1989, pp. 511–562.

[10]Krettenauer, K., and Schumann, U., "Numerical Simulation of Turbulent Convection over Wavy Terrain," *Journal of Fluid Mechanics*, Vol. 237, 1992, pp. 261–299.

[11]Dörnbrack, A., "Broadening of Convective Cells," *Quarterly Journal of the Royal Meteorological Society*, Vol. 123, No. 540, 1997, pp. 829–847.

[12]Stull, R. B., "An Introduction to Boundary Layer Meteorology," *Atmospheric Sciences Library*, Kluwer Academic, Norwell, MA, 1988, pp. 117–120.

[13]Crow, S. C., "Stability Theory for a Pair of Trailing Vortices," *AIAA Journal*, Vol. 8, No. 12, 1970, pp. 2172–2179.

[14]Leweke, T., and Williamson, C. H. K., "Cooperative Elliptice Instability of a Vortex Pair," *Journal of Fluid Mechanics*, Vol. 360, 1998, pp. 85–119.

[15]Moet, H., Darracq, D., Laporte, F., and Corjon, A., "Investigation of Ambient Turbulence Effects on Vortex Evolution Using LES," AIAA Paper 2000-0756, 2000.

[16]Lin, Y. L., Han, J., Zhang, J., Ding, F., Arya, S. P., and Proctor, F. H., "Large Eddy Simulation of Wake Vortices in the Convective Boundary Layer," AIAA Paper 2000-0753, 2000.

[17]Sammonds, R., and Stinnet, G., Jr., "Criteria Relating Wake Vortex Encounter Hazard to Aircraft Response," *Journal of Aircraft*, Vol. 14, No. 10, 1977, pp. 981–987.

[18]McMillan, O., Schwind, R., Nielsen, J., and Dillenius, M., "Rolling Moments in a Trailing Vortex Flowfield," *Journal of Aircraft*, Vol. 15, No. 5, 1978, pp. 280–286.

[19]de Bruin, A. C., "WAVENC, Wake Vortex Evolution and Wake Vortex Encounter, Publishable Synthesis Report," National Aerospace Lab., NLR-TR-2000-079, Amsterdam, 2000.

[20]Gerz, T., and Holzäpfel, F., "Wingtip Vortices, Turbulence, and the Distribution of Emissions," *AIAA Journal*, Vol. 37, No. 10, 1999, pp. 1270–1276.

[21]Hoheisel, H., and Geisler, P., "Results of DLR-ONERA-Experiments on the DLR-F4/1-Wing-Body-Engine-Configuration," Institut für Entwurfsaerodynamik, DLR-IB 129-91/26, Braunschweig, Germany, 1991.

[22]Michels, B., and Jochum, A., "Heat and Moisture Flux Profiles in a Region with Inhomogeneous Surface Evaporation," *Journal of Hydrology*, Vol. 166, No. 3–4, 1995, pp. 383–407.

[23]Kaimal, J. C., Wyngaard, J. C., Haugen, D. A., Coté, O. R., Izumi, Y., Caughey, S. J., and Readings, C. J., "Turbulence Structure in the Convective Boundary Layer," *Journal of Atmospheric Sciences*, Vol. 33, No. 11, 1976, pp. 2152–2168.

[24]Fedorovich, E., and Kaiser, R., "Wind Tunnel Model Study of Turbulence Regime in the Atmospheric Convective Boundary Layer," *Buoyant Convection in Geophysical Flows, NATO ASI Series, Series C: Mathematical and Physical Sciences*, edited by E. J. Plate, E. E. Fedorovich, D. X. Viegas, and J. C. Wyngaard, Vol. 513, Kluwer Academic, Norwell, MA, 1998, p. 359.

[25]Jeong, J., and Hussain, F., "On the Identification of a Vortex," *Journal of Fluid Mechanics*, Vol. 285, 1995, pp. 69–94.

[26]Sreedhar, M., and Ragab, S., "Large Eddy Simulation of Longitudinal Stationary Vortices," *Physics of Fluids*, Vol. 6, No. 7, 1994, pp. 2501–2514.

[27]Hegen, G., "Wake Encounter Test in DNW Wind Tunnel—Test Number: 98-1116," National Aerospace Lab., NLR-CR-98291, Amsterdam, 1998.

[28]MacPherson, J. I., and Betts, A. K., "Aircraft Encounters with Strong Coherent Vortices over the Boreal Forest," *Journal of Geophysical Research*, Vol. 102, No. D24, 1997, pp. 29,231–29,234.

[3]

# The turbulent decay of trailing vortex pairs in stably stratified environments

F. Holzäpfel, T. Gerz, R. Baumann

Aerospace Science and Technology, 2001

Volume 5, Number 2, Pages 95–108

*Aerosp. Sci. Technol.* 5 (2001) 95–108

S1270-9638(00)01090-7/FLA

# The turbulent decay of trailing vortex pairs in stably stratified environments

Frank Holzäpfel *, Thomas Gerz, Robert Baumann

Institut für Physik der Atmosphäre, DLR Oberpfaffenhofen, 82234 Weßling, Germany

Received 4 April 2000; revised and accepted 22 November 2000

**Abstract**

The decay of trailing vortex pairs in thermally stably stratified environments is investigated by means of large eddy simulations. Results of in-situ measurements in the wakes of different aircraft are used to find appropriate intitializations for the simulation of wake turbulence in the quiescent atmosphere. Furthermore, cases with weak atmospheric turbulence are investigated. It is shown that the early development of the vortices is not affected by turbulence and develops almost identically as in 2D simulations of wake vortices in stably stratified environments. In a quiescent atmosphere the subsequent vortex decay is controlled by the interaction of short-wave disturbances, owing to the aircraft induced turbulence, and baroclinic vorticity, owing to stable stratification. As a consequence, vertical vorticity streaks between the vortices are induced which are substantially intensified by vortex stretching and finally lead to rapid turbulent wake-vortex decay. When in addition atmospheric turbulence is also present, the long-wave instability is dominantly promoted. For very strong stratification ($Fr < 1$) it is observed that wake vortices may rebound but lose most of their strength before reaching the flight level. Finally, the simulation results are compared to the predictive capabilities of Greene's approximate model. © 2001 Éditions scientifiques et médicales Elsevier SAS

**wake vortices / stable stratification / turbulence / short-wave instability / coherent structures / numerical simulation**

**Zusammenfassung**

**Turbulent zerfallende Nachlaufwirbel in stabil geschichteter Umgebung.** Der turbulente Zerfall von Flugzeug-Wirbelschleppen in thermisch stabil geschichteter Umgebung wird mittels der Grobstruktursimulation untersucht. Die Parametrisierung der Turbulenz in den Nachlaufwirbeln wird von in situ Messungen abgeleitet, die im Nachlauf verschiedener Flugzeuge durchgeführt wurden. Weiterhin werden Fälle mit schwacher atmosphärischer Turbulenz untersucht. Zunächst bleiben die Wirbel von der Turbulenz unbeeinflußt; sie verhalten sich nahezu wie in 2D Simulationen von Wirbelschleppen in stabil geschichteter Umgebung. Der anschließende Zerfallsprozess wird in nicht turbulenter Umgebung durch die Wechselwirkung kurzwelliger Störungen und baroklin erzeugter Wirbelstärke geprägt. Zwischen den Nachlaufwirbeln werden vertikale Wirbelröhren induziert, die zunächst durch Wirbelfadenstreckung maßgeblich verstärkt werden und schließlich einen rapiden turbulenten Zerfall der Wirbelschleppe initiieren. In einer Umgebung mit atmosphärischer Turbulenz dominiert die langwellige Instabilität. In sehr stabiler Schichtung ($Fr < 1$) können die Wirbel zwar bis auf Flugniveau wiederaufsteigen, jedoch verklingt ihre Intensität gleichzeitig nahezu vollständig. Abschließend wird das Vorhersagepotential von Greene's parametrischem Wirbelschleppenmodell mit den Ergebnissen der Simulationen verglichen. © 2001 Éditions scientifiques et médicales Elsevier SAS

**Wirbelschleppe / stabile Schichtung / Turbulenz / kurzwellige Instabilität / kohärente Strukturen / numerische Simulation**

* Correspondence and reprints.
*E-mail address:* frank.holzaepfel@dlr.de (F. Holzäpfel).

## 1. Introduction

The continuous increase of air traffic which increasingly congests airports due to their relative stagnation of capacities [32], on the one hand, and intentions to build super-large civil aircraft, on the other hand, have reinduced extensive wake vortex research in the last years. In spite of comprehensive previous research efforts, basic understanding of the influence of meteorological conditions on wake vortex physics still is quite controversial [29]. This may be due to the fact that wake vortices need large domains and high resolution in both simulation and experiment to be investigated properly. In both approaches, the Reynolds numbers which can be achieved are far from reality. On the other hand, in field experiments the meteorological conditions cannot be controlled or reproduced and are – as well as the wake vortices – difficult to measure in the required temporal and spatial resolution.

The impact of stable stratification on wake vortices has been discussed controversly for some years. Whereas some analyses show that wake vortices may accelerate their descent due to baroclinic effects [3,26] or may oscillate in a similar way as a displaced buoyant parcel of fluid [22] several investigations based on high-resolution 2D simulations [5,13,19,24,28] demonstrate that an early deceleration phase is followed by a subsequent acceleration. Similar results were achieved much earlier with a simple point vortex method [11]. Agreement with experiments [4,23,31] which indicate that the vortices decelerate and stop their descent after roughly $1/4$ of the oscillation period was obtained in early 2D simulations by fortune because the subsequent acceleration period was supressed by an overestimated diffusion [10,20]. Consensus seems to emerge from recent 3D simulations [4,6,21, 25,30] which corroborate our current results: during the early descent the wake vortices simultaneously decelerate and approach each other. A subsequent acceleration is not seen or is widely damped.

The recent 3D studies focus upon different aspects of the evolution of the trailing vortices: Schowalter et al. [25] performed a spatial large eddy simulation (LES) and concentrated on the initialization and development of the wake vortices as a function of time and space. In contrast to the 2D studies they did not find an acceleration phase, which they attribute to a modified distribution of the baroclinically produced vorticity [26]. Garten et al. [6] investigated the single-wavelength excited evolution of the Crow instability in ambient stratification, putting much effort on the vortex reconnection. In both works no turbulent fluctuations are initialized, and a symmetry boundary condition midway between the vortices is prescribed which inhibits vortex decay by turbulent vorticity transport across the boundary and the formation of asymmetric disturbances as the short-wave instability. Switzer and Proctor [30] initialized almost isotropic ambient turbulence on three different turbulence levels and state that depending on the degree of stratification and turbulence long and/or small-scale instabilities dominate the decay. Robins and Delisi [21] and Delisi and Robins [4] introduced turbulence by initializing their vortex pair as a superposition of many counter-rotating vortices with axes perturbed sinousoidally at different wavelengths and phases. They infer that the Crow instability is promoted by stable stratification and decelerates the descent compared to 2D simulations [21]. When perturbations are initialized on sufficiently small length scales they find that stratification causes a more rapid growth of short-wave instabilities at the expense of long-wave instabilities [4].

In our large eddy simulations we distinguish explicitly different sources of turbulence. Turbulence may stem from the aircraft or, additionally, from weak, anisotropic and decaying atmospheric turbulence. We first compare 2D and 3D results in terms of the temporal development of characteristic quantities such as descent height, vortex spacing and circulation. It is shown that the early development of the trailing vortices is not affected by the different turbulence scenarios. The following decay mechanisms, however, depend strongly on both the prescribed stratification and turbulence. The different mechanisms are discussed. Finally, results of Greene's approximate model [9] are compared to the simulated cases.

## 2. Numerical approach and parameters

Our code LESTUF is based on a Boussinesq large-eddy simulation code which uses the classical Smagorinsky closure and was originally developed to simulate turbulence under influence of constant background shear and stratification [16]. The code solves the discretized equations on a staggered grid with finite differences of second order accuracy in space and time. The discretization scheme is weakly diffusive and not dissipative. Meanwhile, LESTUF has proved its reliability in several wake vortex studies [7,8,13] in turbulent and stratified surroundings.

For most simulations we chose a domain size of $L_x \times L_y \times L_z = 408 \times 256 \times 540$ m$^3$ with a uniform grid of $\Delta y = \Delta z = 1$ m in spanwise, $y$, and vertical direction, $z$. In flight direction, $-x$, a resolution of $\Delta x = 6.375$ m was used. Periodic boundary conditions are employed in all three directions. The influence of neighbouring wakes results in the production of some artificial vorticity along the boundaries which is due to a small kink in the initial velocity distribution across the boundaries. The resulting disturbances are negligible since the boundaries are sufficiently far apart from the primary vortices. An effective Reynolds number, based on circulation and turbulent viscosity at core radius, of 7400 was achieved [8].

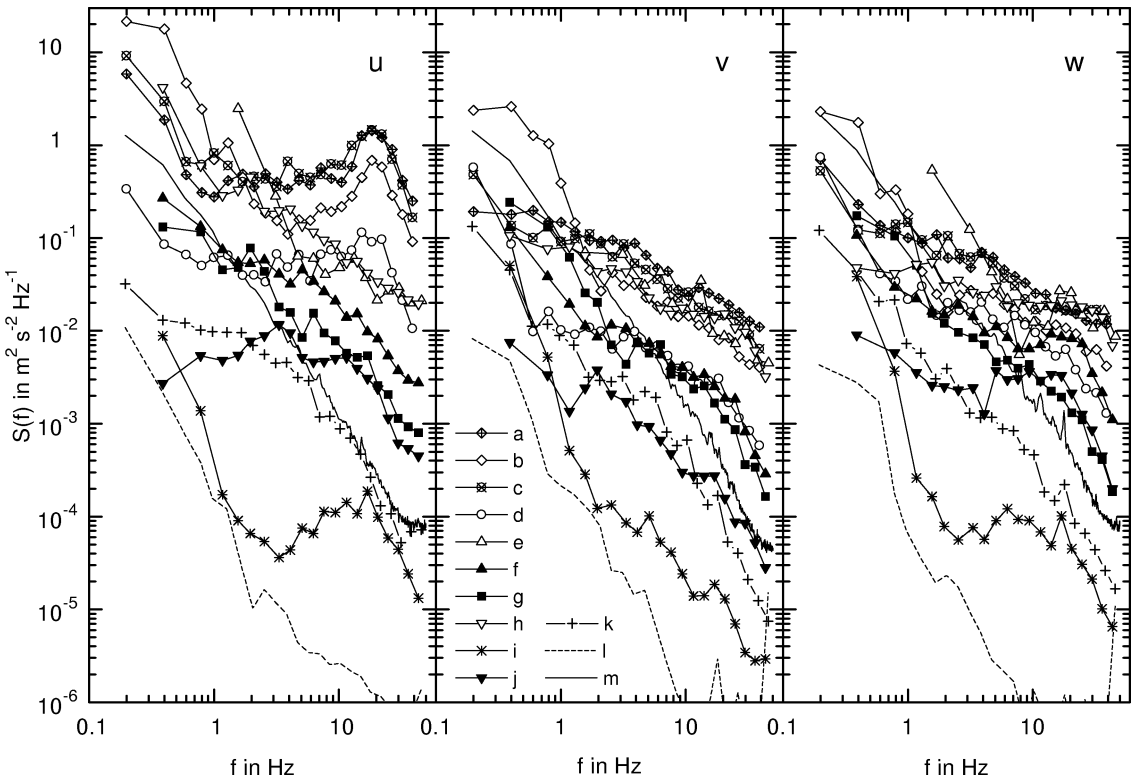


**Figure 1.** Power density spectra established from in-situ measurements behind different cruising aircraft and in free atmosphere. Open symbols denote near-field and closed symbols far-field data: (a) B737-300, $\Delta x = 43$–$57$ m, jet; (b) B737-300, $\Delta x = 40$–$60$ m, wake; (c) A340, short distance, jet; (d) A340, short distance, wake; (e) A310-300, $\Delta x = 100$–$150$ m; (f) A310-300, $\Delta x = 450$–$600$ m; (g) A310-300, $\Delta x = 800$ m; (h) VFW614, $\Delta x = 100$ m, center; (i) VFW614, $\Delta x = 80$ m, below; (j) VFW614, $\Delta x = 1.6$ km; (k) B727, $\Delta x = 15$ km; (l) free atmosphere, VFW614 case, $z = 8.2$ km; (m) convective boundary layer, $z = 1\,\text{km} \equiv 0.55 z_i$.

Two different approaches concerning the initialized turbulence were pursued. In case *(b)* the wake vortices develop in quiescent atmosphere; turbulence then only stems from the turbulent aircraft boundary layer, the mixing of the separated flows at the trailing edges, and the turbulent exhaust jets. Case *(b)* is a conservative approach which explores maximum life spans. From in-situ five-hole-probe velocity measurements performed with the DLR research aircraft FALCON chasing B737, A340, A310, B727, and VFW614 (ATTAS) aircraft in different distances, power density spectra were established (see *figure 1*) which reveal that the intensity of the aircraft induced turbulence may vary with several orders in magnitude. Maximum rms values of about 5.4 m/s (see *table I*) were found in the axial velocity component when the FALCON immerged into the exhaust jet region at small distances. Minimum rms values of 0.036 m/s were measured (curve (i)) at the lower edge of the downwash, in an airmass which was probably displaced by the downwash and did not directly experience aircraft-induced turbulence. Two spectra obtained from measurements in the undisturbed atmosphere are also included for comparison. The spectra of undisturbed air at high altitude show

**Table I.** Root mean square velocities determined by integration over spectra in *figure 1*. Frequencies below 1 Hz are excluded in integration to avoid adulterations caused by aircraft movements in the wake (cases (a)–(k)).

| | $u'$ [m/s] | $v'$ [m/s] | $w'$ [m/s] |
|---|---|---|---|
| (a) | 5.4 | 1.1 | 1.0 |
| (b) | 3.6 | 0.76 | 0.7 |
| (c) | 5.5 | 0.94 | 1.0 |
| (d) | 1.5 | 0.35 | 0.51 |
| (e) | 2.4 | 0.88 | 1.3 |
| (f) | 0.76 | 0.35 | 0.53 |
| (g) | 0.52 | 0.35 | 0.33 |
| (h) | 1.6 | 0.79 | 0.91 |
| (i) | 0.057 | 0.036 | 0.047 |
| (j) | 0.35 | 0.12 | 0.28 |
| (k) | 0.19 | 0.14 | 0.13 |
| (l) | 0.05 | 0.06 | 0.04 |
| (m) | 0.77 | 0.81 | 0.94 |

significantly lower values than the data from the convective boundary layer [14]. It is noteworthy that the latter spectra are situated well within the aircraft-induced spectra. The distinct variations of the aircraft induced turbulence were taken into account in the simulations by adding initially a three-dimensional random pertubation field to the swirling flow such that the perturbations reach maximum rms values of 0.02 m/s, 0.2 m/s or 2 m/s at the core radius, $r_c$, and decay exponentially for smaller and larger radii. The best guess of 2 m/s was used as standard case *(b)*.

In case *(a)*, in addition to the aircraft-boundary layer turbulence, weak to moderate, anisotropic, and decaying atmospheric turbulence is superimposed on the whole velocity field. The atmospheric turbulence which is described in detail in [8] obeys prescribed spectra with rms velocities of 0.38 m/s in horizontal and 0.21 m/s in vertical direction. The length scales of the most energetic eddies amount to 60–90 m and local maximum velocities to approximately ±1.4 m/s. The resulting dissipation rate is $\varepsilon = 3.2 \cdot 10^{-5}\,\mathrm{m^2/s^3}$.

The wake vortices were initialized as superposition of two Lamb–Oseen vortices where the tangential velocity profile of one vortex is given by

$$v_t(r) = \frac{\Gamma_0}{2\pi r}\left(1 - \exp\frac{-r^2}{r_0^2}\right), \quad r_0 = \frac{r_c}{1.121} \qquad (1)$$

with a core radius of $r_c = 4$ m. A root-circulation of $\Gamma_0 = 565\,\mathrm{m^2/s}$ and a vortex spacing of $b_0 = 47$ m were employed to represent the cruising B-747 aircraft with an elliptical wing loading. In contrast to the single Lamb–Oseen vortex the superposition of two vortices is not a particular solution of the Navier–Stokes equations. A transient self-adaption phase to a dipole family which is a quasi-steady solution of the Euler equations may introduce additional perturbances to the flow [27]. However, Sipp et al. [27] show that for our small ratio $r_{c0}/b_0 = 0.085$ the distortions are weak.

The mean potential temperature gradient of the atmosphere, $\mathrm{d}\Theta/\mathrm{d}z$, was constant in each calculation and the corresponding Brunt–Väisälä frequency

$$N = \left(\frac{g}{\Theta_0}\,\frac{\mathrm{d}\Theta}{\mathrm{d}z}\right)^{1/2} \qquad (2)$$

varied between 0 and 0.056/s ($\mathrm{d}\Theta/\mathrm{d}z = 0$–$10\,\mathrm{K}/100$ m). Since our previous 2D investigations [13] showed that the prominent phenomena are only intensified by increasing the stratification from $N = 0.01$/s to $N = 0.04$/s but do not change in principle, we consider here two benchmark cases with $N = 0.014$/s and $N = 0.04$/s. However, in 2D the vortex behaviour is categorically modified for even higher stratification such that the vortices rise to the flight path. Therefore, the case $N = 0.056$/s is also included in the current study to see whether this hazardous scenario is likely to occur in 3D.

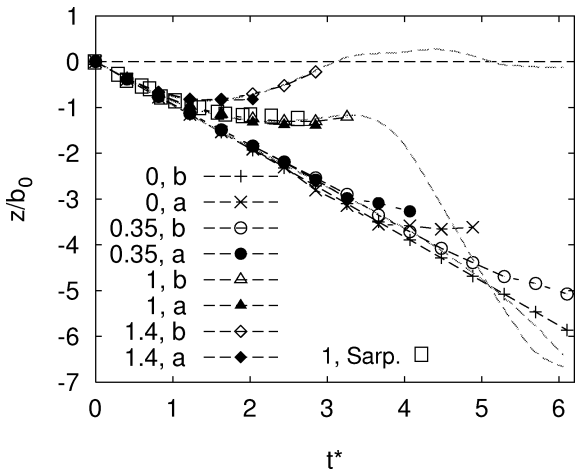


**Figure 2.** Normalized descent distance versus time for different turbulence scenarios (*(b), (a)*) and Brunt–Väisälä frequencies, $N^* = 0, 0.35, 1, 1.4$. Grey dashed curves denote 2D simulations [13]. Squares are Sarpkaya's experimental data [23].

## 3. Results and discussion

Most results are presented in non-dimensionalized form. The characteristic scales are based on the initial vortex separation, $b_0$, and circulation, $\Gamma_0$, leading to the time scale

$$t' = \frac{2\pi {b_0}^2}{\Gamma_0} = \frac{b_0}{w_0} = 24.6\,\mathrm{s}, \qquad (3)$$

where $w_0$ is the initial descent speed of the vortex pair. For the normalized time and Brunt–Väisälä frequency it follows $t^* = t/t'$ and $N^* = Nt'$, respectively. This means that the Brunt–Väisälä frequencies investigated are $N^* = 0, 0.35, 1.0$, and 1.4. The inverse of $N^*$ corresponds to the vortex Froude number. The normalized eddy dissipation rate in case *(a)* is $\varepsilon^* = (\varepsilon b_0)^{1/3}/w_0 = 0.06$.

### 3.1. Descent height and vortex spacing

*Figure 2* depicts the temporal development of the normalized descent height[†], $z/b_0$. Results of 2D simulations without any turbulence [13] (grey dashed lines) are also included. We observe that for early times ($t^* < 1$) neither stratification nor turbulence alter the descent of the vortex pair. Later on, however, it is clearly seen that the level of stratification controls the decelerated descent; the introduction of turbulence and changes of the type

[†] The vortex centers were determined by searching the local minima of the second eigenvalue $\lambda_2$ of the symmetric tensor $S^2 + \Omega^2$ which is a measure for coherent vortex structures [15]. $S$ and $\Omega$ are the symmetric and antisymmetric parts of the velocity gradient tensor $\nabla u$.

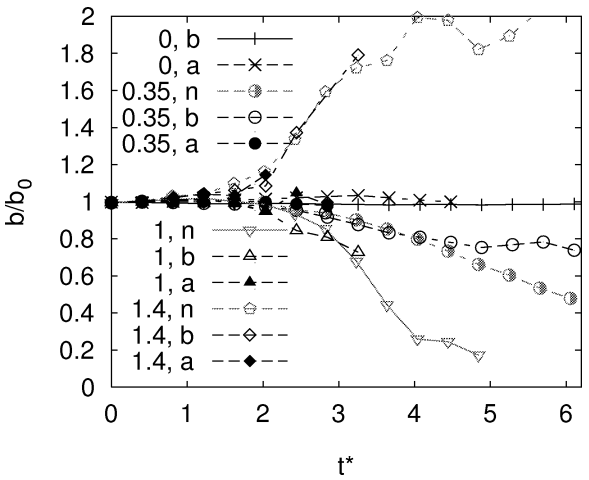


**Figure 3.** Normalized vortex spacing versus time for different turbulence scenarios (*(n), (b), (a)*) and Brunt–Väisälä frequencies, $N^* = 0, 0.35, 1, 1.4$. Cases *n* denote no turbulence.

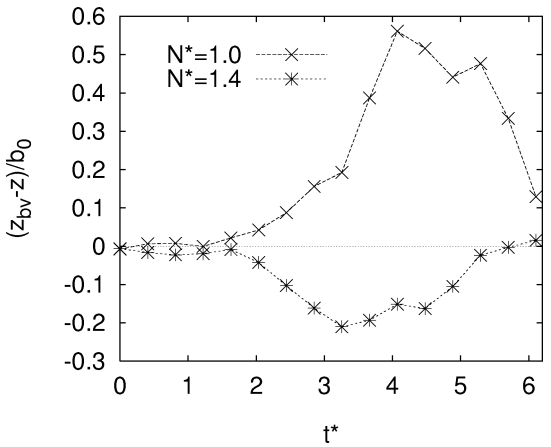


**Figure 4.** Normalized vertical offset between centroid of BV and vortex core position for two different stratifications.

of turbulence (*(b)* or *(a)*) only alter this behaviour marginally. The late acceleration of descent, which is seen for moderate to strong stratification in 2D, cannot be identified in the turbulent cases. The trajectories cease earlier with turbulence when they cannot be determined uniquely because of advanced vortex destruction (see below). In general the lifespan is shorter, the higher the stratification for a given turbulence (and, vice versa, the higher the degree of initial turbulence for a given stratification). In the neutral and quiescent atmosphere (case *b* with $N^* = 0$), the descent continues beyond times of $t^* = 12$ and reaches altitudes below $z/b_0 = -10$ (not shown). In contrast to that, *figure 2* demonstrates that either weak stratification (case *(b)* with $N^* = 0.35$) or weak atmospheric turbulence (case *(a)* with $N^* = 0$) is sufficient to reduce the longevity of wake vortices considerably. For $N^* = 1.4$, the 2D simulations show that the vortices may rebound to the glide path. The same rebound is observed if boundary-layer turbulence is superimposed (case *(b)*). However, the vortices then lose identity after $t^* = 3$; if also (even weak) atmospheric turbulence is present, the process of erosion is faster ($t^* = 2$) such that no coherent piece of vortex is observed to rebound. Note that the simulations also agree well with Sarpkaya's towing tank experiments [23] for $N^* = 1$.

The major trends of the temporal evolution of the vortex spacing, $b/b_0$ (see *figure 3*), are also independent of the prescribed turbulence for a given stratification. The spacing remains constant for neutral stratification. For stratifications increased up to $N^* = 1$ the vortices start to approach each other after $t^* \approx 2$. Minor deviations of the vortex spacing at identical stratification levels indicate spatial deformation of the vortex lines by turbulence. For $N^* = 1.4$, the vortex spacing increases with time.

We conclude that the agreement between turbulent and laminar cases regarding vortex descent and vortex spacing clearly indicates that the underlying physics of the early development is intrinsically two-dimensional. The observations that the vortices approach each other for $N^* \leqslant 1$ and, at the same time, decelerate (which is seemingly a contradiction regarding the concept of mutual velocity induction) can be fully explained when analyzing the flows induced by primary and counter-rotating baroclinic vorticity (BV) (cf. Figs. 7, 9, 10 in [13]). The BV is produced along the border of the adiabatically heated vortex oval by the baroclinic torque [26] according to

$$\frac{\mathrm{D}\omega}{\mathrm{D}t} \sim \frac{1}{\rho^2}\nabla\rho \times \nabla p. \tag{4}$$

The BV, which grows and accumulates along the separating streamline from bottom to top when the vortex pair is descending through stably stratified air, induces an upward and inward motion on the vortex oval. The upward motion weakens the primary descent speed, the approaching vortices decelerate. On the other hand, when $N^* = 1.4$, the BV-induced upward velocity dominates the descent speed and the oval starts to rebound at $t^* = 1.6$ (see *figure 2*). Now BV accumulates from top to bottom along the separating streamline. It still induces an upward but now outward flow on the oval and, hence, the vortices rise quicker and separate. This behaviour can be better understood when analyzing the vertical offset between the vortex center and the centroid of the BV. Comparing *figures 3* and *4* we see that the vortices separate (approach) when the centroid of BV is situated below (above) the vortex cores. (For $N^* = 1.4$ the effect of vortex separation is additionally intensified by local BV production which is stronger at the lower part of the oval due to the strong vertical temperature gradient.) We explain the different time delays for the onset of the deceleration (*figure 2*) and for the onset of

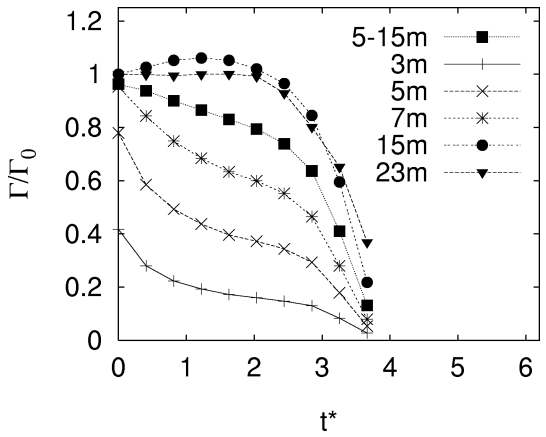


**Figure 5.** Case *(a)*, $N^* = 0.35$. Normalized circulation versus time computed over circles with different radii 3 m to 23 m; normalized circulation averaged over radii from 5 m to 15 m.

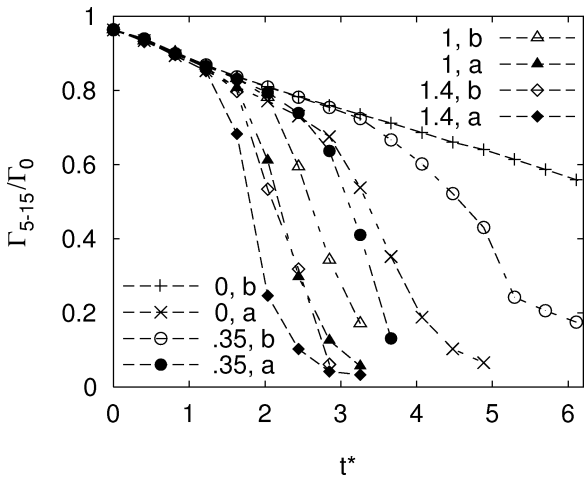


**Figure 6.** Normalized circulation averaged over circles with radii from 5 m to 15 m versus time.

the change of vortex spacing as follows: about 1 $t'$ is necessary to produce BV sufficient for the retardation of the oval; additional 0.5 to 1 $t'$ is required to establish the vertical offset between BV centroid and vortex center by advection.

### 3.2. Circulation

*Figure 5* displays examplarily for case *(a)* with $N^* = 0.35$, the decay of circulation computed over different radii. For times up to $t^* = 2.5$ an exponential type decay is observed on small and intermediate radii which is due to internal diffusion (core radius growth). Maximum circulation is found at $r = 15$ m because at larger radii the integration area also encloses some BV which reduces $\Gamma/\Gamma_0$. After $t^* = 2.5$ – the beginning of the subsequent rapid decay – the BV is in part detrained such that maximum circulation values are found at $r = 23\,\text{m} \approx b_0/2$. In the following we use a circulation $\Gamma_{5-15}$ which is averaged over circles with radii from 5 m to 15 m. ‡

*Figure 6* shows that the initial decay is identical for all cases. Then, the individual curves detach from the bunch of curves at different times to initiate a phase of rapid decay. The higher the turbulence level and the stronger the stratification the earlier the final decay of circulation starts. Different turbulence scenarios only play a significant role for the onset of rapid decay when stratification is neutral to weakly stable ($N^* = 0, 0.35$). Generally we note that in all our scenarios, except for the unlikely case of zero stratification and no ambient turbulence, the circulation always drops to values below 20% of the initial strength within $6t'$ which is less than 2.5 minutes.

It is noteworthy that at the time when the vortices have rebounded to 10 m below the glide path (case *(b)*, $N^* = 1.4$), the circulation has reduced already to 5% of its initial value. Hence, from this and from the trajectory discussion above, we learn that the vortex rebound expected at very strong stratification (strong inversion layers), which is suspected to be very hazardous from an operational point of view, is probably harmless because of the advanced erosion of vortex coherence and strength.

### 3.3. Variation of aircraft-induced turbulence

Two further simulations were performed for case *(b)* with $N^* = 0.35$ where the initialized maximum rms turbulence values were reduced from 2 m/s to 0.2 m/s and 0.02 m/s. These variations over two orders of magnitude were carried out to take into account the uncertainty concerning realistic aircraft boundary-layer turbulence levels, to check the sensitivity to the prescribed turbulence, and, particularly, to conservatively explore maximum lifespans of wake vortices in stably stratified environments. *Figure 7* indicates that, when changing the aircraft-induced turbulence by two orders of magnitude, the descent height remains unaffected until $t^* = 4.5$ and differs by one initial vortex spacing only at $t^* = 6$. From *figure 8* we learn that factor of 10 stronger aircraft turbulence leads only to a time shift for onset of rapid decay of less than $\Delta t^* = 0.8$. At $t^* = 6$ the circulation of all vortices is reduced to about 20% of the initial value. These facts overall indicate a minor sensitivity of the underlying decay mechanism on the strength of the boundary-layer perturbations and show that the cases *(b)* can be read as

‡ Such a definition is especially appropriate when numerical predictions are to be compared to field measurements due to several reasons: Only intermediate radii are reliably accessible by LIDAR; some averaging of data is included which reduces its scatter; measurement errors due to the neighbouring vortex are less sensitive to the viewing angle [1]; and $\Gamma_{5-15}$ correlates well to effects of wake encounters [12].

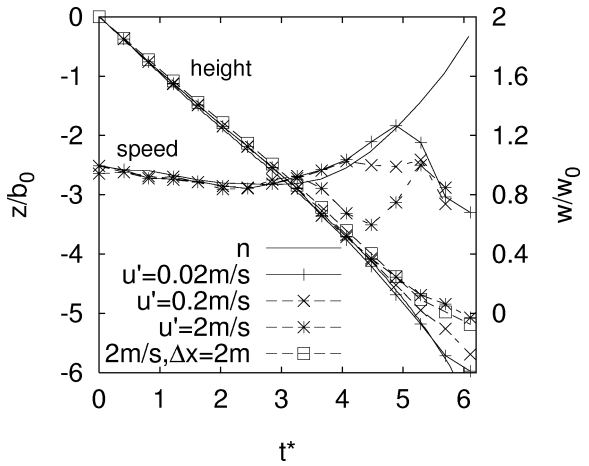


**Figure 7.** Descent height (left ordinate) and speed (right ordinate) versus time for different initial levels of aircraft induced turbulence and one case with increased axial resolution, $N^* = 0.35$.

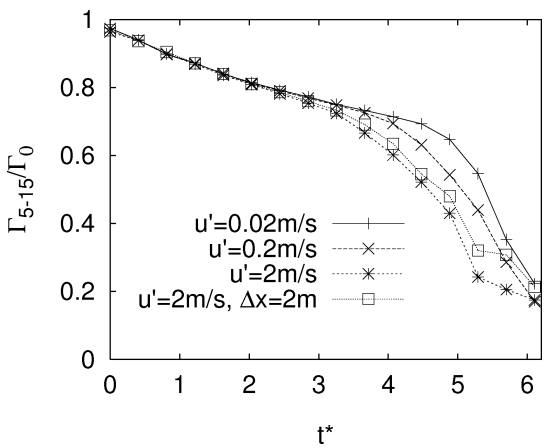


**Figure 8.** $\Gamma_{5-15}/\Gamma_0$ versus time for different prescribed levels of aircraft turbulence and one case with increased axial resolution, $N^* = 0.35$.

conservative estimates of the lifespan of wake vortices in a stably stratified atmosphere.

Moreover, in *figure 7* the descent speed, $w/w_0$, once again elucidates the sequence of the 2D/3D behaviour. All wakes follow, at least to a certain extent, the de-accelerated descent of the 2D simulation until the phase of 3D vortex destruction (see *figure 8*) commences. The acceleration occurs when the induced descent speed, which is increased due to the vortex approach, dominates the deceleration caused by BV. To our knowledge only one experimental work [31] reports weak acceleration.

### 3.4. Structural development

The development of the vortex structure during decay is depicted in *figure 9* for case *(b)* without stratification

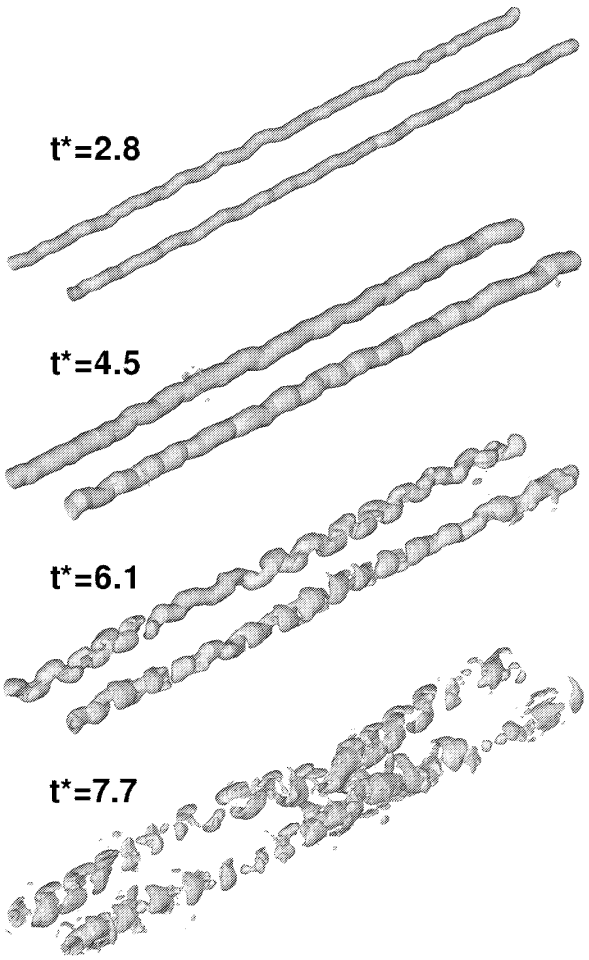


**Figure 9.** Perspective view of $\lambda_2^*$-surfaces for case *b*, $N^* = 0$; $\lambda_2^*(t^* = 2.8) = -3000$, others: $\lambda_2^* = -1200$.

in normalized $\lambda_2$-surfaces (see footnote in section 3.1) for several instants of time. At $t^* = 2.8$ pertubations can be identified which resemble the early stages of the development of the short-wave instability [33]. Indeed, the phase relation (in-phase in horizontal view and out-of-phase in side view) and the wave length of $\lambda \approx 4r_c$ correspond roughly to the characteristics observed in the short-wave or so-called cooperative elliptic instability [17,18]. Since the axial resolution of the simulations was not sufficient to properly resolve the short-wave instability, the amplitude of the instability is somewhat modulated along the vortex axes. With advancing time the short-wave amplitudes are growing. Finally, at $t^* = 7.7$ the formation of the Crow instability [2] becomes evident.

With weak stratification, $N^* = 0.35$, the structural development shown in *figure 10* is distinctly modified. Although at $t^* = 2.8$ the wake vortices still look almost identical for weak and neutral stratification, the subsequent growth rates of the short-wave and the long-wave

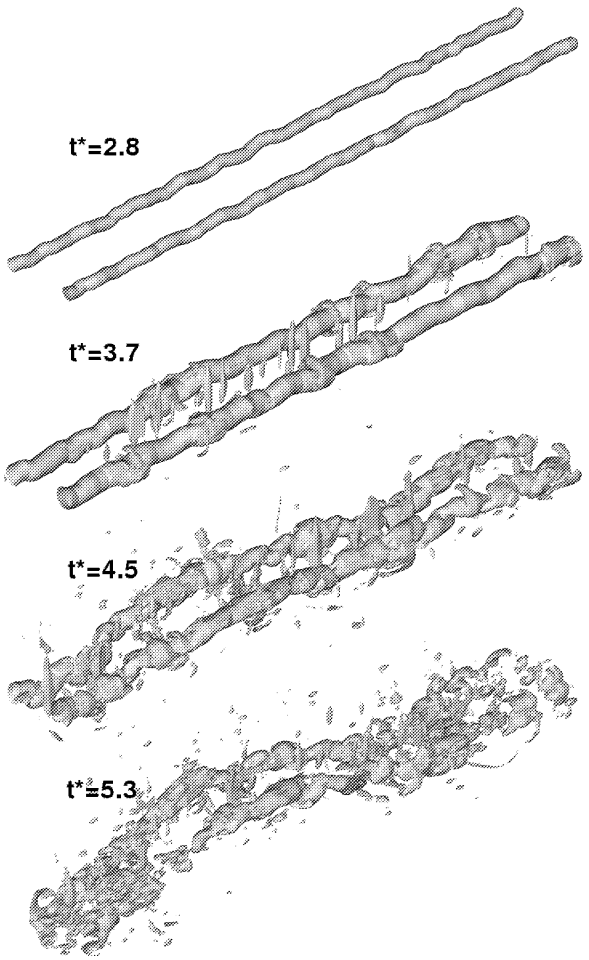


**Figure 10.** Perspective view of $\lambda_2^*$-surfaces for case *b*, $N^* = 0.35$; $\lambda_2^*(t^* = 2.8) = -3000$, others: $\lambda_2^* = -1200$.

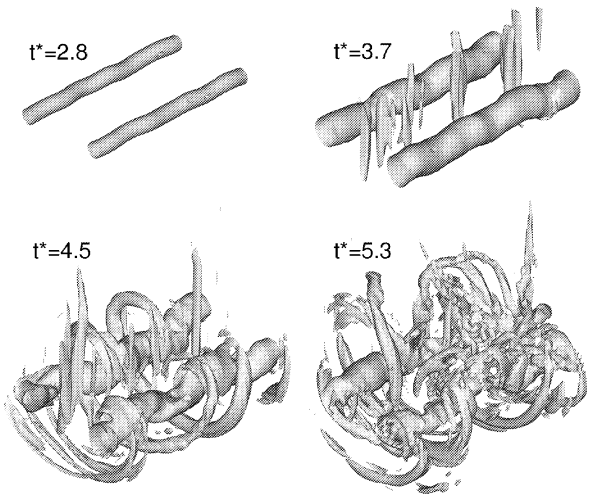


**Figure 11.** As *figure 10* with increased axial resolution ($\Delta x = 2$ m) in an axially shortened domain.

amplitudes are substantially larger for the stratified case (compare stages at $t^* = 4.5$). This is possibly due to the reduction of the vortex spacing for $t^* > 2$ (see *figure 3*) which sustains amplification of short-wave instabilities. Furthermore, at $t^* = 3.7$ vertical $\lambda_2^*$-streaks between the vortices (also seen in [4]) become visible which play – as we will show below – a crucial role regarding the accelerated decay. The vertical streaks, ultimately, produce turbulence which explains the less clear formation of the short-wave structures. For simulations with reduced levels of aircraft turbulence we find that the $\lambda_2^*$-surfaces are smoother such that the short-wave instability is seen somewhat more clearly. The overall decay is delayed and the long-wave (Crow) instability is less obvious (not shown).

Case *(b)*, $N^* = 0.35$ was repeated with an increased axial resolution of $\Delta x = 2$ m in an axially reduced domain of $L_x = 96$ m to ensure that our investigations are meaningful in spite of the insufficient resolution of the short-wave disturbances. *Figures 7* and *8* indicate that the most important parameters, descent height and circulation decay, are almost identically reproduced. The somewhat delayed decay for $t^* > 4$ may be due to the exclusion of the Crow instability in the short domain. The comparison of the structural development in *figures 10* and *11* underlines the similarity of the evolution until $t^* = 3.7$. With finer resolution, sure enough, the short-wave oscillation is better resolved but the vertical structures at $t^* = 3.7$ occur likewise. Considering the deformation of the vortices later, a distinct similarity still persists. However, the noticeable azimuthal structures are obviously less coherent in the coarser grid. Regarding the similarity of the statistical results in *figures 7* and *8*, such coherence does not seem to play a major role in the decay process.

For strong stratification ($N^* = 1$), short-wave perturbations develop even faster (compare *figure 12(a)* at $t^* = 2.4$ with *figure 10* at $t^* = 2.8$ and 3.7), and the shape is even more disturbed. *Figure 12(b)*, showing a higher $\lambda_2^*$-value at the same time, indicates that the production of the azimuthal BV structures ('ribs') is modulated already by small short-wave pertubations. This induces strong vortical structures along the mid plane between the vortices which in turn trigger the rapid decay. Crow instability is not evident in cases *(b)* for strong stratification, $N^* \geqslant 1$. The promotion of short-wave instabilities at the expense of long-wave instabilities for strong stratifications is also reported in an experimental and numerical study [4].

In the cases *(a)* (with weak and decaying atmospheric turbulence, *figures 13, 14*), we find phenomenologically very similar developments for all investigated stratifications. However, with atmospheric turbulence as well as stronger stratification the vortices decay quicker. As

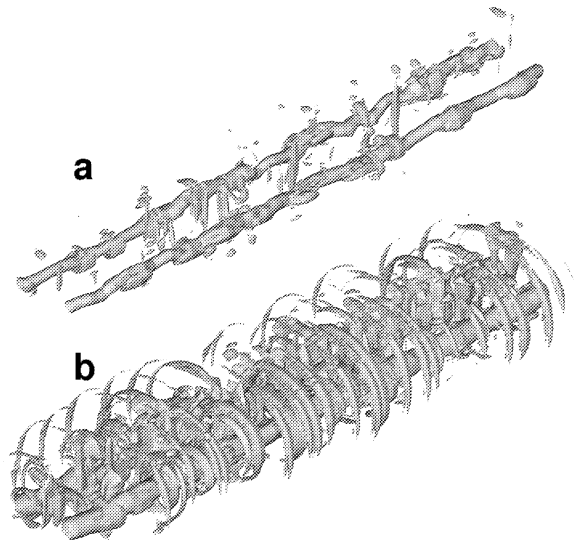


**Figure 12.** Perspective view of $\lambda_2^*$-surfaces for case *(b)*, $N^* = 1$ at $t^* = 2.4$: (a) $\lambda_2^* = -3000$, (b) $\lambda_2^* = -600$.

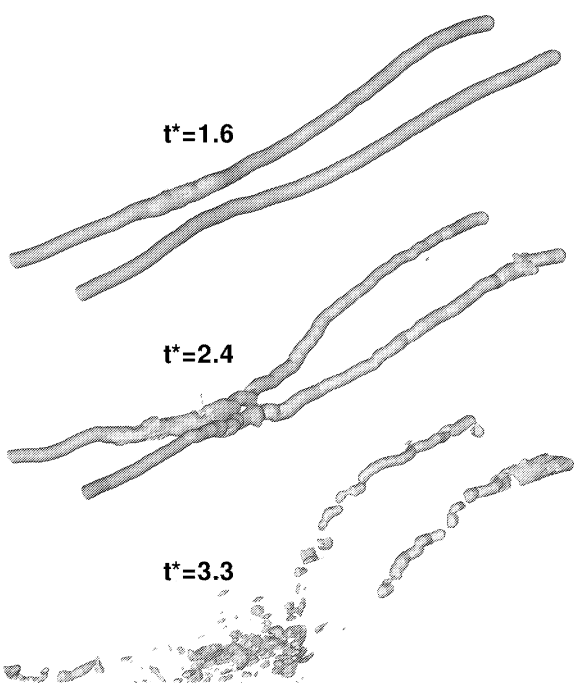


**Figure 13.** Perspective view of $\lambda_2^*$-surfaces for case *(a)*, $N^* = 0.35$, $\lambda_2^* = -3000$.

Robins and Delisi [21], and, later in a more refined consideration, Garten et al. [6] pointed out, the approach of the vortices caused by BV and the perturbation growth due to the Crow instability combine to accelerate the coming together of portions of the vortices. This can be seen by comparing *figures 13* and *14* for $t^* = 1.6$. Later,

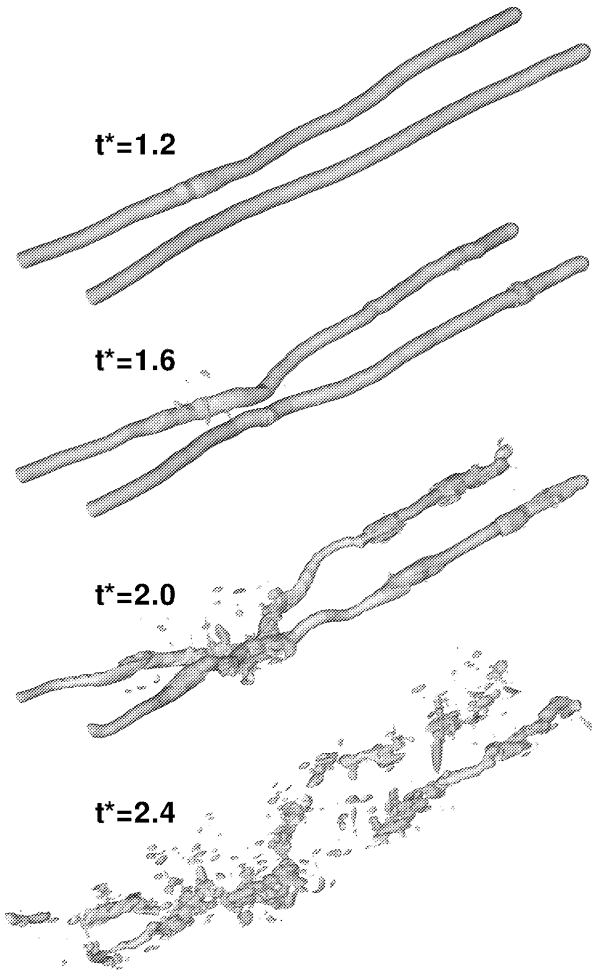


**Figure 14.** Perspective view of $\lambda_2^*$-surfaces for case *(a)*, $N^* = 1$, $\lambda_2^* = -3000$.

the final destruction originates from the portions were the vortices link first. Short-wave disturbances show up where separation is minimum (*figure 13* for $t^* = 2.4$) and then spread out rapidly along the vortices. This is in contrast to other results [6,21] where the formation of longer living descending vortex rings is observed. We thus argue that the interference of BV structures with short-wave disturbances leads to the rapid destruction as known from case *(b)*. The short-wave disturbances are forced by small-scale turbulence from the aircraft-boundary layer and are absent in the other studies. The accelerated decay as a result of interaction of short-wave and long-wave instabilities was demonstrated experimentally ([18], their section 5).

### 3.5. Decay mechanism

In order to explain the decay mechanisms observed in our simulations we show *figures 15*, *16* and *17* which

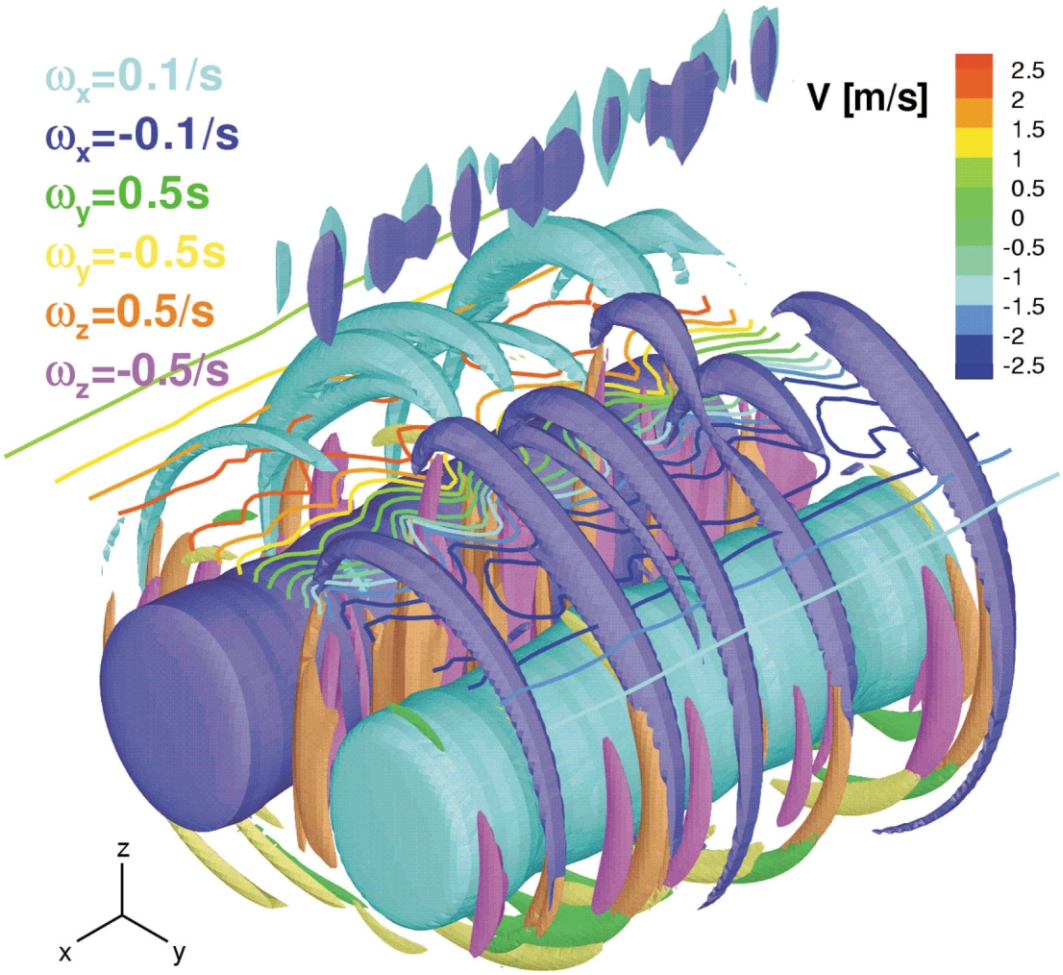


**Figure 15.** Iso-surfaces of all three vorticity components in a perspective view and iso-lines for lateral velocity $v$ in a horizontal plane above the vortices. Case *(b)*, $N^* = 0.35$, $t^* = 2.8$, high axial resolution.

display iso-surfaces of all three vorticity components at $t^* = 2.8$ in perspective, top, and front view, respectively, for case *(b)*, $N^* = 0.35$, and high axial resolution (see *figure 11* for the corresponding $\lambda_2^*$-surfaces). Above the vortices a horizontal plane with iso-lines for the lateral velocity component, $v$, is included ('$v$-plane'). The top-view elucidates that the rib-like structures of baroclinically produced $\omega_x$ induce below lateral velocities, $v$, which are directed towards the symmetry plane between the vortices. The induced wavy velocity field exhibits steep axial gradients of the lateral velocity, $\partial v/\partial x$, and, equivalently, vertical vorticity, $\omega_z \sim \partial v/\partial x$. In detail, each 'BV-rib' induces a tongue-like structure which is flanked by the origin of a pair of counter-rotating vorticity streaks, $\omega_z$. This vorticity is then strongly stretched by the accelerating downward motion between the main vortices yielding very intense $\omega_z$-streaks (note that the iso-surface of $\omega_z$ has a five times higher magnitude than $\omega_x$). Assuming stationarity, vortex stretching changes vorticity according to

$$\frac{\mathrm{D}\omega_z}{\mathrm{D}t} = w\frac{\partial \omega_z}{\partial z} = \omega_z \frac{\partial w}{\partial z}. \tag{5}$$

The integration from a position 0 midway between the vortices in the '$v$-plane' to a vertical position 1 between the vortex centers gives

$$\int_0^1 \frac{\partial}{\partial z}(\ln \omega_z)\,\mathrm{d}z = \int_0^1 \frac{\partial}{\partial z}(\ln w)\,\mathrm{d}z, \tag{6}$$

which leads to

$$\frac{\omega_{z1}}{\omega_{z0}} = \frac{w_1}{w_0}. \tag{7}$$

From vertical positions 0 to 1 the downwards directed velocity increases from $w_0 \approx -0.3\,\mathrm{m/s}$ to $w_1 \approx -6\,\mathrm{m/s}$

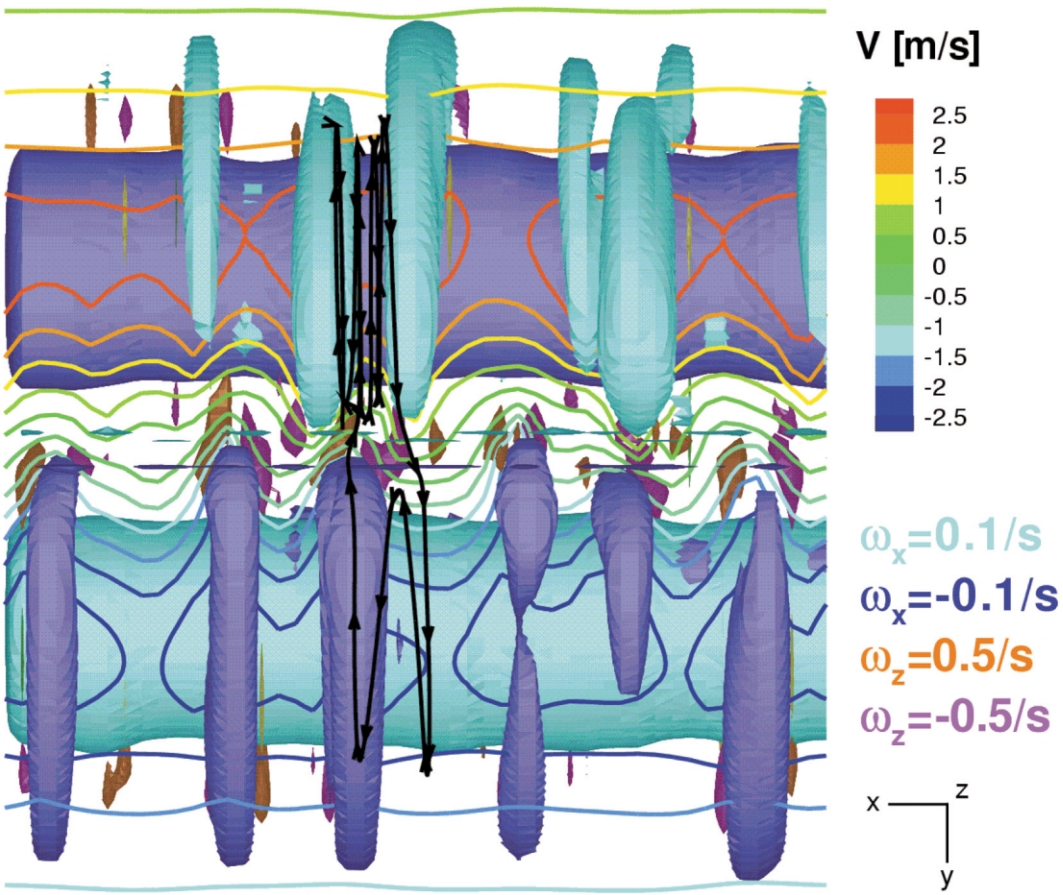


**Figure 16.** Top view of *figure 15*. The black streamline indicates transport across the symmetry plane.

which yields an intensification of $\omega_z$ by a factor of $\omega_{z1}/\omega_{z0} = w_1/w_0 = 20$. Below the main vortex centers, $\omega_z$ is reduced by vortex broadening which is caused by the deceleration experienced during advection towards the lower stagnation point (*figure 17*). Then, the vorticity is tilted, and becomes visible again after another acceleration first in the lateral, $\omega_y$, and then again in the vertical vorticity component, $\omega_z$. The central vertical streaks acting like counter-rotating rolls are outmost effective in exchanging fluid between the two vortices. This is demonstrated by a streamline which crosses the symmetry plane twice (*figures 16, 17*). Aside from a general strong turbulence production caused by counter-rotating vortices in the whole oval, the coherent lateral exchange of fluid across the centerline enables the rapid turbulent diffusion of primary vorticity from one side to the other. This effect is prerequisite for the rapid turbulent decay of vortex pairs. We found that similar mechanisms which comprise the steepening of $\partial v/\partial x$ and vortex stretching are also responsable for the rapid decay observed in weak to moderate atmospheric turbulence (not shown).

### 3.6. Parameterized model

Here, we apply Greene's approximate model [9] (GM) to the simulated cases. In GM the impulse of the aircraft wake, $I_0 = \rho_0 b_0 \Gamma_0$, is reduced by the sum of three forces comprising a viscous force, a turbulence force, and the buoyancy force. The constants in the viscous term and the turbulence term are set to $C_D = 0.2$ and to 0.41, respectively.

*Figure 18* shows that in case *(a)* satisfactory agreement is achieved regarding the descent. Similar deviations – underestimation of the descent for weak stratification and overestimation for very strong stratification – are also found in cases *(b)*. However, for strong stratification (see *figure 19*) GM predicts zero circulation when $\Gamma_{5-15}/\Gamma_0$ is merely reduced to 0.5. The agreement of GM with the development of the circulation integrated over the halfplane indicates that GM assumes implicitly that the primary vorticity and the BV cancel each other immediately. However, the LES predicts well the separated vorticity for time spans during which the hazard of the vortices is underestimated by the simple model.

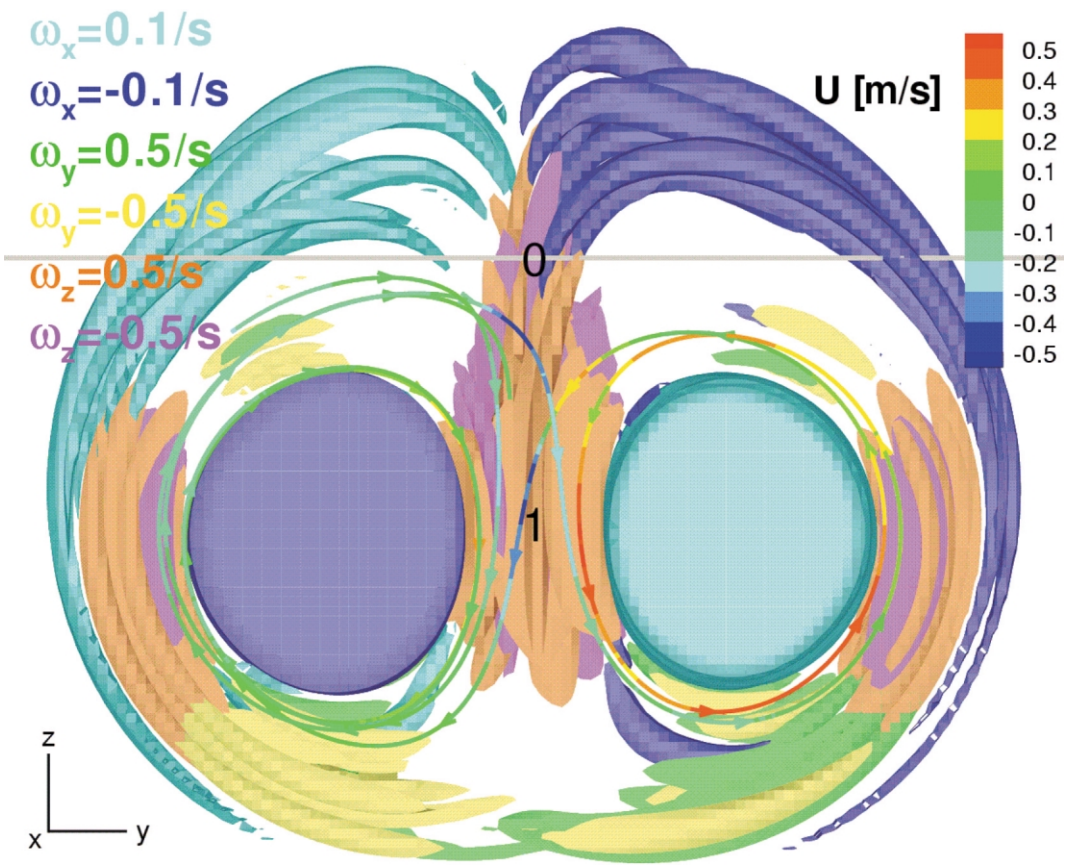


**Figure 17.** Front view of *figure 15*. Here the streamline is colour-coded according to its axial velocity $u$. The vertical position of the plane which shows lateral velocities in *figures 15, 16* is marked by grey line.

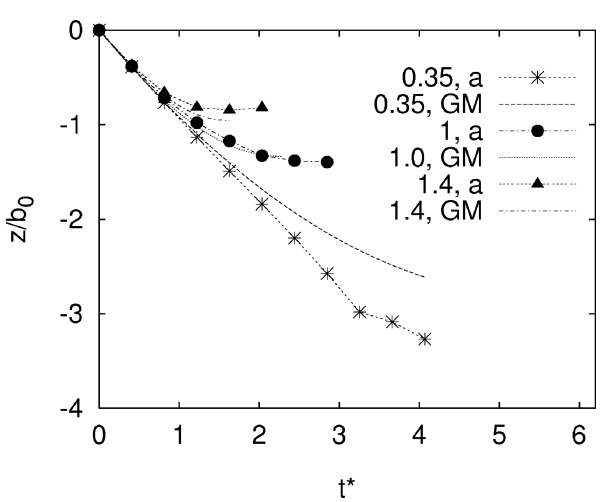


**Figure 18.** Comparison of normalized descent distance versus time between predictions of LES and Greene's model for atmospheric turbulence.

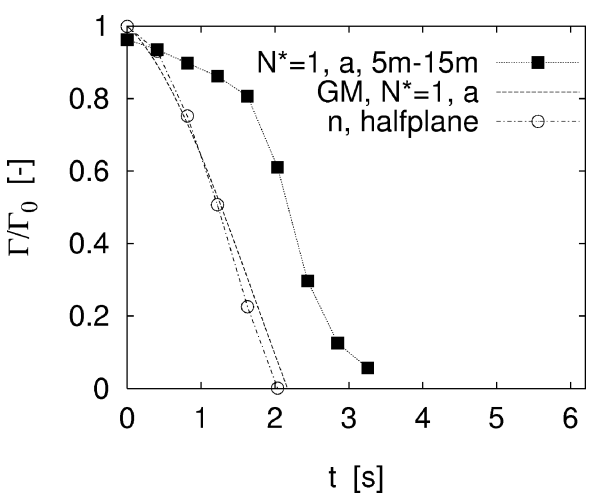


**Figure 19.** Case *(a)*, $N^* = 1$. Comparison of $\Gamma_{5-15}/\Gamma_0$ to normalized circulation of Greene's model. Furthermore, circulation determined by integration over one halfplane for case $n$.

## 4. Conclusions

We have performed LES of wake vortices in a stably stratified atmosphere with which we aim at more realistic conditions compared to previous 3D work [4,6,21,25,30]: we used a relatively high effective Reynolds number, initialized the vortices with relatively tight vortex cores, superimposed aircraft induced turbulence, and considered weak atmospheric turbulence.

The simulations elucidate that the early development of the wake vortices is only affected by the degree of stratification, and not by different turbulence scenarios as prescribed in our study. Descent speed, vortex spacing, and circulation develop almost identically for constant stratification – and can be described in a two-dimensional framework – until different destruction mechanisms initiate a phase of final decay.

Aircraft induced turbulence triggers short-wave instability modes. Owing to those disturbances, the baroclinically produced vorticity rearranges in rib-like structures which induce counter-rotating vertical vorticity-streaks between the primary vortices. These vorticity-streaks are substantially intensified by vortex stretching, and wrap around the main vortices. This results in rapid turbulence production inside the oval, and, in particular, represents an efficient exchange mechanism of primary vorticity across the center plane which leads to rapid circulation decay. Hence, in a calm atmosphere, it is the interaction of primarily independent processes (short-wave instability and baroclinic vorticity production) which initiates the quick dissolution of coherence and decay of circulation of the main vortices. In some cases at later stages also the long-wave (Crow) instability is established. Furthermore, the variation of the intensity of aircraft induced turbulence in a quiescent atmosphere allowed for the conservative estimation that stable stratification reduces the longevity of wake vortices considerably.

When in addition also weak and decaying atmospheric turbulence is prescribed, the sequence of dominant instability processes is reversed: first the Crow instability develops and short-wave disturbances accelerate the decay when the vortices link and thus suppress the formation of descending vortex rings. When atmospheric turbulence is present, the vortices decay sooner for a given level of stratification.

In a very strongly stratified and quiescent atmosphere, wake vortices may rebound to the flight level. This very hazardous scenario from an operational point of view is probably harmless because the vortices quickly lose almost all of their intensity during ascent.

Finally, it is shown that Greene's approximate model successfully predicts the vortex descent. However, the model overestimates the decay of circulation because it assumes intrinsically that main and baroclinically produced vorticity of opposite sign cancel each other immediately which, according to our LES, is only partially the case at late times.

## Acknowledgements

This work was supported by the European Commission in the frame of the Brite/EuRam project WAVENC (No. BE97-4112).

## References

[1] Campbell S.D., Dasey T.J., Freehart R.E., Heinrichs R.M., Matthews M.P., Perras G.H., Rowe G.S., Wake Vortex Field Measurement Program at Memphis, TN Data Guide, Project Report NASA/L-2, Lincoln Laboratory, Massachusetts Institute of Technology, 1997.

[2] Crow S.C., Stability theory for a pair of trailing vortices, AIAA J. 8 (1970) 2172–2179.

[3] Crow S.C., Motion of a vortex pair in a stably stratified fluid, Poseidon Research Rep. 1, Santa Monica, CA, 1974.

[4] Delisi D.P., Robins R.E., Short-scale instabilities in trailing wake vortices in a stratified fluid, AIAA J. 38 (2000) 1916–1923.

[5] Garten J.F., Arendt S., Fritts D.C., Werne J., Dynamics of counter-rotating vortex pairs in stratified and sheared environments, J. Fluid Mech. 361 (1998) 189–236.

[6] Garten J.F., Werne J., Fritts D.C., Arendt S., Direct numerical simulations of the Crow instability and subsequent vortex reconnection in a stratified fluid, subm. to J. Fluid Mech.

[7] Gerz T., Ehret T., Wingtip vortices and exhaust jets during the jet regime of aircraft wakes, Aerosp. Sci. Technol. 1 (1997) 463–474.

[8] Gerz T., Holzäpfel F., Wingtip vortices, turbulence, and the distribution of emissions, AIAA J. 37 (1999) 1270–1276.

[9] Greene G.C., An approximate model of vortex decay in the atmosphere, J. Aircraft 23 (1986) 566–573.

[10] Hecht A.M., Bilanin A.J., Hirsh J.E., Turbulent trailing vortices in stratified fluids, AIAA J. 19 (1981) 691–698.

[11] Hill F.M., A numerical study of the descent of a vortex pair in a stably stratified atmosphere, J. Fluid Mech. 71 (1975) 1–13.

[12] Hinton D.A., Tatnall C.R., A Candidate Wake Vortex Strength Definition for Application to the NASA Aircraft Vortex Spacing System (AVOSS), NASA Technical Memorandum 110343, Langley Research Center, Hampton, Virginia, 1997.

[13] Holzäpfel F., Gerz T., Two-dimensional wake vortex physics in the stably stratified atmosphere, Aerosp. Sci. Technol. 3 (1999) 261–270.

[14] Holzäpfel F., Gerz T., Frech M., Dörnbrack A., Wake Vortices in a Convective Boundary Layer and their Influence on Following Aircraft, J. Aircraft 37 (2000) 1001–1007.

[15] Jeong J., Hussain F., On the identification of a vortex, J. Fluid Mech. 285 (1995) 69–94.

[16] Kaltenbach H.-J., Gerz T., Schumann U., Large-eddy simulation of homogeneous turbulence and diffusion in stably stratified shear flow, J. Fluid Mech. 280 (1994) 1–40.

[17] Laporte F., Darracq D., Corjon A., On the Vortex-Turbulence Interaction: DNS of Elliptic Instability of a Vortex Pair, AIAA Paper 99-3417 (1999).

[18] Leweke T., Williamson C.H.K., Cooperative elliptice instability of a vortex pair, J. Fluid Mech. 360 (1998) 85–119.

[19] Pavlenko A.A., Influence of the Calm Atmosphere Stratification on the Evolution of the Vortex Behind an Aircraft, ISTC Moscow, Annual Report, Project No. 201-95 (1996) 33–40.

[20] Robins R.E., Delisi D.P., Numerical study of vertical shear and stratification effects on the evolution of a vortex pair, AIAA J. 28 (1990) 661–669.

[21] Robins R.E., Delisi D.P., Numerical simulation of three-dimensional trailing vortex evolution in stratified fluid, AIAA J. 3 (1998) 981–985.

[22] Saffman P.G., The motion of a vortex pair in a stratified atmosphere, SIAM LI (1972) 107–119.

[23] Sarpkaya T., Trailing vortices in homogeneous and density-stratified media, J. Fluid Mech. 136 (1983) 85–109.

[24] Schilling V., Siano S., Etling D., Dispersion of aircraft emissions due to wake vortices in stratified shear flows: A two-dimensional numerical study, J. Geophys. Res. 101 (1996) 20965–20974.

[25] Schowalter D.G., DeCroix D.S., Switzer G.F., Lin Y.-L., Arya S.P., Toward Three-Dimensional Modeling of a Wake Vortex Pair in the Turbulent Planetary Boundary Layer, AIAA Paper 97-0058 (1997).

[26] Scorer R.S., Davenport L.J., Contrails and aircraft downwash, J. Fluid Mech. 43 (1970) 451–464.

[27] Sipp D., Jacquin L., Cossu C., Self-adaption and viscous selection in concentrated two-dimensional vortex dipoles, Phys. Fluids 12 (2000) 245–248.

[28] Spalart P.R., On the motion of laminar wing wakes in a stratified fluid, J. Fluid Mech. 327 (1996) 139–160.

[29] Spalart P.R., Airplane trailing vortices, Annu. Rev. Fluid Mech. 30 (1998).

[30] Switzer G.F., Proctor F.H., Numerical Study of Wake Vortex Behavior in Turbulent Domains with Ambient Stratification, AIAA Paper 2000-0755 (2000).

[31] Tomassian J.D., The motion of a vortex pair in a stratified medium, Ph.D. Dissertation, Univ. of California, Los Angeles, 1979.

[32] Urbatzka E., Wilken D., Estimating runway capacities of German airports, Transportation Planning and Technology 20 (1997) 103–129.

[33] Widnall S.E., Bliss D.B., Zalay A., Theoretical and experimental study of the instability of a vortex pair, in: Olsen et al. (Eds.), Aircraft Wake Turbulence and its Detection, Plenum Press, 1971, p. 305.

[4]

# Probabilistic Two-Phase Wake Vortex Decay and Transport Model

F. Holzäpfel

Journal of Aircraft, 2003

Volume 40, Number 2, Pages 323–331

JOURNAL OF AIRCRAFT
Vol. 40, No. 2, March–April 2003

# Probabilistic Two-Phase Wake Vortex Decay and Transport Model

Frank Holzäpfel*
*DLR, German Aerospace Research Center, D-82234 Weßling, Germany*

**A new parametric wake vortex transport and decay model is proposed that predicts probabilistic wake vortex behavior as a function of aircraft and environmental parameters in real time. The probabilistic two-phase wake vortex decay model (P2P) accounts for the effects of wind, turbulence, stable stratification, and ground proximity. The model equations are derived from the analytical solution of the spatiotemporal circulation evolution of the decaying potential vortex and are adapted to wake vortex behavior as observed in large-eddy simulations. Vortex decay progresses in two phases, a diffusion phase followed by rapid decay. Vortex descent is a nonlinear function of vortex strength. Probabilistic components account for deviations from deterministic vortex behavior inherently caused by the stochastic nature of turbulence, vortex instabilities, and deformations, as well as uncertainties and fluctuations that arise from environmental and aircraft parameters. The output of P2P consists of confidence intervals for vortex position and strength. To assign a defined degree of probability to the predictions reliably, the model design allows for the continuous adjustment of decay parameters and uncertainty allowances, based on a growing amount of data. The application of a deterministic version of P2P to the Memphis wake vortex database yields favorable agreement with measurements.**

## Nomenclature

| | | |
|---|---|---|
| $A$ | = | constant |
| $b$ | = | vortex spacing |
| $g$ | = | gravitational acceleration |
| $N$ | = | Brunt–Väisälä frequency |
| $q$ | = | rms turbulence velocity |
| $R$ | = | mean radius |
| $Ri$ | = | Richardson number |
| $r$ | = | radial coordinate |
| $r_c$ | = | core radius |
| $T$ | = | parameter for vortex age |
| $t$ | = | time |
| $u$ | = | axial velocity |
| $v$ | = | lateral velocity |
| $w$ | = | descent speed |
| $y$ | = | spanwise coordinate |
| $z$ | = | vertical coordinate |
| $\Gamma$ | = | circulation |
| $\Delta t$ | = | time step |
| $\varepsilon$ | = | eddy dissipation rate |
| $\Theta$ | = | potential temperature |
| $\nu$ | = | (effective) kinematic viscosity |

*Subscripts*

| | | |
|---|---|---|
| $l$ | = | lower limit |
| $u$ | = | upper limit |
| 0 | = | initial value |
| 1 | = | first decay phase |
| 2 | = | second decay phase |
| 5–15 | = | average over circles with radii from 5 to 15 m |

*Superscripts*

| | | |
|---|---|---|
| $*$ | = | normalized quantity |
| $-$ | = | mean quantity |

## Introduction

AS a consequence of lift, aircraft generate a pair of long-lived counter-rotating wake vortices that bear a potential risk for following aircraft. Current wake-vortex separation standards between consecutive aircraft contribute significantly to the capacity constraints of congested airports. From experience and research results gained during the past 30 years, it has become evident that the separation standards may be overly conservative for a variety of meteorological situations.[1,2] A parametric model capable of reliably predicting vortex positions and strengths in real time in a measured or forecasted atmospheric environment along the glide path might, therefore, permit air-traffic controllers to ease some of the regulations without loss of safety. Several reduced spacing systems[3–5] that employ vortex decay and transport models of different complexity have been developed. However, none of the systems is operational today. Other applications of parametric wake vortex models include encounter investigations within flight simulation environments, for example, Ref. 6, safety analyses that estimate the hazard probability of new approach and landing procedures,[7] and studies that simulate different aspects of reduced spacing systems, for example, the predictability of wake vortices based on virtual environmental measurement data in a convectively driven atmospheric boundary layer.[8]

The first wake vortex model presented in 1986 by Greene[9] assumes that the impulse per unit length of a wake is reduced by the sum of viscous drag, buoyancy force, and turbulent decay. From a single equation, circulation, velocity, and vertical position of the wake can be determined. Greene's model was extended by Corjon and Poinsot[10] by adding ground and crosswind effects 10 years later. Sarpkaya[11] eliminated the viscous drag in Greene's[9] model and proposed an empirical model for turbulent decay that relies on the eddy dissipation rate instead of turbulent kinetic energy. More recently, Sarpkaya et al. adapted the descent rate to observations by introducing variable vortex spacing.[12] The Canadian vortex forecast system[13] models the evolution of multiple discrete vortices in a two-dimensional crossplane starting from a near wake database that acounts for the aircraft geometry. Effects of the ground and nonuniform wind shear are included; decay due to ambient turbulence is

Received 30 November 2001; revision received 8 October 2002; accepted for publication 12 October 2002. 

*Research Scientist, Institute of Atmospheric Physics, Oberpfaffenhofen.

adapted from approaches from either Ref. 9 or 11. Another model that accounts for effects of ambient turbulence, crosswind shear, and ground proximity was proposed by Kantha.[14] Recently, Mokry[15] presented a two-dimensional continuous vortex sheet method that captures vortex sheet rollup, interaction with ambient shear layers and the ground.

Note that despite the significant number of available wake vortex models none of these models considers all effects of the first-order impact parameters, which are aircraft configuration, turbulence, stable stratification, shear, and proximity of the ground. In particular, they are all deterministic. Not specified are deviations from predicted values that are inherently caused by the stochastic nature of turbulence, complex vortex instabilities and deformations, uncertainty of aircraft parameters, and uncertainties and fluctuations of environmental parameters. The probabilistic two-phase wake vortex decay model (P2P) proposed here is designed to predict wake vortex behavior within defined confidence intervals. For this purpose, the model concept allows for the continuous adjustment of decay parameters and uncertainty allowances, based on a growing amount of observations and simulations. Currently, the decay parameters are "calibrated" based on different large-eddy simulation (LES) data.[16,17] The LES data suggest that vortex decay progresses in two phases, a diffusion phase followed by rapid decay,[1,18] and that vortex descent is not a linear function of vortex strength. The model accounts for the effects of wind, turbulence, stable stratification, and ground proximity. Wake shear-layer interaction is not parameterized. It is believed that the associated complex vortex behavior[19] cannot be predicted reliably in an operational environment. Situations where shear layer effects are not covered by uncertainty allowances have to be diagnosed, and reduced spacing operations must be ruled out.

After an introduction of the model concept, the equations that describe circulation decay and descent rate are derived and adapted to the LES data. Then the probabilistic components of P2P are discussed. The paper concludes with applications of P2P to the Memphis wake vortex database.[20] A comprehensive comparison to different measurements[20,33,34] is in preparation.

## Model Concept

P2P is designed to include as much knowledge as possible gained from both experimental and numerical wake vortex research with a focus on operational needs. For this purpose the model concept comprises the following elements.

First, in contrast to most other models, P2P employs a well-defined and experimentally accessible definition for vortex strength. Unlike single vortices where the circulation reaches a definite constant value at large radii, the circulation of vortex pairs strongly depends on the method of its evaluation. P2P uses a circulation $\Gamma_{5-15}$ that is averaged over circles with radii from 5 to 15 m or, alternatively, from 3 to 10 m, for several reasons. 1) The estimation of the root circulation may be extremly difficult for a vortex pair that evolves in the atmosphere. This is the case in measurement and simulation. At radii where $\Gamma(r)$ should run into saturation, influences of the neighbouring vortex, secondary vortices, ambient turbulence, or baroclinic vorticity may drastically modify the circulation values. The upper integration limit of $r = 15$ m avoids these difficulties for larger aircraft. 2) The averaging of $\Gamma$ over a radius interval reduces the scatter in turbulent vortices and enables estimations of disintegrating vortices. 3) Small radii that are not reliably accessible by lidar are excluded. 4) Because the final aim of P2P is to predict vortex behavior to allow for dynamic spacing between consecutive aircraft, an operationally useful circulation definition is employed that correlates well with effects of potential wake encounters.[21] Note that $\Gamma_{5-15}$ is only calculated from the velocity components that are perpendicular to the flight direction or from the corresponding vorticity, regardless of the actual orientation of the vortex axis. This implies that large-scale deformations or the formation of the Crow instability may considerably reduce $\Gamma_{5-15}$, whereas circulation in a local plane perpendicular to the vortex axis is not necessarily mitigated.

Second, P2P is based on a well-founded equation for vortex evolution. Because there is no rigorous solution for the evolution of turbulent vortex pairs, the hydrodynamic basis of P2P relies on the equation that describes the spatiotemporal circulation evolution of the decaying potential vortex

$$\Gamma(r,t)/\Gamma_0 = 1 - \exp(-r^2/4\nu t) \tag{1}$$

Equation (1) constitutes an analytical solution of the Navier–Stokes equations for a non-stationary, plane, rotating flow.[22] In P2P, this relation is extended and adapted to LES results of different groups[16,17] to describe vortex decay and descent.

Third, P2P contains probabilistic components to meet the variability of wake vortex behavior that is caused by manifold governing physical mechanisms,[23] turbulence, and uncertainties regarding environmental conditions. The output of P2P consists of lower and upper bounds for vortex position and circulation. The final goal is to determine reliably the probability with which the actual vortex evolution is met by predictions. For this purpose, P2P has to be applied to as much available data as possible to give it an outmost broad phenomenological and statistical basis. The design of P2P allows an ongoing adaption to observations and an adjustment to a desired confidence level.

The model is formulated in normalized form where the characteristic scales are based on initial vortex separation and circulation leading to the timescale

$$t' = 2\pi {b_0}^2 \big/ \Gamma_0 = b_0/w_0 \tag{2}$$

## Circulation

It is assumed that the evolution of $\Gamma^*_{5-15}$ can be described by two consecutive decay phases as observed in LES[16,17] (Figs. 1 and 2). In the first phase, termed diffusion phase, the normalized, radii-averaged circulation can be formally calculated as

$$\Gamma^*_{5-15}(t^*) = \frac{1}{11}\sum_{r=5\,\mathrm{m}}^{15\,\mathrm{m}} A - \exp\frac{-r^{*2}}{4\nu_1^*\left(t^* - T_1^*\right)} \tag{3}$$

Because the vortices are not decaying potential vortices but are generated by the rollup of a vorticity sheet, an adaption of vortex parameters is introduced by the constants $A$ and $T_1^*$ where $-T_1^*$ corresponds to the age of the vortices at $t^* = 0$ and reflects the vortex structure at that time. $A$ is a constant to adjust $\Gamma^*_{5-15}(t^* = 0)$. Figure 3 shows a comparison of Eq. (3) with $A = 1.09$, $T_1^* = -2.22$, and an effective viscosity $\nu_1^* = 1.78 \times 10^{-3}$ ($\nu_1 = 0.16$ m$^2$/s) to the LES baseline case[16] of a vortex evolution in a quiescent, neutrally stratified atmosphere.

For the sake of simplicity, the averaging over different radii as performed in Eq. (3) is omitted, which leads to

$$\Gamma^*_{5-15}(t^*) = A - \exp\left[-R^{*2}\big/\nu_1^*\left(t^* - T_1^*\right)\right] \tag{4}$$

The mean radius $R^*$ corresponds approximately to the mean value of 10 m within the averaging interval 5–15 m. $R^{*2}$, which includes the

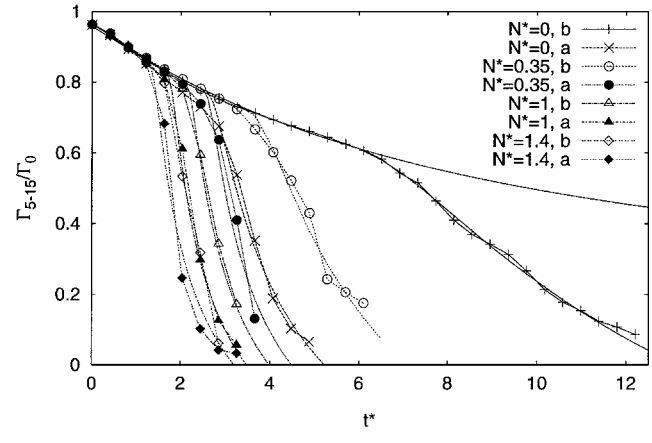


**Fig. 1 Circulation from LES[16] and respective fits of P2P for different turbulence scenarios and different degrees of stratification.**

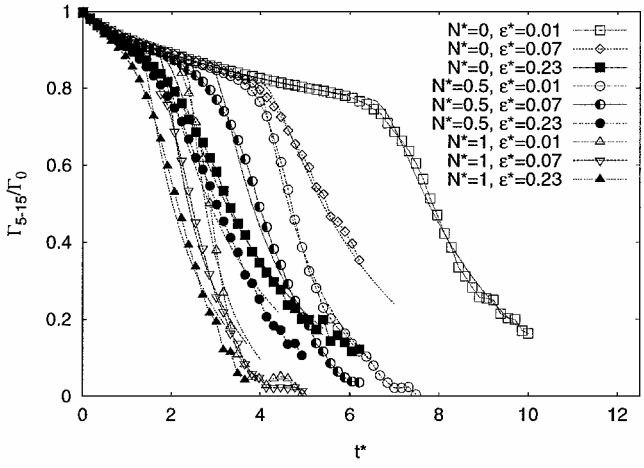


**Fig. 2 Circulation from LES[17] and respective fits of P2P for different degrees of turbulence and stratification.**

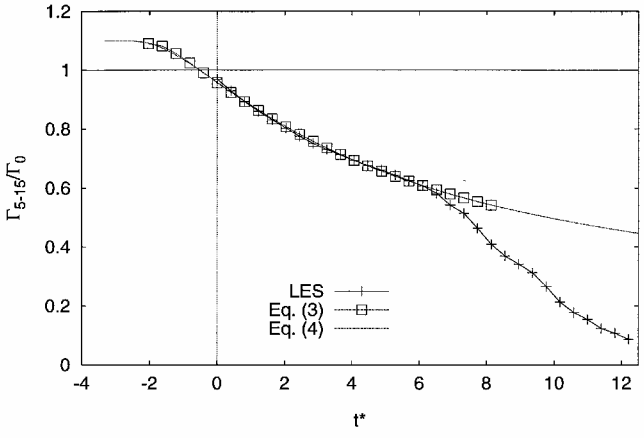


**Fig. 3 Circulation evolution in the diffusion phase for LES[16] in quiescent atmosphere and respective fits with Eqs. (3) and (4).**

factor one-quarter of Eq. (3), is determined as 0.0121. (In the LES, $b_0 = 47$ m.) The parameters $A = 1.1$ and $T_1^* = -3.48$ are slightly modified, whereas the viscosity remains unchanged. This simplification still gives a very good representation of the diffusion phase (Fig. 3).

The second phase is called the rapid decay phase. Different instability and decay mechanisms,[19,24] as well as large-scale deformations (deviation of local vortex axis from flight direction), lead to an accelerated reduction of $\Gamma^*_{5-15}$. The original cause for the release of the rapid decay phase (turbulence, stable stratification, shear) may be diverse, and also many details of the respective mechanisms may vary considerably from case to case. Nevertheless, it is assumed that in all cases a two-phase evolution of $\Gamma^*_{5-15}$ prevails as observed in numerical investigations[16,17,25] and lidar measurements.[26] The rapid decay phase is described by

$$\Gamma^*_{5-15}(t^*) = A - \exp\left[-R^{*2}\Big/\nu_1^*\left(t^* - T_1^*\right)\right] - \exp\left[-R^{*2}\Big/\nu_2^*\left(t^* - T_2^*\right)\right] \tag{5}$$

where the onset time of rapid decay at $T_2^*$ and the respective decay rate that is adjusted by the effective viscosity $\nu_2^*$ depend on meteorological parameters. Figures 1 and 2 show circulation evolutions from our LES[16] and from the LES of Proctor and Switzer[17] together with the respective fits of P2P for different turbulence levels and different degrees of stable temperature stratification. Stratification is characterized with a normalized Brunt–Väisälä frequency [discussed later in Eq. (16)]. Our LES distinguish between two cases case b, where only aircraft-induced turbulence is superimposed on the vortices, and case a, where the turbulent vortices evolve in an anisotropic atmospheric turbulence with rms velocities of 0.38 m/s in the horizontal and 0.21 m/s in the vertical directions, respectively. Proctor and Switzer characterize turbulence with the normalized eddy dissipation rate, $\varepsilon^* = (\varepsilon b_0)^{1/3}/w_0$. The LES of both Refs. 16 and 17 show that the initial decay rate is very similar for the different cases. The reduced decay rate observed in the diffusion phase of Proctor and Switzer's[17] LES is mainly caused by their Richardson number correction for rotational effects (see Ref. 27), which reduces the diffusion in the vortex core region. The higher the turbulence and the stronger the stratification, the earlier the individual curves detach from their common evolution in the diffusion phase to initiate the rapid decay phase. The effect of aircraft-induced turbulence (case b) seems to correspond roughly to the effect of ambient turbulence with an eddy dissipation rate of $\varepsilon^* = 0.01$. The good agreement of the fits of P2P according to Eqs. (4) and (5) with the LES substantiates the appropriateness of the approach.

## Decay Parameters

The values of $T_2^*$ and $\nu_2^*$ have to be determined as functions of meteorological parameters. Basically, the impact of turbulence can be parameterized based on turbulent kinetic energy (TKE) or, alternatively, eddy dissipation rate. An analysis[28] of 525 wake vortex measurements of the Memphis database evaluates the potential of the respective quantities. Figure 4 shows cumulative distributions of the instant in time of the last circulation measurement by lidar for three different turbulence regimes. It is assumed that this instant in time is correlated to the longevity of the vortices. The TKE* criterion shown in Fig. 4a separates vortex longevity in the low- and intermediate turbulence regimes insufficiently, whereas the correlation

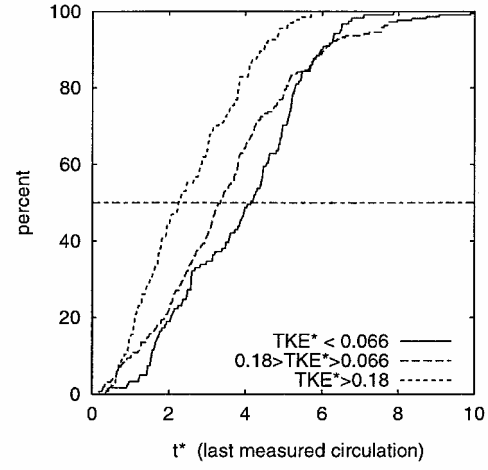


a)

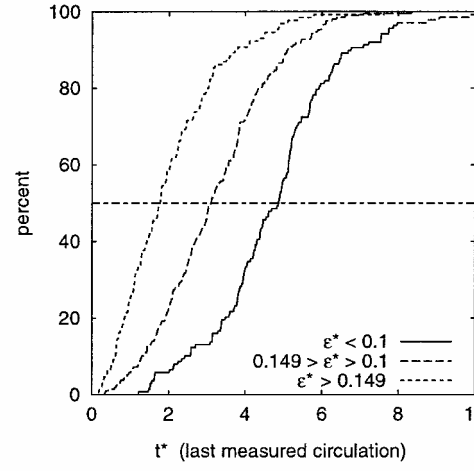


b)

**Fig. 4 Cumulative distribution of the time of last lidar measurement of 525 cases for three different classes of turbulence characterized by a) normalized TKE and b) normalized eddy dissipation rate.**

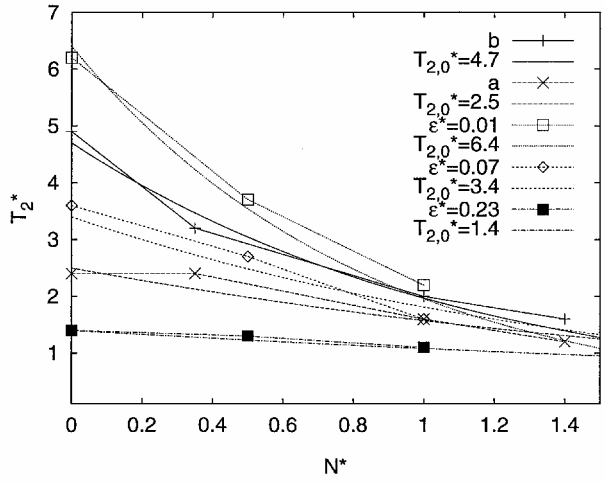


**Fig. 5 Decay parameter, $T_2^*$, as a function of stratification and turbulence determined for LES (symbols) and corresponding fits to Eq. (6).**

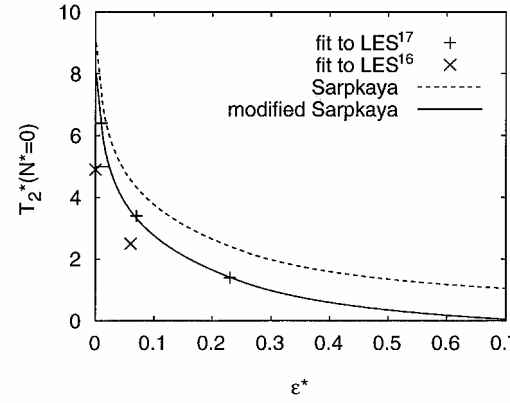


**Fig. 6 Decay parameter $T_2^*$ for neutral stratification as a function of $\varepsilon^*$ for different LES, the Sarpkaya[11] model and a modification of Sarpkaya's model.**

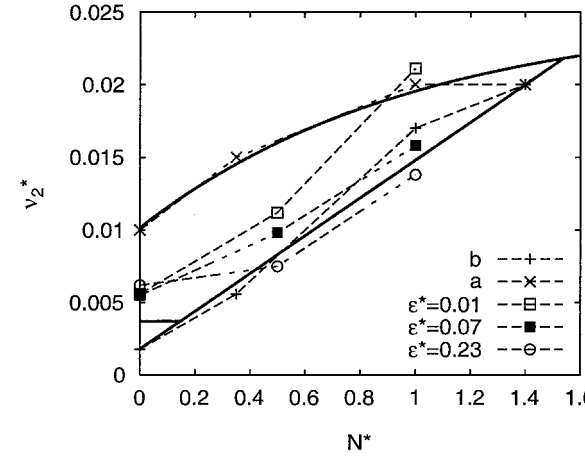


**Fig. 7 Decay parameter $\nu_2^*$ as function of stratification for different turbulence levels as fitted to LES[16,17] and corresponding limiting curves (——) according to Eqs. (9) and (10).**

of longevity and $\varepsilon^*$ shown in Fig. 4b is much more distinct. This result corroborates the assumption[11] that the intensity of atmospheric fluctuations in the length-scale range that affects vortex decay may be well characterized by $\varepsilon^*$, that is, the crucial length-scale range of wake vortices resides in the inertial subrange of turbulence spectra of atmospheric boundary layers. In contrast, TKE* data are sensitive to the choice of the averaging time frame, that is, the longer the averaging interval, the more energy is contributed from larger scales that are irrelevant for vortex decay. Therefore, in P2P, the parameterization of the impact of turbulence is based on $\varepsilon^*$, although it is difficult to deduce $\varepsilon^*$ from measurements in an operational environment.

Figure 5 shows the dependency of $T_2^*$ [determined by fitting Eq. (5) to the LES data] on $N^*$ for different turbulence levels. Increased values of turbulence and stratification both reduce $T_2^*$. As soon as turbulence or stratification is strong, the impact of the other respective parameter becomes minor. Note that the onset time of rapid decay, $T_2^*$, coincides well with visually determined inflexion points of the $\Gamma_{5-15}^*$ curves (Figs. 1 and 2) and, remarkably, also with the point in time at which axial cross sections of vorticity show a transition[19] from a quasi-laminar state (turbulence on length scales $L \ll r_c$) to a fully turbulent state [$L = \mathcal{O}(r_c)$]. Both transition and inflexion point concurrently indicate that the flow state enters the rapid decay phase. The family of curves in Fig. 5 that correspond to specific turbulence levels can be fitted by

$$T_2^* = T_{2,0}^* \exp\left(-0.185 T_{2,0}^* N^*\right) \tag{6}$$

where the turbulence level is characterized by the time constant for rapid decay in the neutrally stratified atmosphere, $T_{2,0}^* = T_2^*(N^* = 0)$.

The dependency of $T_{2,0}^*$ on $\varepsilon^*$ for the LES data is shown in Fig. 6 by symbols. Furthermore, the model of Sarpkaya[11] that relates the time at which a "catastrophic demise event" takes place in nonstratified environments to $\varepsilon^*$ is displayed. The Sarpkaya[11] approximation is based on various analyses, observations, and simulations and covers a wide range of turbulence intensities. Subtracting one timescale from the Sarpkaya[11] curve (modified Sarpkaya) yields very good agreement with the data derived from Proctor and Switzer's[17] LES. P2P takes advantage of the extrapolation of Proctor and Switzer's data to higher turbulence levels by the Sarpkaya[11] model for $\varepsilon^* > 0.0235$,

$$T^* = 0.804 \varepsilon^{*\frac{3}{4}}, \qquad \varepsilon^* > 0.2535$$

$$T^{*\frac{1}{4}} \exp(-0.70 T^*) = \varepsilon^*, \qquad \varepsilon^* > 0.0235 \tag{7}$$

and adapts it according to $T_{2,0}^* = T^* - 1$ (Fig. 6, solid line). For $\varepsilon^* \leq 0.0235$, our conservative baseline LES case in which wake vortices are initialized with superimposed aircraft-induced turbulence in a quiescent, neutrally stratified atmosphere provides the upper threshold

$$T_{2,0}^* = 5, \qquad \varepsilon^* \leq 0.0235 \tag{8}$$

The $T_2^*$ values that are calculated from Eqs. (6–8) are varied by $\pm 20\%$ in two subsequent runs of P2P to account for uncertainties of $T_2^*$.

Figure 7 shows that the correlation of $\nu_2^*$ values with turbulence and stratification is less distinct than for $T_2^*$. The LES of Proctor and Switzer[17] and our LES even give contrary tendencies: In our LES, the strongest impact of turbulence is found for neutral stratification, whereas Proctor and Switzer's nonstratified data are insensitive to turbulence. Moreover, in a stably stratified atmosphere, the two LES approaches yield opposite trends regarding the dependency of $\nu_2^*$ on turbulence. Therefore, $\nu_2^*$ is parameterized only as a function of $N^*$, and the uncertainty of the impact of turbulence is taken into account by performing two consecutive P2P-runs that employ the upper and lower bounds of $\nu_2^*$ for a given value of $N^*$. The upper boundary follows

$$\nu_{2,u}^* = 0.025[1 - \exp(-N^* - 0.52)] \tag{9}$$

and the lower boundary is given by

$$\nu_{2,l}^* = 0.0018 + 0.013 N^* \tag{10}$$

Furthermore, a threshold of $\nu_{2,l}^* = 0.0037$ is introduced when $\varepsilon^* > 0.01$ to avoid extensively long-lived vortices in a weakly turbulent environment. Values below that threshold are only applied for essentially quiescent ambient flows.

There is no height variation of meteorological impact parameters in the LES data used for calibration. If measurements or predictions of vertical profiles of $\varepsilon^*(z^*)$ and $N^*(z^*)$ are available, P2P employs a running average. The running average allows a weighting of the impact of the environmental conditions according to the respective residence time of the vortices at a particular vertical position. For example, the running average of the eddy dissipation rate is calculated according to

$$\bar{\varepsilon}^*(t^*) = [(t^* - \Delta t^*)\bar{\varepsilon}^*(t^* - \Delta t^*) + \Delta t^* \varepsilon^*(t^*)]/t^* \tag{11}$$

where the running average is updated every time step. If local wind data are available, the vortices are transported by all available wind components including vertical wind.

## Descent Speed

The simple relation $w^* = \Gamma^*$ holds only if $\Gamma^*$ represents the circulation at the neighboring vortex. For radii-averaged circulations such as $\Gamma^*_{5-15}$, it is not valid. LES and observations indicate that $\Gamma^*_{5-15}$ may decrease substantially without considerable influence on the descent speed.[16] This can readily be understood by considering the simple decaying potential vortex whose tangential velocities decrease less at radii that induce the descent speed for larger aircraft ($b > 15$ m) than in the radii interval $5 \le r \le 15$ m that is used for determination of $\Gamma^*_{5-15}$. However, wake vortices do not evolve like single laminar vortices. Nevertheless, the strategy to develop a relation between $w^*$ and $\Gamma^*_{5-15}$ again is to employ the laminar decaying potential vortex as a basis that is adapted to the behavior observed in LES.

Given the assumption that the vortices decay in accordance with the self-similar velocity profiles of the potential vortex, the descent speed can be calculated as a function of vortex spacing and core radius according to

$$w^* = 1 - \exp\left(-1.257 b^2 / r_c^2\right) \tag{12}$$

The relation between descent speed and $\Gamma^*_{5-15}$ is then implicitly given via the core radius by

$$\Gamma^*_{5-15} = \frac{1}{11} \sum_{r=5\,\mathrm{m}}^{15\,\mathrm{m}} 1 - \exp \frac{-1.257 r^2}{r_c^2} \tag{13}$$

Figure 8 illustrates Eq. (13) graphically. Figure 9 shows the relation of $\Gamma^*_{5-15}$ and descent speed for different vortex separations given by Eqs. (12) and (13). Note that this relation is an implicit function of core radius. For aircraft that already have small vortex separations, a slight decrease of $\Gamma^*_{5-15}$ (caused by an increase of core radius) would decrease the descent speed, whereas for large vortex separations, the descent speed would be affected only when $\Gamma^*_{5-15}$ reaches small values, that is, when the core radius is of the order of vortex separation. Comparison with the descent speed observed in the LES baseline case (Fig. 9) indicates that Eqs. (12) and (13) yield a

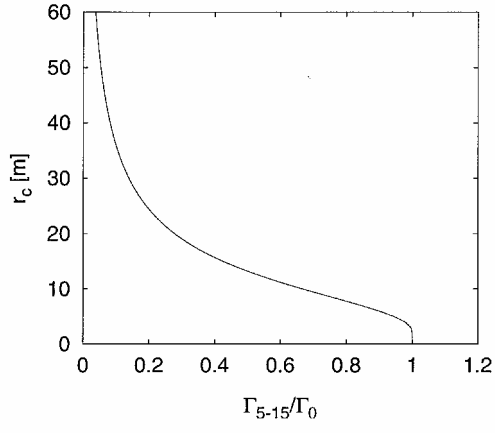


**Fig. 8 Relation of $r_c$ and $\Gamma^*_{5-15}$ for decaying potential vortex.**

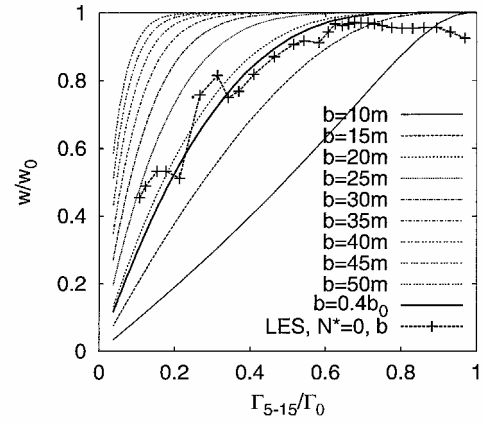


**Fig. 9 Relation of descent speed and $\Gamma^*_{5-15}$ for different vortex separations and LES baseline case,[16] $b_0 = 47$ m.**

useful approximation with an effective vortex spacing of $b = 0.4b_0$. To avoid an iterative solution of Eq. (13) during model predictions, the effective core radii $r_c$ are interpolated as a function of $\Gamma^*_{5-15}$ using a look-up table.

In stably stratified cases, the buoyancy force additionally reduces the descent speed. This effect is not contained in the kinematic approximation given by Eqs. (12) and (13). Therefore, Greene's slightly modified concept of impulse reduction by the buoyancy force[9] is calculated in parallel to the earlier described algorithm to yield a descent speed $w^*_{\mathrm{buoy}} = \Gamma^*_{\mathrm{buoy}}$, where $\Gamma^*_{\mathrm{buoy}}$ results from

$$\frac{\mathrm{d}\Gamma^*_{\mathrm{buoy}}}{\mathrm{d}t^*} = 0.4525 N^{*\sqrt{2}\cdot 2} \Delta z^* \tag{14}$$

The resulting descent speed is then obtained by weighting $w^*$ [from Eq. (12)] with the relative decrease of the descent speed due to buoyancy, $w^*_{\mathrm{buoy}}/w^*_0 = w^*_{\mathrm{buoy}}$, according to

$$w^*_{\mathrm{res}} = w^* w^*_{\mathrm{buoy}} \tag{15}$$

Model results with LES[16] show that the descent speed is underestimated for $N^* < 1$ and overestimated for $N^* > 1$. This is due to a decrease of vortex separation for $N^* < 1$ and an increase of vortex separation for $N^* > 1$. The superscript $\sqrt{2}$ used in Eq. (14) for $N^*$ yields a good correction for the vortex-spacing modified descent speed. The normalized local Brunt–Väisälä frequency is defined as

$$N^* = [g/\Theta_0(\Delta\Theta/\Delta z)]^{\frac{1}{2}} t' \tag{16}$$

The nonlinear dependency of descent rate on circulation gives P2P the following capabilities. 1) It allows for a reduction of circulation without the reduction of the descent rate during the early vortex evolution. Robins et al.[29] show in their case studies that the early trajectories, until the vortices leave a predefined corridor, are best predicted when the descent rate is not reduced by turbulent circulation decay, that is, the descent rate almost retains its theoretical value. 2) It allows for stagnating vortices with nonzero circulation in strongly stably stratified environments. In other models,[9,10] circulation and descent are coupled directly such that both quantities become zero at identical times. 3) It enables rebounding vortices in very strongly stratified environments. Rebound of vortices that is of high relevance for the safety of following aircraft occurs when $w^*_{\mathrm{buoy}}/w^*_0$ becomes negative. All of these features are in accordance with LES data (Fig 10).

The effect of the ground on vortex trajectories is modeled following the approach of Robins et al.[29]. Image vortices are introduced when the primary vortices have reached a height of $1.5b_0$ above ground. At a height of $0.6b_0$, counter-rotating ground effect vortices and their respective image vortices are introduced at an angle of 45 deg inboard below the primary vortices at a distance of $0.4b_0$. Another pair of secondary vortices with images is introduced when the first pair has rotated 180 deg around the primary vortices. The strength of the secondary vortices is a function of the rotation angle

and reaches a maximum of $\Gamma_s^* = 0.4w^*$ after traveling 90 deg. The decay rate is not modified in ground effect because a comparison of different decay models yields only negligible impact on vortex trajectories.

## Probabilistic Approach

Precise deterministic wake vortex predictions are not feasible operationally for several reasons. Primarily, it is the nature of turbulence that deforms and transports the vortices in a stochastic way and leads to considerable spatiotemporal variations of vortex position and strength. Moreover, aircraft parameters, and especially the state of the atmospheric boundary layer with its intrinsic variability, can only be measured or predicted with limited accuracy. Finally, uncertainties with respect to the accuracy of circulation and position derived from lidar measurements add up in a comparison of measurement and prediction. The scatter resulting from all of these factors only allows the prediction of wake vortex behavior within uncertainty bounds and a respective probability.

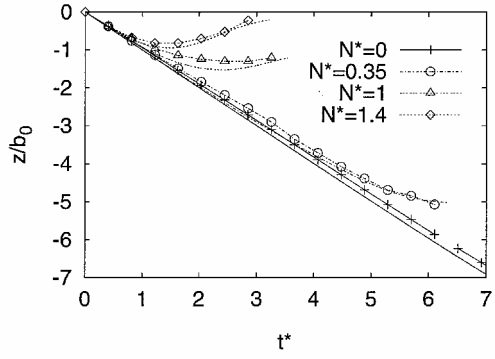


**Fig. 10 Comparison of descent between LES[16] (symbols) and P2P (lines) in quiescent atmosphere with different degrees of stratification.**

P2P uses several components that take into account these uncertainties. Figure 11 shows exemplarily the output of P2P that consists of upper and lower bounds for vertical and lateral position, as well as circulation. Two runs, each with a combination of decay parameters for the upper bound ($T_{2,u}^* = 1.2\,T_2^*$, $\nu_{2,u}^*$) and lower bound ($T_{2,l}^* = 0.8\,T_2^*$, $\nu_{2,l}^*$), vary the onset time of rapid decay and the respective decay rate. For the diffusion phase, no parameter variations are performed because the early wake vortex evolution has no impact on aircraft separations. A constant uncertainty allowance of $0.2\,\Gamma_0^*$ is added to (subtracted from) the upper (lower) curve of circulation evolution. Obviously, only the upper limit of the circulation prediction is of practical significance because operational wake vortex predictions have to be conservative. For vertical and lateral position, an uncertainty allowance of one initial vortex spacing is employed. Additionally, the increased scatter of vortices in turbulent environments is modeled by the assumption that the rms value of ambient turbulence serve as superimposed propagation velocity. When started from the upper (lower) curves for descent rate and lateral displacement that result from decay parameter variations, the final upper (lower) bounding curves for vortex positions are calculated according to

$$y_{u(l)}^*, z_{u(l)}^* = y^*, z^* + (-)\left(1 + \int q^*(z^*)\,\mathrm{d}t^*\right) \qquad (17)$$

The validity of this approach was recently demonstrated for a convective boundary-layer situation.[8] In Fig. 11, the limiting curves

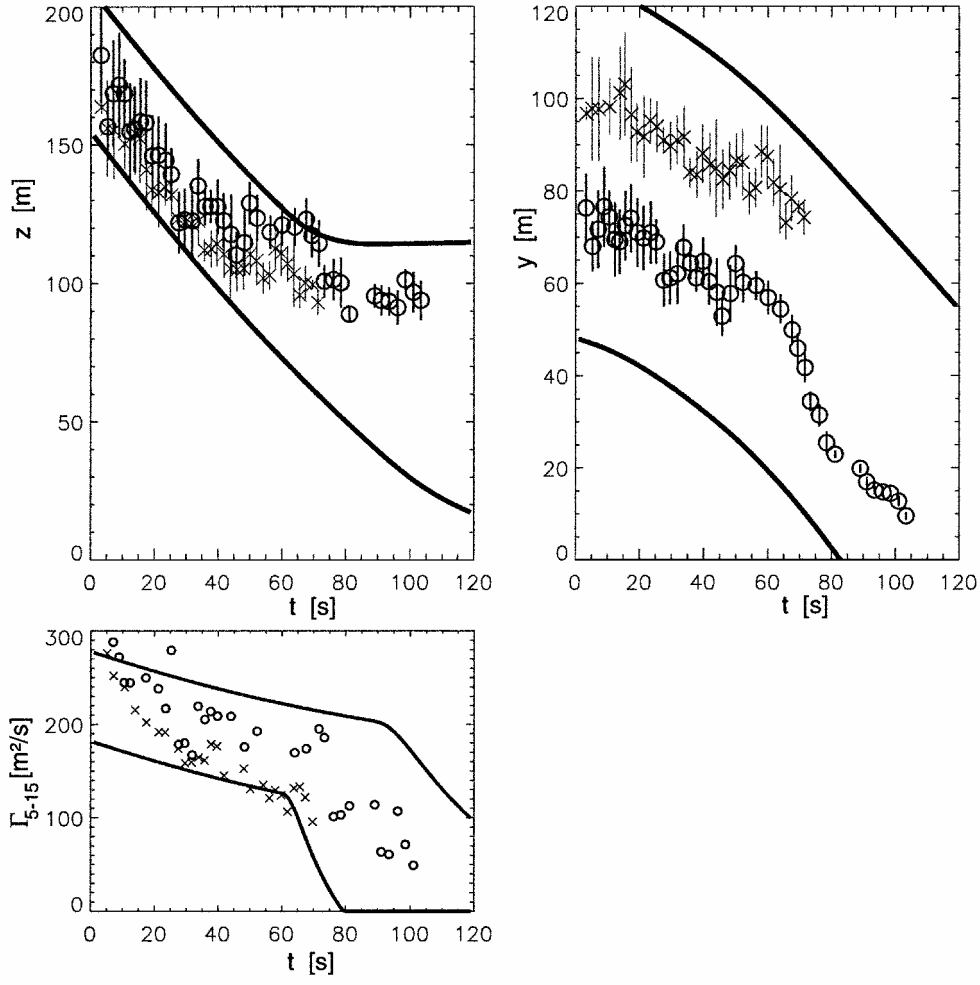


**Fig. 11 Comparison of P2P predictions with lidar observations with error bars, for Memphis[20] case 1282 (B727 aircraft): ——, bounds of expected behavior; ○, port vortex: and ×, starboard vortex.**

enclose almost all measured data. Only some operationally insignificant early circulation values are underestimated. Possibly the early circulation values that considerably exceed the theoretical circulation can be attributed to the rollup process of multiple vortices because the evaluation of lidar spectra, based on the assumption of axisymmetric vortices, employs the product of maximum velocity and distance to the vortex center. As a result, secondary vortices are interpreted as high tangential velocities on large radii, hence, high circulation.

## Application

P2P essentially is designed to predict the bounds of wake vortex behavior in a probabilistic sense. The respective capabilities of P2P will be discussed in detail in another publication. Here, a deterministic version of P2P, where the uncertainty allowances are neglected, is applied to a larger number of Memphis wake vortex measurements.[20]

Obviously, the scatter of individual Memphis circulation data is too large to infer the typical decay characteristics of wake vortices. In particular, lidar measurements often cease at a level of circulation at which the rapid decay would set in, according to LES. A possible explanation is that the associated large-scale deformation and the transition to fully turbulent vortices complicate the evaluation of circulation. Moreover, highly precise lidar measurements in the late (second) phase of complex vortex evolution would render only a little representative data because they represent just a single plane. Only the averaging along many planes would yield meaningful $\Gamma^*_{5-15}$ values.

Therefore, in this section, a statistical approach is followed in which a large number of cases that meet specific criteria[28] are averaged. The resulting mean behavior is discussed to evaluate basic capabilities and properties of the model formulation, in particular, with respect to the two-phase circulation decay. Environmental conditions are classified according to wake vortex behavior classes[30] that are based on a bulk Richardson number[31]

$$Ri_b = N^2 \Big/ \left(\frac{\Delta u}{\Delta z}\right)^2 + \left(\frac{\Delta v}{\Delta z}\right)^2 \tag{18}$$

where the vertical gradients of the mean horizontal wind components are considered in a height interval that ranges from 40 to 200 m. There are 144 cases assigned to the class stable stratification defined by $Ri > 1$ and 138 cases to the class turbulence with $Ri < 0.25$. The eddy dissipation rate is calculated from spectra that are established from 30-min averages of ultrasonic anemometer measurements on a 40-m-high tower. An average Brunt–Väisälä frequency is determined from measurements of potential temperature by soundings of a radio acoustic sounding system and radio sondes. To avoid ground effects, only data of aircraft with a flight altitude above $5b_0$ is used. The initial height of the vortices is taken from beacon altitude.

The deterministic version of P2P applies two sets of decay parameters, $T_2^*$ and $\nu_2^*$, for a given environmental situation. To achieve an appropriate statistical weighting of the resulting predictions, these are varied in 11 consecutive runs in increments of 10% between their upper and lower bounds. The statistics of measurements, on the other hand, are susceptible to the duration of individual measurements and the resulting data mix. To ensure the comparability of measurement and prediction, the predictions are teminated when the magnitude of the last circulation measurement is reached or when the last vertical position is measured, respectively. Without this procedure, which provides an identical data mix in measurement and prediction, the resulting curves deviate substantially. Furthermore, the results are compared to Greene's[9] model that employs measurements of TKE

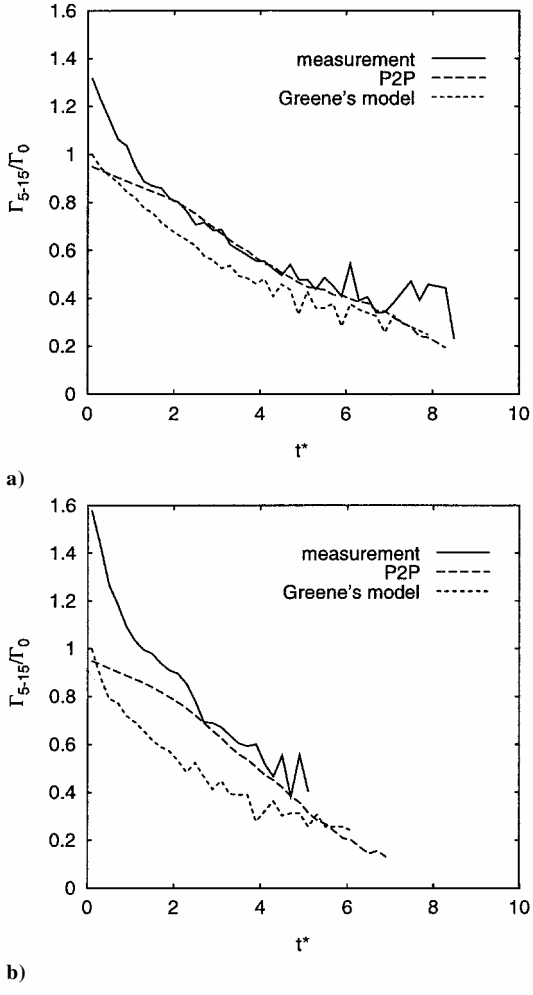


**Fig. 12 Comparison of measured and predicted mean evolution of $\Gamma^*_{5-15}$ in a) stable class (144 cases) and b) turbulent class (138 cases).**

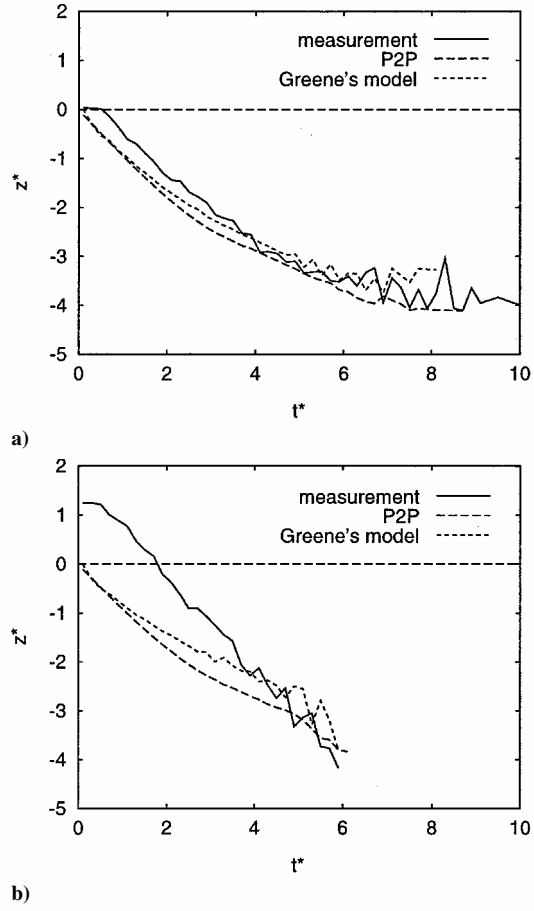


**Fig. 13 Comparison of measured and predicted mean descent in a) stable class and b) turbulent class.**

on the 40-m tower. The constant for turbulent decay is set to 0.41, according to Ref. 32.

Figure 12a demonstates very good agreement between measurements and P2P in the stable class when the initial overestimation of circulation by lidar is neglected. In the turbulent class (Fig. 12b) the overestimation of circulation is even more pronounced and persists longer so that agreement is achieved later. Note that the two-phase decay of P2P is masked completely in the mean evolution of $\Gamma^*_{5-15}$. This implies that the two-phase decay may well be hidden in the scatter of the lidar data (cf. Fig. 11). Greene's[9] model underestimates consistently and nonconservatively the circulation measurements. The measured vertical position shown in Fig. 13a indicates a delayed onset of descent that might reflect the rollup phase of the vortices. Such a delay could easily be implemented in P2P. Later, the descent rate is well predicted by P2P and slightly underestimated by Greene's model. In the turbulent case, the initial height is strongly overestimated for unknown reasons ($z^* = 0$ corresponds to beacon altitude), which makes it difficult to compare descent rates. Currently, P2P is applied to further data sets.[20,33,34]

## Conclusions

A probabilistic real-time wake vortex transport and decay model termed P2P is proposed. Circulation decay and descent rate are parameterized in analogy to the decaying potential vortex. Detailed wake vortex characteristics achieved by high-resolution numerical simulations are transferred to the real-time model by the adjustment of parameters. The deviations between different LES determine the variability of the decay parameters. Circulation decay precedes in two phases, a gradual and a subsequent rapid decay. The respective decay rates are adjusted by an effective viscosity. The introduction of an effective vortex spacing and effective core radii allow the derivation of equations that describe the nonlinear dependence of descent rate and radii-averaged circulation and that reproduce descent characteristics found in LES and measurements. The favorable comparison of a deterministic version of P2P to measurement data has demonstrated the suitability of the two-phase approach. In particular, it is shown that the two-phase decay characteristics are hidden in the mean evolution of averaged measurement data. P2P accounts for all relevant environmental parameters, such as wind, turbulence, stable stratification, and ground proximity, with the exception of shear. It is assumed that the effects of constant background shear are well covered by the probabilistic approach. Because of the high sensitivity of wake vortex behavior on shear layer characteristics, it is believed that the associated complex vortex behavior cannot be predicted reliably in an operational environment. Situations where shear layer effects are not covered by uncertainty allowances have to be diagnosed, and reduced spacing operations must be ruled out.

Although good results have already been achieved without further adjustment of the model, the benefits of P2P will fully appear when a fine-tuning process has been accomplished based on a sufficiently large amount of data. Currently, P2P is applied to different data sets accomplished at Memphis International Airport,[20] Dallas-Fort Worth International Airport, the Aircraft Wake Vortex Prediction and Measurement Campaigns WakeOP at Fairchild-Dornier Airport, Oberpfaffenhofen, Germany, and WakeTOUL at Tarbes Airport, France. However, the quality of measurements used for tuning will affect the magnitude of uncertainty allowances. For example, the distance of the wind measurement site to the considered section of the glide path and the degree of homogeneity of the wind field will have a strong impact on the allowances for vortex dispersion. To achieve maximum accuracy and, consequently, maximum safety and efficiency of a reduced spacing system, a refined tuning process should be conducted for every individual site with its individual peculiarities. Another criterion for maximum operating efficiency is that the probabilities of the predicted confidence intervals should ideally be identical for all operationally relevant phases of vortex evolution. Therefore, a variable formulation of the currently static uncertainty allowances may be useful. Further refinements of P2P could be achieved by applying boundary-layer scaling laws to derive an anisotropic, height-dependent parameterization of turbulence-driven spreading of the confidence intervals. The scaling laws could be based on the diagnosed type of atmospheric boundary layer.

## Acknowledgments

Thanks are extended to many friends and colleagues, such as Alexandre Corjon, Michael Frech, Thomas Gerz, and George Greene, who supported the current work by fruitful discussions and cooperation. In particular, Tobias Zinner for the Memphis data analysis, Fred Proctor and George Switzer for providing the large-eddy simulation data, and Robert Robins and Donald Delisi for their hospitality, support, and the ground effect model are acknowledged. The supply of the Memphis database by NASA Langley Research Center is greatly acknowledged.

## References

[1]Gerz, T., Holzäpfel, F., and Darracq, D., "Commercial Aircraft Wake Vortices," *Progress in Aerospace Sciences*, Vol. 38, No. 3, 2002, pp. 181–208.

[2]Hallock, J. N., Greene, G. C., and Burnham, D. C., "Wake Vortex Research—A Retrospective Look," *Air Traffic Control Quarterly*, Vol. 6, No. 3, 1998, pp. 161–178.

[3]Gurke, T., and Lafferton, H., "The Development of the Wake Vortex Warning System for Frankfurt Airport: Theory and Implementation," *Air Traffic Control Quarterly*, Vol. 5, No. 1, 1997, pp. 3–29.

[4]Le Roux, C., and Corjon, A., "Wake Vortex Advisory System Implementation at Orly Airport for Departing Aircraft," *Air Traffic Control Quarterly*, Vol. 5, No. 1, 1997, pp. 31–48.

[5]Hinton, D. A., "An Aircraft Vortex Spacing System (AVOSS) for Dynamical Wake Vortex Spacing Criteria," *The Characterization and Modification of Wakes from Lifting Vehicles in Fluids*, CP-584, AGARD, 1996, pp. 23.1–23.11.

[6]de Bruin, A., "Wake Vortex Evolution and Encounter (WAVENC)," *AIR and SPACE EUROPE*, Vol. 2, No. 5, 2000, pp. 84–87.

[7]Frech, M., "VORTEX-TDM—A Parameterized Wake Vortex Transport and Decay Model and its Meteorological Input Data Base," DFS Deutsche Flugsicherung, Offenbach, Germany, March 2001.

[8]Frech, M., and Holzäpfel, F., "A Probabilistic Prediction Scheme for Wake Vortex Evolution in a Convective Boundary Layer," *Air Traffic Control Quarterly*, Vol. 10, No. 1, 2002, pp. 23–41.

[9]Greene, G. C., "An Approximate Model of Vortex Decay in the Atmosphere," *Journal of Aircraft*, Vol. 23, No. 7, 1986, pp. 566–573.

[10]Corjon, A., and Poinsot, T., "Vortex Model to Define Safe Aircraft Separation Standards," *Journal of Aircraft*, Vol. 33, No. 3, 1996, pp. 547–553.

[11]Sarpkaya, T., "New Model for Vortex Decay in the Atmosphere," *Journal of Aircraft*, Vol. 37, No. 1, 2000, pp. 53–61.

[12]Sarpkaya, T., Robins, R. E., and Delisi, D. P., "Wake–Vortex Eddy-Dissipation Model Predictions Compared with Observations," *Journal of Aircraft*, Vol. 38, No. 4, 2001, pp. 687–692.

[13]Jackson, W., Yaras, M., Harvey, J., Winckelmans, G., Fournier, G., and Belotserkovsky, A., "Wake Vortex Prediction—An Overview," Transport Canada, Rept. TP 13629E, Montreal, March 2001.

[14]Kantha, L. H., "Empirical Model of Transport and Decay of Wake Vortices Between Parallel Runways," *Journal of Aircraft*, Vol. 33, No. 4, 1996, pp. 752–760.

[15]Mokry, M., "Numerical Simulation of Aircraft Trailing Vortices Interacting with Ambient Shear or Ground," *Journal of Aircraft*, Vol. 38, No. 4, 2001, pp. 636–643.

[16]Holzäpfel, F., Gerz, T., and Baumann, R., "The Turbulent Decay of Trailing Vortex Pairs in Stably Stratified Environments," *Aerospace Science and Technology*, Vol. 5, No. 2, 2001, pp. 95–108.

[17]Proctor, F. H., and Switzer, G. F., "Numerical Simulation of Aircraft Trailing Vortices," 9th Conf. on Aviation, Range and Aerospace Meteorology, Paper 7.12, American Meteorology Society, Orlando, Florida, Sept. 2000, pp. 511–516.

[18]Spalart, P. R., "Airplane Trailing Vortices," *Annual Review of Fluid Mechanics*, Vol. 30, 1998, pp. 107–138.

[19]Holzäpfel, F., Hofbauer, T., Gerz, T., and Schumann, U., "Aircraft Wake Vortex Evolution and Decay in Idealized and Real Environments: Methodologies, Benefits and Limitations," *Advances in LES of Complex Flows*, edited by R. Friedrich and W. Rodi, Vol. 65, Fluid Mechanics and its Applications, Kluwer Academic, Dordrecht, The Netherlands, 2002, pp. 293–309.

[20]Campbell, S. D., Dasey, T. J., Freehart, R. E., Heinrichs, R. M., Matthews, M. P., Perras, G. H., and Rowe, G. S., "Wake Vortex Field Measurement Program at Memphis, TN, Data Guide," Lincoln Lab., Project Rept. NASA/L-2, Massachusetts Inst. of Technology, Cambridge, MA, Jan. 1997.

[21]Hinton, D. A., and Tatnall, C. R., "A Candidate Wake Vortex Strength Definition for Application to the NASA Aircraft Vortex Spacing System (AVOSS)," NASA TM 110343, Sept. 1997, p. 32.

[22]Zierep, J., "Ähnlichkeitsgesetze und Modellregeln der Strömungslehre," Braun, Karlsruhe, Germany, 1982.

[23]Sarpkaya, T., "Decay of Wake Vortices of Large Aircraft," *AIAA Journal*, Vol. 36, No. 9, 1998, pp. 1671–1679.

[24]Holzäpfel, F., Hofbauer, T., Darracq, D., Moet, H., Garnier, F., and Ferreira Gago, C., "Analysis of Wake Vortex Decay Mechanisms in the Atmosphere," *Aerospace Science and Technology* (submitted for publication); also 3rd ONERA–DLR Aerospace Symposium, S3–2, Paris, June 2001, p. 10.

[25]Jeanmart, H., and Winckelmans, G. S., "VLES of Aircraft Wake Vortices in a Turbulent Atmosphere: A Study of Decay," *Advances in LES of Complex Flows*, edited by R. Friedrich and W. Rodi, Vol. 65, Fluid Mechanics and its Applications, Kluwer Academic, Dordrecht, The Netherlands, 2002, pp. 311–326.

[26]Vaughan, J. M., Brown, D. W., Constant, G., Eacock, J. R., and Foord, R., "Structure, Trajectory and Strength of B747 Aircraft Wake Vortices Measured by Laser," *The Characterisation and Modification of Wakes from Lifting Vehicles in Fluids*, CP-584, AGARD, 1996, pp. 10-1–10-10.

[27]Shen, S., Ding, F., Han, J., Lin, Y.-L., Arya, S. P., and Proctor, F. H., "Numerical Modeling Studies of Wake Vortices: Real Case Simulations," AIAA Paper 99-0755, Jan. 1999.

[28]Zinner, T., "Analyse und Modellierung des Verhaltens von Flugzeugwirbelschleppen in der Atmosphäre," Diploma Thesis, Inst. of Atmospheric Physics, DLR, German Aerospace Research Center, Oberpfaffenhofen, Germany, 2001.

[29]Robins, R. E., Delisi, D. P., and Greene, G. C., "Algorithm for Prediction of Trailing Vortex Evolution," *Journal of Aircraft*, Vol. 38, No. 5, 2001, pp. 911–917.

[30]Frech, M., and Zinner, T., "The Concept of Wake Vortex Behaviour Classes and an Analysis of the ICAO Separation Distances," *Journal of Aircraft* (submitted for publication).

[31]Stull, P. R., "An Introduction to Boundary Layer Meteorology," *Atmospheric Sciences Library*, Kluwer Academic, Dordrecht, The Netherlands, 1988, pp. 175–180.

[32]Robins, R. E., and Delisi, D. P., "Further Development of a Wake Vortex Predictor Algorithm and Comparisons to Data," AIAA Paper 99-0757, Jan. 1999.

[33]Dasey, T. J., Cole, R. E., Heinrichs, R. M., Matthews, M. P., and Perras, G. H., "Aircraft Vortex Spacing System (AVOSS) Initial 1997 System Deployment at Dallas/Ft. Worth (DFW) Airport," Lincoln Lab., Project Rept. NASA/L-3, Massachusetts Inst. of Technology, Cambridge, MA, July 1998.

[34]Gerz, T., "Wake Vortex Prediction and Observation: Towards an Operational System," 3rd ONERA–DLR Aerospace Symposium, S1–3, Paris, June 2001, p. 10.

[5]

# Strategies for Circulation Evaluation of Aircraft Wake Vortices Measured by Lidar

F. Holzäpfel, T. Gerz, F. Köpp, E. Stumpf, M. Harris, R.I. Young, A. Dolfi-Bouteyre

Journal of Atmospheric and Oceanic Technology, 2003

Volume 20, Number 8, Pages 1183–1195

# Strategies for Circulation Evaluation of Aircraft Wake Vortices Measured by Lidar

FRANK HOLZÄPFEL, THOMAS GERZ, AND FRIEDRICH KÖPP

*Institut für Physik der Atmosphäre, DLR, Oberpfaffenhofen, Germany*

EIKE STUMPF

*Institut für Aerodynamik und Strömungstechnik, DLR, Braunschweig, Germany*

MICHAEL HARRIS AND ROBERT I. YOUNG

*Sensors and Electronics Division, QinetiQ, Malvern, Worcestershire, United Kingdom*

AGNÈS DOLFI-BOUTEYRE

*Applied and Theoretical Optics Department, ONERA, Palaiseau, France*

(Manuscript received 18 April 2002, in final form 15 October 2002)

ABSTRACT

An assessment of different methods for circulation evaluation from lidar measurement data of aircraft wake vortices is performed. The surface integral of vorticity serves as baseline case that is compared to a method that evaluates the lidar line-of-sight velocity midway between the vortices and to another method that calculates radii averages of circulations derived from tangential velocities. Systematic deviations from nominal circulation are discussed based on analytical vortices. High-resolution numerical simulation data are applied to perform virtual lidar measurements that reproduce, explain, and quantify (i) the frequently observed initial overestimation of circulation and (ii) the scatter of circulation data caused by the genuine variability of wake vortices in the atmospheric boundary layer. The theoretically derived characteristics of the different evaluation methods are verified against lidar data recorded by several lidar teams during the Wake Vortex Forecasting and Measuring Campaign at Oberpfaffenhofen (WakeOP), performed in spring 2001 at Fairchild Dornier Airport in Oberpfaffenhofen, Germany.

## 1. Introduction

As an unavoidable consequence of lift, aircraft generate counterrotating pairs of trailing vortices (cf. Fig. 1), which constitute a potential hazard to following aircraft. The resulting separation distances between consecutive aircraft contribute substantially to capacity shortages of congested airports. Both the complexity of wake vortex physics and the limited experimental access impede comprehensive analyses of wake vortex physics that would allow the mitigation of wake vortex restrictions under appropriate conditions (Gerz et al. 2002). In particular, in laboratory experiments the far-field evolution of wake vortices is not accessible, and in both laboratory experiments and numerical simulations the achievable Reynolds numbers are far from reality.

The only and indispensable access to real wake vortex behavior is provided by lidar measurement techniques that trace full-scale wake vortices in the free atmosphere. Light detection and ranging (lidar) operates by transmitting a laser beam and coherently detecting the radiation backscattered by aerosols. The spectrum of Doppler shifts in the frequency of the backscattered radiation is analyzed to give the line-of-sight (LOS) velocity component of the aerosols and, hence, the air motion, along the beam. From the LOS velocities the circulation of the vortices can be deduced. Details of lidar technology can be found elsewhere (e.g., Constant et al. 1994; Harris et al. 2000).

Circulation constitutes the most important parameter for wake vortex characterization since it describes vortex strength in a form that is correlated with effects of potential wake encounters (Hinton and Tatnall 1997). However, the evaluation of circulation from lidar data involves considerable complications. First, environmental conditions that can neither be controlled nor reproduced have a strong impact on vortex evolution (Spalart 1998; Holzäpfel et al. 2003). Favorable neutral envi-

*Corresponding author address:* Dr. Frank Holzäpfel, Institut für Physik der Atmosphäre, DLR, Oberpfaffenhofen D-82234, Weßling, Germany.
E-mail: Frank.Holzaepfel@dlr.de

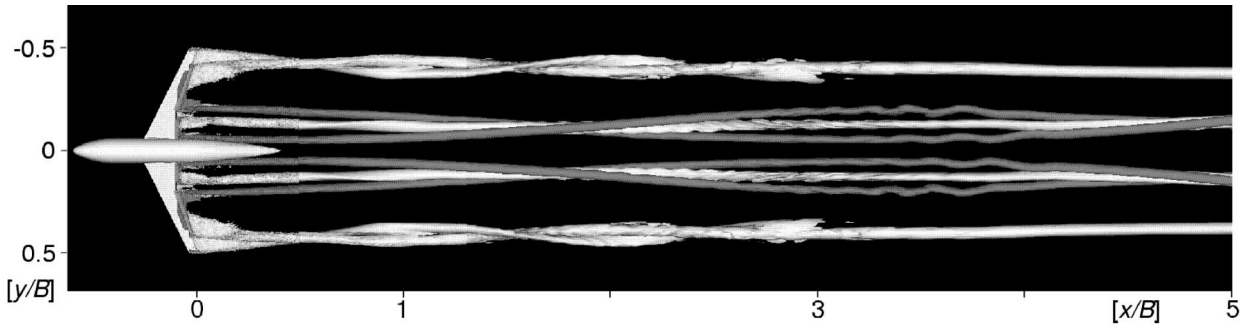


FIG. 1. View from below on simulated near-field wake evolution up to 5 spans behind wing tips of an aircraft in high-lift configuration. Vortex topology illustrated by isosurfaces of vorticity ($\omega_x = \pm 200\ s^{-1}$, gray isosurfaces indicate counterrotating vorticity).

ronmental conditions with minor influences on vortex evolution, that is, weak winds, low turbulence, and neutral temperature stratification, prevail rarely. As a consequence, one also needs to document environmental conditions with considerable extra measurement effort and is forced to investigate trailing vortex behavior within the full complexity of environmental effects. Second, unlike in the case for single vortices where the circulation converges to a definite value at large radii, the proximity of a neighboring vortex affects circulation values wherefore the circulation of vortex pairs strongly depends on the method of its evaluation (Campbell et al. 1997; Harris et al. 2000).

The investigations in the current manuscript are mostly restricted to kinematic effects of wake vortex characteristics on circulation evolution; aspects of lidar technology are neglected. Three different methods to derive circulation are applied to a pair of Lamb–Oseen vortices, to large eddy simulation (LES) results of wake vortices that evolve in a convectively driven atmospheric boundary layer (Holzäpfel et al. 2000), and to simulation results dealing with the roll-up of multiple vortices behind an aircraft in high-lift configuration (Stumpf 2002). The aim of the investigation is to understand the implications of the respective evaluation methods and to serve as a guideline for the proper choice of an evaluation method for circulation based on lidar data. For this purpose (i) the systematic deviation of the circulation derived with the different methods from the root circulation is discussed, (ii) the cause of the frequently observed initial overestimation of circulation is revealed, and (iii) the degree of scatter of circulation data is considered that is due to the genuine variability of wake vortices in the atmospheric boundary layer. Finally, the theoretically derived characteristics of the different evaluation methods are verified against lidar data recorded during the Wake Vortex Forecasting and Measuring Campaign at Oberpfaffenhofen (WakeOP) performed in spring 2001 at Fairchild Dornier Airport in Oberpfaffenhofen, Germany.

## 2. Methods to evaluate circulation

The circulation $\Gamma$ around a plane closed contour $C$ is defined as the line integral of the tangential velocity component, $v_t$:

$$\Gamma \equiv \oint_C v_t\, ds = \int_A \omega\, dA. \tag{1}$$

Employing the Stokes theorem, circulation can equally be expressed by the integral of vorticity $\omega$ over the surface $A$. For circular integration areas, Eq. (1) can be expressed by

$$\Gamma(r) = \int_0^{2\pi} \int_0^r \omega(r, \varphi) r\, dr\, d\varphi, \tag{2}$$

where $r$ denotes the radius and $\varphi$ is the azimuthal angle in a cylindrical polar coordinate system. Equations (1) and (2) can only be applied if two-dimensional velocity data are available. For a single, axisymmetric vortex, circulation on a given radius can be simply obtained from the tangential velocity at that radius according to

$$\Gamma(r) = 2\pi r v_t(r). \tag{3}$$

One appropriate method to calculate circulation of wake vortices is to average circulation over $n_r$ radii in a radii interval, $r_l \le r_i \le r_u$, with a lower bound $r_l$ and an upper bound $r_u$, according to

$$\Gamma_{r_l - r_u} = \frac{1}{n_r} \sum_{i=l}^{u} \Gamma(r_i), \tag{4}$$

where the increment of subsequent radii typically is set to 1 m. For lidar data evaluation it is assumed that the maximum LOS velocity corresponds to the tangential velocity $v_t$ of the respective vortex, and Eq. (3) is used to determine the circulations that are averaged according to Eq. (4). It is advantageous to perform the averaging for both flanks of the vortex (cf. Fig. 2), that is, for opposite directions of the tangential velocity, because then the influence of ambient wind and self-induced descent speed are compensated automatically. This approach is termed method $v_t$.

Radii-averaged circulation according to Eq. (4) can equally be determined from two-dimensional velocity data employing Eq. (2). This is called method $\omega$. Since, however, the vorticity in Eq. (2) cannot be derived from lidar data, method $\omega$ is only used as a reference for

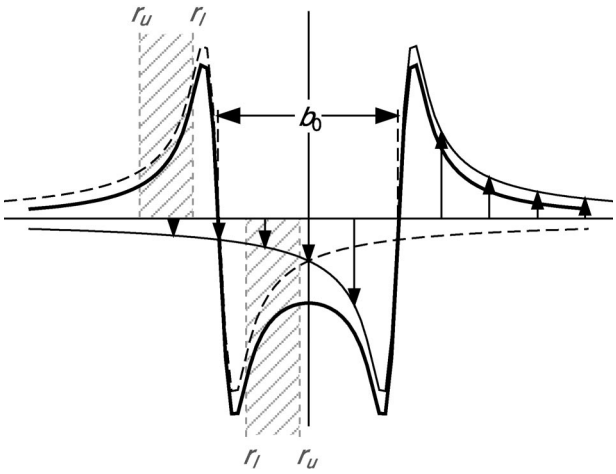


FIG. 2. Sketch of the vertical velocity profiles of two Lamb–Oseen vortices separated by $b_0$ (fine lines) and corresponding vertical velocity envelope of the trailing vortex pair (bold line). Radii interval, $r_l \leq r \leq r_u$, used for averaging of circulation in method $v_t$ indicated for left vortex in gray.

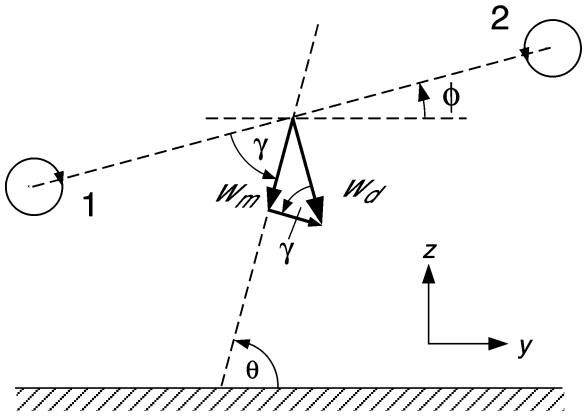


FIG. 3. Sketch to illustrate the definition of lidar scan angle $\theta$, vortex tilt angle $\phi$, effective observation angle $\gamma$, and the coordinate system used in the current article. The axial direction $x$ points against the flight direction.

circulations evaluated from virtual lidar measurements in sections 4 and 5.

For methods $v_t$ and $\omega$, the effect of the neighboring vortex should be restricted by limiting $r_u$ at most to half of the vortex spacing, $b_0/2$. This limitation also reduces disturbing effects of secondary vortices, ambient turbulence, and baroclinic vorticity. The lower limit $r_l$ should be set well above the core radius. Including radii of the order of the core radius and below would decrease the resulting circulation unnecessarily. Furthermore, velocities at small radii are difficult to measure by lidar due to the smaller volume of scatterers. The basic benefit of methods $v_t$ and $\omega$ is that the averaging of $\Gamma$ over a radii interval reduces the scatter in turbulent vortices and, thus, also enables estimations of disintegrating vortices. The radii-averaged circulation definition has a good potential as a measure for vortex strength in reduced spacing operations because it correlates well with hazardous effects induced from potential wake encounters (Hinton and Tatnall 1997).

The downdraft method $w_d$ proposed by Harris et al. (2000) calculates circulation from the downdraft velocity midway between the vortices, $w_d$, according to

$$\Gamma_d = \pi w_d b_0/2. \tag{5}$$

For a pair of undisturbed Lamb–Oseen vortices, $\Gamma_d$ differs negligibly from the root circulation. An advantage of this method is the high lidar signal-to-noise ratio that results from the great volume of air moving near the downdraft velocity midway between the vortices. The effects of crosswind $v$, vertical wind $w$, lidar scan angle $\theta$, and vortex tilt angle $\phi$ on the measured downdraft velocity $w_m$ can be compensated according to

$$w_d = \frac{w_m + v\cos(\theta) - w\sin(\theta)}{\sin(\theta - \phi)}. \tag{6}$$

Figure 3 illustrates that the lidar scan angle and vortex tilt angle can be combined to define an effective lidar observation angle, $\gamma = \theta - \phi$, which denotes the angle between the line that connects the vortex centers and the lidar scan direction. Figure 3 also describes the coordinate system used in this article.

## 3. Analytical considerations

This section aims at illustrating the effects of evaluation methods $v_t$ and $w_d$, averaging interval, and observation angle on the obtained results in circulation. For this purpose it is assumed that an ideal continuous-wave lidar records exact maximum LOS velocities of analytically given wake vortices. These consist of the superposition of two Lamb–Oseen vortices where the tangential velocity profile of one vortex, $v_t(r)$, is given by

$$v_t(r) = \frac{\Gamma_0}{2\pi r}\left(1 - \exp\frac{-1.26r^2}{r_c^2}\right) \tag{7}$$

with a core radius of $r_c = 4$ m, a vortex separation $b_0 = 23.5$ m, and a root circulation $\Gamma_0 = 283$ m$^2$ s$^{-1}$. Figure 2 sketches the respective profiles of the vertical velocity component. It is assumed that the trends observed in our study would also occur for different vortex models. The observation angle of the lidar is kept constant during measurements—an approximation that corresponds to ''frozen'' vortex pairs drifting through the lidar beam. We refer to Campbell et al. (1997) for a similar discussion of the effects of averaging interval and observation angle pertaining to method $v_t$.

For the following considerations the absolute value of $\Gamma_0$ is irrelevant (we employ circulations normalized by $\Gamma_0$ where the normalization is indicated by an asterisk). As a baseline case the radii-averaged circulation uses a lower bound of 5 m and an upper bound of 11 m. To demonstrate the effects of the chosen averaging

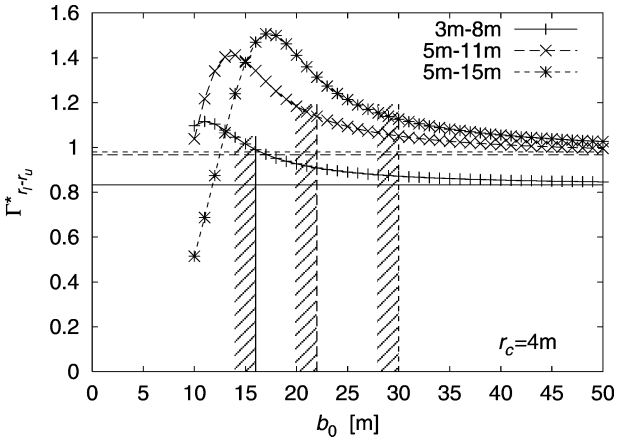


FIG. 4. Here $\Gamma^*_{r_l-r_u}$ determined according to method $v_t$ for a pair of Lamb–Oseen vortices as a function of vortex spacing $b_0$, and for three different averaging intervals. The values of the corresponding single vortices are denoted by horizontal lines. Hatched lines indicate applicable lower boundaries for $b_0$.

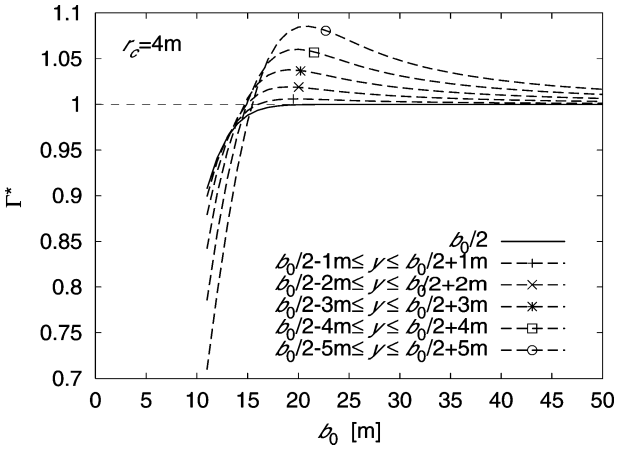


FIG. 5. Circulation determined according to method $w_d$ for a pair of Lamb–Oseen vortices as a function of vortex spacing and averaging length along downdraft velocities.

interval, further results with 3–8- and 5–15-m intervals are included.

### *a. Vertically viewing lidar*

We now restrict the analysis to vertical observation angles; hence, only vertical velocities are measured. Figure 4 depicts the influence of the vortex spacing on normalized circulation obtained by method $v_t$ for three different radii averages. For a singular vortex, $\Gamma^*_{3-8}$, $\Gamma^*_{5-11}$, and $\Gamma^*_{5-15}$ amount to 0.833, 0.967, and 0.979, respectively (horizontal lines). This underestimation of the root circulation is caused by the decreasing circulations on radii smaller than $2r_c$ [at about $2r_c$ the Lamb–Oseen vortex attains the potential flow with $\Gamma(r) = \Gamma_0$]. However, when we apply the analysis to a vortex pair, we find that $\Gamma^*_{5-11}$ and $\Gamma^*_{5-15}$ are overestimated. Figure 2 indicates that the neighboring vortex induces superimposed downward-directed velocities in the averaging interval. In the downwash region the superimposed velocities cause an overestimation of circulation that dominates the weaker underestimation induced in the upward-directed vortex flow. An average over radii between 3 and 8 m, on the other hand, nevertheless underestimates the circulation for $b_0 > 16$ m, since $\Gamma(r)$ in this case is always below $\Gamma_0$.

It becomes evident that for a given vortex spacing the obtained circulation values increase with the upper limit of the averaging interval. That upper limit further dictates the lower limit for vortex spacing (which is twice $r_u$) for which $\Gamma^*_{r_l-r_u}$ can be applied without inclusion of velocities beyond the midpoint. (Therefore, the parts of the curves that fall below those minimum vortex spacings are not discussed.) As an exemplary result we find a maximum overestimation of $\Gamma^*_{5-11} = 1.138$ at the respective lower limit of $b_0 = 22$ m. At $b_0 = 47$ m both effects, the underestimation of the circulation for a singular vortex and the overestimation caused by the neighboring vortex, compensate each other such that $\Gamma^*_{5-11} = 1$.

Circulations determined by the downdraft method $w_d$ as a function of vortex spacing are shown in Fig. 5. Measuring exactly at the midpoint between both vortices (curve $b_0/2$), the normalized circulation attains a value of 1 at $b_0 = 20$ m ($b_0/r_c = 5$). Since the velocities in the downdraft region usually are not smooth, the circulation scatter may be reduced by calculating $w_m$ as an average over laterally adjacent velocities. However, this averaging also overestimates circulation (when $b_0 > 16$ m), since method $w_d$ employs the local minimum velocity and averaging and, thus, includes higher neighboring $w_d$ values (cf. Fig. 2). (When $b_0$ drops below 16 m the overestimation turns into an underestimation because for $b_0/r_c < 4$ lower velocities from the vortex core region are affecting the evaluation.) For vortex spacings of $b_0/r_c > 4$, which in general prevail, we learn that averaging causes an overestimation of circulation that increases with the averaging length and decreases with increasing $b_0/r_c$. For example, averaging along a 2-m (4 m) section causes a maximum overestimation of 0.6% (1.9%) of circulation.

### *b. Oblique viewing lidar*

We now generalize our analysis and allow our ideal lidar to view at angles $\gamma$ between 90° and 45° (again with fixed beam, no scanning). Figure 6 depicts the actual positions where the continuous-wave lidar detects the maximum velocity values along its LOS in a trailing vortex pair. For a single vortex, measurements at an oblique view will not deviate from that at a vertical view as long as the vortex is axisymmetric.

For vertical observation directions ($\gamma = 90°$) the figure corroborates that the LOS velocity maxima are situated on a horizontal line. For observation angles below 90° the actual positions of the measured maximum LOS

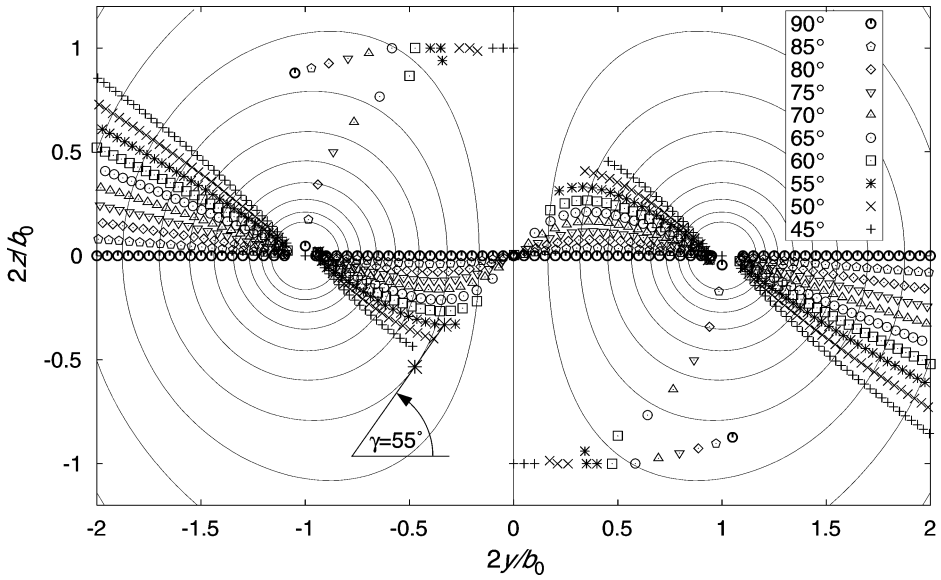


FIG. 6. Actual positions of LOS velocity maxima for different observation angles $\gamma$. Wake vortex topology is illustrated by isolines of the streamfunction. Enlarged asterisks indicate exemplarily the deviation of the actual position of the LOS velocity maximum (small asterisk) and the respective nominal position that would be situated tangent to an isoline of the streamfunction (large asterisk) for $\gamma = 55°$.

velocities deviate from their nominal locations: now the lines of maximum LOS velocity position are curved. The curvature increases with increasing distance to the vortex centers and becomes strongest in the downdraft region where the influence of the neighboring vortex is most prominent.

In the regions around the vortex cores, where the rotational velocities approach zero, even the ideal lidar applied to analytical vortices finds positions with higher LOS velocities far behind or in front of the vortex centers. However, these outliers, which are found for all observation angles, are of no relevance for the evaluation of circulation, because the core region is excluded by the choice of $r_l$.

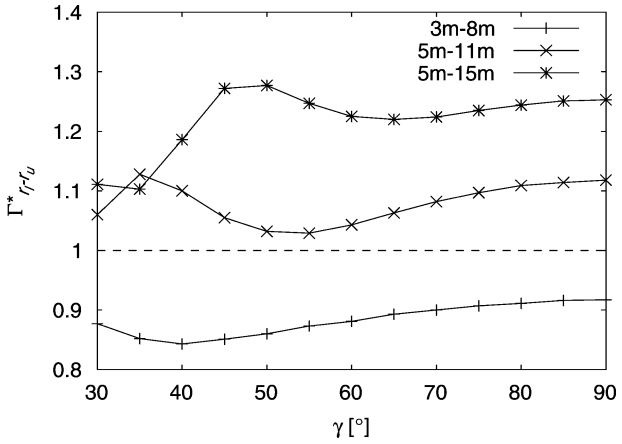


FIG. 7. Here $\Gamma^*_{r_l-r_u}$ determined as a function of observation angle $\gamma$ for method $v_t$ and three different averaging intervals, $r_l$–$r_u$, with $b_0 = 23.5$ m and $r_c = 4$ m.

Figure 7 shows circulations determined with method $v_t$ for different observation angles and radii intervals. The overestimation of $\Gamma^*_{5-11}$ at $\gamma = 90°$ decreases gradually from 1.118 to a minimum of 1.029 at $\gamma = 55°$, then it rises again to a maximum at $\gamma = 35°$, followed by a sharp decline. The overestimation declines generally for angles that deviate from 90° because the contribution of the velocities that are induced by the neighboring vortex decreases with decreasing observation angle: to first order, only the induced vertical velocity component contributes to the overestimation, whereas the induced horizontal velocity component has different signs on the different sides of the vortex core and therefore is compensated in the integration.

It is worthwhile to note that for geometrical reasons the LOS velocities of the adjacent vortex are included in the circulation computation when $\gamma < \gamma_t = \arcsin(2r_u/b_0)$. Then the detected maximum LOS velocity position ''jumps,'' for example, from the left to the right vortex (cf. Fig. 6). For the current parameters ($r_u = 11$ m, $b_0 = 23.5$ m), $\gamma_t$ is 70°. However, the overestimation of $\Gamma^*_{5-11}$ grows from its minimum only again when $\gamma <$ 55° (instead of 70°) because then the contribution of LOS velocities beyond the separating symmetry line $y = 0$ dominates the decreasing overestimation caused by the decreasing observation angles. For observation angles below 35°, the integration domain also includes the decreasing rotational velocities in the adjacent vortex core region and, hence, $\Gamma^*_{5-11}$ decreases again. Figure 7 finally shows that the discussed characteristics of the curve for $\Gamma^*_{5-11}$ are also found but shifted to higher (lower) observation angles when $r_u$ is increased (decreased).

Figure 6 indicates that the actual position of the LOS

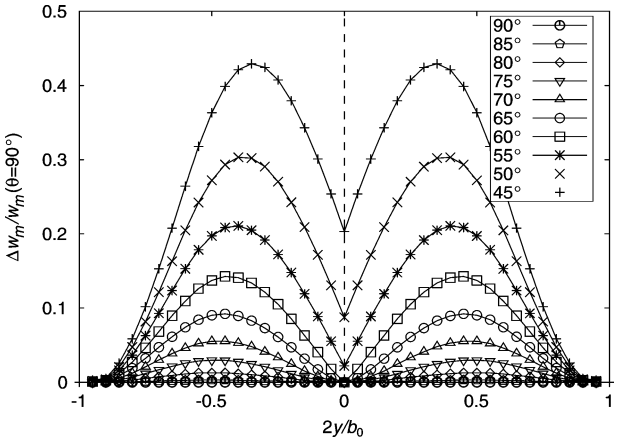


FIG. 8. Relative deviation of LOS velocity maxima (for arbitrary observation angles $\gamma$) from vertical velocities ($\gamma = 90°$) in the downdraft region. LOS velocities are already translated into vertical velocities according to Eq. (6).

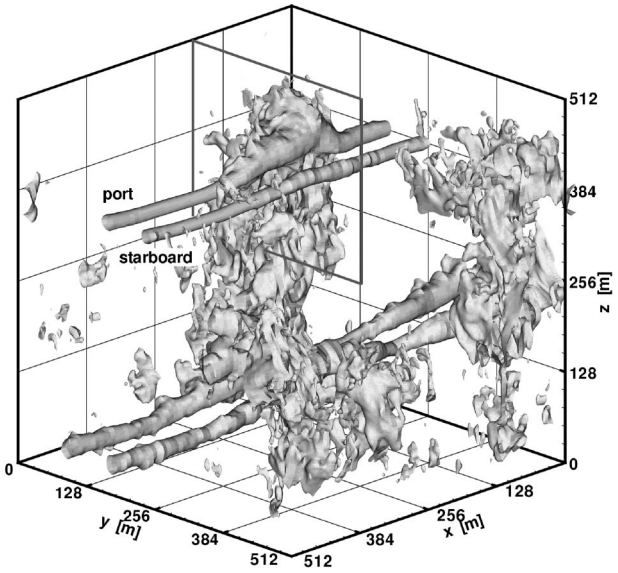


FIG. 9. Isosurfaces of the positive vertical velocity value, $w = 2$ m s$^{-1}$, of the evolving convective boundary layer with three pairs of 5-s-old wake vortices. Plane $x = 192$ m analyzed in Figs. 10 and 11 indicated by gray rectangle.

velocity maximum that is attributed to the midpoint downdraft velocity (for method $w_d$) is situated considerably apart from the midpoint position for $\gamma < 60°$ (the asterisk is the first symbol that does not appear at the midpoint position). As a consequence, the corresponding velocities are adulterated. In Fig. 8 the relative deviations of the downdraft velocities $w_d$ are plotted for the different observation angles where the LOS velocities $w_m$ are already translated into downdraft velocities $w_d$ according to Eq. (6). Figure 8 reveals a considerable excess of $w_d$ at $y = 0$ and, consequently, an overestimation in circulation when $\gamma < 60°$. A closer inspection yields the minor relative error of 0.8% at $\gamma_{\min} = 57°$. If the downdraft velocity is calculated as an average of neighboring positions in order to smooth circulation scatter, overestimations of downdraft velocities occur already for $\gamma > \gamma_{\min}$. These deviations again are caused by the offset between nominal and actual positions of the maximum LOS velocities (see Fig. 6).

## 4. Turbulent environment

In this section we investigate how the vortex evolution in an inhomogeneous turbulent environment affects circulation measurements by lidar. For this purpose an LES of wake vortices in an evolving convectively driven atmospheric boundary layer (Holzäpfel et al. 2000) is analyzed. The LES was performed in a domain with a uniform grid of size $L_x = L_y = L_z = 512$ m. The convective boundary layer simulation was driven by a constant vertical heat flux at the lower surface and three wake vortex pairs were superimposed on the turbulent flow field after the evolving convective boundary layer was well established. Figure 9 illustrates the interaction of convective cells and 5-s-old wake vortices in a perspective view of an isosurface of the upward-directed velocity $w = 2$ m s$^{-1}$. The LES data are rescaled such that the dimensions of the vortices correspond to the vortices in sections 3 and 6. The rms value of the fluctuation velocities of the modeled boundary layer is $q = 1$ m s$^{-1}$, which corresponds to a normalized value of $q^* = q/w_0 = 0.54$, where $w_0$ denotes the initial descent speed of the vortices.

The LES data are used to simulate observations of the upper-left vortex pair by an ideal, vertically viewing lidar. It is assumed that the maximum and minimum velocities of the LES data field in a height interval ranging from 200 to 500 m above ground correspond to the maximum and minimum velocities derived from the spectra of a continuous-wave heterodyne lidar. This implies the following assumptions and simplifications. The angle variation of the scanning lidar and the resulting trigonometrics are neglected for the sake of simplicity. The range resolution always includes the complete vortices with an equal weighting of measured velocities. The velocity maxima and minima do not include the possible biasing effect that can be caused in practice by spectral spreading due to time series windowing (Harris et al. 2000; Campbell et al. 1997). A single lidar scan detects instantaneous velocity data; that is, there is no development of the velocity field during one scan.

The resulting profiles of vertical velocities in a plane at $x = 192$ m (denoted by the rectangle in Fig. 9) are plotted in Fig. 10 in increments of 5 s. This section of the vortices is placed on the shoulder of an updraft and thus is exposed to strong lateral gradients of vertical wind that cause pronounced vortex tilting. The effect of the updraft causes a clearly visible variation of the velocity maxima already at $t = 0$ s. With ongoing time the vortex signatures are progressively eroded such that at $t = 30$ s the vortices can hardly be identified. Note

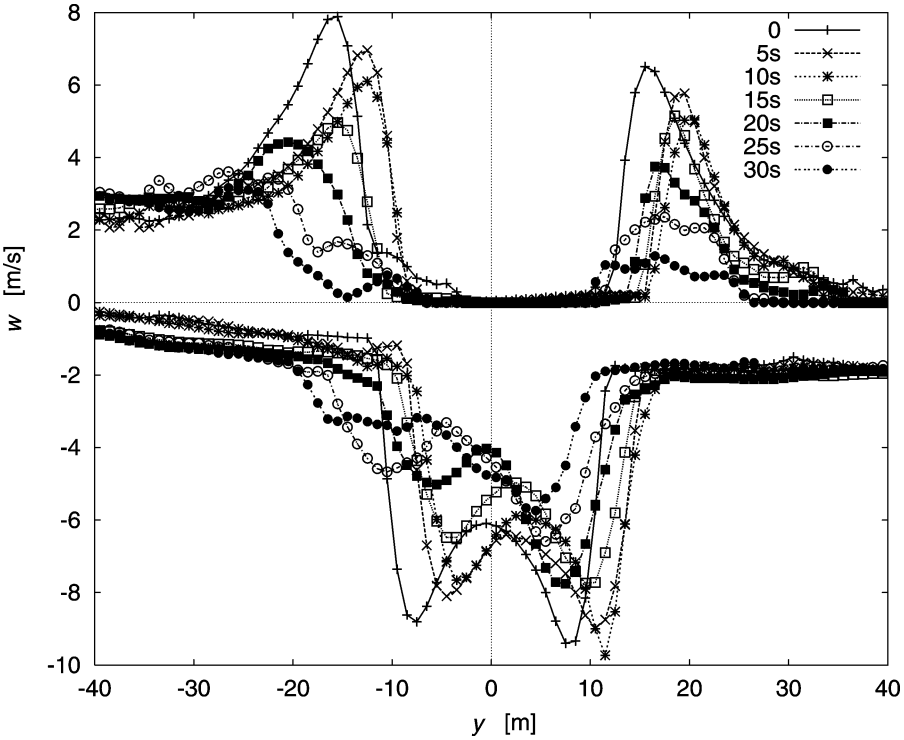


FIG. 10. Profiles of maximum and minimum vertical velocities at $x = 192$ m and different instants of time.

that at $t = 30$ s the vortices, nevertheless, still possess more than 50% of their initial circulation (cf. Fig. 11). This example demonstrates that the evaluation of already strongly deformed vortex signatures still may be worthwhile.

The respective circulation evolutions determined according to methods $v_t$, $w_d$, and $\omega$ are displayed in Fig. 11 where method $w_d$ is shown with and without the correction for vortex tilting. For method $w_d$ no lateral averaging along the downdraft velocities is performed. In the synthetic flow field the vortex positions are determined by searching the local minima of $\lambda_2$[1] with a resolution of 1 m. For real lidar measurements it is assumed that the triangulation method (Köpp et al. 2003, hereafter K03), which is described in more detail in section 6, would yield a similar accuracy for vortex positions and, consequently, vortex spacing and tilt angle.

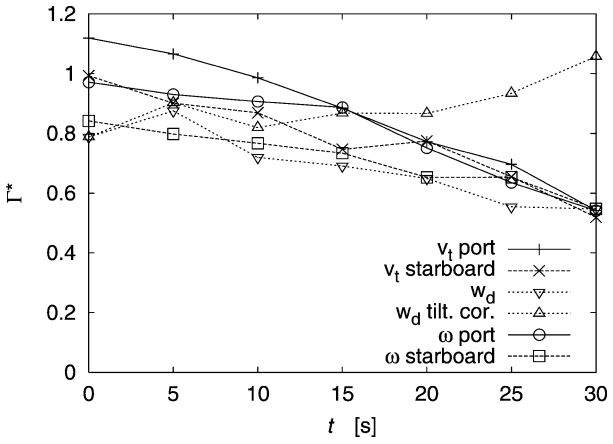


FIG. 11. Circulation evolution for methods $v_t$, $w_d$, and $\omega$ at $x = 192$ m.

The different methods yield initial deviations of almost $\pm 20\%$ and converge with progressing time, except method $w_d$ with tilt correction. In this situation of extreme vortex tilting [$\phi(30\text{ s}) = 59°$] the correction for vortex tilting causes an overestimation of circulation values. As it is shown in the previous section, this is due to the fact that for larger tilt angles the maximum LOS velocities prevail in front of or behind the line connecting the vortex centers, that is, closer to one of the vortices. In the current example the limiting observation angle $\gamma_{\min} = 57°$ ($\phi = 33°$) is reached already at $t = 11$ s. After that time method $w_d$ with tilt correction yields too high values. In reality the variable lidar scan angle and the threshold angle for the tilting correction should always be combined to calculate the effective observation angle that can be used to rule out flawed tilting corrections.

[1] The second eigenvalue $\lambda_2$ of the symmetric tensor $S^2 + \Omega^2$ is a measure for coherent vortex structures according to Jeong and Hussain (1995). Here $S$ and $\Omega$ are the symmetric and antisymmetric parts of the velocity gradient tensor $\nabla u$.

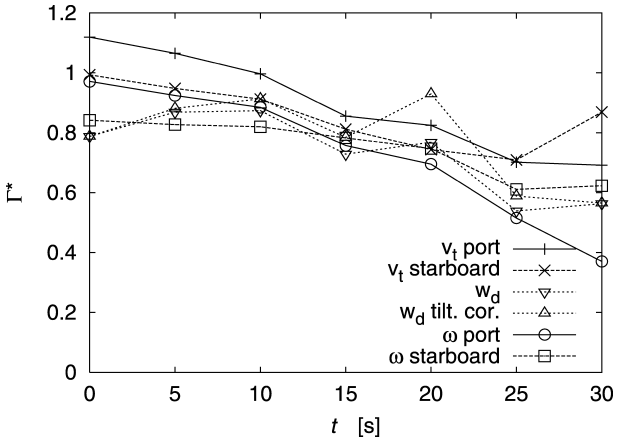


FIG. 12. Circulation evolution for methods $v_t$, $w_d$, and $\omega$ with an axial wind of $u = 1.6$ m s$^{-1}$; initial plane at $x = 192$ m.

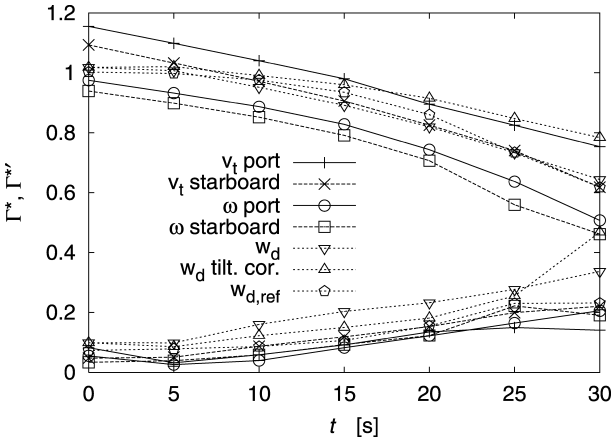


FIG. 13. Evolution of circulation determined by methods $v_t$, $w_d$, and $\omega$ as an average over all simulation planes along the flight direction and respective standard deviations below.

Figure 12 shows circulation evolution where the vortices are advected with an axial wind of $u = 1.6$ m s$^{-1}$ along the flight direction. The initial plane corresponds to the plane evaluated in Fig. 11. The comparison of Figs. 11 and 12 indicates that axial wind may have considerable impact on estimated circulation. In particular, axial wind may cause an ostensible constancy or even increase of circulation with time when less-decayed vortex segments are advected into the measurement plane. Basically, axial wind may increase scatter provided that the spatial vortex evolution features axial gradients.

To reveal a more representative characterization of the three methods, the respective circulations are averaged over all simulation planes along the flight direction (see Fig. 13). Table 1 indicates that the mean initial circulation values correspond well to the theoretical values. In particular, method $\omega$ reproduces almost the theoretical value for $\Gamma^*_{5-11}$ of a single vortex; that is, method $\omega$ is not sensitive to the influence of the neighboring vortex.

Remarkably, the radii-averaging methods $\omega$ and $v_t$, and also method $w_d$ without tilt correction, show similar decay characteristics [$\Gamma^*(t)$ slope], where the systematic initial offset between the different methods is maintained during vortex evolution. Only the downdraft method $w_d$ yields no initial decay until $t = 5$ s. Additionally, circulation is determined by integration of vorticity on circles with a radius of $b_0/2$ as an indication of the real midpoint circulation evolution (termed method $w_{d,\mathrm{ref}}$). The reference method $w_{d,\mathrm{ref}}$ suggests a slower initial decay because the diffusion process that reduces circulation on smaller radii is not present at $y = b_0/2$. Until $t = 15$ s, method $w_{d,\mathrm{ref}}$, which is not affected by tilting effects, follows the curve with tilt correction. Later on, when in some sections tilt angles of 30° are exceeded, method $w_{d,\mathrm{ref}}$ approaches the curve without tilt correction.

Another remarkable observation is the similar magnitude of the standard deviation of the circulation, $\Gamma^{*\prime}$, of methods $v_t$ and $\omega$. Obviously the main benefit of averaging is achieved by the radii average, whereas the additional averaging of the vorticity over the integration area in method $\omega$ is of minor importance. The scatter of method $w_{d,\mathrm{ref}}$ is increased compared to methods $v_t$ and $\omega$ because the integration over the larger area encloses more ambient turbulence. The standard deviation of method $w_d$ indicates larger scatter where the titlting correction reduces the scatter until $t = 20$ s. Later on the scatter is even increased with the correction. This again indicates that the tilt correction may improve estimated circulation for moderate tilt angles but for larger tilting may adulterate results.

## 5. Multiple vortex pairs

Initial overestimations of the root circulation of typically 30%–60% are frequently observed by lidar especially when method $v_t$ is applied (Campbell et al. 1997; Robins et al. 2001; Holzäpfel 2003). That overestimation is associated with an ostensible strong initial ''decay'' such that at a vortex age of roughly one timescale ($t_0 = 2\pi b_0^2/\Gamma_0$) normalized circulation attains a value of one. Recent analyses of numerous experimental data indicate that the completion of roll-up for approaching aircraft equally may last about one timescale (A. Elsenaar 2001, personal communication). The correlation between circulation overestimation and roll-up process is substantiated in this section.

TABLE 1. Theoretical initial circulation and mean initial circulation of LES determined according to the three methods.

| Method | $\Gamma^*_{0,\mathrm{theor}}$ | $\Gamma^*_{0,\mathrm{LES}}$ |
|---|---|---|
| $\omega$ | 0.967 | 0.957 |
| $v_t$ | 1.113 | 1.124 |
| $w_d$ | 1.0 | 1.018 |

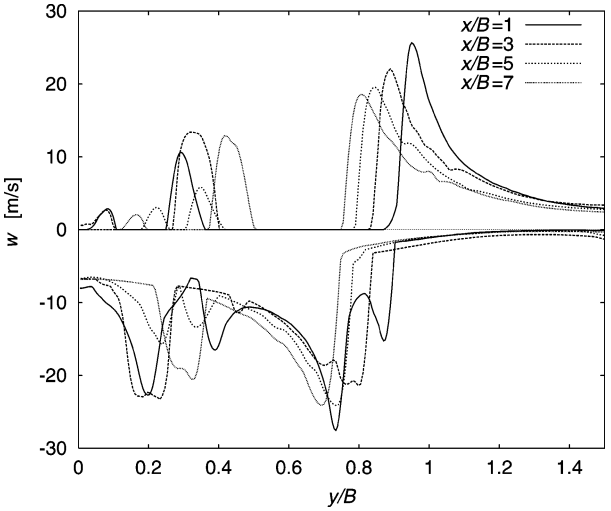


FIG. 14. Lateral profiles of maximum and minimum vertical LOS velocities at different downstream positions of near-field wake flow.

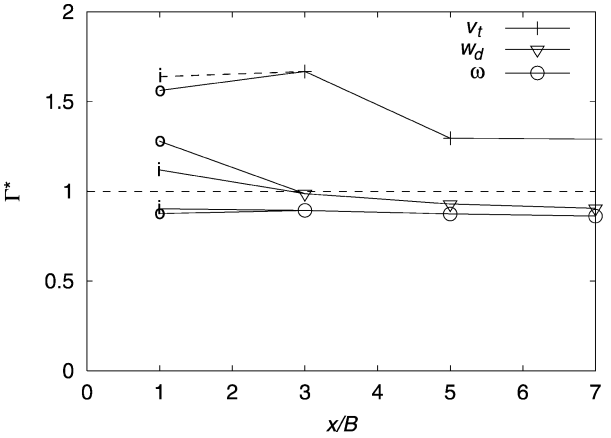


FIG. 15. Circulation at different downstream positions of near-field wake flow determined by methods $v_t$, $w_d$, and $\omega$. Symbol o (i) denotes circulation evaluation for the outer (inner) vortex center at $x/B = 1$. The radii interval applied for method $v_t$ is scaled to correspond to $\Gamma^*_{5-11}$ as used in the previous sections.

To reveal the mechanisms that cause the initial circulation overestimation we perform virtual lidar measurements based on high-resolution numerical simulation data that cover the generation and merger of multiple vortex pairs behind an aircraft model in high-lift landing configuration. The simulation treats the flow around the Deutsches Zentrum für Luft und Raumfahrt (DLR)–Aerodynamische Leistungsverbesserung an subsonischen Transportflugzeugen (ALVAST) model, which is similar to the Airbus A320, by solving the Euler equations up to a half-span downstream of the wing tip. The subsequent vortex evolution is modeled by a direct numerical simulation. Details of the near-field simulation approach are described in Stumpf (2002). Figure 1 illustrates the resulting topology of multiple vortex pairs. The contours of axial vorticity indicate the vortex sheet that forms immediately downstream of the trailing edge of the wing and then becomes organized in two corotating vortices from outer flap edge and wing tip. The counterrotating vortices on smaller lateral positions stem from the inner edge of the outer and inner flaps, respectively, whereas their centric corotating counterpart detaches from the outer edge of the inner flap.

Figure 14 shows the lateral profiles of maximum and minimum LOS velocities that are measured by the ideal vertically viewing lidar at different downstream positions. With increasing downstream distance the separation of the primary vortices decreases driven by the mutual velocity induction of the multiple vortex system. At a downstream position of one span ($x/B = 1$) the two closely spaced velocity minima at $y/B = 0.8$ indicate the merger process of the corotating outer flap edge vortex and the wing tip vortex. The velocity extrema on smaller lateral positions represent the vortices stemming from the inner edge of the outer flap and from the edges of the inner flap. The observed multiple vortex topology clearly illustrates that the assumption of axisymmetric primary vortices that is applied in method $v_t$ [Eq. (3)] is heavily violated as long as the roll-up process to a single vortex pair is not completed. If method $v_t$ is applied nevertheless, the velocity minima corresponding to the secondary vortices are interpreted as high tangential velocities on large radii appendant to the primary vortex, hence, high circulation. Figure 15 shows that the resulting overestimation, which varies between 67% and 29%, is of the order of overestimations found in field measurements. The reduction of the overestimation with increasing distance $x/B$ is caused less by the gradually proceeding roll-up but rather can be explained as follows. Since the triplet of secondary vortices is rotated below the primary vortex outward, the vertical projection of the distance to the primary vortex decreases (see Fig. 14), which, in turn, reduces circulation. This example demonstrates that the manifold of vortex topologies that evolve during roll-up may cause a considerable variability of the initial overestimation of circulation. In contrast, the ambiguity of the actual vortex center location of the merging wing tip and outer flap edge vortex at $x/B = 1$ (see Fig. 14) leads to a comparatively small circulation variation (see Fig. 15).

Method $w_d$ is less sensitive to remaining secondary vortices as long as these are sufficiently separated from the midpoint position. At $x/B = 1$ we state an overestimation of up to 28% and an increased sensitivity to the determination of vortex core position. From $x/B = 3$ onward the small decay rate is caused by the slowly approaching primary vortices. Method $\omega$ obtains an almost constant circulation of 0.9 because 10% of the circulation was dissipated in the preceding simulation of the flow around the aircraft.

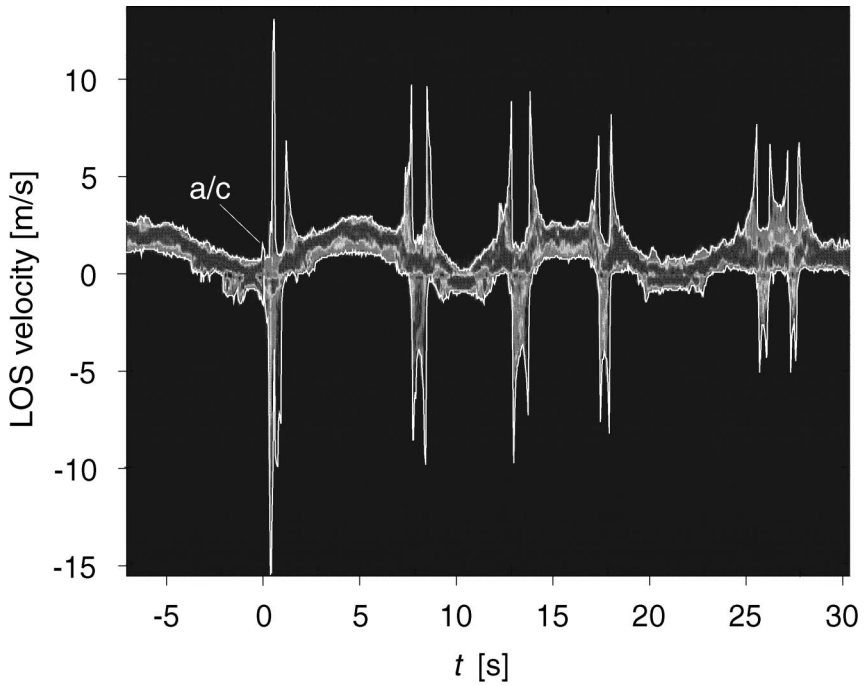


FIG. 16. Lidar spectra of several intersections with the wake vortices measured by the QinetiQ lidar team during WakeOP (flight 1-13). Aircraft hit at $t = 0$ *s*. White lines indicate maximum LOS velocities; the shading represents the signal contribution in each velocity bin.

## 6. Field measurements

The Wake Vortex Forecasting and Measuring Campaign at Oberpfaffenhofen (WakeOP) was performed at the airfield of Fairchild Dornier in Oberpfaffenhofen, Germany, from 29 March to 4 May 2001. An outline of the campaign is given in Gerz (2001). Besides a large variety of meteorological measurement systems, three 10-$\mu$m continuous-wave lidars were operated to trace the wake vortices generated by DLR's VFW 614 aircraft ATTAS. The circulation of the ATTAS varied between 113 and 168 $m^2$ $s^{-1}$ with a mean value of $\Gamma_0 = 142$ $m^2$ $s^{-1}$, and the reference timescale was $t_0 = 12.6$ s on average.

It was successfully demonstrated that vortex spacing and trajectories can be obtained with significantly higher accuracy when triangulating the vortex core intersections of two or three simultaneously measuring lidars (K03). For this purpose the lidars were placed at a lateral offset of approximately 80 m and were scanned in a vertical plane, aligned perpendicular to the aircraft's flight direction. Vortex core intersections of a lidar give accurate angular information but poor range information. The triangulation method combines two series of accurate angular measurements with an extended Kalman filter to produce the horizontal and vertical positions of the vortices with high accuracy. Here we employ WakeOP lidar data to verify our theoretical considerations concerning the evaluation strategies of circulation. For this purpose vortex positions determined with the triangulation method are applied.

Figure 16 illustrates several interesting features of the lidar spectra that are already translated into LOS velocities. The aircraft passed almost directly above the lidar at an altitude of 146 m. The lidar scan range was from 60° to 95° with a scan rate of 8° $s^{-1}$. The mean crosswind was approximately 2.5 m $s^{-1}$, measured by a separate wind-profiling lidar, and this was consistent with the observed horizontal vortex drift velocity. For full details of the measurement geometry see K03.

The background wind field with its fluctuations is evidenced in Fig. 16 by the width and the noisy appearance of the oscillating trace. The tiny solid bar at $t = 0$ s that lasts for a small fraction of a second indicates that the lidar beam strikes the aircraft. The flow observed immediately afterward shows high velocities and complex structure, which represents the multiple vortices that form during roll-up. Clearly, the evaluation of circulation of such structures is not feasable. The subsequent vortex pairs display the classic vortex pattern. Eventually the vortices drift out of the scanning region. The drift leads to an apparent stretching of the profiles when scanning with the wind, and a contraction when scanning against the wind.

Figure 17 shows lidar spectra of five intersections with the decaying vortex pair. The lidar settings were analogical to that in Fig. 16. The comparison of simulation and measurement (Figs. 10, 17) clearly points out similar characteristics of the LOS velocity evolution during vortex decay. At earlier times the vortex signatures are distinct albeit not perfectly symmetric, whereas at later times the vortex signatures are pro-

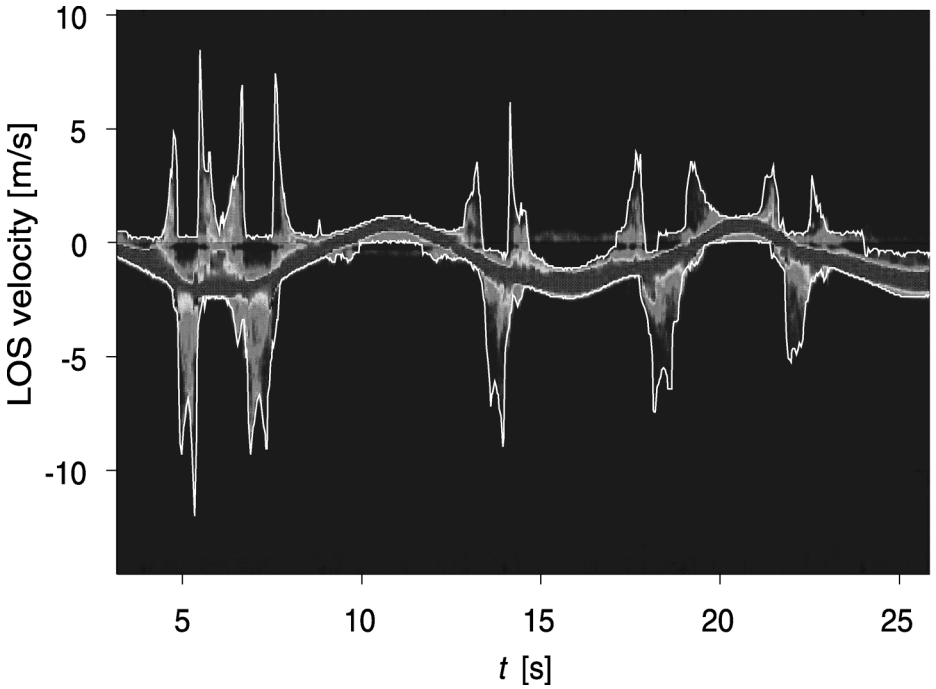


FIG. 17. Lidar spectra of five intersections with the decaying wake vortex pair measured by the QinetiQ lidar team during the campaign WakeOP (flight 8-01).

gressively eroded such that, for example, the two downdraft peaks vanish in favor of an unstructured downwash region.

Figure 18 depicts the evolution of mean normalized circulation determined from data of the three lidar teams with methods $v_t$ and $w_d$ together with the respective standard deviations. The circulations are normalized by theoretical circulations that are calculated individually from aircraft weight and flight speed of every overflight (OF). The different curves denote averages of the circulations of all evaluated OFs that are combined regardless of the prevailing weather conditions and adjusted aircraft configurations. In spite of the unspecific combination of the respective samples, the statistics corroborate the previously described characteristics of the different evaluation methods.

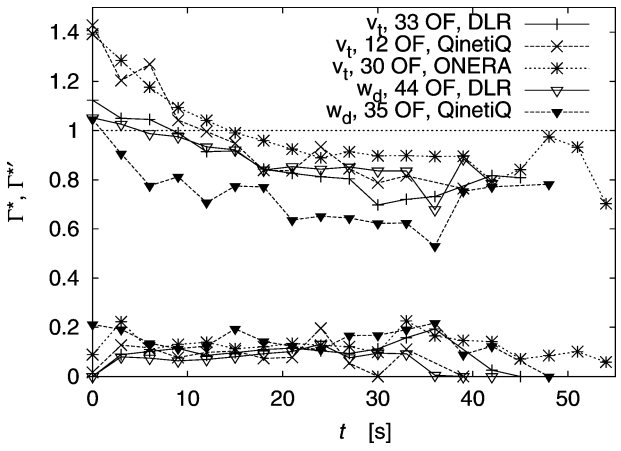


FIG. 18. (top) Mean normalized circulation evolution and (bottom) respective standard deviation, vs time determined from lidar measurements during WakeOP. Circulation values are averages over 3-s intervals. Evaluation method, number of OFs, and lidar teams are indicated in the legend.

1) *Initial overestimation* (cf. section 5). Method $v_t$ applied to QinetiQ and the Office National d'Etudes et de Recherches Aérospatiales (ONERA) data clearly exhibits an initial overestimation of nominal circulation by roughly 40%. At about one timescale (12 s) the curves reach a circulation of one. For individual measurements maximum overestimations of 90% are found.
2) *Scatter*. The standard deviations of the lidar field measurements (Fig. 18) are of the same order of magnitude as found in the LES (Fig. 13). Since in the LES the roll-up is not considered, standard deviations start from a lower level and increase with time driven by atmospheric turbulence. The higher initial standard deviations and, in particular, the maximum of ONERA's standard deviation at 3 s reflect the enhanced variability of the initial overestimation that can be caused by the complex topology of multiple vortex pairs during roll-up. Method $w_d$ applied to QinetiQ data yields, indeed, increased standard deviations compared to method $v_t$ for data of the same lidar team.

Since in the field data the average environmental turbulence intensity is even higher than in the sim-

ulations ($q^*_{\text{meas}} = 0.88$, $q^*_{\text{LES}} = 0.54$)—in which measurement uncertainties are excluded—we conclude that errors originating from lidar measurement accuracy appear to be negligible compared to the genuine circulation scatter caused by the complex response of wake vortices to turbulent environments.

Circulations evaluated by DLR show less systematic overestimation and reduced scatter. However, such circulation data are only achieved in an interactive and iterative evaluation procedure where an experienced scientist is in the loop and introduces adequate threshold levels for the signal intensity attributed to the LOS velocity and rejects spurious data. Nevertheless, these data follow the expected trends discussed below.

3) *The effect of neighbor vortex and internal diffusion.* Method $v_t$ initially yields slightly higher circulation values compared to method $w_d$ caused by the superimposed velocities of the neighbor vortex. These are followed by a slightly steeper circulation decline, which originates from diffusion processes in the vortex. The final decay phase is not observed because in most cases the vortices were already advected out of the observation area covered simultaneously by both lidar systems before the final decay.

## 7. Summary

The evolution and decay of circulation of aircraft trailing vortices constitutes an essential issue of wake vortex research. For full-scale vortices this key parameter can, to date, only be derived from lidar measurements. The current manuscript investigates the impact of different effects that inherently modify circulation values during the different phases of vortex evolution in the atmospheric boundary layer. To understand the nature of the circulation, assessment is a vital interest for all those who aim at safely reducing aircraft separations.

For this purpose, different circulation evaluation methods are applied to (i) analytically given Lamb–Oseen vortices and to virtual lidar velocity data established from (ii) a numerical simulation of the flow around an aircraft in high-lift configuration, which provides the peculiarities of a near-field multiple vortex topology; and to (iii) LES of wake vortices in a convectively driven atmospheric boundary layer, which represents vortex evolution in an inhomogeneous turbulent environment. The investigations reveal specific characteristics of the different evaluation methods and explain and quantify systematic deviations from root circulation.

Averaging over a radii interval of a single vortex leads to a small underestimation of the root circulation due to reduced circulation values at small radii. This underestimation is reproduced well also for vortex pairs when circulation is determined by the integration of vorticity. The degree of the underestimation depends on the averaging interval, the core radius, and the vortex spacing. On the other hand, the evaluation of radii-averaged circulation from vertical maximum LOS velocities according to method $v_t$ leads to an overestimation of the root circulation due to the impact of the neighboring vortex. The degree of the overestimation again is a function of the last named parameters and the observation angle $\gamma$. The overestimation decreases slightly when the angle of observation deviates from 90°. In the quite large angle domain $90° \geq \gamma \geq 40°$ it varies between 2.9% and 11.8%.

The downdraft method $w_d$ evaluates circulation from the tangential velocity midway between the vortices. This position corresponds to the radius where the determined circulation comes most close to root circulation. For sufficiently tight vortex cores, method $w_d$ causes a slight overestimation of the root circulation only when the downdraft velocities are smoothed by averaging. However, the correction for vortex tilting may significantly adulterate circulation values when the (observation) angle between the line connecting the vortex centers and the scan direction falls short below 57°. In a real turbulent vortex already smaller tilt angles may cause ambiguous tilt corrections.

During the roll-up of the complex near-field wake topology generated by a high-lift wing the assumption that the sensed maximum line-of-sight velocities can be attributed to the tangential velocities of a pair of axisymmetric vortices does not hold. As a result the circulation evaluation from lidar data can be flawed. Fortunately, the roll-up phase typically is accomplished after one timescale and therefore is irrelevant for separations to following aircraft. As long as the roll-up to a single vortex pair is not completed, the radii-averaging method $v_t$ interprets vorticity stemming, for example, from the edges of a flap as high tangential velocities on large radii, hence, high circulation. Initial overestimations of the root circulation of 30%–70% are found in measurements and simulation. Method $w_d$ is less sensitive to remaining secondary vortices as long as these are sufficiently separated from the midpoint position.

LES data indicate that considerably eroded vortices, which already have lost the classic signature and therefore can scarcely be identified as wake vortices, nevertheless may still possess more than 50% of their initial circulation. This result emphasizes the difficulties associated with the investigation of final vortex decay. Since, on the other hand, vortex decay is of primary interest for wake vortex separations, we recommend to push the evaluation of already strongly deformed vortex signatures as far as possible.

A comparison of measurements accomplished during the WakeOP campaign and the LES data corroborates our theoretical findings. In particular, we show that the degree of scatter of circulation data observed after the completion of roll-up appears to be mostly due to the genuine variability of wake vortices in the atmospheric

boundary layer. This scatter, consequently, neither can be avoided nor should be artificially smoothed. The only way to further reduce this intrinsic scatter is to average over several nominally identical measurements with respect to aircraft configuration and atmospheric conditions where the measurements can be based on multiple overflights and/or multiple lidars.

We have shown that the two investigated circulation evaluation methods are of complementary character and therefore should both be applied if possible. It was further shown that the circulation of the primary vortices may be best approximated when an experienced scientist evaluates data in an interactive and iterative evaluation procedure. However, for circulation evaluation in an operational reduced spacing system, time-consuming interactive procedures are inapplicable. Here the radii-averaged approach $v_t$ seems most appropriate. Sure enough, the method suffers from a systematic overestimation of the root circulation but there is no overestimation in terms of encounter metrics for follower aircraft. The velocities that apparently increase circulation would also be sensed by a following aircraft in an encounter. Further advantages are that no ambient wind data are needed to evaluate circulation, the radii averaging reduces scatter, and the observation angle domain is less restricted.

*Acknowledgments.* We gratefully acknowledge the three lidar teams and the ATTAS flight crew for their contributions to the WakeOP database. The measurement campaign WakeOP was funded by the DLR project Wirbelschleppe, the European Commission in the framework of C-Wake, and the U.K. Department of Trade and Industrie under the CARAD program.

REFERENCES

Campbell, S. D., T. J. Dasey, R. E. Freehart, R. M. Heinrichs, M. P. Matthews, G. H. Perras, and G. S. Rowe, 1997: Wake Vortex Field Measurement Program at Memphis, TN, data guide. Project Rep. NASA/L-2, Lincoln Laboratory, Massachusetts Institute of Technology, Cambridge, MA, 100 pp.

Constant, G., R. Foord, P. A. Forrester, and J. M. Vaughan, 1994: Coherent laser radar and the problem of aircraft wake vortices. *J. Mod. Opt.,* **41,** 2153–2173.

Gerz, T., 2001: Wake vortex prediction and observation: Towards an operational system. *Proc. Third ONERA–DLR Aerospace Symp.,* Paris, France, ONERA and DLR, S1–3.

——, F. Holzäpfel, and D. Darracq, 2002: Commercial aircraft wake vortices. *Prog. Aerosp. Sci.,* **38,** 181–208.

Harris, M., J. M. Vaughan, K. Huenecke, and C. Huenecke, 2000: Aircraft wake vortices: A comparison of wind-tunnel data with field trial measurements by laser radar. *Aerosp. Sci. Technol.,* **4,** 363–370.

Hinton, D. A., and C. R. Tatnall, 1997: A candidate wake vortex strength definition for application to the NASA Aircraft Vortex Spacing System (AVOSS). NASA Tech. Memo. 110343, Langley Research Center, Hampton, VA, 32 pp.

Holzäpfel, F., 2003: Probabilistic two-phase wake vortex decay and transport model. *J. Aircr.,* **40,** 323–331.

——, T. Gerz, M. Frech, and A. Dörnbrack, 2000: Wake vortices in a convective boundary layer and their influence on following aircraft. *J. Aircr.,* **37,** 1001–1007.

——, T. Hofbauer, D. Darracq, H. Moet, F. Garnier, and C. Ferreira Gago, 2003: Analysis of wake vortex decay mechanisms in the atmosphere. *Aerosp. Sci. Technol.,* in press.

Jeong, J., and F. Hussain, 1995: On the identification of a vortex. *J. Fluid Mech.,* **285,** 69–94.

Köpp, F., and Coauthors, 2003: Characterisation of aircraft wake vortices by multiple-lidar triangulation. *AIAA J.,* in press.

Robins, R. E., D. P. Delisi, and G. C. Greene, 2001: Algorithm for prediction of trailing vortex evolution. *J. Aircr.,* **38,** 911–917.

Spalart, P. R., 1998: Airplane trailing vortices. *Annu. Rev. Fluid Mech.,* **30,** 107–138.

Stumpf, E., 2002: Numerical investigation of the effect of the high-lift configuration of a transport aircraft on its vortex wake. *New Results in Numerical and Experimental Fluid Mechanics III,* S. Wagner et al., Eds., Notes on Numerical Fluid Mechanics, Vol. 77, Springer-Verlag, 50–57.

[6]

# Analysis of wake vortex decay mechanisms in the atmosphere

F. Holzäpfel, T. Hofbauer, D. Darracq, H. Moet, F. Garnier, C. Ferreira Gago

Aerospace Science and Technology, 2003

Volume 7, Number 4, Pages 263–275

Available online at www.sciencedirect.com
SCIENCE DIRECT®
Aerospace Science and Technology 7 (2003) 263–275
Aerospace Science and Technology
www.elsevier.com/locate/aescte

# Analysis of wake vortex decay mechanisms in the atmosphere ☆

# Analyse der Zerfallsmechanismen von Wirbelschleppen in der Atmosphäre

Frank Holzäpfel [a,*], Thomas Hofbauer [a], Denis Darracq [b], Henri Moet [b], François Garnier [c], Cecile Ferreira Gago [c]

[a] *Institut für Physik der Atmosphäre, DLR Oberpfaffenhofen, 82234 Weßling, Germany*
[b] *CERFACS, 31057 Toulouse, France*
[c] *Département de Physique Unité d'Environnement Atmosphérique, ONERA, 92320 Châtillon, France*

Received 10 October 2001; received in revised form 13 December 2002; accepted 26 February 2003

**Abstract**

Results of high-resolution numerical simulations of aircraft wake vortex evolution and decay in different regimes and atmospheric conditions are presented. The different cases comprise (i) the near field interaction of a trailing vortex with an exhaust jet, (ii) the evolution of single vortices and counter-rotating vortex pairs in homogeneous isotropic turbulence, as well as (iii) the decay of wake vortices in a turbulent stably stratified atmosphere, and (iv) in a weakly turbulent sheared environment. The different cases are used to analyse common aspects of vortex dynamics and decay mechanisms. In all scenarios the formation of coherent secondary vorticity structures that enclose the primary vortices is observed. These secondary vorticity structures deform and weaken the primary vortices and in some cases lead to rapid vortex decay. It is shown that the mean swirling flow effectively rearranges and intensifies any secondary vorticity by tilting and stretching. The secondary vorticity may either originate from the turbine jet, ambient turbulence or may be produced baroclinically. Based on the observed phenomena, eleven postulates are established that pinpoint fundamental aspects of the observed decay mechanisms.


**Zusammenfassung**

Mittels hochauflösender numerischer Simulationen wird die Entwicklung und der Zerfall von Flugzeug-Wirbelschleppen unter verschiedenen atmosphärischen Bedingungen untersucht. Die betrachteten Szenarien umfassen (i) die Wechselwirkung eines Triebwerksstrahls mit einem Nachlaufwirbel, (ii) die Entwicklung von Einzelwirbeln und gegensinnig rotierenden Wirbelpaaren in homogener isotroper Turbulenz, (iii) den Wirbelschleppenzerfall in einer turbulenten stabil geschichteten Atmosphäre und (iv) in einer schwach turbulenten Umgebung mit überlagerter Windscherung. Die Untersuchungen konzentrieren sich auf den verschiedenen Fällen gemeinsame Aspekte der Wirbeldynamik und des Zerfalls. Stets werden kohärente Sekundärwirbelstrukturen beobachtet, die die Primärwirbel umschließen. Die Sekundärwirbel deformieren und schwächen die Wirbelschleppe und können ihren schnellen Zerfall auslösen. Es wird gezeigt, dass die mittlere Wirbelströmung die zunächst inkohärente sekundäre Wirbelstärke in effektiver Weise durch Kippen umorganisiert und mittels Streckung verstärkt. Die sekundäre Wirbelstärke kann durch den Triebwerksstrahl, die Umgebungsturbulenz oder barokline Produktion eingebracht werden. Es werden elf Postulate aufgestellt, die wesentliche Aspekte der beobachteten Zerfallsmechanismen beschreiben.


*Keywords:* Wake vortices; Numerical simulation; Exhaust jet; Turbulence; Stable stratification; Shear; Secondary vorticity structures

*Schlüsselwörter:* Wirbelschleppe; Numerische Simulation; Triebwerksstrahl; Turbulenz; Stabile Schichtung; Scherung; Sekundärwirbelstrukturen

☆ This article was presented at ODAS 2001.

* Corresponding author.
*E-mail address:* frank.holzaepfel@dlr.de (F. Holzäpfel).

1270-9638/03/$ – see front matter 
doi:10.1016/S1270-9638(03)00026-9

## 1. Introduction

The lift exerted on aircraft wings produces long-lived trailing vortices. Especially during an aircraft's critical landing phase these can endanger following aircraft. To avoid wake vortex encounters, follower aircraft must maintain a safe distance to a landing aircraft up ahead of them. In order to increase airport capacities whilst at least maintaining safety levels, the knowledge of wake vortex behaviour under varying meteorological conditions achieves considerable significance. Also, the influence of aircraft design on the strength of the shed vortices and the related potentially more rapid decay is of crucial importance.

The mostly prevailing decay mechanism in cruise altitude, the so-called Crow instability [2], can frequently be observed being visualized by contrails. Minor atmospheric turbulence is sufficient to trigger sinusoidal oscillations of the vortices that lead to vortex reconnection and, finally, the formation of descending vortex rings. Although the Crow instability is well understood in principle, the longevity of vortex rings and their effects on encountering aircraft are discussed controversly.

Another controversy applies to the temporal evolution of vortex intensity and decay. Two radically different concepts are debated, namely the concept of gradual and predictable decay and the concept of stochastic collapse [30]. In the latter concept a phase of minor gradual decay is followed by a rapid decay phase [9] which coincides with a transition to fully turbulent vortices [15,26]. The controversy can in part be resolved by the insight that the observed circulation evolution largely depends on its definition. On small radii a gradual decay is observed which reflects diffusion in the vortex core region, whereas larger radii are not affected by this diffusion and rapid circulation decay sets only in when instability mechanisms have developed. On the other hand, rapid decay could well be masked in lidar[1] measurements due to several reasons: (i) gradual spatial deformation of vortices will apparently decrease gradually swirl velocities in the measurement plane, (ii) the advection of deformed vortices through the measurement plane will cause substantial scatter. If that scatter shall be reduced by averaging of circulation data from several flights, characteristic features of circulation evolution are smeared out, (iii) the late phase of potentially rapid circulation decay is not accessible by lidar probably because vortices decay turbulently [15] or can not be distinguished from their turbulent environment. So numerical approaches have to be employed to contribute to a comprehensive understanding of vortex decay characteristics. The above mentioned and further implications of circulation evaluation from lidar data are discussed in detail in [16].

In-situ measurements in the wakes of various aircraft have shown that the exhaust jets contribute dominantly to aircraft-induced wake turbulence compared to other sources like boundary layer separation [14]. So the turbine jet constitutes a top candidate to affect wake evolution by aircraft design. Turbulence, stratification and shear, on the other hand, are the primary influences on vortex evolution in the atmosphere. All the mentioned scenarios are tackled in this manuscript. Merely, the effect of ground proximity is not considered.

In the current article, a condensed survey is given on four wake vortex calculations that were in part already described in previous publications. In each of the four cases different numerical approaches and parameters are applied (cf. Table 1). A detailed description of the approaches would go beyond the scope of this paper and is given elsewhere [6,11,14,24]. However, the dissimilar pecularities of the described approaches on one hand, and the similar topologies of the resulting vortex evolutions on the other hand, indicate a relative independency of results from specific methodological aspects. This finding encourages us to consider the extracted common aspects of wake vortex decay as generic and universally valid results. The analysed phenomena are related to the formation of coherent secondary vorticity structures and their impact on vortex decay. We argue that the observed effects, though extremely difficult to verify experimentally, generally occur in wake vortex evolution and play a crucial role for vortex decay. Based on the current results, eleven postulates are derived that characterize prominent mechanisms of wake vortex decay. The interrelation of azimuthal vorticity structures and wake vortex decay was first pointed out by Risso et al. [27] and is typical for three-dimensional turbulence initialization [19].

## 2. Vortex jet interaction

In the near field of the aircraft wake the exhaust jets of the turbines are entrained into the two counter-rotating wingtip vortices which at the same time roll up from the sheet of vorticity induced by the wings [7]. To investigate the highly complex entrainment and mixing process of the turbulent jet into a trailing vortex it is convenient to identify two overlapping regimes [5,22]: the jet regime and the deflection regime. In the current numerical approach these two regimes are modeled sequentially. First the turbulent jet evolves temporarily and uninfluenced by the wake flow. Then in the deflection regime the interaction of jet and wake flow is modeled. The characteristic dimensions of the numerical set-up are provided by a wind tunnel experiment [1] and are based on similarity parameters of a large transport aircraft with two engine jets. The experimental results show that the vortex flow does not affect the engine jet behaviour until a downstream distance of 0.5–1 wing spans. For modern large transport aircraft, the characteristic size of the jet regime is of the order of 1–50 diameters of the nozzle exit, while the deflection regime, scaled to the wingspan, extends

[1] LIght Detection And Ranging, remote sensing technique to measure the line-of-sight velocity along a Laser beam that scans wake vortices.

Table 1
Survey of cases, numerical codes, methods, vortex Reynolds numbers, $Re = \Gamma/\nu$, boundary conditions in flight direction, $x$, lateral direction, $y$, and vertical direction, $z$ (per. stands for periodic and nr. for non-reflecting), ratio of domain size, $L$, to vortex core radius, $r_c$, and number of grid points across core radius

| Case | Jet (Section 2) | HIT (Section 3) | Strat (Section 4) | Shear (Section 5) |
|---|---|---|---|---|
| Code | PEGASE [6] | NTMIX3D [31] | LESTUF [18] | MESOSCOP [28] |
| Method | DNS | LES | LES | DNS |
| $Re$ | 5000 (jet: 1000) | $100 \cdot 10^6$ | $\infty$ | 2200 |
| Boundary conditions | per. × nr. × nr. | periodic | periodic | per. × per. × free slip |
| $L_x/r_c \times L_y/r_c \times L_z/r_c$ | $12 \times 66.9 \times 66.9$ | $28.2^3$; $28.2 \times 56.4^2$(SV$_{5.5}$) | $102 \times 64 \times 135$ | $68.8 \times 128 \times 85.3$ |
| $r_c/\Delta x \times r_c/\Delta y \times r_c/\Delta z$ | $7.5 \times 10 \times 10$ | $2.3^3$ | $0.63 \times 4 \times 4$ | $0.93 \times 3 \times 3$ |

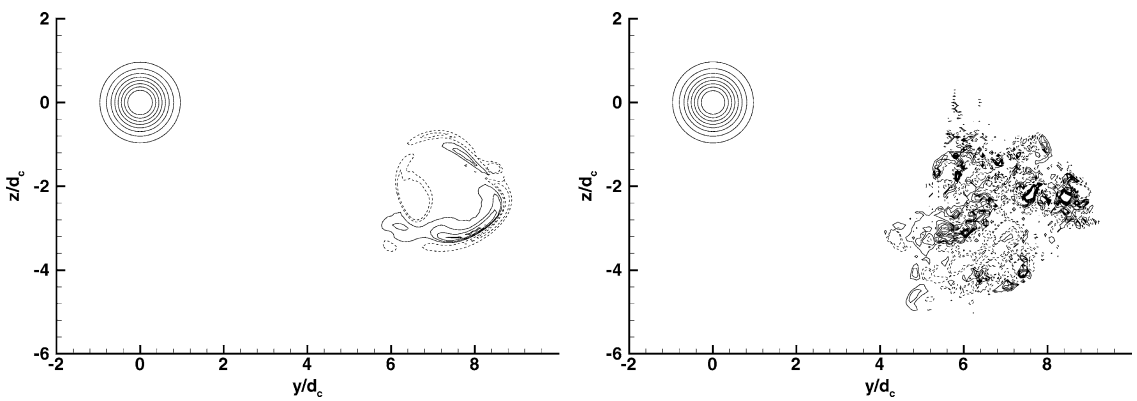


Fig. 1. Normalized axial vorticity contours in a vertical lateral cross-section at $x/B = 0.5$ (left) and $x/B = 1$ (right). Dashed lines denote negative vorticity; contour range from $-1$ to 4 in steps of 0.5.

downstream of the airplane to a distance of about 1–10 wingspans.

The simulations are performed with a temporal DNS of the three-dimensional Navier–Stokes equations. Key parameters of all simulations are listed in Table 1. For details of the numerical method we refer to [6]. The axial length of the domain of 6 nozzle radii corresponds to twice the wavelength of the maximum growth rate of the first azimuthal instability of a spatially evolving jet [23]. An unstable nozzle outlet velocity profile [23] is prescribed which is superimposed by three-dimensional Gaussian shape random perturbations. When the jet simulation has reached an age that corresponds to a downstream distance of 0.5 wing spans ($x/B = 0.5$), the cross-section of the domain is enlarged and a Lamb–Oseen vortex is superimposed on the flow field at a distance of 14 vortex core radii from the jet center (Fig. 1).

The tangential velocity profile, $v_\theta(r)$, of the Lamb–Oseen vortex is given by

$$v_\theta(r) = \frac{1.4 v_0 r_c}{r}\left(1 - \exp\frac{-1.256 r^2}{r_c^2}\right), \tag{1}$$

where $v_0$ denotes the maximum tangential velocity at the core radius $r_c$. The ratio of the jet radius at the nozzle exit and the initial vortex core radius amounts to $r_{\text{jet}}/r_c = 1.3$ and the ratio of the maximum jet and tangential velocities at $x/B = 0.5$ to $u_{\text{jet}}/v_0 = 2.72$. In all cases dimensionless time, $t^* = t/t_0$, is normalized by the vortex time scale, $t_0 = 2r_c/v_0$. Here it is set zero at the beginning of the second simulation when the jet has reached an age of $t^* = 9$. The conversion of time to downstream distance is established employing the Taylor assumption with the experimental free stream velocity of $u_0/v_0 = 2.2$.

Fig. 1 depicts cross-sections of axial vorticity at $x/B = 0.5$ and $x/B = 1$. The undisturbed concentric vorticity contours represent the trailing vortex whereas the two opposite-signed regions of vorticity at $x/B = 0.5$ reflect the most unstable mode of the jet instability. These unstable structures burst subsequently and the jet reaches a fully turbulent state at $x/B = 1$. Fig. 2 shows axial and azimuthal vorticity contours in a perspective view at different instants of time. At $t^* = 90$ the fully turbulent jet is deflected and entrained by the vortex-induced velocity field and starts to wrap around the primary vortex. During that process the jet's vorticity is progressively stretched and rearranges to coherent – but now spiral-shaped – secondary vorticity structures (SVS) of opposite signs ($t^* = 110$).

Fig. 3 sketches how a passive tracer that initially extends radially between $4r_c$ and $6r_c$ is stretched in a Rankine vortex. At $32t_0$ the tracer completely encloses the vortex center and is stretched by a factor of $5\pi$. In the long-term limit the passive tracer would be evenly distributed between $4r_c$ and $6r_c$. A similar stretch-rate of approximately one revolution in $30t_0$ takes place from $t^* = 90$ to 120 (see Fig. 2).

Fig. 2 shows, furthermore, that the counter-rotating secondary vortex rings approach each other driven by a self-induced propagation velocity. At the same time they increase

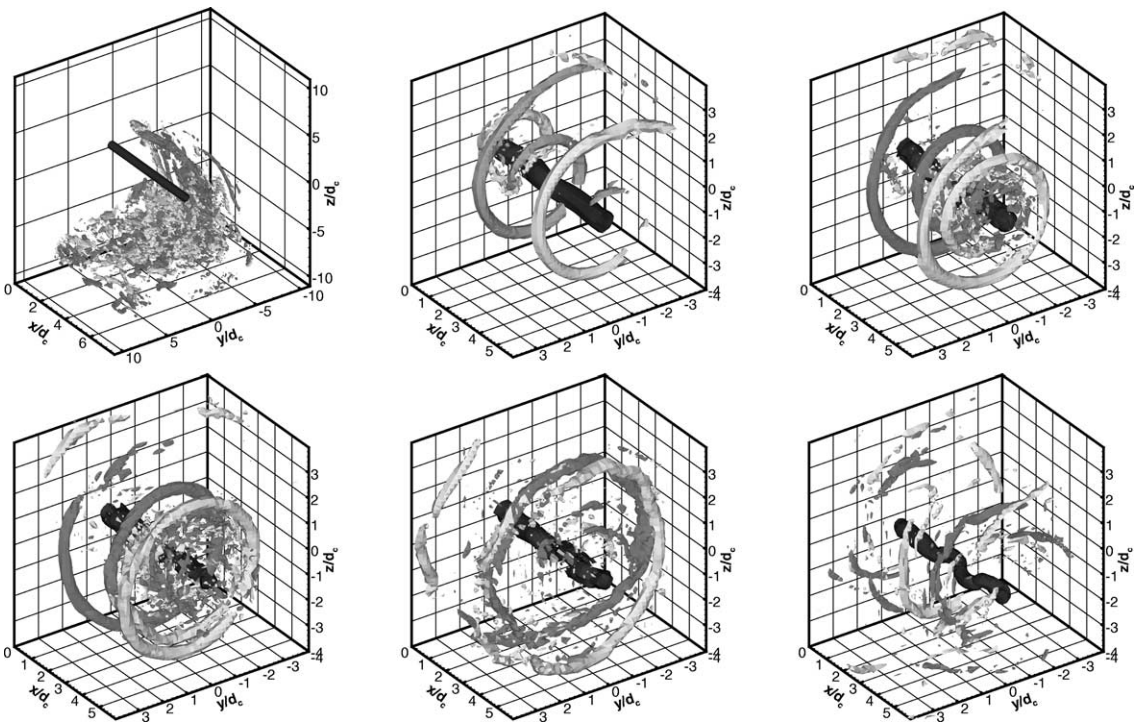

Fig. 2. Subset of the computational domain showing vorticity contours in a perspective view at $t^* = 90, 110, 120, 130, 150$, and 210 (from left to right). Black surface denotes axial component ($\omega_x^* = 3$), azimuthal components ($\omega_\theta^* = 1\ (-1)$) are plotted dark grey (light grey).

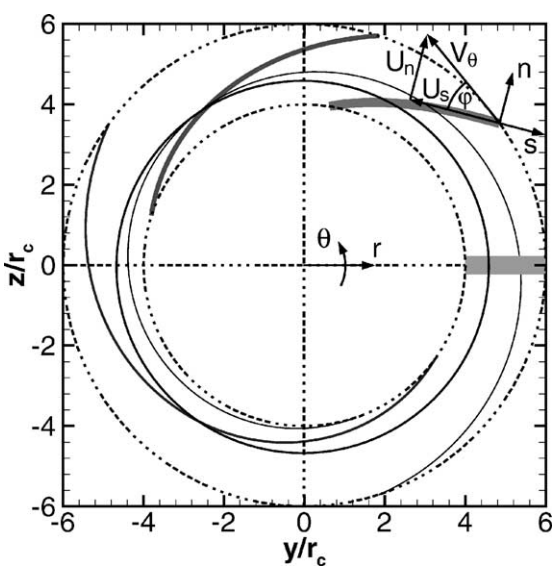


Fig. 3. Schematic of a passive tracer that initially extends between $4r_c$ and $6r_c$ and is stretched in a Rankine vortex. Different instants in time, $t = n115.2\pi^2 r_c^2/\Gamma$, are plotted at which the tracer encloses the $n$th part of the vortex where $n = 1/8, 1/4, 1/2$, and 1. Axisymmetric and instantaneous local Cartesian coordinate systems as well as representation of tangential velocity, $V_\theta$, in both coordinate systems are illustrated for usage in Section 7.

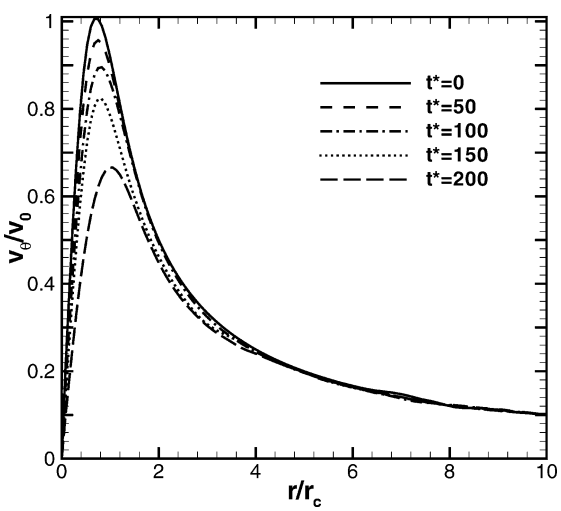


Fig. 4. Tangential velocity profiles of wake vortex at different instants in time. Velocity profiles are averaged over axial and azimuthal directions.

in radius due to mutual induction which again stretches the SVS. Finally, the counter-rotating SVS connect ($t^* = 150$) and decay by direct turbulent interaction ($t^* = 210$).

During that process the primary vortex has been stretched and deformed in turn by SVS driven induction. Fig. 4 indicates that maximum tangential velocities are progressively reduced but circulation is essentially unmodified at $r = 4r_c$ (see Fig. 5).

## 3. Vortex evolution in homogeneous isotropic turbulence

The effects of ambient turbulence on vortex dynamics are studied using the numerical code NTMIX3D [31] that solves the Navier–Stokes equations for a three-dimensional

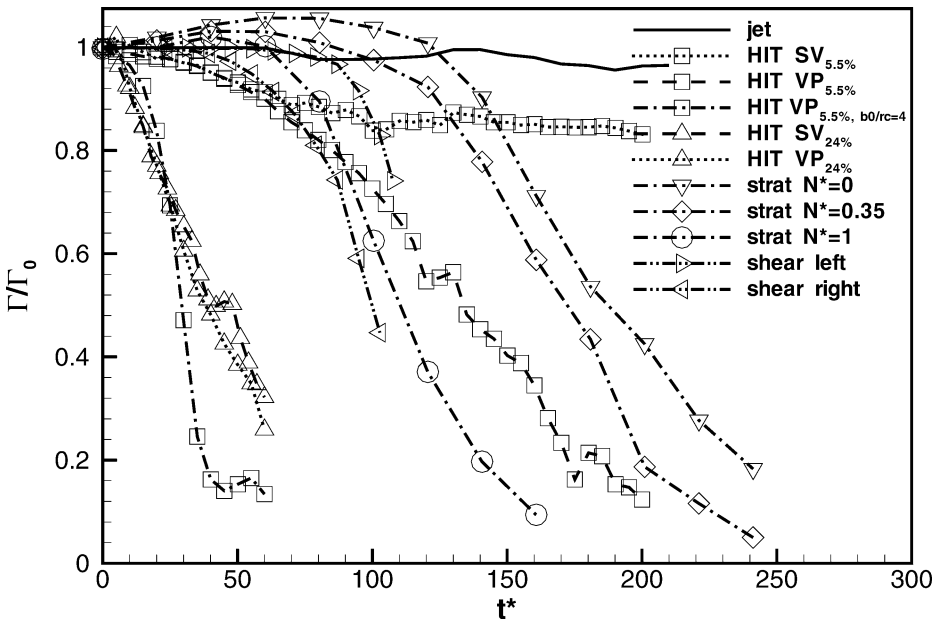


Fig. 5. Temporal evolution of axially averaged normalized circulation for all the cases. Circulations are integrated over locally centered circles with radii of $4r_c$. For vortex pair with small vortex separation ($VP_{b_0/r_c=4}$) circulation is determined on $r = b_0/2 = 2r_c$.

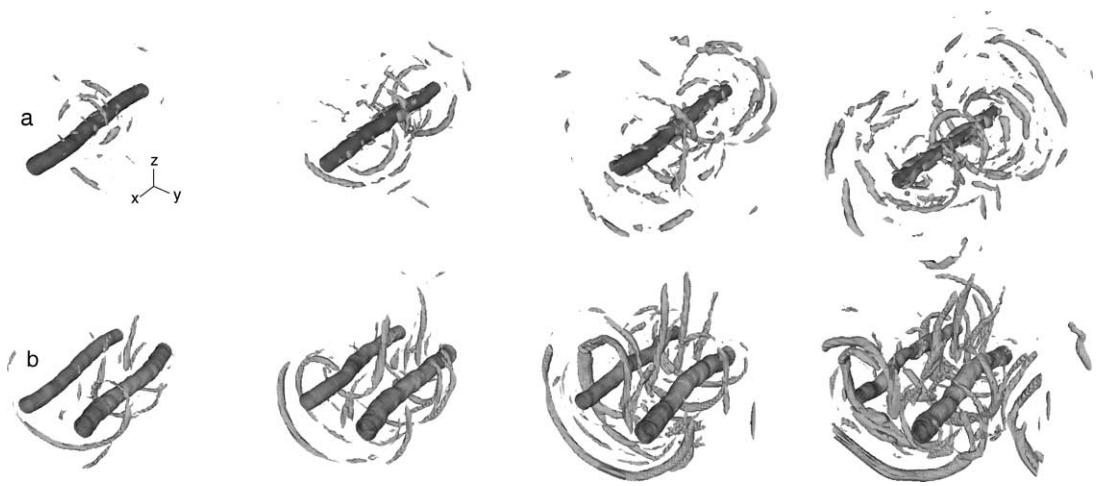


Fig. 6. Sequence of perspective views of iso-surfaces of $\lambda_2$ for vortices with $I_a = 5.5\%$ at $t^* = 25, 50, 75, 100$. (a) Single vortex, (b) vortex pair with $b_0/r_c = 8$.

unsteady flow. The code is applied in its LES version where the subgrid-scale fluxes are modeled according to the Boussinesq gradient approach and the subgrid-scale viscosity is estimated from the kinetic energy at cut-off that is assessed by the filtered structure function [4].

A field of homogeneous isotropic turbulence (HIT) is generated from a given spectrum with random phases for each mode which is subsequently allowed to adjust in a preparatory run. The resulting turbulence is characterized with respect to wake vortex parameters by the ratio of root-mean-square velocity and maximum tangential velocity of the vortex, $I_a = u'/v_0$, and the ratio of integral length scale to vortex core radius $\Lambda/r_c = 5.8$. Since the linear superposition of two Lamb–Oseen vortices may introduce additional perturbances to the flow [29], the wake vortices are allowed to form quasi-steady dipoles in a two-dimensional viscous pre-simulation. For further details regarding the numerical approach and turbulence initialization see Table 1 and [24].

Figs. 6, 9 display the temporal evolution of a single vortex (SV) and two vortex pairs (VP) with different vortex separations, $b_0/r_c$, for the turbulence intensity $I_a = 5.5\%$ in a sequence of perspective views of iso-surfaces of $\lambda_2$.[2] Different values for $\lambda_2$ are chosen to visualize the primary vortices and the SVS. In Fig. 6 eddies of the ambient turbulence field become visible when they are intensified

[2] The second eigenvalue $\lambda_2$ of the symmetric tensor $S^2 + \Omega^2$ is a measure for coherent vortex structures [17], where $S$ and $\Omega$ denote the symmetric and antisymmetric parts of the velocity gradient tensor. For coherent vortex structures, the resulting $\lambda_2$ iso-surfaces largely correspond to iso-surfaces of the vorticity norm.

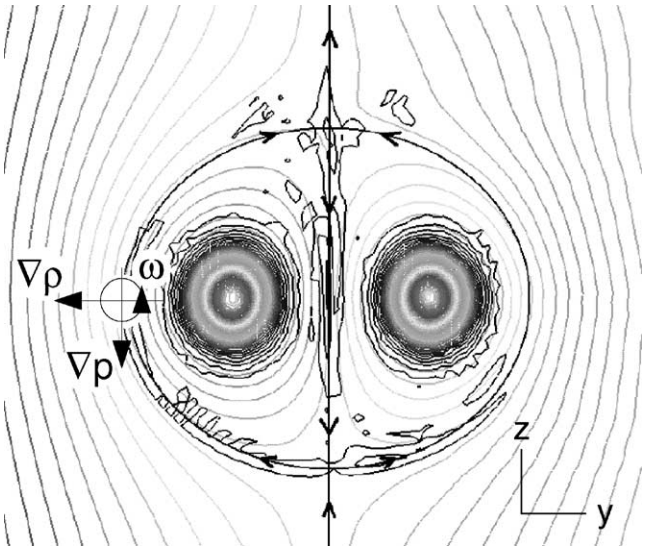


Fig. 7. Iso-lines of vorticity and streamfunction in a reference frame that descends with the vortices. Additionally, the baroclinical vorticity production in a stably stratified atmosphere is illustrated.

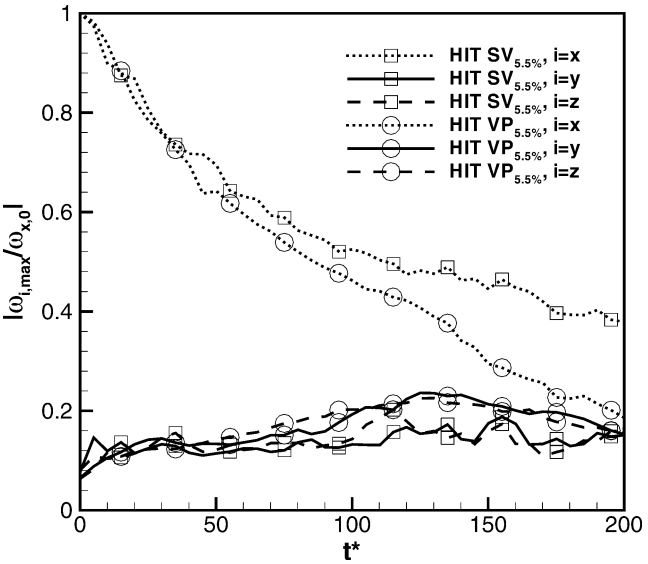


Fig. 8. Temporal evolution of the extrema of each vorticity component of the single vortex and vortex pair cases with $I_a = 5.5\%$ and $b_0/r_c = 8$. Vorticity extrema are averaged over the axial direction, $x$, and are normalized by the initial maximum of axial vorticity, $\omega_{x,0}$.

by vortex stretching which is induced by the primary vortices. The amount, length and intensity of the SVS increase with time. The numerous coherent SVS deform the primary vortices and lead initially to a similar decay rate in the single vortex case and the case with large vortex separation (see Fig. 5). At $t^* = 60$ the decay rates of vortex pair and single vortex start to deviate from each other and, eventually, at $t^* = 100$ the decay of the single vortex levels off. It should be noted that for the single vortex case a domain of transversally doubled size was used to assure the independence of results from the shear produced in between the single vortex and its periodic counterparts. For vortex pairs this shear is much weaker because neighbouring vortices induce velocities of the same direction and magnitude in the vicinity of the periodic boundaries.

Additionally to the mechanisms that produce SVS around a single vortex, the topology of vortex pairs provides a further mechanism that can be explained by considering streamlines in a framework that descends with the vortices (see Fig. 7). Along the streamlines that connect the two distinct hyperbolic stagnation points, the flow is accelerated and descelerated which exerts both stretching and squeezing of embedded eddies. Fig. 6 illustrates that while for the single vortex all SVS tend to be aligned azimuthally, the vortex pair produces also vertical vorticity streaks midway between the vortices (stretching by vertical gradients of the vertical velocity $\partial w/\partial z$ in the vicinity of the upper stagnation point) and oval-shaped streaks (stretching by lateral gradients of the lateral velocity $\partial v/\partial y$ in the vicinity of the lower stagnation point). These additional SVS contribute to decay by turbulent diffusion and, in particular, by exchange of vorticity in between the counter-rotating vortices. The comparison of decay rates for SV and VP in Fig. 5 indicates that the latter mechanisms advance decay effectively.

Fig. 8 depicts the evolution of the extrema of each vorticity component normalized by the initial maximum of axial vorticity, $\omega_{x,0}$ for the cases shown in Fig. 6. This representation allows to quantitatively assess the efficiency of vortex stretching mechanisms. Due to diffusion processes the axial vorticity maxima decrease with time. However, the lateral and vertical vorticity maxima, $\omega_{y,\max}$, $\omega_{z,\max}$, which at $t^* = 0$ represent eddies of the background turbulence, increase with time, driven by vortex stretching, and roughly triplicate initial values around $t^* = 125$. $\omega_{y,\max}$ and $\omega_{z,\max}$ are of similar magnitude throughout the whole evolution, because the SVS appear alternately in both components. Since the vortex pair exerts stretching both across (cf. Fig. 3) and along (cf. Fig. 7) streamlines, its vorticity maxima grow faster and maintain higher values than in the single vortex case. Finally, all vorticity components of the vortex pair have decayed to a similar level at $t^* = 200$, when circulation is reduced to 20%. The vorticity extrema of the case SV start to deviate from those of case VP at approximately $t^* = 60$, a time that correlates well to the deviation of the respective circulation evolutions (see Fig. 5). At $t^* = 100$, when the circulation of case SV remains almost constant, the decay of $\omega_x$ is reduced and the SVS are not further stretched, i.e. vorticity values $\omega_{y,\max}$, $\omega_{z,\max}$ merely fluctuate around constant values.

When vortex separation is reduced, the evolution of the circulation shows a very different decay behaviour. After a short phase of gradual decay governed by turbulent diffusion, the elliptic/short-wave instability [20,21] is developing weakly (linear phase) (see Fig. 9). Subsequently, for $t^* > 15$ the Crow/long-wave instability is largely amplified and the circulation starts to decay rapidly (which in part is due to the fact that circulation is only determined from the vorticity


Fig. 9. As Fig. 6 for vortex pair with $b_0/r_c = 4$ at $t^* = 15, 25, 50$.

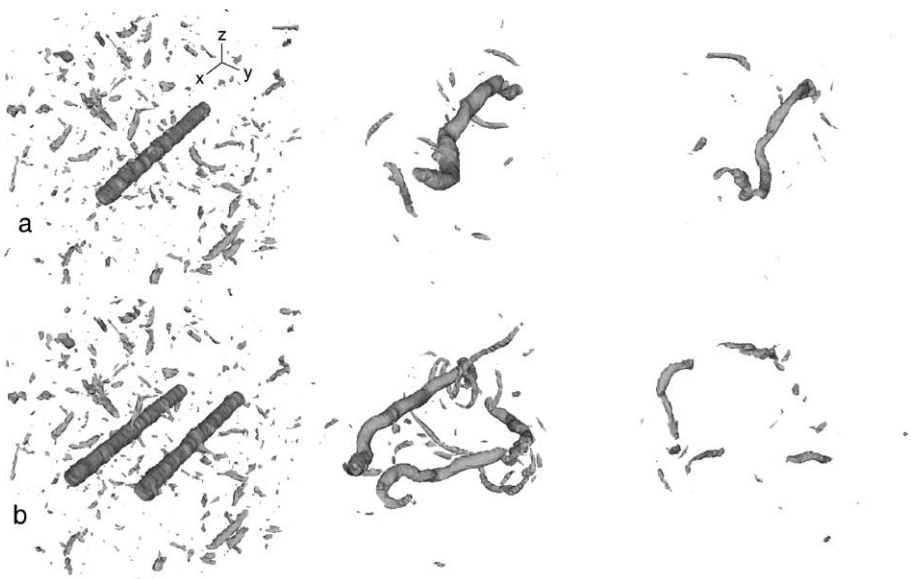


Fig. 10. Sequence of perspective views of iso-surfaces of $\lambda_2$ for (a) a single vortex and (b) a vortex pair with $I_a = 24\%$ and $b_0/r_c = 8$ at $t^* = 0, 30, 60$.

component aligned with the flight direction). After reconnection of the two primary vortices at $t^* = 25$ a vortex ring is formed at $t^* = 50$. This ring remains coherent for a certain time but deforms under its own induction and loses strength.

In the highly turbulent case ($I_a = 24\%$) depicted in Fig. 10 the primary vortices are too weak to essentially stretch the turbulent eddies. Here it is the strong ambient turbulence that directly deforms and destroys the vortices rapidly. No differences between the decay of the vortex pair and the single vortex are seen (see also Fig. 5). This indicates that interactions between the vortices of the vortex pair do not contribute to decay in strong turbulence.

## 4. Vortex decay in a turbulent stably stratified atmosphere

The large-eddy simulation code LESTUF which solves the Boussinesq-approximated Navier–Stokes equations and uses the classical Smagorinsky closure is employed to simulate wake vortex evolution in a thermally stably stratified atmosphere with superimposed moderate, anisotropic, and decaying turbulence. The turbulence, which is described in detail in [8], obeys prescribed spectra with $I_a = 3.6\%$, and $\Lambda/r_c = 12$. Turbulence induced by the aircraft is superimposed on the vortices by adding initially three-dimensional random perturbations with a maximum turbulence intensity of $I_v = 12\%$ at the core radius. The prescribed mean potential temperature gradient of the atmosphere, $d\Theta/dz$, is constant in each calculation and the corresponding normalized Brunt–Väisälä frequencies $N^* = (g/\Theta_0 \cdot d\Theta/dz)^{1/2}(2\pi b_0^2/\Gamma_0)$ are set to 0, 0.35, and 1. The pair of superimposed Lamb–Oseen vortices is initialized with a ratio of $b_0/r_c = 12$ for which a self-adaption phase is not necessary because the resulting distortions are weak [29]. For further details regarding the numerical set-up we refer to [14] and Table 1.

Fig. 11 depicts iso-contours of the lateral and vertical vorticity components that are induced by the wake vortices (represented by tubular $\lambda_2$-contours) in a stably stratified turbulent atmosphere for two degrees of stratification. In the case $N^* = 0.35$, the iso-lines of the lateral velocity, $v$, illustrate the converging flow that is induced by the wake vortices. This converging flow is deformed by turbulence such that the iso-line $v = 0$ (bold) meanders along the symmetry plane between the vortices. As described in quantitative detail in [14], such a superposition of turbulent and wake vortex induced velocities produces axial gradients of the lateral velocity, $\partial v/\partial x$, and, equivalently, vertical vorticity, $\omega_z \sim \partial v/\partial x$ in a volume above and midway

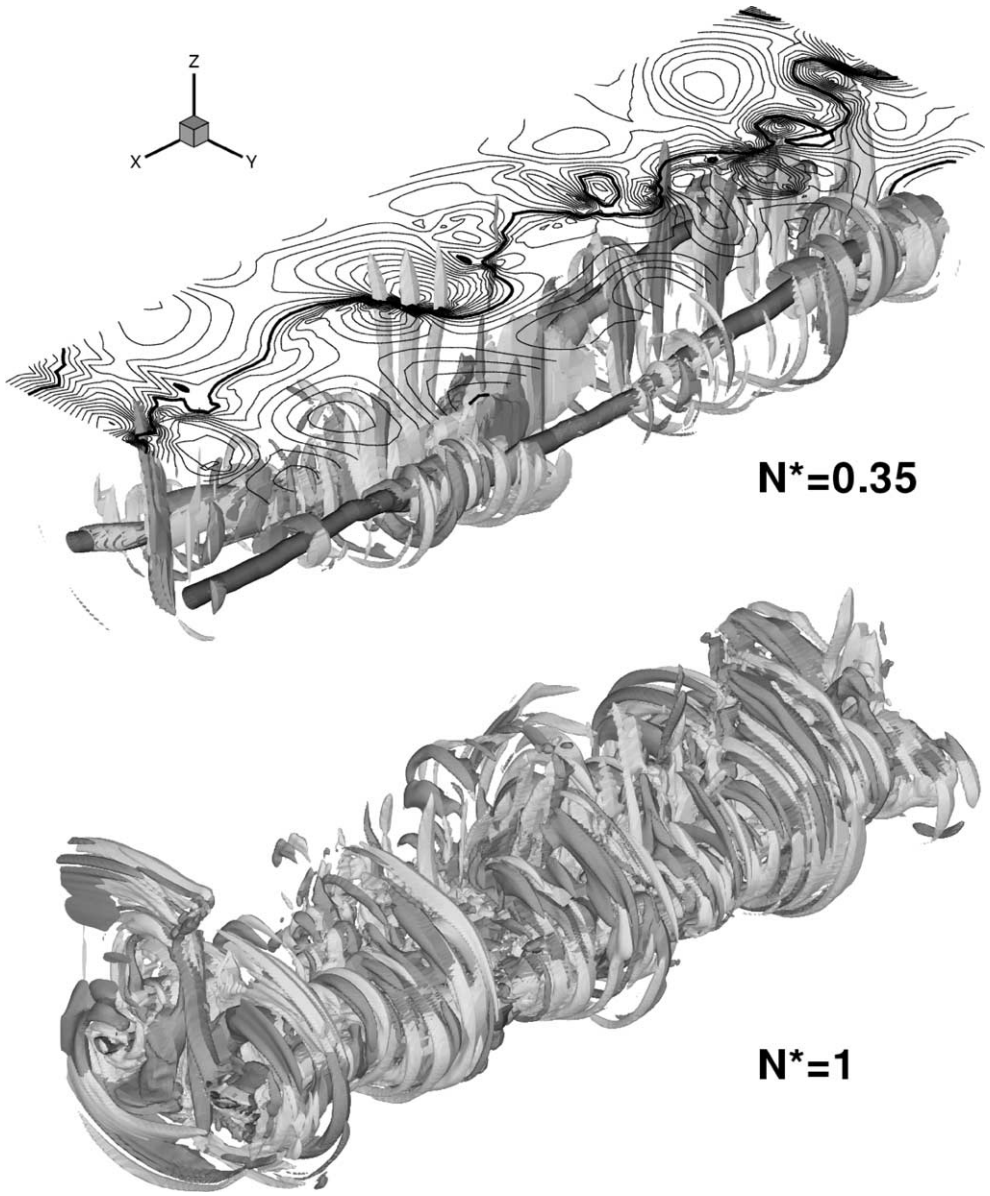


Fig. 11. Wake vortex evolutions in a turbulent and weakly stratified ($N^* = 0.35$) and in a turbulent and strongly stratified ($N^* = 1$) atmosphere at $t^* = 120$. Iso-surfaces of lateral and vertical vorticity components ($\omega_y^* = \omega_z^* = 0.125$ ($-0.125$) plotted dark grey (light grey)) in a perspective view. Wake vortices are represented by black tubular $\lambda_2$-contours. For $N^* = 0.35$, iso-lines for lateral velocity, $v$, are plotted in a horizontal plane above the vortices.

between the vortices. The resulting vertical vorticity streaks, $\omega_z$, are amplified by vortex stretching due to the acceleration of the downwards directed flow between the main vortices. Then, the vorticity is tilted, and wraps around the primary vortices.

The intense SVS in Fig. 11 below demonstrate that strong stable stratification ($N^* = 1$) intensifies these effects considerably. The source of this intensification is the baroclinical vorticity, $\omega_x$, which is produced by the baroclinic torque according to

$$\frac{D\omega_x}{Dt} \sim \frac{1}{\rho^2}\nabla\rho \times \nabla p \tag{2}$$

along the oval-shaped interface (see Fig. 7) between the ambient flow and the adiabatically heated flow that descends with the vortices [13]. This baroclinical vorticity additionally induces lateral velocities above the vortices that are directed towards the symmetry plane. Herewith it intensifies the axial gradients of the lateral velocity which finally cause the vertical and azimuthal vorticity structures and the related decay. Fig. 5 quantifies the impact of a stably stratified atmosphere on the longevity of wake vortices.

## 5. Wake vortices in a turbulent environment with constant shear

Shear flows exhibit vigorous and variform influences on wake vortex transport and decay. Wake vortices that interact

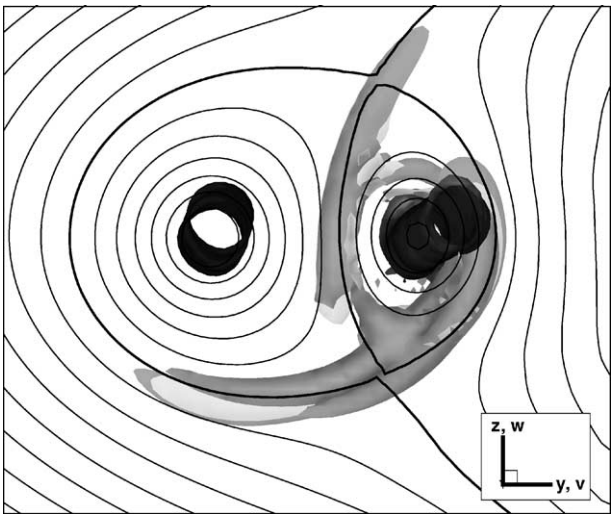


Fig. 12. Axial view of wake vortices in a turbulent environment with constant positive background shear at $t^* = 47$. Iso-surfaces of lateral and vertical vorticity components ($\omega_y^* = \omega_z^* = 0.63$ ($-0.63$) plotted dark grey (light grey)); wake vortices represented by black tubular $\lambda_2$-contours. Streamlines in a reference system that moves with the vortices in the plane $x = L_x/2$.

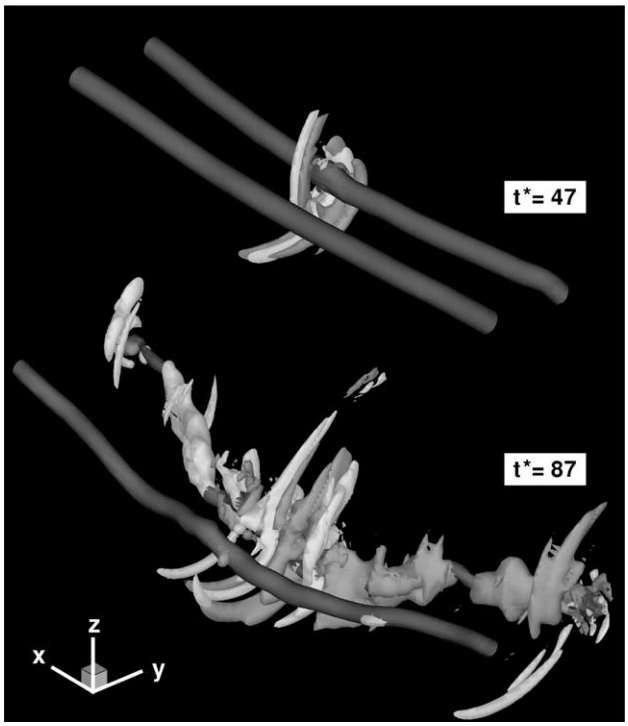


Fig. 13. Wake vortices in turbulent sheared environment in a perspective view. Iso-surfaces as in Fig. 12.

with a shear layer may experience vortex tilting, separation and subsequent rebound of vortices, whereupon the vortex with opposite signed vorticity to the shear layer shows the stronger tendency to rebound [25]. It is again the vortex with opposite-signed vorticity that decays distinctly faster when the vortex pair immerges into a turbulent shear-layer [12]. Also the spectacular rebound observed at London-Heathrow Int'l Airport [10] can be at least in part attributed to shear-layer effects [15]. However, these effects are not observed in laminar flows with constant shear [11].

Here, we report a DNS of vortex evolution in a constantly sheared and turbulent environment. For this purpose the code MESOSCOP [28] is employed which solves the Boussinesq-approximated Navier–Stokes equations. The pair of Lamb–Oseen vortices with a vortex spacing of $b_0/r_c = 8$ is perturbed sinusoidally with an amplitude of $0.01b_0$ at the wavelength of $8.6b_0$ to trigger the Crow instability which allows to study the influence of vortex spacing on decay. The weak homogenous and initially isotropic ambient turbulence is characterized by $I_a = 0.7\%$, and $\Lambda/r_c \approx 8$. The prescribed constant background strain just compensates the strain that the left vortex would induce on the right vortex center. Employing the common normalization for vortex pairs the shear corresponds to $(\partial v/\partial z)(2\pi b_0^2/\Gamma_0) = 1$.

Fig. 12 shows the wake vortices represented by black tubular $\lambda_2$-contours in an axial view. The corresponding streamlines indicate an intrinsic asymmetry of the vortex flow, as known from analytical investigations of wake vortices subjected to background shear [3] (compare Fig. 7 for the unsheared case). The formation of SVS (grey iso-surfaces of lateral and vertical vorticity) is in striking correlation with the streamline that separates the fluid in and outside the vortex oval. The right vortex, which is composed of opposite signed vorticity compared to the background vorticity of the shear, is closely encompassed by the SVS. A vertical streak evolves above the vortex pair that lags progressively behind the descending vortices because it develops partially outside the oval that descends with the vortices. This structure is similar as in unsheared cases (cf. Fig. 11) but here it is deflected to the right due to the advection by the background shear flow.

The perspective view for two different instants, depicted in Fig. 13, gives a spatial impression of the evolution of the flow structures. At $t^* = 47$ the SVS indicate that vortex stretching of ambient turbulence is most effective near the right vortex at the axial position where the vortices are closest. At this particular position the area around the right vortex which is enclosed by the bold separating streamline achieves the smallest size (cf. Fig. 12). Consequently, the SVS structures that extend from the stagnation points (i) have to cover a small distance to completely encompass the vortex and (ii) the SVS experience strong acceleration and, hence, strong stretching in the vicinity of the right vortex. Fluid, almost at rest at the stagnation point, follows the streamlines to locations of high circumferential velocity in close proximity to the right vortex core, resulting in strong acceleration. Contrary to non-sheared cases, the distance between left vortex (same signed vorticity as the background shear) and vortex oval boundary is increased, which gives an explanation for unbalanced decay rates and prolongated lifetimes of the vortices [11].

At $t^* = 87$ SVS have formed all along the right vortex and have initiated a rapid decay phase (see Fig. 5). As a

result of the initial perturbation the vortices link at about $t^* = 100$ which initiates rapid decay also for the left vortex. This is combined with tilting of the closely spaced vortex segments caused by mutual induction of the unequally strong vortices.

## 6. Comparison of decay characteristics

So far we employed normalized time based on the vortex time scale, $t_0 = 2r_c/v_0$, to allow for the comparison of decay characteristics of both single vortex and vortex pair cases (see Fig. 5). We found in Section 3 that a reduction of normalized vortex spacing by a factor of two may accelerate decay by a factor of four. Alternatively, we now employ the normalization of time that is commonly used for vortex pairs and is based on the time scale $t_0 = 2\pi b_0^2/\Gamma_0$. Fig. 14 indicates that now the decay rates of the two cases HIT, $I_a = 5.5\%$ with a variation of vortex separation by a factor of two almost coincide. This means that the time normalization for vortex pairs considers the effects of vortex separation correctly even when the underlying decay mechanisms may differ considerably (cf. Figs. 6, 9). Another consequence is that increasing vortex core radii for a given vortex separation reduces lifetime only slightly, whereas a reduction of $b_0$ may be very beneficial for an accelerated vortex decay.

A comparison of all cases in Fig. 14 indicates that the life span of the vortices is basically correlated to the intensity of ambient turbulence. However, the specific pecularities of the different cases, like additional superposition of aircraft-induced turbulence in the stratified cases or initial perturbation of the vortex spacing in the sheared case, modify the ranking according to background turbulence. Imposing additionally a stable temperature stratification with $N^* = 1$ may reduce wake vortex lifetime by roughly two time units whereas an increase of ambient turbulence from $I_a = 5.5\%$ by a factor of four may shorten wake vortex life by four time units. In contrast, dimensional analysis tells us that the life span of wake vortices in a given environment may be halved by a reduction of vortex spacing by a factor of $\sqrt{2}$.

## 7. Formation of secondary vorticity and decay mechanisms

As shown in the previous sections the formation of coherent secondary vorticity around the primary vortices is a prominent feature of wake vortex evolution in the atmosphere. In the following we list common aspects of the related mechanisms.

(i) Incoherent vorticity of background turbulence achieves coherence by tilting and stretching. It is the primary vortex that alignes (tilting) and reinforces (stretching) random vorticity such that SVS are produced.

(ii) However, a single vortex filament that is stretched will conserve its circulation (Helmholtz theorem). Hence, the vorticity of the vortex filament may be increased considerably by stretching, but its far field effect in terms of velocity induction is not modified.

(iii) Although the merger of several coherent vorticity filaments of equal sign may generate larger SVS, this mechanism likewise does not amplify far field effects.

(iv) Far field velocity induction (circulation) is generated and increased when vorticity of arbitrary orientation which has no far field effect is aligned to coherent structures by the tilting process.

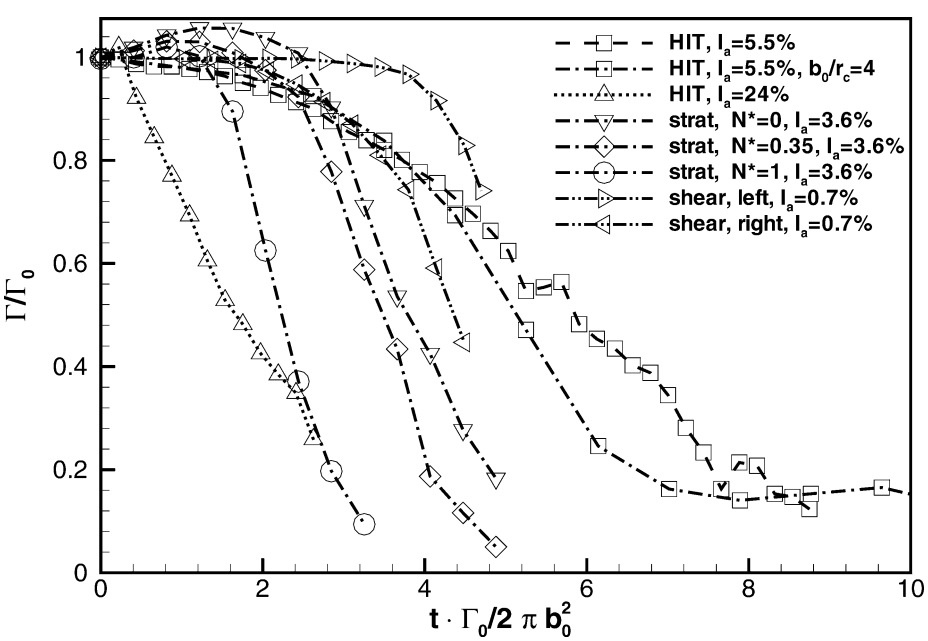


Fig. 14. Temporal evolution of normalized circulation where the common normalization of time for vortex pairs is employed. Circulations determined as in Fig. 5.

(v) The tilting mechanism is effective for any vorticity structure that at least contains some radial vorticity component and (vi) tilting provokes simultaneous stretching. This can be illustrated by considering vortex tilting and stretching in a background flow given by a single plane potential vortex, $V_\theta(r) = \Gamma/(2\pi r)$. Viscous and baroclinic effects are neglected.

For convenience, the secondary vorticity, $\omega_s$, is given in an instantaneous local Cartesian coordinate system with direction $s$ along the spiral-shaped vortex line, and $n$ away from the center of curvature (cf. Fig. 3). The tilting and stretching terms read

$$\frac{D\omega_n}{Dt} = \omega_s \frac{\partial U_n}{\partial s}, \qquad \frac{D\omega_s}{Dt} = \omega_s \frac{\partial U_s}{\partial s}, \tag{3}$$

where the velocity gradients along the vortex line, $\partial U_n/\partial s$, $\partial U_s/\partial s$, are prescribed by the background flow $V_\theta(r)$. For the tilting term it follows

$$\begin{aligned}\frac{D\omega_n}{Dt} &= \omega_s \frac{\partial U_n}{\partial r}\frac{\partial r}{\partial s} = \omega_s \frac{\partial (V_\theta \sin\varphi)}{\partial r}\frac{\partial r}{\partial s} \\ &= \omega_s \frac{\Gamma}{2\pi r^2}\sin^2\varphi,\end{aligned} \tag{4}$$

where $\varphi$ denotes the angle between $V_\theta$ and $U_s$. In analogy the stretching term yields

$$\begin{aligned}\frac{D\omega_s}{Dt} &= \omega_s \frac{\partial U_s}{\partial r}\frac{\partial r}{\partial s} = \omega_s \frac{\partial (V_\theta \cos\varphi)}{\partial r}\frac{\partial r}{\partial s} \\ &= \omega_s \cos\varphi \frac{\Gamma}{2\pi r^2}\sin\varphi.\end{aligned} \tag{5}$$

Eqs. (4) and (5) specify the limits of the processes: Tilting is strongest for radially oriented vorticity filaments because $\partial r/\partial s = \sin\varphi = 1$ and tilting ceases for azimuthally oriented structures because in azimuthal direction $\sin\varphi = 0$. Radially aligned filaments are not yet stretched because $\cos\varphi = 0$, whereas azimuthally oriented structures can not be further stretched ($\sin\varphi = 0$). In summary, radially oriented vorticity is first tilted and then tilted and stretched simultaneously until both processes decay when in the long-term limit the SVS tend to be aligned azimuthally.

(vii) SVS can deform primary vortices. In particular, counter-rotating SVS can stretch (squeeze) the primary vortices when approaching (departing from) each other (see Fig. 2, $t^* = 210$).

(viii) In a reference frame that descends with the vortex pair the vortices are engulved by a oval-shaped streamline with stagnation points below and above the vortices (see Fig. 7). Due to the low velocities at the stagnation points already minor disturbances are sufficient to displace the stagnation points which enables entrainment of ambient vorticity into the oval (see Fig. 11). Entrained vorticity is subsequently intensified according to the right equation in (3) by vortex stretching along streamlines in the accelerated flow midway between the vortices or along the half moon shaped streamlines around the vortices.

(ix) Counter-rotating vorticity streaks produced midway between the vortices can be effective in exchanging fluid across the symmetry line. This effect is prerequisite for direct cancelation of primary vorticity [3,14].

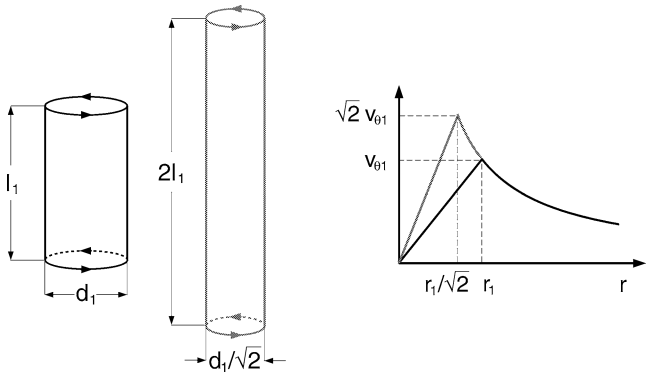


Fig. 15. Sketch to illustrate the increase of rotational energy of a stretched Rankine vortex.

(x) A primary vortex that stretches SVS as depicted in Fig. 3 performes work on the SVS. During the stretching process the SVS gain rotational energy, whereas the primary vortex, in turn, loses rotational energy. This can be delineated phenomenologically by considering a vortex tube with a Rankine tangential velocity distribution that is stretched by a factor of 2 (see Fig. 15). The increase in length corresponds to a contraction by a factor of $1/\sqrt{2}$ (mass conservation). During stretching angular momentum is conserved ($r v_\theta = \text{const.}$), which means that the potential vortex region is not affected by stretching. But the angular velocity of the contracted vortex core is doubled according to $\Omega_2 = r_1^2/r_2^2 \Omega_1$ because $r_2 = r_1/\sqrt{2}$. The work performed on the vortex core, $W_{1,2}$, which corresponds to its gain of rotational energy, $\Delta E$, amounts to

$$\begin{aligned}W_{1,2} &= E_2 - E_1 = \frac{1}{2}\left(m\frac{r_2^2}{2}\Omega_2^2 - m\frac{r_1^2}{2}\Omega_1^2\right) \\ &= \frac{1}{2}\left(m\frac{r_1^2}{4}4\Omega_1^2 - m\frac{r_1^2}{2}\Omega_1^2\right) = E_1.\end{aligned} \tag{6}$$

Hence, a doubling of length corresponds directly to a doubling of rotational energy of the flow in the vortex core of the SVS. The described mechanism is in direct analogy to the energy transfer from large eddies to small eddies in turbulent flows [32]. In our cases it is most obvious in the jet vortex interaction where rotational energy of the primary vortex decreases only on smaller radii (Fig. 4) and in the low-turbulence cases of Section 3 (Figs. 5, 6, 8). In particular, in the single vortex case HIT $SV_{5.5\%}$ circulation decay ends at a time of $t^* = 100$ when the SVS are not further stretched.

(xi) The formation of SVS may trigger the formation of cooperative instabilities as the short-wave instability [21] and the Crow [2] instability.

With the exception of cooperative instabilities the described mechanisms are independent from the ratio of vortex core radius and vortex separation. We therefore assume that the relatively large vortex cores that we used here and that are commonly employed in numerical simulations do not derogate the current results.

## 8. Conclusions

The presented numerical simulations of wake vortex evolution in the atmosphere indicate that stretching, tilting and merger of ambient vorticity caused by the primary vortices are the prominent mechanisms in vortex evolution and decay. In the cases with low to moderate turbulence possibly combined with thermal stable stratification and/or constant shear as well as with jet–vortex interactions these mechanisms create spatially and temporarily extended coherent secondary vortices out of the ambient incoherent flow. At first, the creation of these secondary vorticity structures consumes energy of the primary vortices. Secondly, the secondary vorticity structures, in turn, have a far field impact, and thus, deform the primary wake vortices. It is shown that these mechanisms lead to an initially gradual and subsequent rapid decay. Whereas continous decay can be attributed to diffusion and the work that the primary vortices perform on the secondary vorticity structures, rapid decay is associated with the interaction of secondary vorticity with the primary vortex pair which causes an exchange and mutual annihilation of primary vorticity, also in combination with instability mechanisms and the transition to fully turbulent vortices. For single vortices, longitudinal stretching of secondary vorticity and the mutual exchange of primary vorticity between counter-rotating vortex pairs does not apply. Therefore, the decay of single vortices is strongly reduced when the energy transfer from primary to secondary vortices ceases because the secondary vortices are no longer stretched substantially when they tend to be aligned azimuthally. In a highly turbulent atmosphere, the primary vortices are too weak and the time scales of vortex decay are too short to essentially stretch atmospheric eddies. As a consequence, the wake vortices are rapidly disrupted directly by ambient turbulence.

It should be noted that numerical simulations of wake vortices in the atmosphere unavoidably suffer from limited resolution of the vortex core region. Whereas DNS only reach small Reynolds numbers it is the type of subgrid-scale closure that controls vortex core evolution in LES [15]. Both approaches do not meet the complex interaction of turbulence and rotation at high *Re* flows together with the peculiarities of specific aircraft configurations and environmental conditions. This limitation will persist despite the enormous increase of computational power and the development of smart numerical methods. Full-scale experiments will remain both challenging and mandatory to ensure the validity of the conclusions drawn from numerical simulations.

## References

[1] S. Brunet, L. Jacquin, P. Geffroy, Experiment on heated jets/wake vortex interaction, ONERA RT 15/2496 DAFE/Y, 1999.
[2] S.C. Crow, Stability theory for a pair of trailing vortices, AIAA J. 8 (1970) 2172–2179.
[3] C.P. Donaldson, A.J. Bilanin, Vortex wakes of conventional aircraft, AGARDograph 204, 1975.
[4] F. Ducros, P. Comte, M. Lesieur, Large-eddy simulation of spatially growing boundary layer over an adiabatic flat plate, Internat. J. Heat Fluid Flow 16 (1995) 341–348.
[5] F. Garnier, F.C. Beaudoin, P. Woods, N. Louisnard, Engine emission alteration in the near field of an aircraft, Atmosph. Environ. 31 (1997) 1767–1781.
[6] C. Ferreira Gago, S. Brunet, F. Garnier, Numerical investigation of turbulent mixing in a jet/wake vortex interaction, AIAA J. 40 (2002) 276–284.
[7] T. Gerz, T. Ehret, Wingtip vortices and exhaust jets during the jet regime of aircraft wakes, Aerosp. Sci. Technol. 1 (1997) 463–474.
[8] T. Gerz, F. Holzäpfel, Wingtip vortices, turbulence, and the distribution of emissions, AIAA J. 37 (1999) 1270–1276.
[9] T. Gerz, F. Holzäpfel, D. Darracq, Commercial aircraft wake vortices, Prog. Aerosp. Sci. 38 (2002) 181–208.
[10] J.S. Greenwood, J.M. Vaughan, Measurements of aircraft wake vortices at Heathrow by laser doppler velocimetry, Air Traffic Control Quarterly 6 (1997) 179–203.
[11] T. Hofbauer, Numerische Untersuchungen zum Einfluss von Windscherung und Turbulenz auf Flugzeugwirbelschleppen, Ph.D. Dissertation, DLR, Oberpfaffenhofen, 2002.
[12] T. Hofbauer, T. Gerz, Shear-layer effects on the dynamics of a counter-rotating vortex pair, AIAA Paper 2000-0758, 2000.
[13] F. Holzäpfel, T. Gerz, Two-dimensional wake vortex physics in the stably stratified atmosphere, Aerosp. Sci. Technol. 3 (1999) 261–270.
[14] F. Holzäpfel, T. Gerz, R. Baumann, The turbulent decay of trailing vortex pairs in stably stratified environments, Aerosp. Sci. Technol. 5 (2001) 95–108.
[15] F. Holzäpfel, T. Hofbauer, T. Gerz, U. Schumann, Aircraft wake vortex evolution and decay in idealized and real environments: methodologies, benefits and limitations, in: R. Friedrich, W. Rodi (Eds.), Advances in LES of Complex Flows, Kluwer, Dordrecht, 2002, 2002, pp. 293–309.
[16] F. Holzäpfel, T. Gerz, F. Köpp E. Stumpf, M. Harris, R.I. Young, A. Dolfi-Bouteyre, Strategies for circulation evaluation of aircraft wake vortices measured by lidar, J. Atmos. Ocean. Tech., accepted for publication.
[17] F. Jeong, J. Hussain, On the identification of a vortex, J. Fluid Mech. 285 (1995) 69–94.
[18] H.-J. Kaltenbach, T. Gerz, U. Schumann, Large-eddy simulation of homogeneous turbulence and diffusion in stably stratified shear flow, J. Fluid Mech. 280 (1994) 1–40.
[19] L. Kleiser, U. Schumann, Spectral simulations of the laminar-turbulent transition process in plane poiseuille flow, in: Spectral Methods for Partial Differential Equations, SIAM, Philadelphia, 1984, pp. 141–163.
[20] F. Laporte, D. Darracq, A. Corjon, On the vortex-turbulence interaction: DNS of elliptic instability of a vortex pair, AIAA Paper 99-3417, 1999.
[21] T. Leweke, C.H.K. Williamson, Cooperative elliptice instability of a vortex pair, J. Fluid Mech. 360 (1998) 85–119.
[22] R.C. Miake-Lye, M. Martinez-Sanchez, R.C. Brown, C.E. Kolb, Plume and wake dynamics, mixing and chemistry behind a high speed civil transport, J. Aircraft 30 (1993) 467–479.
[23] A. Michalke, G. Hermann, On the inviscid instability of a circular jet with external flow, J. Fluid Mech. 114 (1982) 343–359.
[24] H. Moet, D. Darracq, F. Laporte, A. Corjon, Investigation of ambient turbulence effects on vortex evolution using LES, AIAA Paper 2000-0756, 2000.
[25] F.H. Proctor, D.A. Hinton, J. Han, D.G. Schowalter, Y.-L. Lin, Two-dimensional wake vortex simulations in the atmosphere: Preliminary sensitivity studies, AIAA Paper 97-0056, 1997.
[26] F.H. Proctor, G.F. Switzer, Numerical simulation of aircraft trailing vortices, in: 9th Conf. on Aviation, Range and Aerospace Meteorology 7.12, 2000, pp. 511–516.
[27] F. Risso, A. Corjon, A. Stoessel, Direct numerical simulations of wake vortices in intense homogeneous turbulence, AIAA J. 35 (1997) 1030–1040.

[28] U. Schumann, T. Hauf, H. Höller, H. Schmidt, H. Volkert, A mesoscale model for the simulation of turbulence, clouds and flow over mountains: Formulation and validation examples, Beitr. Phys. Atmosph. 60 (1987) 413–446.

[29] D. Sipp, L. Jacquin, C. Cossu, Self-adaption and viscous selection in concentrated two-dimensional vortex dipoles, Phys. Fluids 12 (2000) 245–248.

[30] P.R. Spalart, Airplane trailing vortices, Annu. Rev. Fluid Mech. 30 (1998) 107–138.

[31] A. Stoessel, An efficient tool for the study of 3d turbulent combustion phenomena on MPP computers, in: Proceedings of the HPCN 95 Conference, Springer-Verlag, 1995, pp. 306–311.

[32] H. Tennekes, J.L. Lumley, A First Course in Turbulence, MIT Press, Cambridge, MA, 1972.

[7]

# Adjustment of Subgrid-Scale Parametrizations to Strong Streamline Curvature

F. Holzäpfel

AIAA Journal, 2004

Volume 42, Number 7, Pages 1369–1377

AIAA JOURNAL
Vol. 42, No. 7, July 2004 (Tentative)

# Adjustment of Subgrid-Scale Parametrizations to Strong Streamline Curvature

Frank Holzäpfel*
*DLR, German Aerospace Research Center, Oberpfaffenhofen, 82234 Weßling Germany*

**A subgrid-scale model correction for large eddy simulations that address flowfields with embedded areas of poorly resolved strong streamline curvature effects is proposed. The devised modification is termed NaCoo and provides an isotropic correction of the subgrid-scale viscosity based on local centrifugal stability. The degree of stability is identified via a rotational Richardson number that is determined based on non-Galilean-invariant streamline curvature at every grid point. NaCoo allows for a more realistic representation of inadequately resolved coherent turbulent vortices. Its main benefits are 1) conservation of the peak vorticity in the vortex cores, 2) reduction of vortex core radius growth rates, 3) an approach to properties of tangential velocity profiles found in experiments 4) allowance for appropriate turbulence levels in the vicinity of the vortices, and 5) non suppression of vortex core meandering. The derivation of NaCoo, its properties, and sensitivity to numerical and vortex parameters are described in detail. Applications of the correction to single vortices and aircraft wake vortices in a quiescent and turbulent environment demonstrate the capabilities of the pragmatic correction.**

## Nomenclature

| | | |
|---|---|---|
| $a$ | = | acceleration |
| $b$ | = | vortex spacing |
| $C$ | = | constant |
| $c_S$ | = | model coefficient |
| $D$ | = | magnitude of deformation tensor, $D_{ij} = 2S_{ij}$ |
| $e$ | = | unit vector |
| $F_r$ | = | restoring force |
| $p$ | = | dynamic pressure fluctuation |
| $Ri$ | = | Richardson number |
| $r$ | = | radial coordinate |
| $r_c$ | = | vortex core radius |
| $S_{ij}$ | = | strain rate tensor |
| $t$ | = | time |
| $u$ | = | axial velocity |
| $v$ | = | (lateral) velocity |
| $w$ | = | vertical velocity |
| $x$ | = | axial coordinate |
| $y$ | = | lateral coordinate |
| $z$ | = | vertical coordinate |
| $\alpha$ | = | model coefficient |
| $\Gamma$ | = | circulation |
| $\Delta$ | = | effective mesh size |
| $\nu$ | = | kinematic viscosity |
| $\rho$ | = | density |
| $\tau_{ij}$ | = | subgrid-scale (SGS) fluxes of momentum |
| $\Omega$ | = | magnitude of vorticity |
| $\omega$ | = | oscillation frequency |

*Subscripts*

| | | |
|---|---|---|
| $n$ | = | normal direction |
| SGS | = | subgrid scale |
| $t$ | = | tangential direction |
| $\theta$ | = | azimuthal direction |
| 0 | = | initial value |

*Superscripts*

| | | |
|---|---|---|
| $*$ | = | normalized quantity, based on $b_0$, $\Gamma_0$ |
| $'$ | = | normalized quantity, based on $\Delta$, $r_{c0}$, $\Gamma_0$ |
| $''$ | = | SGS fluctuation |

Received 27 October 2003; revision received 25 February 2004; accepted for publication 26 February 2004. 

*Research Scientist, Institute of Atmospheric Physics; frank.holzaepfel@dlr.de.

## I. Introduction

A SEEMINGLY endless number of efforts have been geared toward the achievement of approaches for adequate numerical treatment of turbulent flows with pronounced streamline curvature and rotation effects. An impressive amount of semi-empirical modifications for curvature effects were developed for the class of Reynolds-Averaged Navier–Stokes approaches, in particular, for the widespread, cost-efficient, and robust k–$\epsilon$ turbulence model.[1] Until today, numerous corrections had been suggested for eddy-viscosity models,[2] during which time it was generally recognized that the more costly second-moment turbulence closures have a fundamental advantage over eddy-viscosity models due to the explicit appearance of rotation and curvature terms in the transport equations.[3,4] The even more costly large-eddy simulation (LES) explicitly simulates the Navier–Stokes equations and, thus, fully considers the effects of curvature and rotation in the resolved scales. Therefore, LES have been applied to improve the fundamental understanding of the effects of rotating flows.[5] Driven by the ever-growing computational power, LES is also increasingly used for applied problems.[6,7] However, such applications often demand an unpleasant tradeoff between the complexity of the tackled problem and an adequate numerical representation such that the impact of the subgrid-scale (SGS) closure may become more dominant. Another more specific way to circumvent resolution requirements is the vorticity confinement method,[8] which preserves tight vortices even in coarse numerical meshes. Recent developments of this method try to counterbalance vorticity confinement and numerical diffusion.[9] This could allow researchers to address problems where vortex decay is of relevance.

LES explicitly simulate turbulent eddies that are resolved on a computational grid, whereas smaller-scale fluctuations are smoothed and modeled by SGS closures. If the scales of eddies that dominate turbulent transport are resolved, the subgrid model primarily has to provide an appropriate energy sink that prevents a tailback of small-scale energy. If, however, the larger-scale turbulence is suppressed by stabilizing body forces, such as the buoyancy force in a stably stratified environment or centrifugal forces in a rotating flow, or is damped in the vicinity of a wall, the SGS model may locally control turbulent transport. As a consequence, the flow regions that are strongly affected by body forces may represent a

solution of the SGS model rather than of the Navier–Stokes equations. Even without strong damping of the resolved turbulence, the velocity gradients of poorly resolved embedded areas of strong coherent rotation may dominate turbulent fluctuations. As a consequence, simulation results may be adulterated because, in general, the effects of centrifugal and Coriolis forces are not represented by the SGS closure.

These effects become most objectionable when an appropriate resolution of all involved length scales is not feasible. An example is given by simulations that investigate the interaction of aircraft wake vortices with environmental conditions, which basically suffer from limited resolution. This becomes immediatly clear for an LES of wake vortex evolution in a convectively driven atmospheric boundary layer.[10] Ideally, the LES should resolve length scales spanning the order of approximately 0.1 m in the strongly rotating vortex cores to the order of 1000 m in the atmosphere, where the latter length scale roughly corresponds to the inversion height of a convective boundary layer. An appropriate equidistant numerical mesh would need $\mathcal{O}(10^{12})$ mesh points, whereas current grids are limited to about $10^7$–$10^9$ meshes. There are many other applications where it is desirable to model flows with strong streamline curvature with a modest number of grid points and without the need to resolve all details of the flow. An example for a geophysical flow is the simulation of tornadoes, technical applications that comprise the flow around aircraft wings in high-lift configuration, fighter aircraft under high angles of attack, or swirl combuster-type flows. In the latter example, the simulation of chemical reactions may dominate the numerical effort and an adequate representation of the swirling flowfield must be realized based on a relatively coarse grid.

The dynamic SGS model,[11] which is widespread for lower Reynolds number applications, suppresses successfully the SGS viscosity in a poorly resolved rectilinear vortex, provided that the direction employed for the averaging of SGS model coefficients coincides with the axis of rotation. However, in a test of the dynamic model, we already found that for small angles of less than 5 deg between the axis of rotation and the averaging direction, spurious SGS viscosity patches develop in the vortex core region that distort the vortex and cause numerical instability. The complex deformations that wake vortex pairs experience during their evolution prevent the determination of directions of statistical homogeneity that would allow for adequate averaging. A possible alternative is the Lagrangian dynamic model,[12] which accumulates averages along streamlines, a procedure that, however, is not Galilean-invariant.

The suggested SGS model modification termed NaCoo provides an isotropic correction of the SGS viscosity based on the degree of local centrifugal stability. The stability is identified via a rotational Richardson number that is determined based on streamline curvature at every grid point. The name NaCoo refers to the procedure that determines the curvature radius in natural coordinates. NaCoo was already partially introduced in Ref. 13. The title of this paper employs the objective "Strong" to characterize the degree of streamline curvature that increases when the center of a vortex is approached where the curvature eventually tends to infinity, whereas the curvature radius inversely goes to zero. Because of its low additional computational expense, NaCoo is suitable for LES approaches that follow the efficient philosophy of investment of as much as possible of the available computational resources in an outmost resolution of the grid scale flow and to consume as little as possible for sophisticated SGS closures and numerical schemes. The approach can, in principle, be adapted to any eddy-viscosity closure model. In contrast to the dynamic SGS model, which requires averaging of SGS model coefficients to stabilize the solution, the current approach is calculated locally at every grid point and, thus, may resolve even the smallest embedded vortices.

Because the correction is sensitive to streamline curvature, it is not Galilean-invariant. However, for many practical applications, including aircraft wake vortices, this is not a severe shortcoming because streamline curvature is determined naturally in an inertial frame of reference. A Galilean-invariant criterion for curvature and rotation can be defined when the direction of the principal axes of the strain rate tensor[14] is tracked. The higher complexity and increased numerical effort (20% plus vs our approach with a 5% penalty) of this alternative to streamline curvature[14] may counterbalance the advantage of Galilei invariance, at least for the large number of cases where Galilei invariance is of no relevance. Further SGS model modifications for streamline curvature effects are described in Refs. 15 and 16.

After a brief introduction of the applied basic equations and numerical methods appears in Sec. II, and the effects of the Smagorinsky closure on a single vortex are discussed in Sec. III. In Sec. IV, the stabilizing and destabilizing effects of streamline curvature are reviewed, and in Sec. V, the SGS correction NaCoo is introduced and compared to Proctor's approach.[13] Furthermore, aspects of the Galilei invariance issue are assessed. Section VI describes applications of NaCoo to single vortices and to aircraft wake vortices in a quiescent and turbulent environment. Finally, the sensitivity of the correction on numerical and vortex parameters is discussed in Sec. VII.

Beyond the applications shown in this paper, NaCoo has been applied to simulations of aircraft-generated multiple vortex systems that are expected to trigger cooperative instability mechanisms that lead to a premature onset of decay.[17] Another application of NaCoo addresses the reproduction of turbulence levels measured in wake vortices at different distances behind the generating aircraft (personal communication with R. E. Robins in 2003). **Q2**

## II. Governing Equations

To provide the background for the discussion of the streamline curvature correction, the basic equations and numerical methods of the applied code LESTUF[18] are briefly introduced. LESTUF was originally developed for studies of stratified, sheared, and homogeneous turbulence. In space and time the code solves the mass conservation equation

$$\frac{\partial u_i}{\partial x_i} = 0 \tag{1}$$

and the Navier–Stokes equations for the resolved velocity vector

$$\frac{\partial u_i}{\partial t} + \frac{\partial}{\partial x_j} u_i u_j = -\frac{1}{\rho}\frac{\partial p}{\partial x_i} - \frac{\partial \tau_{ij}}{\partial x_j} \tag{2}$$

in an unsteady, incompressible, and three-dimensional fluid flow. In Eq. (2), friction is represented by the SGS fluxes of momentum that result from the nonlinear term in Eq. (2) after filtering on the mesh scale. They are parameterized following an ansatz by Deardorff[19]

$$\tau_{ij} := \overline{u_i'' u_j''} - \tfrac{1}{3}\overline{u_i'' u_i''}\delta_{ij} = -2\nu_{\mathrm{SGS}} S_{ij} \tag{3}$$

with the strain rate tensor

$$S_{ij} = \frac{1}{2}\left(\frac{\partial u_i}{\partial x_j} + \frac{\partial u_j}{\partial x_i}\right) \tag{4}$$

The SGS viscosity is modeled by Smagorinsky's approach[20] (Fig. 1)

$$\nu_{\mathrm{SGS}} = (c_S \Delta)^2 (2 S_{ij} S_{ji})^{\frac{1}{2}} \tag{5}$$

where the constant $c_S = 0.165$ is set to the theoretical value for isotropic turbulence.

The physical fields are discretized on a Cartesian staggered grid and integrated in space and time by second-order finite differencing. Time advancement is performed by a prognostic step for advection and diffusion by the use of the second-order Adams–Bashforth scheme, followed by a diagnostic step that solves the Poisson equation for the dynamic pressure. The integration scheme is nondissipative and only weakly dispersive. The computational grid is equidistant, and periodic boundary conditions are employed in all directions. For anisotropic numerical meshes, the effective mesh size is calculated according to the fitting formula of Scotti et al.[21]

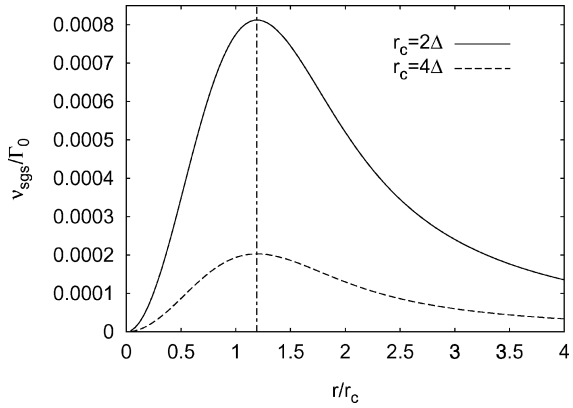


**Fig. 1 Radial profiles of normalized SGS viscosity for Smagorinsky closure and two different numerical resolutions.**

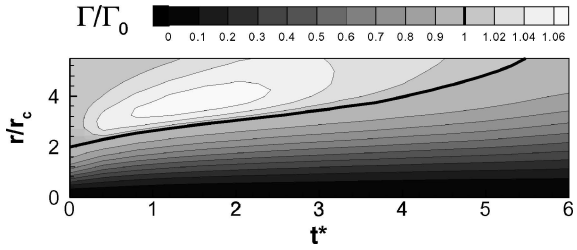


**Fig. 2 Temporal evolution of radial circulation distribution of a turbulent wake vortex in quiescent environment.**

## III. Effects of the Smagorinsky Approach

To illustrate the effects of strong streamline curvature, the Lamb–Oseen vortex is employed as a generic vortex. Any other analytically given continuously differentiable vortex profile could have been used. The tangential velocity profile of the Lamb–Oseen vortex consists of rigid-body rotation close to its center and a smooth blend to the potential vortex on large radii according to

**Q3**
$$v_\theta(r) = (\Gamma_0/2\pi r)\left[1 - \exp\left(-1.257r^2/r_c^2\right)\right] \tag{6}$$

As baseline case, a vortex with a core radius of $r_{c0} = 4$ m and a circulation of $\Gamma_0 = 565\ \mathrm{m}^2/\mathrm{s}$ is employed. To represent wake vortices generated by a B-747 aircraft, two counter-rotating vortices with a vortex spacing of $b_0 = 47$ m are superposed. For wake vortices, time is normalized by the time scale $2\pi b_0^2/\Gamma_0$.

To illustrate the impact of the Smagorinsky closure on coherent vortices, the Smagorinsky eddy viscosity [Eq. (5)] normalized by $\Gamma_0$ is derived for the Lamb–Oseen vortex

**Q4**
$$\nu_{\mathrm{SGS}}(r)/\Gamma_0 = \left[(c_S\Delta)^2/\pi r_c^2\right] \times \left[r_c^2/r^2 - \left(1.257 + r_c^2/r^2\right)\exp\left(-1.257r^2/r_c^2\right)\right] \tag{7}$$

and plotted in Fig. 1 for different vortex core resolutions. In Eq. (5), the strain rate tensor is applied for convenience in curvilinear coordinates, because then only the radial-tangential component of the strain rate tensor, $(r/2)[(\partial v_\theta/r)/\partial r]$, contributes to $\nu_{\mathrm{SGS}}$.

Note that in Eq. (7) the resolution of the vortex core, $(\Delta/r_c)$, enters to the power of two. Therefore, in poorly resolved vortex cores enhanced values of SGS viscosity are generated (Fig. 1) that cause large vortex core growth rates and a strong reduction of peak vorticity. Figure 1 delineates that $\nu_{\mathrm{SGS}}$ increases from zero at $r = 0$ (rigid-body rotation) to a maximum at $1.19r_c$ and then decreases again. (Obviously, when $r = 0$ is approached, molecular diffusion becomes relevant. Because this is a singular situation, molecular diffusion can be neglected in the LES.) As a consequence, the radial velocity profiles deviate from the family of self-similar Lamb–Oseen vortex profiles that develop for laminar simulations with constant viscosity. This is shown in Fig. 2, which shows the temporal evolution of the radial circulation distribution of a turbulent wake vortex in a quiescent environment. At $t^* = 0$, the initialized Lamb–Oseen vortex attains the maximum circulation of one at about $r > 2r_{c0}$. Later on, an overshoot of circulation is produced that reaches a maximum of 7% at around $t^* = 1.5$.

In this simulation, aircraft-induced turbulence was taken into account by the initial addition of a three-dimensional random perturbation field to the swirling flow, such that the perturbations reach maximum rms values of 2 m/s at the core radius and decay exponentially for smaller and larger radii. This type of turbulence initialization is referred to as case b. In Sec. VI, another scenario termed case a is considered: In addition to the aircraft-induced turbulence, weak to moderate, anisotropic, and decaying atmospheric turbulence is superimposed on the whole velocity field. The atmospheric turbulence obeys prescribed spectra with rms velocities of 0.38 m/s in the horizontal and 0.21 m/s in the vertical direction. The length scales of the most energetic eddies amount to 60–90 m. The turbulence initializations of both cases are described in detail in Ref. 22.

## IV. Centrifugal Stability

Although the concept of centrifugal stability is well known from the literature,[23] it is briefly introduced here for an easier understanding of the following sections. Figure 3 and Eq. (8) illustrate that a fluid element in a vortex flow that is radially displaced by $dr$ and retains its angular momentum ($v_\theta r = \text{const}$) experiences a restoring force. The restoring force is proportional to the difference between the centripetal forces acting on the displaced fluid element and its environment; that is, it is proportional to the difference between the velocity of the fluid element squared and the velocity of the surrounding mean vortical flow squared and inversely proportional to the local curvature radius

$$F_r = -\rho\left[\frac{v_{\theta,r+dr}^2}{r+dr} - \frac{\hat{v}_\theta^2}{r+dr}\right], \qquad \hat{v}_\theta = \frac{v_\theta r}{r+dr} \tag{8}$$

By means of a Taylor series expansion and with higher-order terms neglected, $F_r$ can be expressed differentially

$$F_r \approx -\frac{1}{r^3}\frac{\partial}{\partial r}\left[\rho(v_\theta r)^2\right]dr \tag{9}$$ **Q5**

Equating the restoring force to the inertia of the fluid element yields a differential equation that describes undamped oscillations of the displaced fluid element

$$\frac{\partial^2 r}{\partial t^2} + \underbrace{\frac{1}{r^3}\frac{\partial}{\partial r}\left[(v_\theta r)^2\right]}_{\omega^2} r = 0 \tag{10}$$ **Q6**

The restoring force, the oscillation frequency, and, hence, the vortex stability achieve maximum values at the vortex center and vanish at about $2r_c$ where the vortex attains constant circulation (cf. Fig. 3).

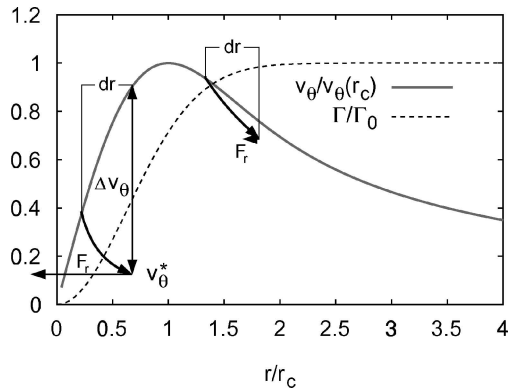


**Fig. 3 Schematic of the restoring force experienced by a radially displaced fluid element in a Lamb–Oseen vortex and respective circulation profile.**

For negative gradients of $v_\theta r$, the oscillation frequency becomes imaginary and the vortex becomes unstable. Unstable flow conditions may occur, for example, at the edges of a swirling jet where they cause enhanced mixing or in the boundary-layer flow along a concave wall where instability may lead to the formation of Görtler vortices.

## V. SGS Model Correction

### A. Richardson Number

The following considerations are based on the Richardson number for streamline curvature effects that Bradshaw[24] derived in analogy to the gradient Richardson number for buoyancy effects in stably stratified flows. Bradshaw's Richardson number

$$Ri = \frac{2v}{r^2}\frac{\partial vr}{\partial r}\Bigg/\left(\frac{\partial v}{\partial r}\right)^2 \tag{11}$$

relates the oscillation frequency squared of the radially displaced fluid element [$\omega^2$ in Eq. (10)] to the square of a "typical frequency scale of the shear flow." However, the choice of the latter frequency scale is misleading. For example, in an axisymmetric vortex, $\partial v/\partial r$ vanishes at the core radius. As a consequence, the Richardson number would go to infinity at $r = r_c$, where erroneously maximum stability would be assumed as it was in Ref. 25. (Recently, the flaw in Ref. 25 was revised.[26]) As shown in the preceding section, however, maximum stability is attained in the center of the vortex. A consistent formulation is achieved when the deformation tensor squared is employed in the denominator instead. In curvilinear coordinates, chosen for convenience, this corresponds to

$$Ri = \frac{2v_\theta}{r^2}\frac{\partial v_\theta r}{\partial r}\Bigg/2\left(r\frac{\partial v_\theta/r}{\partial r}\right)^2 \tag{12}$$

Radial profiles of the components of Eq. (12) are plotted for the Lamb–Oseen vortex in Fig. 4. The oscillation frequency in the numerator normalized by $(\pi r_c^2/\Gamma_0)^2$ inceases from zero at $r/r_c > 2$ to its maximum of $\pi/2$ at the vortex center. The normalized deformation tensor in the denominator has a maximum at $r_c = 1.19$, attains the same value as the oscillation frequency at the core radius, goes to zero at the vortex center and to low values on large radii. Consequently, the Richardson number increases monotonically from zero at $r/r_c > 2$, reaches a value of 1 at $r = r_c$, and goes to infinity when approaching $r = 0$.

Shen et al.[15] extended the Richardson number formulation to three dimensions

$$Ri = \Omega^2/D^2 + \Omega/D \tag{13}$$

Because Eq. (13) cannot discriminate between vorticity of a plane shear flow and vorticity of coherent rotation, an additional discriminator algorithm has to be applied.

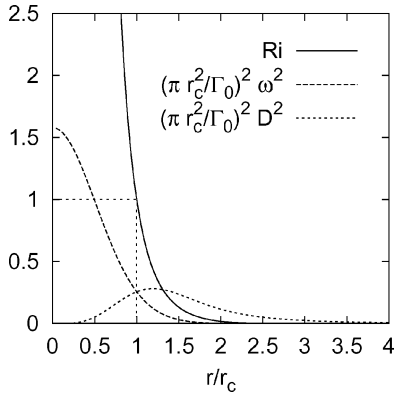


**Fig. 4 Radial profiles of Richardson number, normalized oscillation frequency squared, and normalized deformation tensor squared for a Lamb–Oseen vortex.**

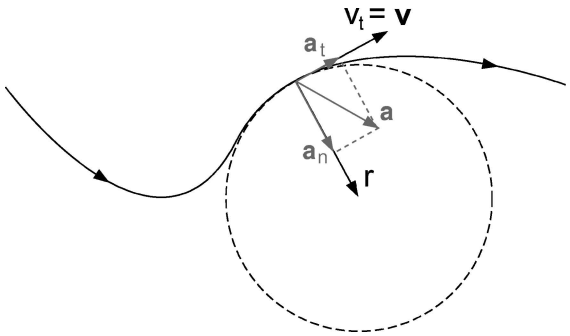


**Fig. 5 Determination of the tangential velocity $v_t$ and the curvature radius $r$ in natural coordinates.**

We apply instead the modified ansatz by Bradshaw [Eq. (12)] in natural coordinates

$$Ri = \frac{2v_t}{r}\left(\frac{v_t}{r} + \frac{\partial v_t}{\partial r}\right)\Bigg/D^2 \tag{14}$$

that does not require a discriminator function. It employs the tangential velocity directly along a local streamline whose curvature is given by an inscribed circle with radius $r$ (Fig. 5). For an undisturbed axisymmetric vortex, both Richardson number formulations described by Eqs. (13) and (14) yield very similar results. However, for plane shear, the curvature radius in Eq. (14) goes to infinity and $Ri = 0$. In the potential vortex, the shear vorticity, $\partial v_t/\partial r$, and curvature vorticity, $v_t/r$, just balance each other such that $Ri = 0$ again.

### B. Natural Coordinate System

Equation (14) employs the tangential velocity $v_t$ along a local streamline whose curvature is given by an inscribed circle with radius $r$ (Fig. 5) and the respective velocity gradient, $\partial v_t/\partial r$. These quantities are calculated at every grid point, following the approach of Hirsch.[27,28] In the natural coordinate system, the magnitude of the tangential velocity corresponds to the local velocity magnitude

$$v_t = |\boldsymbol{v}| \tag{15}$$

The magnitude of the curvature radius is calculated according to

$$r = |\boldsymbol{v}^2|\big/|\boldsymbol{a}_n| \tag{16}$$

where the acceleration in the direction of the curvature radius follows from

$$\boldsymbol{a}_n = \boldsymbol{a} - \boldsymbol{v}(\boldsymbol{a}\cdot\boldsymbol{v})/|\boldsymbol{v}^2| \tag{17}$$

with the advective acceleration vector

$$\boldsymbol{a} = (\boldsymbol{v}\cdot\nabla)\boldsymbol{v} \tag{18}$$

Finally, the velocity gradient in the direction of the curvature radius

$$\frac{\partial v_t}{\partial r} = (\boldsymbol{e}_n\cdot\nabla)\boldsymbol{v} \tag{19}$$

is determined based on the unit vector pointing in the direction of the curvature radius

$$\boldsymbol{e}_n = \boldsymbol{a}_n/|\boldsymbol{a}_n| \tag{20}$$

The velocity gradient tensor, the deformation tensor, and Eqs. (15–20) are calculated in LESTUF within one loop, such that NaCoo increases the numerical effort by only 5%.

### C. Implementation

Shen et al.[15] implement the Richardson number by modifying the SGS viscosity according to

$$\nu_{SGS} = \nu_{SGS,stand}(1 - \alpha Ri)^{0.5} \tag{21}$$

where $\alpha$ is a constant to adjust the impact of the curvature correction. NaCoo is implemented following Boysan (see Ref. 1) according to

$$\nu_{SGS} = \nu_{SGS,stand}[1/(1 + \alpha Ri)] \tag{22}$$

Boysan suggested this type of implementation for a source term modification in the dissipation equation of the k–$\epsilon$ turbulence model.

The effects of the different Richardson number formulations and their implementations are shown in Fig. 6. In both cases, the corrections substantially reduce $\nu_{SGS}$ in the vortex core region compared to the unmodified Smagorinsky approach. With NaCoo, $\nu_{SGS}$ smoothly goes to small values when approaching the vortex center, whereas the Shen et al. approach [Eqs. (13) and (21)] gives a relatively abrupt transition to zero at $r/r_c \approx 1.2$. The observed differences of the SGS viscosity profiles can be attributed primarily to the different types of implementation. We prefer the smooth transition for the sake of physical plausibility (maximum stability reached in vortex center) and numerical stability. Formulations (21) and (22) also allow for intensified momentum transport in unstable situations with $Ri < 0$.

### D. Galilei Invariance

Galilei invariance, the independence of a physical model from translational motions, serves as the criterion for the universality of turbulence models. For many applications, like the ones addressed here, the violation of the concept of Galilei invariance poses no serious limitations because the applications are naturally defined in an inertial frame of reference. Nevertheless, note that approaches based on streamline curvature in general do not obey Galilei invariance.

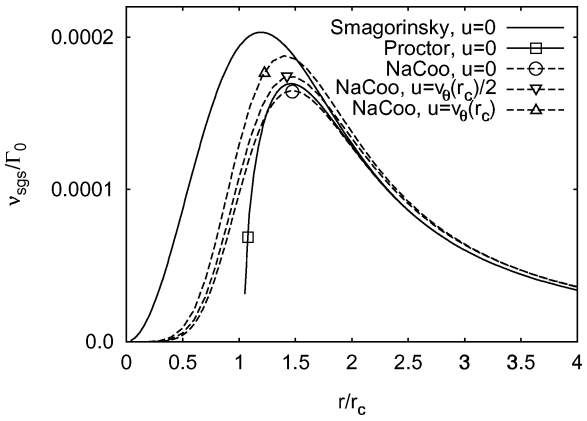


**Fig. 6 Radial profiles of normalized eddy viscosity for Smagorinsky closure and modifications with $\alpha = 1$ and $r_c = 4\Delta$; NaCoo is also applied for two different levels of superimposed constant axial velocities.**

Superimposition, for example, of a constant axial velocity on a vortex in a fixed frame of reference, will transform closed axisymmetric streamlines into helical streamlines with increased curvature radii and, thus, modified values of the Richardson number. An inspection of the Richardson number in Eq. (14) shows that the deformation tensor and $\partial v_t/\partial r$ remain unchanged by the superimposed axial flow. (Note that $\partial v_t/\partial r$ is not susceptible to axial flows because the direction of the curvature radius is invariant.) The magnitude of the curvature radius and the tangential velocity, however, are modified. For example, in a quite strong axial flow, where the axial velocity corresponds to the maximum circumferential velocity, the curvature radius at $r_c$ is increased by a factor of two, whereas the tangential velocity increases only by a factor of $\sqrt{2}$. Consequently, $Ri(r_c)$ achieves a value of 0.5 instead of 1.

Figure 6 shows the respective effects on the SGS viscosity distributions for two different levels of constant superimposed axial flows. With increasing axial velocities, the effects of NaCoo are increasingly reduced. On larger radii, the decreased curvature vorticity, $v_t/r$, cannot fully balance the unmodified shear vorticity, $\partial v_t/\partial r$, such that the SGS viscosity increases slightly in that area. This increase reaches a maximum of less than 6% in the case of $u = v_\theta(r_c)$ and decreases again for higher axial velocities. A pragmatic way to avoid this small overestimation is to limit $Ri$ to positive values at the expense that the intensified SGS momentum transport in unstable situations with $Ri < 0$ is suppressed.

## VI. Applications

### A. Single Vortices

To illustrate the effects of the streamline curvature corrections, LES of the evolution of single Lamb–Oseen vortices with $\Gamma_0 = 565$ m$^2$/s and $r_{c0} = 4$ m resolved by four grid points were performed. Figure 7 shows cross sections of axial vorticity for vortices with an initially superimposed random perturbation field according to case *b* (Sec. III) at times of $t = 0$ s and $t = 20$ s. With NaCoo, the peak vorticity of the initialized Lamb–Oseen vortex is well preserved and turbulence is damped to a reasonable level. In contrast, the high levels of SGS viscosity predicted by the standard Smagorinsky closure strongly damp both mean and fluctuating vorticity such that turbulent fluctuations become almost indiscernible.

Figure 8a compares the radial tangential velocity profiles that have developed from initialized Lamb–Oseen vortices at $t = 20$ s. With the unmodified Smagorinsky model the almost 20% reduction in maximum velocity is situated on an increased radius of $1.29r_{c0}$. Maximum velocities are also reduced with both corrections, but in the rigid-body vortex region the velocity profiles are almost conserved (preservation of peak vorticity) due to the suppressed SGS viscosity. As a consequence, the shapes of the resulting velocity profiles deviate substantially from the initiated Lamb–Oseen vortices. In the radii range between maximum velocity and potential vortex, an outer vortex core is formed that can be characterized by $r^C$ with $C$ between $-0.35$ and $-0.5$.

At $t = 80$ s, the velocity profile achieved with NaCoo approximates properties of the Rosenhead vortex (often also refered to as

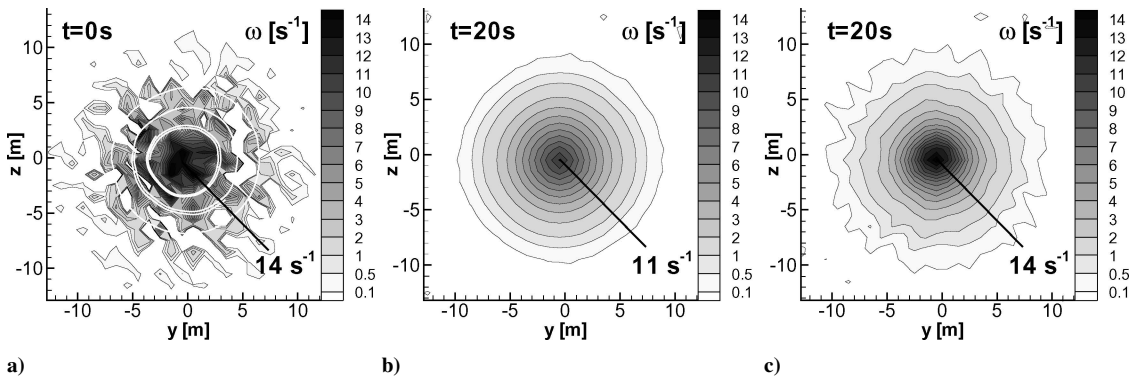


**Fig. 7 Vorticity distribution of a Lamb–Oseen vortex with initially superimposed random perturbations at a) $t = 0$ s with white streamlines and at b) $t = 20$ s applying the standard Smagorinsky closure and c) at $t = 20$ s applying NaCoo with $r_c = 4\Delta$ and $\alpha = 2$.**

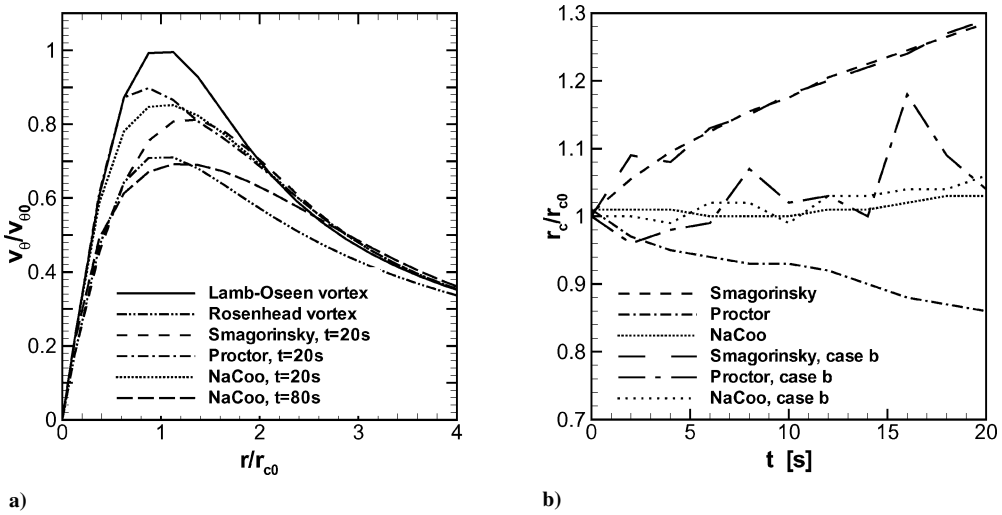


a) b)

**Fig. 8 Comparison of vortex evolution employing the Smagorinsky closure and modifications with $r_c = 4\Delta$ and $\alpha = 2$: a) radial profiles of tangential velocity at different times and b) temporal evolution of core radii.**

the Hallock–Burnham vortex). The Rosenhead vortex corresponds roughly to wake vortex profiles deduced from lidar field measurement data and wind-tunnel data.[29]

Figure 8b delineates the temporal evolution of vortex core radii with and without initially superimposed random perturbations. Core radii are determined as the mean distance between the vortex center and the maximum of the tangential velocity where the mean distance is an average over four individual distances calculated in four different directions, respectively. The unrealistically large growth rates with the unmodified Smagorinsky closure are not affected by turbulence. In the undisturbed vortex, Proctor's correction (see Ref. 15) even causes shrinking core radii because the region around the velocity maximum experiences diffusion only from larger radii (Fig. 6), such that the velocity maximum is shifted toward the rigid-body vortex (Fig. 8a). The disadvantage of the vorticity-based Richardson number formulation (13) becomes visible in the turbulent case: Without the normally used discrimination procedure that identifies vorticity of coherent rotation, turbulent vorticity patches receive no damping, even outside the stable core region, as is reflected in the unsteady evolution of core radii. In contrast, NaCoo, which generates reasonable small core growth rates, is not affected by the initialized spotty structure of vorticity because it is controlled by streamline curvature that is only marginally distorted by the superimposed random perturbations (Fig. 7a).

### B. Aircraft Wake Vortices

Figure 9 compares the evolution of key parameters of a pair of turbulent counter-rotating wake vortices in a quiescent (case b) and a turbulent (case a) environment with and without NaCoo. The LES without the curvature correction are described in detail in Ref. 22.

As in the preceding single vortex simulations, vortex growth rate is substantially reduced with NaCoo, but is not affected by different turbulence initializations until the initiation of a phase of rapid vortex decay. When fully turbulent vortices have developed for case a at $t^* = 3$ and for case b at $t^* = 6.5$ (Fig. 10 shows respective turbulence structure) the definition of a core radius holds only in a statistical sense and the evaluated average core radii start to grow rapidly. This instant coincides with the onset of rapid circulation decay, where circulation is determined as an average over radii intervals ranging from 5 to 15 m. In the initial phase of moderate decay, the diffusion phase, NaCoo reduces the decay rate as expected. In the subsequent rapid decay phase, however, the decay rate of case b with NaCoo is even increased because the initialized turbulence is less suppressed (Fig. 7). As expected, the descent rate is not modified by the curvature correction. The descent speed is mutually induced by each vortex at the center of its respective neighboring vortex and, due to the large vortex separation of almost 12 initial core

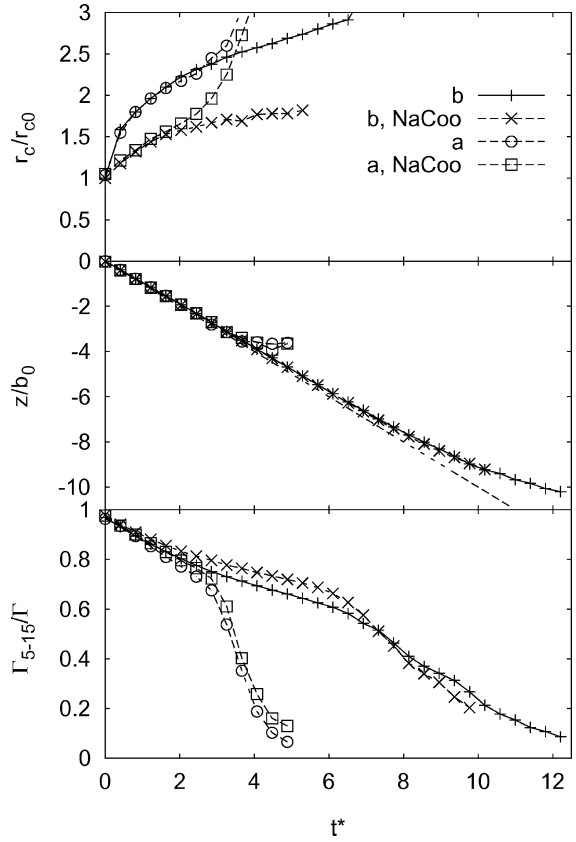


**Fig. 9 Evolution of normalized vortex core radius, descent rate, and 5–15 m averaged circulation for turbulent wake vortex pairs of a B747 aircraft in quiescent (case b) and turbulent (case a) environment. NaCoo employed with $r_c = 1.7\Delta$ and $\alpha = 2$.**

radii, these velocities reside in the potential vortex region of the respective neighboring vortex where $Ri \approx 0$.

Because of the major difficulties connected with measurements in the core of high-Reynolds-number wake vortices, very little experimental data for vortex core sizes and growth rates are available. Recent evaluations of three different experimental approaches suggest that minimum wake vortex core radii may be on the order of 1% of the wingspan of the aircraft.[30] Unfortunately, an adequate numerical resolution of such tight vortices is hardly feasible; we employ a ratio of $r_c/B = 8.5\%$ that nevertheless, allows for an adequate

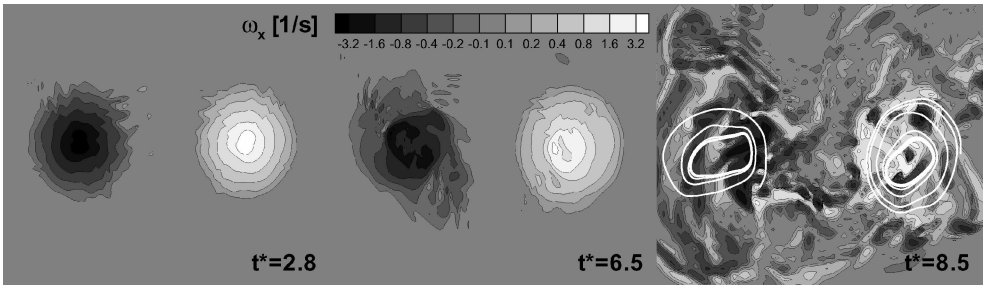


**Fig. 10 Vertical–lateral cross sections of axial vorticity distribution of wake vortices initialized with aircraft-induced turbulence in a quiescent atmosphere employing NaCoo with $r_c = 1.7\Delta$ and $\alpha = 2$.**

representation of main properties of wake vortices.[6] Reference 30 finds, furthermore, that the vortex cores of aircraft with retracted flaps grow roughly less than a factor of two before the onset of instability mechanisms. This corresponds well with our simulation results with NaCoo.

Figure 10 shows the evolution of the flow topology in vertical–lateral cross sections of the wake vortices for case b. Note that, already at $t^* = 4$, maximum axial velocities attain the same magnitude as the maximum swirl velocity components. In spite of the lack of Galilei invariance, this causes no apparent consequences for wake vortex evolution (Fig. 9). The seemingly fully incoherent flow structure at $t^* = 8.5$ represents vortices that still exhibit one-third of their initial circulation (Fig. 9) and a descent speed reduced by only 23%. It is only the white streamlines that elucidate the lingering coherence of the vortex motion. The smooth streamlines show the qualification of our current approach to determine the Richardson number based on local streamline curvature even in complex and fully turbulent situations of coherent rotation. Recent particle image velocimetry measurements[31] corroborate that the shown complex flow topologies are typical for wake vortices at high Reynolds numbers.

## VII. Sensitivity

In this section, the relation of SGS viscosity-driven vortex core radius growth to the numerical resolution of the vortex, its circulation, and the curvature correction is investigated. For the decaying potential vortex, core radius growth can be described by[32]

$$r_c/r_{c0} \sim \sqrt{\nu t / r_{c0}^2} \tag{23}$$

The Smagorinsky eddy viscosity [Eq. (7)] at the core radius amounts to

$$\nu_{\mathrm{SGS}}(r_c) = \left[(c_S\Delta)^2 / \pi r_c^2\right] 0.358\Gamma_0 \tag{24}$$

The simplifying assumption, that in the LES the core radius growth can be characterized by Eq. (23) employing the value of the SGS viscosity at the instantaneous core radius [Eq. (24)], yields an analytical expression of core radius growth as a function of the numerical resolution of the initial vortex core and its circulation

Q8

$$\frac{r_c}{r_{c0}} = \left[1 + C\frac{0.114(c_S\Delta)^2\Gamma_0 t}{(1+\alpha) r_{c0}^4}\right]^{\frac{1}{4}} \tag{25}$$

In Eq. (25), the effect of NaCoo is considered by the factor $(1+\alpha)$ in the denominator. This factor results from the implementation of NaCoo via a modified SGS viscosity according to Eq. (22) and $Ri(r = r_c) = 1$. Equation (25) indicates that, in the longer term, SGS viscosity causes vortex core radii growth proportional to $t^{1/4}$. The $t^{1/4}$ dependency arises from the fact that the SGS viscosity is not a constant fluid property but, in turn, depends on $\Delta^2/r_c^2$.

Figure 11 delineates vortex core evolution vs time according to Eq. (25) (solid lines) and different LES results (symbols) where time is normalized according to $t' = (\Delta^2/r_{c0}^2\ \Gamma_0/r_{c0}^2 t)^{1/4}$. Vortex core radii evolve along two tangents with a continuous transition in between. Depending on the constant $\alpha$, the vortex core remains

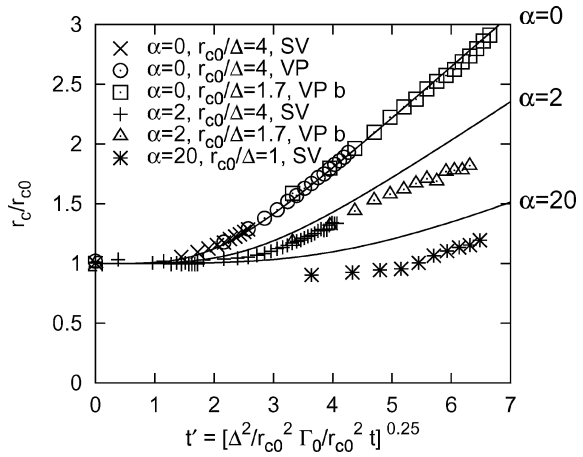


**Fig. 11 Evolution of normalized core radii against normalized time; ——, parametrization according to Eq. (25) and $C = 12$.**

constant during a time span of one to three time units. This means, for example, that, according to Eq. (25), a vortex with $r_{c0}/\Delta = 10$, $\Gamma_0/r_{c0}^2 = 10\ \mathrm{s}^{-1}$, and $\alpha = 2$, would grow only for 4.6% during a period of $t' = 2$ or $t = 160$ s. Without NaCoo, the same parameter combinations would cause an increase in core radii by 12.4%. At later times vortex cores grow proportional to $t^{1/4}$ where the slope can be adjusted by $\alpha$.

In Fig. 11, symbols denote simulation results of single vortices and vortex pairs with different resolutions of the core radii with and without superimposed turbulence. Without NaCoo ($\alpha = 0$), vortex growth is described consistently by Eq. (25) with $C = 12$. With the curvature correction, vortex growth is somewhat overestimated by the analytical description. The deviation of the analytical curve from simulation results is probably mainly caused by the simplifications used to derive Eq. (25). In particular, the assumption that $\nu_{\mathrm{SGS}}(r_c)$ may represent some global $\nu$ in Eq. (23) is less appropriate because, with NaCoo, the SGS viscosity exhibits a strong gradient in the vicinity of $r_c$ (Fig. 6). Q9

Figure 11 indicates further that, at later times, vortex growth is somewhat delayed for case b with $\alpha = 2$. A much weaker delay also seems to be present for case b and $\alpha = 0$. This is possibly caused by a redistribution of angular momentum driven by the resolved turbulence in the vortices shown in Fig. 10. The inviscid, large-scale fluctuations conserve to first order the angular momentum that sustains the potential vortex flow and may compensate to a certain extent for the core growth caused by the SGS model.

To discuss the trends for very high values of $\alpha$, one simulation is performed with $\alpha = 20$ (Fig. 12). Now vortex core growth is suppressed for a significant period of time. Intially, vortex cores even tend to shrink. Because SGS viscosity achieves larger values only on larger radii, angular momentum is sucked from larger radii without supply from smaller radii. This unequal angular momentum transport initially shifts the tangential velocity maximum along the rigid-body vortex toward smaller radii (Fig. 12). Later on the vortex grows more rapidly.

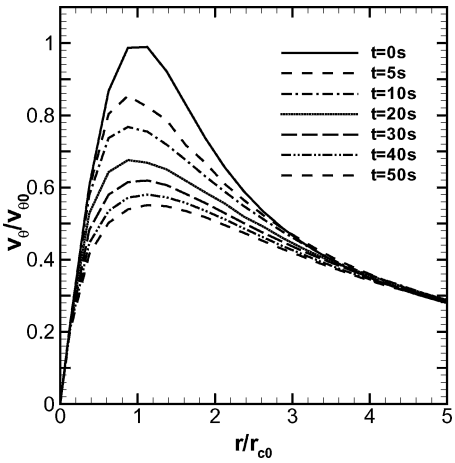


**Fig. 12 Tangential velocity profiles for $\alpha = 20$ and $r_c/\Delta = 1$ at different times.**

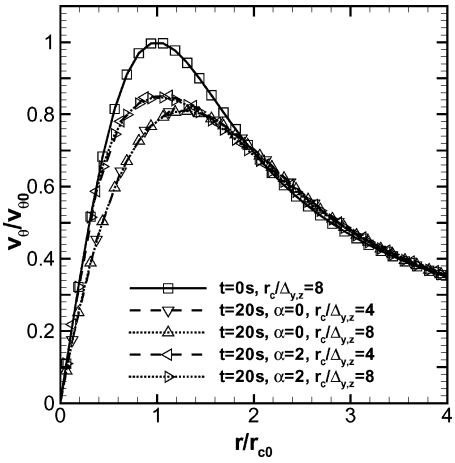


**Fig. 13 Tangential velocity profiles for $r_c/\Delta = 4$ and different numerical resolutions in vortex plane with and without NaCoo; initialized profile and profiles at $t = 20$ s.**

To avoid indistinguishable superimposed effects of numerical resolution requirements on vortex growth, core radii were always resolved by four grid points. Different values for $r_{c0}/\Delta$ were achieved by variation of the resolution perpendicular to the plane of rotation that employed the fitting formula for anisotropic meshes.[21] Nevertheless, the contribution of discretization errors was assessed by the repetition of simulations with a doubled vortex core resolution and a respective adjustment of the axial grid spacing to achieve identical values of $\Delta$ in both simulations. Notably, the tangential velocity profiles that result from the different resolutions displayed in Fig. 13 are almost identical and cannot be distinguished from each other by the naked eye. This result demonstrates grid independence at the employed level of discretization for the second-order accurate scheme.

We conclude that Eq. (25) can already be used in the design phase of the numerical simulation to adjust vortex core growth rates caused by SGS viscosity for given values of $r_{c0}$, $\Delta$, and $\Gamma_0$. For our parameter combinations (Sec. VI) a value of $\alpha = 2$ appears appropriate.

## VIII. Conclusions

An adjustment of SGS parametrizations to strong streamline curvature effects is proposed. Effects of SGS closures on inadequately resolved regions of coherent rotation are analyzed by application of the Smagorinsky closure approximation to Lamb–Oseen vortices. In regions where resolved fluctuations are damped due to centrifugal stability, the SGS viscosity may achieve excessive values that further damp the resolved turbulence in the vortex and its peak vorticity and, finally, lead to untimely disintegration of vortices.

The correction termed NaCoo identifies the local degree of centrifugal stability via a rotational Richardson number that is determined from local streamline curvature at every grid point. The Richardson number, in turn, is used to modify the SGS viscosity such that SGS momentum transport is increased in unstable and decreased in stable situations. The basic principle of this approach is applicable to any other eddy-viscosity closure model. The Richardson number rests on the formulation devised by Bradshaw.[24] His Richardson number employs a plane shear squared in the denominator and, thus, assumes erroneously maximum stability at the core radius of a vortex. Here, instead the deformation tensor is used whereby a proper distribution of stability with a maximum in the center of the vortex is attained.

Features of NaCoo are discussed in comparison with other approaches from literature. The capability to resolve the slightest local streamline curvature, the balanced weighting of the correction by the type of its implementation, and the minor additional numerical effort of only 5% constitute beneficial properties of NaCoo. Main benefits of NaCoo are 1) conservation of the peak vorticity in the vortex cores, 2) reduction of vortex core radius growth rates, 3) an approach to properties of tangential velocity profiles found in experiments, 4) allowance for appropriate turbulence levels in the vicinity of the vortices, and 5) non suppression of vortex core meandering. These features, which corroborate results of experimental studies of turbulent vortices[29,30,31,33,34] denote a significant step toward a more physical modeling of inadequately resolved vortices by LES. Q10

Applications of NaCoo to single vortices and to aircraft wake vortices in a quiescent and turbulent environment illustrate the performance of the streamline curvature correction. In particular, it is shown that streamline curvature constitutes a robust criterion for coherent rotation, even in fully turbulent and apparently incoherent flow topologies. A relation is derived that allows for the selective adjustment of vortex growth rates caused by SGS viscosity, depending on the numerical resolution of the vortex and its circulation. The relation, which indicates that vortex cores grow according to $t^{1/4}$ after a transient constancy, is corroborated by different applications.

For wake vortices, the turbulence structure within the vortices becomes more realistic and resembles flow topologies found in high-Reynolds-number laboratory experiments.[31] Vortex core growth rates can be substantially reduced to growth rates found in vortex cores of aircraft with retracted flaps.[30] Nevertheless, global parameters like wake vortex transport and decay are little affected by the correction because well-resolved secondary vorticity structures control vortex evolution.[6]

## Acknowledgments

The scientific perceptions and the fruitful discussions that the author shared with Christoph Hirsch during their common stay at the Engler-Bunte Institute of the University of Karlsruhe established the basis for the current manuscript. The instrumental support during implementation and assessment of NaCoo by Thomas Gerz is greatly acknowledged. The feedback received from Robert Baumann and Robert E. Robins concerning their experiences with applications of NaCoo is appreciated.

## References

[1]Sloan, D. G., Smith, P. J., and Smoot, L. D., "Modeling of Swirl in Turbulent Flow Systems," *Progress in Energy and Combustion Science*, Vol. 12, No. 3, 1986, pp. 163–250.

[2]Fu, S., and Qian, W. Q., "Development of Curvature Sensitive Nonlinear Eddy-Viscosity Model," *AIAA Journal*, Vol. 40, No. 11, 2002, pp. 2225–2233.

[3]Jakirlić, S., Hanjalić, K., and Tropea, C., "Modeling Rotating and Swirling Turbulent Flows: A Perpetual Challenge," *AIAA Journal*, Vol. 40, No. 10, 2002, pp. 1984–1996.

[4]Weber, R., Visser, B. M., and Boysan, F., "Assessment of Turbulence Modeling for Engineering Prediction of Swirling Vortices in the Near Burner Zone," *International Journal of Heat and Fluid Flow*, Vol. 11, No. 3, 1990, pp. 225–235.

[5]Sreedhar, M., and Ragab, S., "Large Eddy Simulation of Longitudinal Stationary Vortices," *Physics of Fluids*, Vol. 6, No. 7, 1994, pp. 2501–2514.

[6]Holzäpfel, F., Hofbauer, T., Darracq, D., Moet, H., Garnier, F., and Ferreira Gago, C., "Analysis of Wake Vortex Decay Mechanisms in the Atmosphere," *Aerospace Science and Technology*, Vol. 7, No. 4, 2003, pp. 263–275.

[7]Pierce, C. D., and Moin, P., "Large Eddy Simulation of a Confined Coaxial Jet with Swirl and Heat Release," AIAA Paper 98-2892, June 1998. **Q11**

[8]Fan, M., Wenren, Y., Dietz, W., Xiao, M., and Steinhoff, J., "Computing Blunt Body Flows on Coarse Grids Using Vorticity Confinement," *Journal of Fluids Engineering*, Vol. 124, No. 4, 2002, pp. 876–885.

[9]Costes, M., and Kowani, G., "An Automatic Anti-Diffusion Method for Vortical Flows Based on Vorticity Confinement," *Aerospace Science and Technology*, Vol. 7, No. 1, 2003, pp. 11–21.

[10]Holzäpfel, F., Gerz, T., Frech, M., and Dörnbrack, A., "Wake Vortices in a Convective Boundary Layer and Their Influence on Following Aircraft," *Journal of Aircraft*, Vol. 37, No. 6, 2000, pp. 1001–1007.

[11]Germano, M., Piomelli, U., Moin, P., and Cabot, W. H., "A Dynamic Subgrid-Scale Eddy Viscosity Model," *Physics of Fluids A*, Vol. 3, No. 7, 1991, pp. 1760–1765.

[12]Meneveau, C., Lund, T. S., and Cabot, W. H., "A Lagrangian Dynamic Subgrid-Scale Model of Turbulence," *Journal of Fluid Mechanics*, Vol. 319, 1996, pp. 353–385.

[13]Holzäpfel, F., Hofbauer, T., Gerz, T., and Schumann, U., "Aircraft Wake Vortex Evolution and Decay in Idealized and Real Environments: Methodologies, Benefits and Limitations," *Advances in LES of Complex Flows*, edited by R. Friedrich, and W. Rodi, Vol. 65, Fluid Mechanics and its Applications, Kluwer Academic Publishers, Dordrecht, The Netherlands, 2002, pp. 293–309.

[14]Spalart, P. R., and Shur, M., "On the Sensitization of Turbulence Models to Rotation and Curvature," *Aerospace Science and Technology*, Vol. 1, No. 5, 1997, pp. 297–302.

[15]Shen, S., Ding, F., Han, J., Lin, Y.-L., Arya, S. P., and Proctor, F. H., "Numerical Modeling Studies of Wake Vortices: Real Case Simulations," AIAA Paper 99-0755, Jan. 1999. **Q12**

[16]Lewellen, D. C., Lewellen, W. S., and Xia, J., "The Influence of a Local Swirl Ratio on Tornado Intensification Near the Surface," *Journal of the Atmospheric Sciences*, Vol. 57, No. 4, 2000, pp. 527–544.

[17]Gerz, T., Baumann, R., and Holzäpfel, F., "Parametric LES Studies of Far-Field Wakes Shed by Large Aircraft," Inst. of Atmospheric Physics, C-Wake Rept. TR2.2.2-1, Oberpfaffenhofen, Germany, 2003.

[18]Kaltenbach, H.-J., Gerz, T., and Schumann, U., "Large-Eddy Simulation of Homogeneous Turbulence and Diffusion in Stably Stratified Shear Flow," *Journal of Fluid Mechanics*, Vol. 280, 1994, pp. 1–40.

[19]Deardorff, J. W., "A Numerical Study of Three-Dimensional Turbulent Channel Flow at Large Reynolds Numbers," *Journal of Fluid Mechanics*, Vol. 41, 1970, pp. 453–480.

[20]Smagorinsky, J., "General Circulation Experiments with the Primitive Equations: I. The Basic Experiment," *Monthly Weather Review*, Vol. 91, No. 3, 1963, pp. 99–164.

[21]Scotti, A., Meneveau, C., and Lilly, D. K., "Generalized Smagorinsky Model for Anisotropic Grids," *Physics of Fluids A*, Vol. 5, No. 9, 1993, pp. 2306–2308.

[22]Holzäpfel, F., Gerz, T., and Baumann, R., "The Turbulent Decay of Trailing Vortex Pairs in Stably Stratified Environments," *Aerospace Science and Technology*, Vol. 5, No. 2, 2001, pp. 95–108.

[23]Lord Rayleigh, O. M., "On the Dynamics of Revolving Fluids," *Proceedings of the Royal Society of London, Series A: Mathematical an Physical Sciences*, Vol. 93, 1917, pp. 148–154.

[24]Bradshaw, P., "The Analogy Between Streamline Curvature and Buoyancy in Turbulent Shear Flow," *Journal of Fluid Mechanics*, Vol. 36, 1969, pp. 177–191.

[25]Cotel, A. J., and Breidenthal, R. E., "Turbulence Inside a Vortex," *Physics of Fluids*, Vol. 11, No. 10, 1999, pp. 3026–3029.

[26]Cotel, A. J., "Turbulence Inside a Vortex: Take Two," *Physics of Fluids*, Vol. 14, No. 8, 2002, pp. 2933–2934.

[27]Hirsch, C., "Ein Beitrag zur Wechselwirkung von Turbulenz und Drall," Ph.D. Dissertation Univ. of Karlsruhe, Karlsruhe, Germany, 1995. **Q13**

[28]Hirsch, C., and Leuckel, W., "A Curvature Correction for the k–$\epsilon$ Model in Engineering Applications," *Engineering Turbulence Modelling and Experiments 3: Proceedings of the Third International Symposium*, Elsevier, New York, 1996, pp. 71–80.

[29]Gerz, T., Holzäpfel, F., and Darracq, D., "Commercial Aircraft Wake Vortices," *Progress in Aerospace Sciences*, Vol. 38, No. 3, 2002, pp. 181–208.

[30]Delisi, D. P., Greene, G. C., Robins, R. E., Vicroy, D. C., and Wang, F. Y, "Aircraft Wake Vortex Core Size Measurements," AIAA Paper 2003-3811, June 2003. **Q14**

[31]Vollmers, H., "Detection of Vortices and Quantitative Evaluation of Their Main Parameters from Experimental Velocity Data," *Measurement Science and Technology*, Vol. 12, No. 8, 2001, pp. 1199–1207.

[32]Zierep, J., *Ähnlichkeitsgesetze und Modellregeln der Strömungslehre*, Braun, Karlsruhe, Germany, 1982. **Q15**

[33]Holzäpfel, F., Lenze, B., and Leuckel, W., "Quintuple Hot-Wire Measurements of the Turbulence Structure in Confined Swirling Flows," *Journal of Fluids Engineering*, Vol. 121, No. 3, 1999, pp. 517–525.

[34]Rokhsaz, K., Foster, S. R., and Miller, L. S., "Exploratory Study of Aircraft Wake Vortex Filaments in a Water Tunnel," *Journal of Aircraft*, Vol. 37, No. 6, 2000, pp. 1022–1027.

R. So
*Associate Editor*

[8]

# Probabilistic Two-Phase Aircraft Wake Vortex Model: Application and Assessment

F. Holzäpfel, R.E. Robins

Journal of Aircraft, 2004

Volume 41, Number x, Pages xxx–xxx

JOURNAL OF AIRCRAFT
Vol. 41, No. 5, September–October 2004

# Probabilistic Two-Phase Aircraft Wake-Vortex Model: Application and Assessment

Frank Holzäpfel*
*DLR, German Aerospace Center, 82234 Wessling, Germany*
and
Robert E. Robins†
*NorthWest Research Associates, Inc., Bellevue, Washington 98009-3027*

**Predictions of the parametric probabilistic two-phase aircraft wake-vortex transport and decay model P2P are compared with field observations. The two-phase decay model predicts probabilistic wake-vortex behavior as a function of aircraft and environmental parameters in real time. Observation data from field deployments accomplished at the International Airports Memphis and Dallas Fort Worth and from the WakeOP campaign performed at the airfield in Oberpfaffenhofen, Germany, are employed. In a scoring procedure, the predictive capabilities of a deterministic version of P2P are compared to Sarpkaya's model. Based on 211 Memphis cases, it is shown that the probabilistic model predicts conservative confidence intervals for vortex decay with the exception of four cases in which constant background wind shear increases vortex lifetime. Nonetheless, the aircraft spacing reduction potential based on vortex decay appears to be small. In contrast, consideration of advection outside the lateral limits of a safety corridor results in a large potential spacing reduction. Vortex drift is investigated based on input from different wind measurement devices with a focus on the spatial and temporal variability of the crosswind. Safety corridor clearances based on short-term weather forecasts yield promising results. Further, it is found that shear layers can modify vortex transport such that predicted uncertainty allowances are exceeded.**

## Nomenclature

| | | |
|---|---|---|
| $A$ | = | constant |
| $b$ | = | vortex spacing |
| $C$ | = | constant to adjust turbulent spreading |
| $g$ | = | gravitational acceleration |
| $N$ | = | Brunt–Väisälä frequency |
| $q$ | = | rms turbulence velocity |
| $R$ | = | mean radius |
| $r$ | = | radial coordinate |
| $T$ | = | parameter for vortex age |
| $t$ | = | time |
| $U$ | = | horizontal wind velocity |
| $u$ | = | axial velocity |
| $v$ | = | lateral velocity |
| $w$ | = | vertical velocity; descent speed |
| $y$ | = | spanwise coordinate |
| $z$ | = | vertical coordinate |
| $\Gamma$ | = | circulation |
| $\varepsilon$ | = | eddy dissipation rate |
| $\theta$ | = | potential temperature |
| $\Lambda$ | = | one-half the longitudinal integral scale of atmospheric turbulence |
| $\nu$ | = | (effective) kinematic viscosity |

*Subscripts*

| | | |
|---|---|---|
| 0 | = | initial value |
| 1 | = | first decay phase |
| 2 | = | second decay phase |
| 5–15 | = | average over circles with radii from 5 to 15 m |
| $u$ | = | upper limit |
| $y$ | = | lateral direction |
| $z$ | = | vertical direction |

*Superscript*

| | | |
|---|---|---|
| $*$ | = | normalized quantity |

Received 6 May 2003; presented as Paper 2003-3809 at the AIAA 21st Applied Aerodynamics Conference, Orlando, 23 June 2003; revision received 6 October 2003; accepted for publication 15 October 2003. 

*Research Scientist, Institute of Atmospheric Physics, Oberpfaffenhofen; frank.holzaepfel@dlr.de.

†Research Scientist, P.O. Box 3027. Senior Member AIAA.

## Introduction

AIRCRAFT-GENERATED wake vortices pose a potential risk for following aircraft. Mandated separation distances between consecutive aircraft that are meant to eliminate this risk unfortunately contribute significantly to the capacity constraints of major airports. However, experience and research results acquired over several decades have shown that wake-vortex separation standards might be overly conservative for a variety of meteorological situations.[1,2] Therefore, a parametric model that is capable of reliably predicting vortex positions and strengths in real time in a measured or forecasted atmospheric environment in the vicinity of the glide slope might be a useful tool for easing regulations without loss of safety.

Several parametric wake-vortex models that predict deterministic vortex behavior (see Refs. 3–6 for some of the better known models) are available. Not specified in these models are deviations from predicted values inherently caused by the stochastic nature of turbulence, complex vortex instabilities and deformations, and the uncertainty of environmental parameters that determine the vortices' behavior in the atmospheric boundary layer. The newly developed probabilistic two-phase wake-vortex transport and decay model P2P (Ref. 7) considers these deviations and predicts uncertainty allowances for vortex trajectories and vortex strength. The performance of a wake-vortex algorithm and, in particular, the size of the applied uncertainty allowances depend on the accuracy and variability of input parameters. Therefore, an assessment of wake-vortex model predictions must always consider the characteristics of the meteorological and wake-vortex observation systems.

Comparisons of wake-vortex prediction algorithms with observations are available in Refs. 8 and 9. Sensitivity studies on the impact of atmospheric conditions on a complete prototype wake-vortex

spacing system are given in Refs. 10 and 11. For this purpose either synthetic weather data[10] or the assumption that the observed environmental parameters persist for 30 min is used.[11]

In the current manuscript, P2P first is briefly introduced, and then an overview of the utilized databases is given. A deterministic version of P2P is compared to Sarpkaya's model[9] based on the statistics of 211 Memphis cases. The statistics of the Memphis cases are compared to 41 WakeOP cases, where environmental parameters are provided by different sensors and by a short-term weather forecast model system. The quality of vortex predictions is discussed with regard to the variability of environmental parameters. Probabilistic predictions are used to assess the performance of P2P and illustrate the significance of wind shear for vortex decay and transport. Finally, the aircraft spacing reduction potential based on vortex drift and decay is assessed.

## Probabilistic Two-Phase Wake-Vortex Decay Model

A detailed description of P2P is given in Ref. 7. Here we restrict ourselves to an outline of the main properties of the model. P2P accounts for the effects of wind, turbulence, stable thermal stratification, and ground proximity where the interaction with the ground is modeled following the approach described in Ref. 8. Input data that characterize the wake vortices are time of vortex generation and initial position, circulation, and vortex spacing. Environmental input parameters are vertical profiles of crosswind, vertical wind, rms value of ambient turbulence, eddy dissipation rate (EDR), and potential temperature. The model is formulated in normalized form where the characteristic scales are based on initial vortex separation and circulation leading to the timescale $t_0 = 2\pi {b_0}^2/\Gamma_0$. EDR is normalized according to $\varepsilon^* = (\varepsilon b_0)^{1/3}/w_0$, where $w_0 = \Gamma_0/2\pi b_0$ denotes the initial descent speed, and temperature stratification is expressed by the normalized Brunt–Väisälä frequency $N^* = (g/\theta_0\, \mathrm{d}\theta/\mathrm{d}z)^{1/2} t_0$.

P2P employs a circulation $\Gamma^*_{5-15}$, which is averaged over circles with radii from 5 to 15 m or, alternatively, if smaller aircraft are considered, over a smaller radii interval. $\Gamma^*_{5-15}$ combines several advantages for the evaluation of vortex strength from lidar data like the exclusion of small radii that are not reliably sensed by lidar, low sensitivity to observation angles, automatic compensation of vortex motion, and smoothing of scatter by averaging over several radii.[12] Moreover, $\Gamma^*_{5-15}$ is well correlated with effects of potential wake encounters.[13]

The hydrodynamical basis of P2P relies on an equation that describes the spatiotemporal circulation evolution of the decaying potential vortex[14] for a given viscosity $\nu$

$$\Gamma(r,t)/\Gamma_0 = 1 - \exp(-r^2/4\nu t) \tag{1}$$

From this relation the parameterizations of circulation decay and descent speed, which are "calibrated" based on large-eddy simulation (LES) data of different groups, are deduced.[15,16] The LES data suggest that the normalized circulation decays in two phases (see Fig. 1c). The diffusion phase described by part 1 of Eq. (2) is followed by a rapid decay phase[1,15,16] that can be parametrized by the full equation

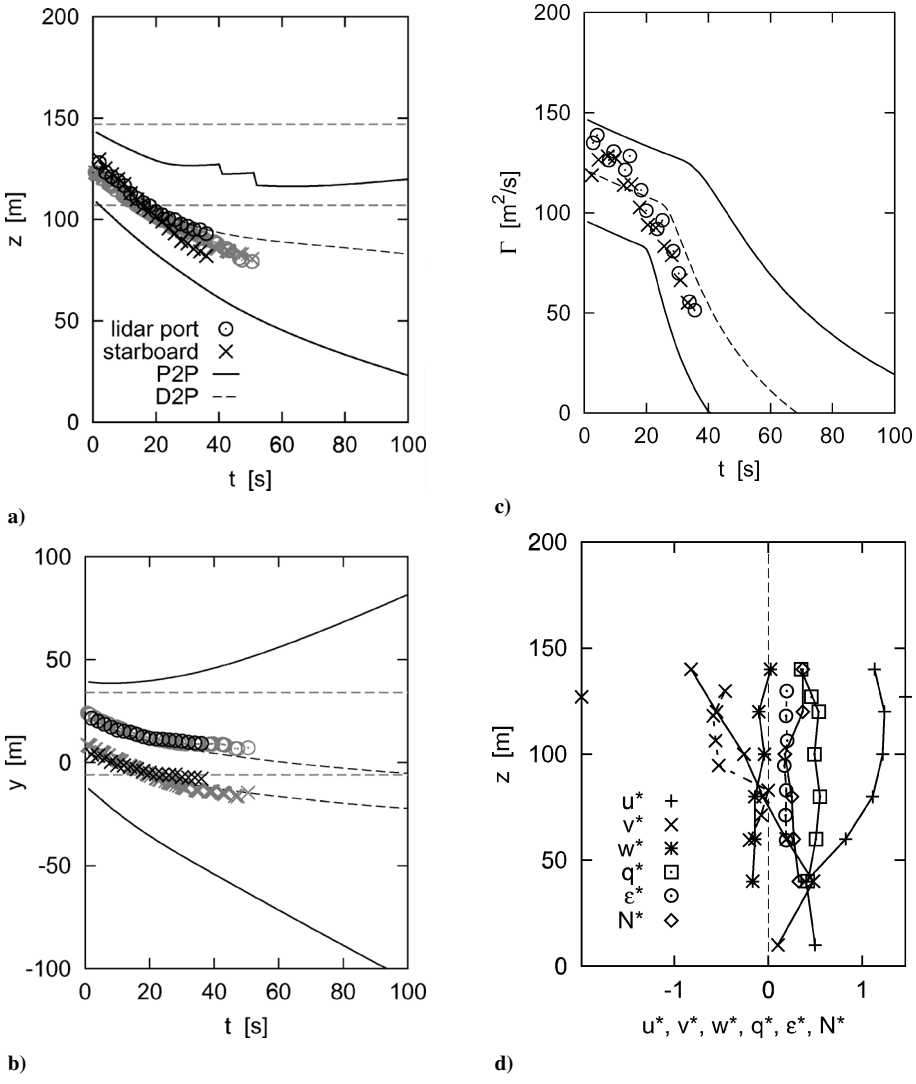


**Fig. 1 Measured and predicted evolution of a) vertical and b) lateral positions and c) circulation of wake vortices from WakeOP flight 7-03 and d) vertical profiles of environmental data.**

$$\Gamma^*_{5-15}(t^*) = \underbrace{A - \exp\frac{-R^2}{\nu_1^*\left(t^* - T_1^*\right)}}_{1} - \exp\frac{-R^2}{\nu_2^*\left(t^* - T_2^*\right)} \quad (2)$$

In Eq. (2) the onset time of rapid decay at $T_2^*$ and the respective decay rate, which is adjusted by the effective viscosity $\nu_2^*$, are functions of ambient turbulence and stratification. $T_1^*$ and $\nu_1^*$ control decay in the diffusion phase, $R$ corresponds to a mean radius, and $A$ is a constant to adjust $\Gamma^*_{5-15}(t^* = 0)$. The descent rate obeys a nonlinear dependence on circulation, which allows for stagnating or even rebounding vortices with nonzero circulation in strongly stably stratified environments as observed in LES[15] and experiments.[17]

Precise deterministic wake-vortex predictions are not feasible operationally. Primarily, it is the nature of turbulence that deforms and transports the vortices in a stochastic way and leads to considerable spatiotemporal variations of vortex position and strength. Moreover, uncertainties of aircraft parameters and the variability of environmental conditions must be taken into account. Therefore, P2P is designed to predict wake-vortex behavior within defined confidence intervals.

In a first step, two consecutive runs of P2P with a variation of the decay parameters $T_2^*$ and $\nu_2^*$ are performed. Second, constant uncertainty allowances of $\pm 0.2\Gamma_0^*$ for circulation and of plus and minus one initial vortex spacing for vertical and lateral locations are added. Finally, the increased scatter of vortices in turbulent environments is modeled by the assumption that the turbulence velocity acts as a superimposed propagation velocity.[18] An example of this applied to the upper bound of lateral position is

$$y_u^* = y^* + C_y \int q^*(z^*)\, \mathrm{d}t^* \quad (3)$$

where $C_y$ is a constant of the order of one. Figure 1 depicts the resulting confidence intervals for a case where vortex evolution agrees well with the mean predictions.

## Wake-Vortex Databases

The quality of wake vortex and coincident meteorological data and the conclusions that can be drawn from the data strongly depend on many factors including the measurement strategy, the type of sensors used, their locations, and the temporal and spatial resolution of the measurements, as well as the aircraft mix and the prevailing meteorological conditions. In the following we give an overview of the databases we have used to evaluate P2P. Because our investigations largely concentrate on Memphis and WakeOP data, a detailed description of the Dallas Fort Worth database is omitted.

### Memphis

A detailed description of the wake-vortex field measurement campaign performed at Memphis International Airport during December 1994 and August 1995 is given in Refs. 19 and 20. We use data of 211 overflights measured at the Armory site, which was located 3 km south of the 36R runway touchdown zone where approaching aircraft were passing over at a height of nominally 150 m. The aircraft mix consisted of 81% medium and 19% heavy aircraft. The vortices were measured by a 10-$\mu$m continuous-wave lidar system with active tracking of the vortex range by real-time analysis of signal characteristics.

The meteorological instrumentation comprised various sensor systems including a 150-ft tower equipped with wind and temperature sensors on five different heights, a Doppler radar with a radio acoustic sounding system (RASS) option capable to measure wind and virtual temperature throughout the atmospheric boundary layer and a sodar to measure wind speeds in lower altitudes up to 400 m. The meteorological site was located at a distance of about 2 km from Armory. The wind velocity and temperature data arising from various sensors were merged to composite vertical profiles by human evaluators.

Eddy dissipation rate and turbulent kinetic energy (TKE) were derived from 30-min series of 10-Hz data measured on the instrumented tower at heights of 5 and 40 m. Vertical profiles of EDR and TKE were generated by applying similarity theory and scalings for the atmospheric boundary layer,[21] where the resulting profiles were required to match observations at a height of 40 m. The mean eddy dissipation rate fed into P2P predictions was $\overline{\varepsilon^*} = 0.083$ and varied between $0.0 \le \varepsilon^* \le 0.30$. The mean Brunt–Väisälä frequency was $\overline{N^*} = 0.21$ within bounds of $0 \le N^* \le 0.58$. Both turbulence and temperature stratification levels represent weak to moderate conditions.

### WakeOP

The wake-vortex forecasting and measurement campaign WakeOP was conducted at the special airfield of Fairchild–Dornier in Oberpfaffenhofen, Germany, from 29 March to 4 May 2001. WakeOP has been accomplished in the framework of the Brite European research program C-Wake and the DLR project Wirbelschleppe. An outline of the campaign is given in Ref. 22. Figure 2 shows an airborne camera image of the WakeOP site with the flight track and the locations of the sensors from which data are obtained for the current study. The photo, which was shot with the high-resolution stereo camera—airborne extended, was provided by the DLR Institute WP. The 10-$\mu$m continuous-wave lidar systems of DLR, ONERA, and QinetiQ (locations denoted by l) were operated to trace the wake vortices generated by DLR's VFW 614 aircraft Advanced Technology and Testing Aircraft System (ATTAS). The ATTAS with a span of 21.5 m and an average weight of 18,000 kg performed overflights at a constant height of nominally 150 m above ground and produced wake vortices with a mean circulation of $\Gamma_0 = 142\ \mathrm{m^2/s}$ and an average timescale of $t_0 = 12.6$ s. The flight tracks were defined according to the prevailing wind conditions to allow for simultaneous wake observations by the three lidars. Wake-vortex trajectories were determined with an accuracy of better than $\pm 4.0$ m by triangulating the vortex core intersections of two simultaneously measuring lidars.[23] Based on vortex positions, circulation was determined as an average over a radii range from 3 to 8 m. For many overflights, doubly and triply sensed position and circulation data are available (see Fig. 1).

We compare the predictive capabilities of P2P based on four different sources of environmental data:

1) A mini-Sodar with a RASS extension provided vertical profiles of the three wind components, vertical fluctuation velocity, and virtual temperature. The vertical resolution was adjusted to 10 or 20 m and the averaging time to 10 min. Based on the assumption of isotropy, the rms value of turbulence was calculated from the vertical fluctuation velocity. The Brunt–Väisälä frequency was derived from the virtual temperature profiles.

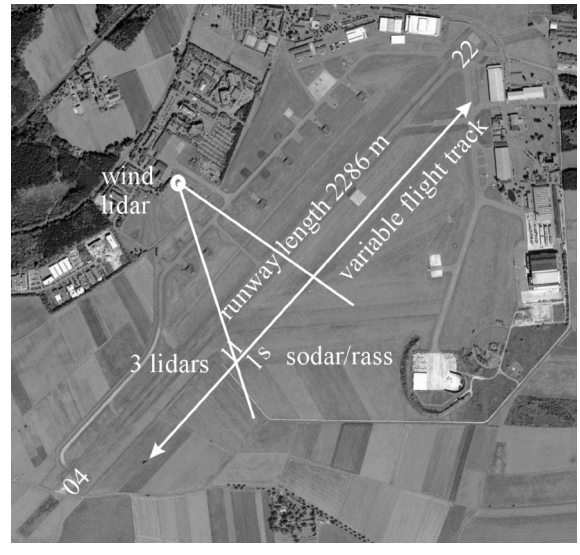


**Fig. 2 WakeOP site, variable flight track, and locations of sensors.**

2) A 2-$\mu$m pulsed Doppler wind lidar scanned under a constant elevation angle of 9 deg such that the measurement plane intersected the air volume in which the vortices evolved about 40 m below the flight track (see Fig. 2). From the line-of-sight wind measurements, which were performed for a period of 80 s after each overflight, vertical profiles of crosswind and eddy dissipation rate were deduced. The $\varepsilon$ profiles were derived from the evaluation of the structure function in adjacent range bins[24] and averaged over several overflights.

3) The horizontal wind vector along the flight track was measured by the standard equipment of the ATTAS aircraft, which consists of the inertial aircraft navigation system and the airspeed system (pitot-static tube and resistence temperature sensor). The wind vector results from the difference of the vectors of ground velocity and wind velocity, where the latter arises from true airspeed and heading. The crosswind during the overflight was calculated as an average over a 10-s period. The particular time period of 10 s was chosen for the smoothing of the 5-Hz data to make sure that the data quality would correspond to operationally available AMDAR (aircraft meteorological data relay) data.[25] Furthermore, the turbulence velocity was derived from the rms value of crosswind fluctuations, which was determined from a 60-s crosswind record centered on the overflight time. Fluctuation quantities are not part of the AMDAR data set.

4) During the WakeOP campaign, the weather forecast model system NOWVIV[26] (now casting wake-vortex impact variables) predicted vertical profiles of wind velocities, virtual potential temperature, and turbulence velocity. NOWVIV was initialized every 12 h with output data from the operational weather forecast model LM of the German Weather Service. It was operated within a 2.1-km grid around the airfield with detailed terrain and land-use information and an increasing vertical spacing from 25 to 50 m throughout the boundary layer. The normalized eddy dissipation rate was derived from the predicted $q$ profiles following Ref. 27 according to

$$\varepsilon^* = \tfrac{1}{2}(q/w_0)(b_0/\Lambda)^{\frac{1}{3}} \tag{4}$$

In Eq. (4) the one-half integral scale of atmospheric turbulence was set to the constant value of 110 m to avoid unrealistically large $\varepsilon^*$ values caused by overestimated turbulence levels close to the ground. Deviations between measured and predicted normalized dissipation rates typically fell below 50%. Above the atmospheric boundary layer, the turbulence parameterization in NOWVIV tends to underestimate turbulence levels. As a consequence, the uncertainty allowances of P2P for lateral transport are rather small according to Eq. (3), which, in turn, increases the sensitivity on the predicted crosswind strength. Therefore, we assume that in low turbulent situations the minimum turbulence intensity of the wind amounts to 10%, and we estimate $q^*(z^*)$ according to

$$q^*(z^*) = \max[0.1|U^*(z^*)|, q^*(z^*)] \tag{5}$$

To ensure conservative predictions of vortex lifetime, we do not use the modified $q^*(z^*)$ values for the calculation of EDR in Eq. (4).

The current investigations are based on 41 overflights for which data from all described components are available. Figure 1 shows exemplarily a complete set of measured and predicted quantities for flight 3 on day 7 (flight # 7-03). In Figs. 1a–1c, the evolution of vertical and lateral positions and circulation of wake vortices against time as measured by two lidar pairings (grey and black symbols) and predicted by P2P (solid lines limit confidence intervals; dashed lines mark mean evolution) are depicted. P2P predictions are based on sodar/RASS data except $\varepsilon^*$, which is provided by Lidar, and the constants for turbulent spreading [see Eq. (3)] are set to $C_y = 1$, $C_z = 0.5$. A flight-path corridor is indicated by straight dashed lines. Figure 1d shows vertical profiles of the respective environmental data (sodar/RASS, solid lines; lidar, dashed lines; aircraft, symbols).

During the overflights, the mean value of the eddy dissipation rate used in P2P predictions was $\overline{\varepsilon^*} = 0.19$ and varied in an interval of $0.13 \le \varepsilon^* \le 0.25$. The mean Brunt–Väisälä frequency was $\overline{N^*} = 0.14$ within bounds of $0 \le N^* \le 0.44$. On average, the atmospheric conditions were more turbulent and less stably stratified in the WakeOP data than in the Memphis data.

## Deterministic Model Performance

To evaluate the basic performance of the two-phase model, a deterministic version without probabilisitic components (termed D2P) is employed to predict mean vortex evolutions (compare Figs. 1a–1c, curved dashed lines), which are compared to predictions of the latest version of Sarpkaya's model.[9] For this purpose the 211 Memphis cases are used in a scoring procedure that is described in detail in Ref. 28. There, Sarpkaya's model, which is part of the current version of aircraft vortex spacing system (AVOSS),[29] was best rated compared to others.[6,8] The scoring procedure evaluates the rms deviations of measurement and prediction of the quantities $y^* = y/b_0$, $z^* = z/b_0$, and $\Gamma^*_{3-10} = \Gamma_{3-10}/\Gamma_0$ for each individual aircraft approach. From the resulting distribution of rms values, the median and the 90th percentile is used to characterize the performance of the models. In contrast to the original scoring procedure,[28] we consider the deviations of measurement and prediction for both vortices and every instant in time where measurements are available. In Ref. 28 statistics are computed only for the vortex having the greatest number of circulation observations, and predicted and observed values are interpolated onto the same uniform time grid.

The scoring results for the Memphis data are presented in Table 1. Although D2P was not designed to predict deterministic vortex behavior and although it was not adapted to the considered data basis in contrast to Sarpkaya's model[9] (decay constant $C$ and effective vortex separation), the comparison is quite good. Note that in Table 1 and in Ref. 28 the calculated rms deviations of all of the investigated models are of similar magnitude. This indicates that major contributions to the rms deviations are probably caused by inconsistencies of the data basis as outlined next and by inherent deviations of wake evolution from deterministic model predictions.

Table 2 contains scoring results of the application of D2P to WakeOP data. The upper row displays the range of scoring results that is achieved when D2P is driven by various combinations of the available measurement data. For example, EDR can be taken from lidar and temperature, and vertical wind from sodar/RASS, and crosswind from ATTAS. In other D2P runs, only data available from one device are used, and the remaining parameters are set to zero. The intervals in Table 2 are also achieved when only aircraft crosswind information is used and D2P assumes the baseline decay and descent rates parameterized for $\varepsilon^* = N^* = 0$. Further, the intervals achieved by a single model, which is driven by different environmental input (upper row of Table 2), even exceed the variations found for the different wake-vortex models applied to the Memphis data (compare Table 1). This finding clearly points up the importance of high-quality environmental data. The D2P rating based on the NOWVIV short-term weather forecasts depicted in the lower row yields remarkably good results. With the exception of lateral transport, the results are well within the range of D2P predictions based on measurements.

On average, the scoring results of WakeOP are better than for Memphis. This can result from several factors. Potentially, the

**Table 1 Statistics for normalized differences between deterministic model predictions and 1995 observations from Memphis International Airport**

| Model | Averages | rms $\Delta y^*$ | rms $\Delta z^*$ | rms $\Delta\Gamma^*$ |
|---|---|---|---|---|
| Sarpkaya's | Median | 0.776 | 0.436 | 0.156 |
| | 90th perc. | 2.33 | 0.912 | 0.276 |
| D2P | Median | 0.783 | 0.427 | 0.187 |
| | 90th perc. | 2.26 | 0.898 | 0.310 |

**Table 2 Statistics for normalized differences between D2P predictions and observations from WakeOP campaign**

| Meteo input | Averages | rms $\Delta y^*$ | rms $\Delta z^*$ | rms $\Delta\Gamma^*$ |
|---|---|---|---|---|
| Sodar/RASS, | Median | 0.663–0.753 | 0.384–0.444 | 0.145–0.156 |
| lidar, aircraft | 90th perc. | 1.32–2.17 | 0.804–1.09 | 0.208–0.264 |
| NOWVIV | Median | 1.12 | 0.402 | 0.155 |
| | 90th perc. | 2.23 | 0.803 | 0.239 |

triangulation strategy[23] has increased the accuracy of lidar data. However, it is probably the immediate proximity of the meteorological sensors to the wake measurement site that explains the superior results regarding lateral transport. On the other hand, the observation times with an average of $\overline{t^*} = 2.7$ were shorter in WakeOP than in Memphis with $\overline{t^*} = 3.8$, with the result that the Memphis predictions have more time to deviate from observations. The shorter durations are caused by the fact that for triangulation two lidars must observe the vortices simultaneously and the intersection of two observation domains is always smaller than the observation domain of a single lidar. Finally, during the WakeOP campaign turbulence levels were higher, which also can reduce observation times but, conversely, can also degrade model performance.

Another remarkable conclusion can be drawn from a comparison of the scoring results for lateral transport based on Memphis measurements and on WakeOP short-term weather forecasts (NOWVIV). The 90th-percentile deviations, which are of high operational relevance because they represent the poorly predicted cases, yield the almost identical values of 2.26 and 2.23 for lateral transport. This result indicates that the magnitude of the forecast error of crosswind roughly corresponds to the spatial variability of the crosswind over a distance of 2 km. The 2-km distance corresponds to the separation between the Memphis sites for wind and wake-vortex data acquisition. This suggests that instantaneous measurement data of a costly 2-km spaced grid of wind measurement instrumentation along the glide path would not yield much superior results compared to a numerical prediction scheme without assimilation of local instrumentation data. Note that this conclusion is preliminary because it is based on a statistically insufficient amount of data. Further, it neglects the impact of the differences just listed between the Memphis and WakeOP data, and, in particular, it assumes that measurement errors can be neglected.

A closer inspection of how the choice of the device that is used for the determination of crosswind affects the performance of D2P is given in Fig. 3. The figure shows statistics for normalized differences between predictions and observations of lateral wake vortex transport based on different sources of crosswind data for 41 WakeOP cases. Results from the Memphis database are included for comparison. The ratings based on lidar crosswind measurements yield the least dispersed results. Possibly, the averaging time of 80 s is most appropriate because it corresponds roughly to the life span of the vortices. Although the lowest median values are reached with sodar and aircraft data, the respective high 90th-percentile values reflect the suboptimal averaging times of 10 min and 10 s, respectively.

The strong significance of temporal and spatial averaging intervals is best illustrated by the wind inhomogenities, which were observed along the flight track of overflight 8-16 (Fig. 4a). A crosswind jump of almost 5 m/s along less than 200-m length of flight track is advected into the measurement domain in less than 60 s by an

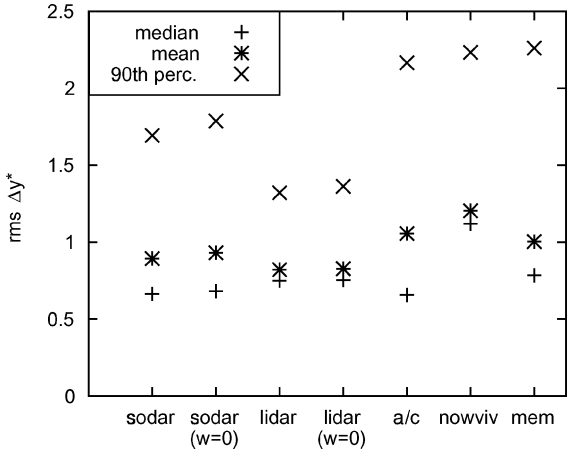


**Fig. 3 Statistics for normalized differences between predictions and observations of lateral wake-vortex transport based on different sources of crosswind data.**

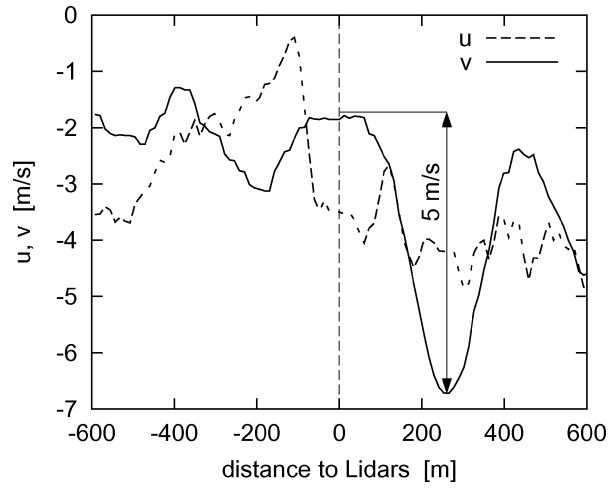


**Fig. 4a Axial wind and crosswind along ATTAS flight track.**

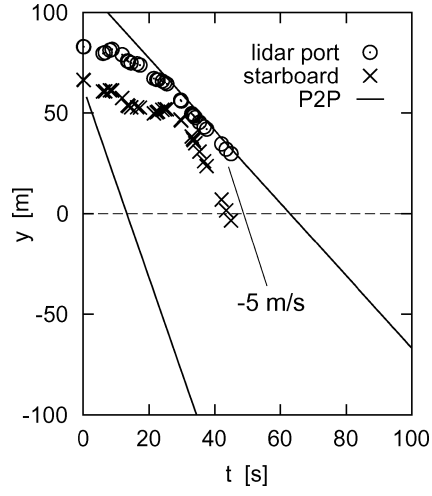


**Fig. 4b Associated lateral vortex drift measured by lidar and predicted by P2P.**

axial wind of about −3 m/s. This is evidenced by the strong lateral acceleration of the vortices delineated in Fig. 4b (line indicates a lateral drift velocity of $v = -5$ m/s). It is most obvious that deterministic wake-vortex predictions must fail here, whereas P2P (based on aircraft wind data) just manages to predict the confidence intervals correctly. P2P predictions driven by sodar and lidar crosswinds yield adequate confidence intervals as a result of the high level of measured turbulence, whereas the lower turbulence predicted by NOWVIV causes insufficient uncertainty allowances (not shown).

Tables 1 and 2 indicate that the deviations of measurement and prediction for lateral transport are roughly doubled compared to vertical transport. This reflects the larger variability and sensitivity associated with crosswind transport compared to the impact of the parameters turbulence, stratification, and vertical wind that control vortex descent. Therefore, for probabilistic predictions we adjust the constants for turbulent spreading to $C_y = 1$ and $C_z = 0.5$.

Finally, Fig. 3 indicates that the exclusion of vertical wind measurements ($w = 0$) can degrade results. Obviously, a more precise temporal descent history along vertical crosswind profiles seems to affect lateral transport favorably. Conversely, we observed situations where the sodar measured positive vertical winds in an updraft, whereas the vortices in immediate proximity of the sodar site experienced negative winds. This means that at least in convective situations, where solar radiation drives the formation of updrafts that are connected to adjacent downdraft regions and both updrafts and downdrafts have extensions that can transport substantial parts of wake vortices in opposite directions,[18] signed vertical wind velocities should not enter the predictions of vertical vortex transport.

In convective atmospheric boundary layers it could be beneficial to use the magnitude of vertical wind velocities to increase vertical uncertainty allowances.

## Probabilistic Model Performance and Aircraft Spacing Reduction Potential

The probabilistic model performance cannot be evaluated by the preceding used scoring approach because increased uncertainty allowances would always improve ratings. Therefore, in this section the probability that the vortices actually evolve within predicted confidence intervals is discussed with regard to a potential runway capacity gain. For an operational system, the uncertainty allowances must be adjusted such that they meet accepted probabilities of appropriate risk metrics. This is beyond the scope of the current manuscript.

The investigations concerning wake-vortex decay are restricted to the Memphis data because there the durations of vortex measurements were generally longer. Vortex transport is considered based on WakeOP data because there vortex trajectory data evaluated by triangulation and a variety of crosswind data sources are available.

### Decay

From the 211 investigated Memphis cases, P2P underestimates circulation for only 0.75% of the measurements provided that the operationally irrelevant initial overestimation of circulation by lidar (compare Fig. 5c) is neglected. In Ref. 12 it is demonstrated that initial overestimations of root circulation by 30–70% can occur when a radii-averaging circulation definition like $\Gamma^*_{5-15}$ is applied. Radii-averaging methods interpret line-of-sight velocities of secondary vortices, which are induced for example by the edges of a flap, as high tangential velocities on large radii of the primary vortex, hence, high circulation. The overestimation ceases when the roll-up process of the multiple vortices that evolve behind an aircraft in high-lift configuration to a single vortex pair is completed.

Rejecting further obviously erroneous measurements, four slightly nonconservative cases (1150, 1151, 1267, 1273) remain. Figure 5 shows case 1150 (B727 aircraft) in detail. The longevity of the vortices in these four cases most likely is caused by shear-layer effects caused by nocturnal low-level jets. All four cases were measured around midnight in a quite stably stratified and low turbulent environment. And in all four cases an unusually long-lived and stalling vortex is observed.

Unfortunately, the crosswind profiles provided by the human evaluator (fine crosses in Fig. 5d) did not result in the observed lateral vortex drift (compare grey dashed lines with symbols in Fig. 5b), but reliable crosswind profiles (bold crosses connected by lines, Fig. 5d) that yield good agreement with the observed vortex drift (black dashed lines, Fig. 5b) could be reconstructed from the measured sodar and tower data. The reconstructed vertical wind profiles

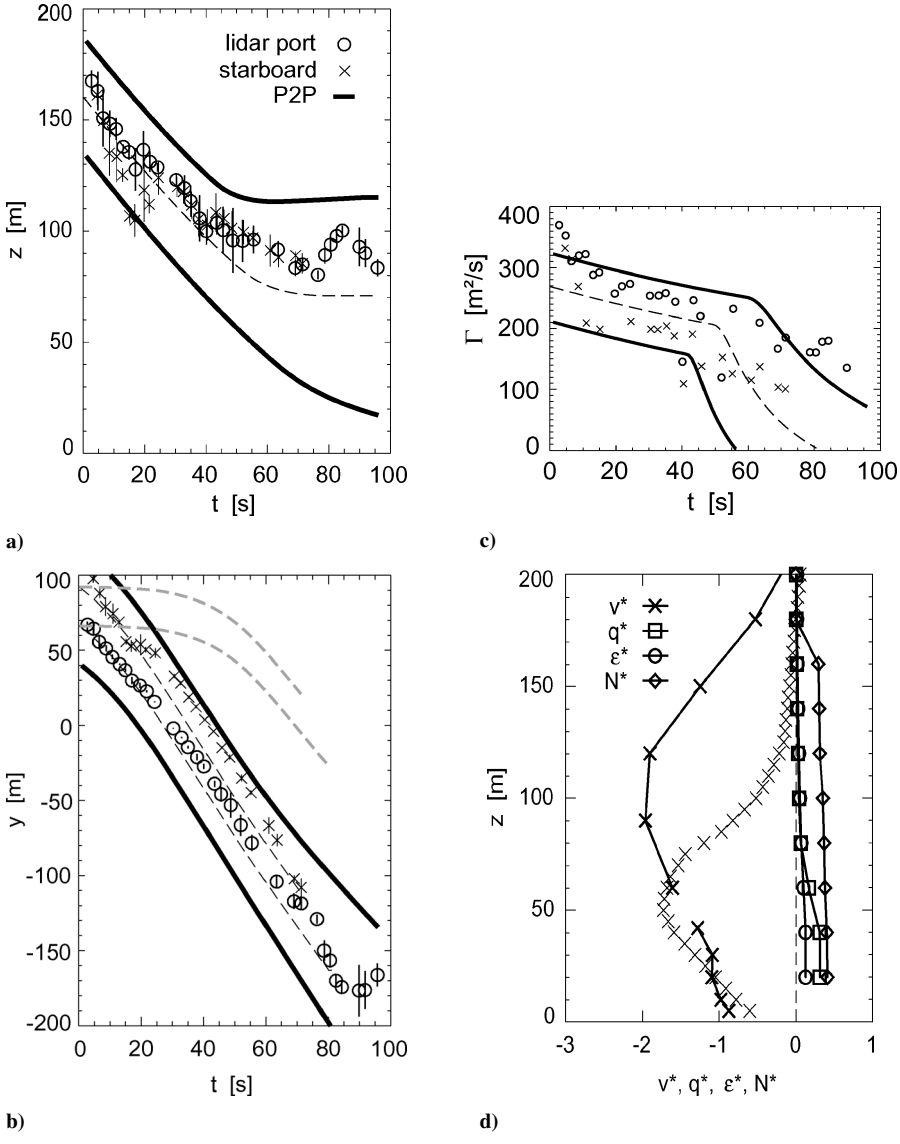


**Fig. 5 a–c) Comparison of P2P predictions with lidar observations for Memphis case 1150 and d) vertical profiles of environmental data.**

contain considerable shear, and in all four cases it is the vortex with the same signed vorticity (SSV vortex) as the vorticity of the background shear that persists longer than its partner vortex by one to three time units.

The fact that for given turbulence the decay of the SSV vortex can be retarded in a constantly sheared environment (compared to the nonsheared environment) is elucidated by numerical simulations,[30,31] which show that vertical shear of $\partial v^*/\partial z^* = 1$ can enhance vortex lifetime by one to two timescales. The shear intensity $\partial v^*/\partial z^* = 1$ represents the case where the background shear just compensates the shear that one vortex excerts on its partner. As a consequence, the destructive effects of mutual strain do not apply for one of the vortices. Further, it can be shown that for the SSV vortex the formation of spiral-shaped secondary vorticity structures, which play a crucial role for vortex decay, is strongly delayed.[32] In case 1150, we determine that there is vertical shear of $\partial v^*/\partial z^* = 0.6$ prevailing in a height interval of 120–180 m. This shear strength seems to be sufficient to reduce the descent and to increase the life span of the SSV vortex noticeably.

Our experience suggests that the complex wake-vortex shear-layer interaction cannot be predicted reliably in an operational environment, in particular because of the difficulties related to the observation and prediction of shear-layer profiles. Therefore, situations where shear-layer effects are not covered by uncertainty allowances have to be identified, and reduced spacing operations based on vortex decay must be ruled out.

Based on the assumption that P2P is capable of predicting upper bounds of the circulation evolution, the respective aircraft spacing reduction potential is assessed. Figure 6 delineates the cumulative distributions of aircraft separations that result from decay predictions of P2P for over 400 cases when an arbitrarily chosen threshold of $\Gamma_t = 100$ m$^2$/s for acceptable vortex strengths is applied. For international civil aviation organization (ICAO) separations (grey bars) a medium approach speed of 70 m/s is assumed. In addition to the 211 Memphis cases, another 191 cases from the 1997 Dallas Fort Worth deployment[33] are included, which lead to similar results. The comparison of the predicted aircraft separations to the currently effective ICAO separations clearly indicates that conservative decay predictions do not allow for reduced spacing. In the majority of the cases, durations predicted by P2P exceed ICAO standards significantly. Reasonably modified circulation threshold values do not alter this statement.

In another study[34] it is found that in 45% of 346 Memphis cases lidar wake-vortex detection times exceed ICAO separations for heavy–heavy aircraft pairings, where the mean circulation at the respective separation of 4 n miles amounts to 0.42 $\Gamma_0$. These findings clearly indicate that it is mainly the transport of vortices away from the glide path by descent and/or advection by crosswind, which is responsible for the high level of safety provided by the currently effective aircraft separation standards. Consequently, these results suggest that in many cases only transport bears the potential to allow for reduced spacing operations with appreciable capacity benefits.

**Transport**

We use the 41 WakeOP cases to evaluate the potential of P2P to predict the time when the vortices have left a safety corridor around the flight track based on different crosswind data sources. The dimensions of the safety corridor are taken from an evaluation of the navigational performance of instrumental landing system (ILS) approaches at Frankfurt International Airport,[35] which is based on 40,000 approaches collected by radar. For the nominal flight altitude of the ATTAS aircraft of 150 m, 95% ($2\sigma$) of the aircraft deviated less than 20 m in lateral and vertical direction from the ILS. Therefore, we define a safety corridor with $\pm 20$ m in both directions.

In addition to the safety corridor and the uncertainty allowances predicted by P2P, another allowance is needed that considers the dimensions of the hazard area around the vortex center position.[36,37] The dimensions of the hazard area depend on the pairing of vortex-generating and following aircraft, the degree of vortex decay, and generally accepted metrics for a safe encounter. In a future operational system, P2P and the dynamically determined dimensions of the hazard area predicted by the DLR Simplified Hazard Area Prediction (SHAPe) model will be linked. The idea is that during one prediction cycle the hazard area shrinks such that aircraft separations can be adjusted to the time when either the hazard area has left the safety corridor or has vanished. Rossow[37] suggests a conservative and static hazard area that can be represented by two wing spans of the wake-generating aircraft in breadth and one wing span in height. This definition corresponds to an one half-span allowance that is added to the vortex center positions in lateral and vertical directions. Because the SHAPe model is still under development, we first neglect the hazard area and then employ the static definition.

Figure 7 shows the cumulative distributions of the vortex ages at which the vortices have left the safety corridor in lateral direction based on lidar observations and P2P predictions. For these predictions P2P employs crosswind data provided either by sodar, lidar, aircraft, or NOWVIV. Table 3 delineates respective quantities that characterize the efficiency of the different approaches. In 76% of the lidar observations, the vortices leave the safety corridor. In the remaining cases, the vortices either stay and decay within the lateral bounds of the corridor, or the observations cease before the vortices could leave the corridor (compare Fig. 1). In P2P predictions, the time to leave the corridor is delayed, and only a reduced fraction of the vortices leave the corridor. This conservative character of the predictions is directly related to the fact that P2P predicts confidence intervals, whereas lidar observations represent two particular vortex

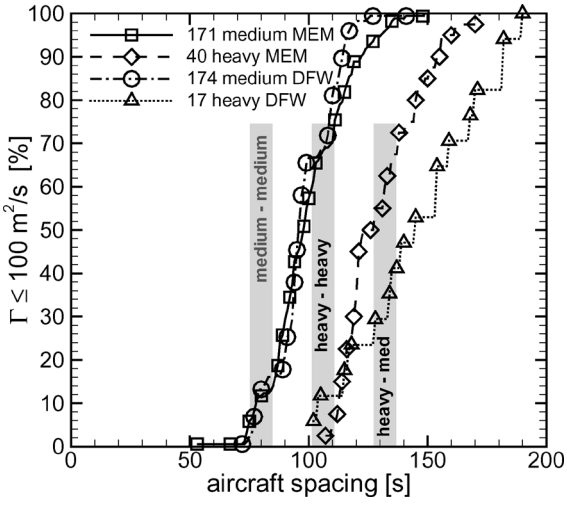


**Fig. 6 Aircraft separations based on conservative decay predictions of P2P.**

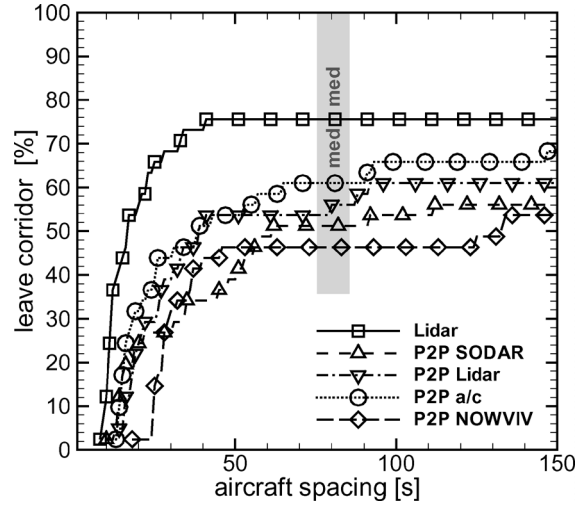


**Fig. 7 Cumulative distributions of times to leave the safety corridor in lateral direction.**

trajectories. The measured average corridor occupation time for the vortices that leave the corridor amounts to 17 s (Table 3). Although this time on average is more than doubled in P2P predictions, there is still potential for appreciable capacity benefits.

Depending on the crosswind source, P2P generates zero to three nonconservative predictions (NoCoPs). NoCoPs denote cases where according to P2P the corridor is cleared from vortices by lateral transport, whereas lidar measurements indicate that there are still vortices inside the corridor. In the investigated cases, the vortices leave the corridor only a few seconds after the predicted clearance. However, all NoCoPs represent nonhazardous situations because the vortices have descended below the corridor floor in advance of the predicted lateral escape. NoCoPs can be entirely avoided when the constant for spreading of the confidence intervals [see Eq. (3)] is increased from $C_y = 1$ to 3.5 for predictions based on lidar and aircraft crosswind data and to $C_y = 1.5$ for crosswind provided by NOWVIV. The percentage of vortices that leave the corridor then decreases to 10, 37, and 46% with average corridor occupation times of 46, 33, and 46 s, respectively.

**Table 3 Efficiency of lateral transport for 41 WakeOP cases based on different crosswind data sources**

| Method | Leave corridor, % | ACOT time, s | NoCoPs, – |
|---|---|---|---|
| Observation | 76 (76) | 17 (20) | —— |
| P2P fed with crosswind from: | | | |
| SODAR | 56 (56) | 37 (46) | 0 (0) |
| Lidar | 61 (61) | 32 (39) | 1 (1) |
| Aircraft | 68 (66) | 35 (38) | 3 (2) |
| NOWVIV | 54 (46) | 44 (39) | 1 (0) |

Table 3 shows further that the efficiency of the approach is only slightly reduced when the static hazard area definition is applied (numbers in brackets). For the ATTAS aircraft, the hazard area is represented by the one half-span length of 10.75 m, which is added to the predicted uncertainty allowances. The introduction of the hazard area either slightly decreases the number of vortices that leave the corridor or it slightly increases the corridor occupation time. The number of NoCoPs remains equal or decreases. Note that the prediction chain NOWVIV-P2P still allows for reduced separations in 46% of the cases with an average corridor occupation time of 39 s and without any NoCoP.

Figure 8 shows the wake evolution of WakeOP overflight 7-08, where wind shear effects modify vortex descent and lateral transport such that the uncertainty allowances of P2P are slightly exceeded. The grey symbols in Figs. 8a and 8b indicate that the vortices start to tilt at a height of 100 m and finally reach a maximum tilt angle of 53 deg. Whereas the port vortex continues to descend undamped, the starboard vortex is stalling at a height of 75 m. At the same time the vortex spacing is increased to a maximum of 2.2 $b_0$. It is not perceptible to what extent the deviation of lateral transport from pure advection is caused by the mutually induced lateral velocity of the tilted vortex pair or the mutual velocity induction of the aircraft vortices with the vorticity patches that are released from the shear layer. Anyway, the described effects are consistent with the topology of wake vortex interaction with shear layers shown by numerical

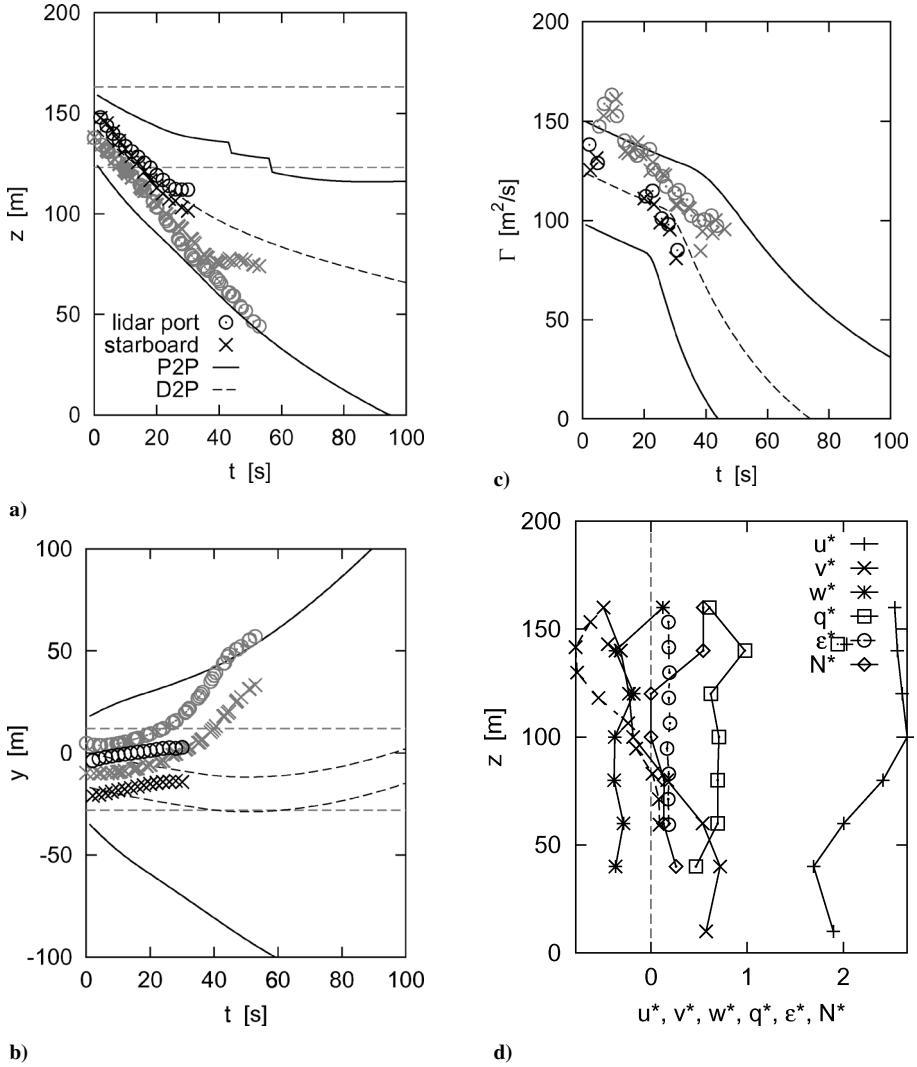


**Fig. 8 Wake evolution of WakeOP overflight 7-08. Detailed description given in WakeOP section.**

simulations.[30,31] We note that compared to the shear assumed in the simulations the maximum normalized shear of 0.3–0.4 measured by lidar and sodar is not very strong. Note that also the axial wind component contains shear of a similar strength.

The different signs of measured and predicted initial lateral drift directions in Fig. 8b indicate that there was considerable variability in the windfield and that potentially higher shear rates could have prevailed in the vicinity of the vortices. This example highlights that shear effects can cause the exceedance of the predicted uncertainty allowances not only regarding decay (see the preceding) but also regarding transport. Further, it illustrates that sufficiently precise observations and, in particular, predictions of shear-layer characteristics are hardly feasible. Even with the applied dedicated wind measurement devices it was not possible to measure shear layers with sufficient accuracy to fully explain the observed vortex behavior. As a consequence, a tradeoff between wind shear prediction capabilities and appropriate uncertainty allowances weighted by the probability of respective shear layers will have to be found.

The relatively small absolute descent distance of the vortices generated by the ATTAS aircraft prevents a meaningful discussion of the potential to reduce aircraft separations based on vortex descent. Although lidar observations indicate an average corridor occupation time of 18 s for 90% of the overflights, it turns out that for aircraft of relatively small size (ATTAS falls towards the lower end of the medium-size category) the upper boundary of the predicted confidence interval often resides close to the boundary of the safety corridor (see Figs. 1a and 8a). As a consequence, already minor modifications of parameters modify statistics significantly such that the results can hardly be transfered to the typical aircraft mix prevailing at large airports.

## Conclusions

The probabilistic two-phase wake-vortex model P2P was applied to observed data from three different field deployments. Altogether, the performance of P2P proves a high level of skill, and the uncertainty allowances appear appropriate. Furthermore, the comparison of a deterministic version of P2P to Sarpkaya's model[9] yields good results. Naturally, the assessment of P2P was done based on a limited number of cases representing only segments of the real weather conditions over which it must finally operate. Therefore, further analyses must complement the current investigations.

Predictions of lateral vortex drift based on different crosswind data sources elucidate the significance of the spatiotemporal wind variability. This variability clearly illustrates the need of probabilistic wake-vortex modeling and the necessity to apply appropriate spatiotemporal resolution in the observations of environmental parameters. It is found that the uncertainties connected with 2-km separated wind observations are of the same order as uncertainties connected to short-term weather forecasts. This result, however, is based on a statistically insufficient amount of data. For vortex descent, uncertainties are noticeably lower. Therefore, we halve the constants for vertical turbulent spreading.

In the majority of the cases, the probabilistic predictions of P2P are conservative. Only flawed crosswind information or pronounced wind shear can cause deficient predictions. Detailed investigations of individual cases reveal that constant wind shear can prolong vortex lifetime, whereas shear layers can modify vertical and lateral transport. These findings corroborate results of numerical simulations.[30,31] Increased uncertainty allowances could eliminate erroneous predictions at the expense of a decreased aircraft spacing reduction potential. Further analyses of observation data are needed to find optimum uncertainty allowances that permit the increase of airport capacity without loss of safety. Apparently, uncertainty allowances are site specific and depend heavily on the available equipment and its performance.

Our investigations indicate that vortex decay proceeds too slowly for appreciable capacity benefits, whereas lateral vortex drift bears considerable potential for safe reduced spacing operations. Clearly, the quality of crosswind measurements and forecasts determines the efficiency of the approach. With regard to the considerable observed crosswind variability, this remains a challenging venture. Almost surprisingly, crosswind provided by short-term weather forecasts would have allowed the safe reduction of separations to below 50 s in 39% of the WakeOP cases. However, this assessment relies on a single control window along the flight path.

A future goal would be to improve short-term weather forecasts by the assimilation of local weather observations. P2P predictions based on now casted environmental parameters could allow for medium-term scheduling applications. Reduced aircraft separations would only be applied provided that current weather observations match weather predictions.

## Acknowledgments

We gratefully acknowledge the essential contributions of all of the teams during the WakeOP trial and the subsequent data processing. The WakeOP campaign has been carried out in the framework of the Brite European research program C-Wake under Contract No. GRD1-1999-10332 and the DLR project Wirbelschleppe. The distribution of the Memphis and Dallas Fort Worth databases by the NASA Langley Research Center, Hampton, Virginia, is greatly appreciated.

## References

[1]Gerz, T., Holzäpfel, F., and Darracq, D., "Commercial Aircraft Wake Vortices," *Progress in Aerospace Sciences*, Vol. 38, No. 3, 2002, pp. 181–208.

[2]Hallock, J. N., Greene, G. C., and Burnham, D. C., "Wake Vortex Research—a Retrospective Look," *Air Traffic Control Quarterly*, Vol. 6, No. 3, 1998, pp. 161–178.

[3]Greene, G. C., "An Approximate Model of Vortex Decay in the Atmosphere," *Journal of Aircraft*, Vol. 23, No. 7, 1986, pp. 566–573.

[4]Corjon, A., and Poinsot, T., "Vortex Model to Define Safe Aircraft Separation Standards," *Journal of Aircraft*, Vol. 33, No. 3, 1996, pp. 547–553.

[5]Sarpkaya, T., "New Model for Vortex Decay in the Atmosphere," *Journal of Aircraft*, Vol. 37, No. 1, 2000, pp. 53–61.

[6]Jackson, W., Yaras, M., Harvey, J., Winckelmans, G., Fournier, G., and Belotserkovsky, A., "Wake Vortex Prediction—An Overview," Transport Canada, Rept. TP 13629E, Montreal, March 2001.

[7]Holzäpfel, F., "Probabilistic Two-Phase Wake Vortex Decay and Transport Model," *Journal of Aircraft*, Vol. 40, No. 2, 2003, pp. 323–331.

[8]Robins, R. E., Delisi, D. P., and Greene, G. C., "Algorithm for Prediction of Trailing Vortex Evolution," *Journal of Aircraft*, Vol. 38, No. 5, 2001, pp. 911–917.

[9]Sarpkaya, T., Robins, R. E., and Delisi, D. P., "Wake-Vortex Eddy-Dissipation Model Predictions Compared with Observations," *Journal of Aircraft*, Vol. 38, No. 4, 2001, pp. 687–692.

[10]Riddick, S. E., and Hinton, D. A., "An Initial Study of the Sensitivity of Aircraft Vortex Spacing System (AVOSS) Spacing Sensitivity to Weather and Configuration Input Parameters," NASA/TM-2000-209849, Jan. 2000.

[11]Rutishauser, D. K., and O'Connor, C. J., "Aircraft Vortex Spacing System (AVOSS) Performance Update and Validation Study," NASA/TM-2001-211240, Oct. 2001.

[12]Holzäpfel, F., Gerz, T., Köpp, F., Stumpf, E., Harris, M., Young, R. I., and Dolfi-Bouteyre, A., "Strategies for Circulation Evaluation of Aircraft Wake Vortices Measured by Lidar," *Journal of Atmospheric and Oceanic Technology*, Vol. 20, No. 8, 2003, pp. 1183–1195.

[13]Hinton, D. A., and Tatnall, C. R., "A Candidate Wake Vortex Strength Definition for Application to the NASA Aircraft Vortex Spacing System (AVOSS)," NASA TM 110343, Sept. 1997.

[14]Zierep, J., *Ähnlichkeitsgesetze und Modellregeln der Strömungslehre*, Braun, Karlsruhe, Germany, 1982, pp. 69–72.

[15]Holzäpfel, F., Gerz, T., and Baumann, R., "The Turbulent Decay of Trailing Vortex Pairs in Stably Stratified Environments," *Aerospace Science and Technology*, Vol. 5, No. 2, 2001, pp. 95–108.

[16]Proctor, F. H., and Switzer, G. F., "Numerical Simulation of Aircraft Trailing Vortices," *Proceedings of the 9th Conference on Aviation, Range and Aerospace Meteorology*, Paper 7.12, American Meteorological Society, Boston, Sept. 2000.

[17]Sarpkaya, T., "Trailing Vortices in Homogeneous and Density-Stratified Media," *Journal of Fluid Mechanics*, Vol. 136, 1983, pp. 85–109.

[18]Frech, M., and Holzäpfel, F., "A Probabilistic Prediction Scheme for Wake Vortex Evolution in a Convective Boundary Layer," *Air Traffic Control Quarterly*, Vol. 10, No. 1, 2002, pp. 23–41.

[19]Dasey, T. J., Campbell, S. D., Heinrichs, R. M., Matthews, M. P., Freehart, R. E., Perras, G. H., and Salamitou, P., "A Comprehensive System for Measuring Wake Vortex Behavior and Related Atmospheric Conditions at Memphis, Tennessee," *Air Traffic Control Quarterly*, Vol. 5, No. 1, 1997, pp. 49–68.

[20]Campbell, S. D., Dasey, T. J., Freehart, R. E., Heinrichs, R. M., Matthews, M. P., Perras, G. H., and Rowe, G. S., "Wake Vortex Field Measurement Program at Memphis, TN, Data Guide," Lincoln Lab., Project Rep. NASA/L-2, Massachusetts Inst. of Technology, Cambridge, MA, Jan. 1997.

[21]Han, J., Arya, S. P., Shen, S., and Lin, Y.-L., "An Estimation of Turbulent Kinetic Energy and Energy Dissiptaion Rate Based on Atmospheric Boundary Layer Similarity Theory," NASA/CR-2000-210298, June 2000.

[22]Gerz, T., "Wake Vortex Prediction and Observation: Towards an Operational System," *Proceedings of the 3rd ONERA–DLR Aerospace Symposium*, 2001, Chap. S1-3.

[23]Köpp, F., Smalikho, I., Rahm, S., Dolfi, A., Cariou, J.-P., Harris, M., Young, R. I., Weekes, K., and Gordon, N., "Characterisation of Aircraft Wake Vortices by Multiple-Lidar Triangulation," *AIAA Journal*, Vol. 41, No. 6, 2003, pp. 1081–1088.

[24]Banakh, V. A., and Smalikho, I. N., "Estimation of the Turbulent Energy Dissipation Rate from the Pulsed Doppler Lidar Data," *Atmospheric and Oceanic Optics*, Vol. 10, No. 12, 1997, pp. 957–965.

[25]Painting, D., *AMDAR Reference Manual*, WMO-No. 958, World Meteorological Organisation, Geneva, 2003, p. 24.

[26]Frech, M., and Tafferner, A., "The Performance of the Model System NOWVIV During the Field Campaign WakeOP," *Proceedings of the 10th Conference on Aviation, Range and Aerospace Meteorology*, Paper J7.4, American Meteorological Society, Boston, May 2002.

[27]Donaldson, C. duP., and Bilanin, A. J., "Vortex Wakes of Conventional Aircraft," NATO, AGARD, AG-204, Paris, May 1975.

[28]Robins, R. E., and Delisi, D. P., "Wake Vortex Algorithm Scoring Results," NASA/CR-2002-211745, June 2002.

[29]Hinton, D. A., "An Aircraft Vortex Spacing System (AVOSS) for Dynamical Wake Vortex Spacing Criteria," *The Characterization and Modification of Wakes from Lifting Vehicles in Fluids*, AGARD, Neuilly-sur-Seine, France, 1996, pp. 23.1–23.11.

[30]Hofbauer, T., "Numerische Untersuchungen zum Einfluss von Windscherung und Turbulenz auf Flugzeugwirbelschleppen," Deutsches Zentrum für Luft- und Raumfahrt, Forschungsbericht 2003-01, Inst. für Physik der Atmosphäre, Oberpfaffenhofen, Germany, 2003.

[31]Hofbauer, T., and Holzäpfel, F., "Behavior of Aircraft Wake Vortices Subjected to Wind Shear," AIAA Paper 2003-3813, June 2003.

[32]Holzäpfel, F., Hofbauer, T., Darracq, D., Moet, H., Garnier, F., and Ferreira Gago, C., "Analysis of Wake Vortex Decay Mechanisms in the Atmosphere," *Aerospace Science and Technology*, Vol. 7, No. 4, 2003, pp. 263–275.

[33]Dasey, T. J., Cole, R. E., Heinrichs, R. M., Matthews, M. P., and Perras, G. H., "Aircraft Vortex Spacing System (AVOSS) Initial 1997 System Deployment at Dallas/Ft. Worth (DFW) Airport," Lincoln Lab., Project Rep. NASA/L-3, Massachusetts Inst. of Technology, Cambridge, MA, July 1998.

[34]Frech, M., and Zinner, T., "Concept of Wake Vortex Behaviour Classes," *Journal of Aircraft*, Vol. 41, No. 3, 2003, pp. 564–570.

[35]Frauenkron, H., Biegholdt, J., Maiss, M., Nalpanis, P., and Smith, E., "FLIP—Flight Performance Using Frankfurt ILS, A Statistical Evaluation of Navigational Performance of ILS-Approaches at Frankfurt International Airport," DFS German Air Navigation Services, Air Traffic Management Division, Offenbach, Germany, Feb. 2001.

[36]Hahn, K.-U., "Coping with Wake Vortex," International Congress of Aeronautical Sciences, ICAS 2002-7.3.1, Sept. 2002.

[37]Rossow, V. J., "Reduction of Uncertainties in Prediction of Wake-Vortex Locations," *Journal of Aircraft*, Vol. 39, No. 4, 2002, pp. 587–596.

# 9 References

Section 9.1 lists a selection of references with contributions by the author in chronological order. The subset of publications which is included and explicitly described in the manuscript is flagged by numbers in brackets. Further external references, which mostly are not cited in the author's integrated publications, are listed in section 9.2.

## 9.1 Selected Author's Contributions

Holzäpfel, F. (1996): Zur Turbulenzstruktur freier und eingeschlossener Drehströmungen. Dissertation, Lehrstuhl für Feuerungstechnik, Universität Karlsruhe

Holzäpfel, F., Lenze, B. (1997): Swirl-induced intermittency – Assessment of a novel effect modifying the turbulence structure of swirling jets. Feuerungstechnik – Kaleidoskop aus aktueller Forschung und Entwicklung, Editor B. Lenze, ISBN 3-00-001593-0, Karlsruhe, pp. 67–91.

Gerz, T., Holzäpfel, F. (1999): Wing-Tip Vortices, Turbulence, and the Distribution of Emissions. AIAA Journal, Vol. 37, No. 10, pp. 1270–1276.

[1] Holzäpfel, F., Gerz, T. (1999): Two-Dimensional Wake Vortex Physics in the Stably Stratified Atmosphere. Aerospace Science and Technology, Vol. 3, No. 5, pp. 261–270.

Holzäpfel, F., Lenze, B., Leuckel, W. (1999): Quintuple Hot-Wire Measurements of the Turbulence Structure in Confined Swirling Flows. Journal of Fluids Engineering, Vol. 121, No. 3, pp. 517–525.

[2] Holzäpfel, F., Gerz, T., Frech, M., Dörnbrack, A. (2000): Wake Vortices in Convective Boundary Layer and Their Influence on Following Aircraft. Journal of Aircraft, Vol. 37, No. 6, pp. 1001–1007.

[3] Holzäpfel, F., Gerz, T., Baumann, R. (2001): The turbulent decay of trailing vortex pairs in stably stratified environments. Aerospace Science and Technology, Vol. 5, No. 2, pp. 95–108.

Meleshko, V.V., Gurzhi, A.A., Dörnbrack, A., Gerz, T., Holzäpfel, F., Hofbauer, T. (2001): Interaction of two-dimensional trailing vortex pair with a shear layer. International Applied Mechanics, Vol. 37, No. 7, pp. 948–957. Russian Original: Prikladnaya Mekhanika, Vol. 37, No. 7, pp. 128–136.

Frech, M., Holzäpfel, F. (2002): A Probabilistic Prediction Scheme for Wake Vortex Evolution in a Convective Boundary Layer. Air Traffic Control Quarterly, Vol. 10, No. 1, pp. 23–41.

Frech, M., Holzäpfel, F., Gerz, T., Konopka, J. (2002): Short-term prediction of the horizontal wind vector within a wake vortex warning system. Meteorological Applications, Vol. 9, No. 1, pp. 9–20.

Gerz, T., Holzäpfel, F., Darracq, D. (2002): Commercial Aircraft Wake Vortices. Progress in Aerospace Sciences, Vol. 38, No. 3, pp. 181–208.

Holzäpfel, F., Hofbauer, T., Gerz, T., Schumann, U. (2002): Aircraft Wake Vortex Evolution and Decay in Idealized and Real Environments: Methodologies, Benefits and Limitations, Fluid Mechanics and its Applications. Vol. 65, Advances in LES of Complex Flows, edited by R. Friedrich, W. Rodi, Kluwer Academic Publishers, Dordrecht, ISBN 1-4020-0486-9, pp. 293–309.

Hofbauer, T., Holzäpfel, F. (2003): Behavior of Aircraft Wake Vortices Subjected to Wind Shear. AIAA Paper 2003–3813.

[4] Holzäpfel, F. (2003): Probabilistic Two-Phase Wake Vortex Decay and Transport Model. Journal of Aircraft, Vol. 40, No. 2, pp. 323–331.

[5] Holzäpfel, F., Gerz, T., Köpp, F., Stumpf, E., Harris, M., Young, R.I., Dolfi-Bouteyre, A. (2003): Strategies for Circulation Evaluation of Aircraft Wake Vortices Measured by Lidar. Journal of Atmospheric and Oceanic Technology, Vol. 20, No. 8, pp. 1183–1195.

[6] Holzäpfel, F., Hofbauer, T., Darracq, D., Moet, H., Garnier, F., Ferreira Gago, C. (2003): Analysis

of wake vortex decay mechanisms in the atmosphere. Aerospace Science and Technology, Vol. 7, Issue 4, pp. 263–275.

[7] Holzäpfel, F. (2004): Adjustment of Subgrid-Scale Parametrizations to Strong Streamline Curvature. AIAA Journal, Vol. 42, No. 7, pp. 1369–1377.

Holzäpfel, F., Frech, M., Hahn, K.-U., Schwarz, C., Joos, H.-D., Ringel, G., Korn, B. (2004): Development of a Concept for the Assessment of A380 Wake Vortices. DLR-IB 553-1/2004, DLR Oberpfaffenhofen, p. 72.

[8] Holzäpfel, F., Robins, R.E. (2004): Probabilistic Two-Phase Aircraft Wake-Vortex Model: Application and Assessment. Journal of Aircraft, Vol. 41, No. 5, pp. 1117–1126.

## 9.2 External References

Aviation Week, August 26, 2002, p. 50.

de Bruin, A.C., Speijker, L.J.P., Moet, H., Krag, B., Luckner, R., Mason, S. (2003): S-Wake Assessment of Wake Vortex Safety. NLR-TP-2003-243, National Aerospace Laboratory NLR.

Delisi, D. P., Greene, G. C., Robins, R. E., Vicroy, D. C., Wang, F. Y (2003): Aircraft Wake Vortex Core Size Measurements. AIAA Paper 2003–3811.

Donaldson, C.duP., Bilanin, A.J. (1975): Vortex Wakes of Conventional Aircraft. NATO, AGARD-AG-204.

Garodz, L. J., Clawson, K. L. (1993): Vortex Wake Characteristics of B757-200 and B767-200 Aircraft Using the Tower Flyby Technique, ERL ARL-199, NOAA Air Resources Lab., Idaho Falls, ID.

Hallock, J.N., Greene, G.C., Burnham, D.C. (1998): Wake Vortex Research – A Restrospective Look, Air Traffic Control Quarterly, Vol. 6, No. 3, pp. 161–178.

Hallock, J.N.: Wake Vortex Bibliography, http://www.volpe.dot.gov/wv/.

Hemm, R., Shapiro, G., Lee, D.A., Gribko, J., Glaser, B. (1999): Benefit Estimates of Terminal Area Productivity Program Technologies. NASA/CR-1999-208989, p. 144.

Köpp, F., Rahm, S., Smalikho, I. (2004): Characterization of Aircraft Wake Vortices by $2-\mu$m Pulsed Doppler Lidar, Journal of Atmospheric and Oceanic Technology, Vol. 21, No. 2, pp. 194–206.

Lamb, Sir H. (1945): Hydrodynamics. Dover Publications, New York (originally published in 1879).

Lanchester, F.W. (1907): Aerodynamics. Constable, London.

Prandtl, L. (1918): Tragflügeltheorie. I. Mitteilung, Nachrichten der K. Gesellschaft der Wissenschaften zu Göttingen, Mathematisch-physikalische Klasse, S. 451–477.

Prandtl, L. (1919): Tragflügeltheorie. II. Mitteilung, Nachrichten der K. Gesellschaft der Wissenschaften zu Göttingen, Mathematisch-physikalische Klasse, S. 107–137.

Rossow, V.J. (1999): Lift-generated vortex wakes of subsonic transport aircraft. Progress in Aerospace Sciences, Vol. 35, No. 6, pp. 507–660.

Spalart, P.R. (1998): Airplane Trailing Vortices. Annual Review of Fluid Mechanics, Vol. 30, pp. 107–138.

Widnall, S. E., (1975): The structure and dynamics of vortex filaments. Annual Review of Fluid Mechanics, Vol. 7, pp. 141–165.